6-2003

Investigation of the Iced Flowfield Characteristics Related to the Stall Margin Instrumentation Used in Icing Conditions

Erik Pederson
Western Michigan University

INVESTIGATION OF THE ICED FLOWFIELD CHARACTERISTICS RELATED TO THE STALL MARGIN INSTRUMENTATION USED IN ICING CONDITIONS

by

Erik Pederson

A Dissertation
Submitted to the
Faculty of The Graduate College
in partial fulfillment of the
requirements for the
Degree of Doctor of Philosophy
Department of Mechanical and Aeronautical Engineering

Western Michigan University
Kalamazoo, Michigan
June 2003

INVESTIGATION OF THE ICED FLOWFIELD CHARACTERISTICS RELATED TO THE STALL MARGIN INSTRUMENTATION USED IN ICING CONDITIONS

Erik Pederson, Ph.D.

Western Michigan University, 2003

The purpose of this dissertation is to investigate the relationship between the flowfield surrounding an iced airfoil and the stall margin instrumentation developed for use in icing conditions. The stall margin system indicates to the pilot the change in available lift due to ice accretions on the leading edge of an airfoil. This system displays the change in the form of a normalized lift coefficient. Four pressure ports are chosen to specifically maintain a constant calibration curve, for pressure versus normalized lift coefficient, regardless of ice shape. This allows these pressures to be used to determine the change in maximum lift coefficient. The instrumentation currently maintains an accuracy of $\pm$ 10%. There was a need to investigate the relationship between the flowfield and the port locations, and the airfoil shape and the port locations. This allowed further understanding of the placement of these ports. Through this investigation, better port locations have been determined and the accuracy and usefulness of the instrumentation has been increased.

This investigation was conducted using wind tunnel testing techniques. A 2-D NACA 23012 pressure model and a 2-D NACA 23012 force model were constructed and tested to determine initial port locations for the stall margin instrumentation. Simulated ice shapes were produced using the LEWICE software from NASA Glenn. The flowfield around the airfoil was mapped using smoke wire flow visualization and hotwire anemometry. A single wire system was used to determine a 2-D profile of the turbulence intensity levels surrounding the ice covered wing. The movement of the separation region behind the ice shape, with change in angle of attack, was also

investigated. The relationship between this movement and the port locations was documented and its significance determined. Through these observations, better port locations for the stall margin instrumentation were determined thus allowing accuracy of the instrumentation to be increased to $\pm$5%.

ProQuest Information and Learning Company
300 North Zeeb Road
P.O. Box 1346
Ann Arbor, MI 48106-1346

ACKNOWLEDGEMENTS

I would like to thank the committee not only for their assistance and guidance in this research but also for the education they have provided me through my years here at Western. The knowledge I have received is invaluable and will be put to good use. I would like to thank Dr. Liou for always challenging me and proving to me that I cannot always predict test questions. I would like to thank Dr. Sahin for truly sparking my interest in Fluids when I took ME 356. I would like to thank Dr. Tanner for imparting to me his knowledge about research ethics. I would like to thank Dr. Merati for his monetary and intellectual support throughout my career at Western. I would especially like to thank Professor Hoadley for guiding me and giving me the knowledge and confidence to achieve any goal I put my mind to. I would also like to thank Professor Hoadley for his unending interest in all things related to Aviation.

DEDICATION

I would like to dedicate this work to my wife. Thank you for the many nights you put up with my frustrations and setbacks. It has been a long road and I could not have done this without your assistance. I apologize for the times that it looked like I was listening to what you said and was really analyzing data in my head. I would also like to dedicate this to my parents for providing me with the up-bringing and environment to facilitate the growth of my curiosity and imagination.

TABLE OF CONTENTS

LIST OF TABLES

LIST OF FIGURES

NOMENCLATURE

ADWT - Advanced Design Wind Tunnel

α or AOA - Angle of Attack also known as AOA

AR - Aspect ratio, equal to b / c

b - Wing span

c - Chord of the wing or airfoil

C_D - Drag Coefficient $C_D = \frac{F_D}{0.5 \cdot \rho \cdot V^2 \times S}$

C_L - Lift Coefficient $C_L = \frac{F_L}{0.5 \cdot \rho \cdot V^2 \times S}$

C_{Lmax} - Maximum obtainable CL in the current airplane/wing configuration

C_{LN} - Normalized Lift Coefficient $C_{LN} = \frac{C_L}{C_{L\max}}$

$C_{Lcruise}$ - Cruise configuration lift coefficient

$C_{L\alpha}$ - Slope of the lift curve or C_L versus α graph

C_{L0} - Lift Coefficient at zero degrees angle of attack

C_M - Pitching Moment Coefficient $C_M = \frac{M_y}{0.5 \cdot \rho \cdot V^2 \times S \times c}$

Cp - standard pressure coefficient $Cp = \frac{p_{static} - p_\infty}{0.5 \cdot \rho \cdot V^2}$

Cpx - pseudo-pressure coefficient determined from four wing surface pressures

δ_1 - boundary layer displacement thickness

δ_2 - boundary layer momentum thickness

F_D - Drag Force

F_L	- Lift Force
FAA	- Federal Aviation Administration
FAR	- Federal Aviation Regulation
h/c	- Ice shape height non-dimensionalized to wing or model chord. This is the perpendicular distance from the wing surface
LWC	- Liquid Water Content of the Cloud (measured in grams/m^3)
MVD	- Median Volume Droplet, this is the same as Mean Effective Drop Diameter (measured in microns)
M	- Mach Number (Air Velocity / Speed of Sound)
M_y	- Pitching Moment
NACA	- National Advisory Committee for Aeronautics (now NASA)
NASA	- National Aeronautics and Space Administration
Q	- Dynamic Pressure $Q = \frac{1}{2}\rho V^2$
Re	- Reynolds Number $\mathrm{Re} = \frac{\rho \cdot V \cdot c}{\mu}$
ρ	- Air Density (0.00238 slug/ft^3 @ Sea Level)
μ	- Air viscosity
S	- Wing Area
SM	- Stall Margin (SM = 1 – C_{LN}); Note: SM = 1 aircraft is stalled
u	- local air velocity (equations 1, 2 and 3)
U_e	- External Air Velocity, Wind Tunnel Air Velocity, Streamwise Velocity out of Boundary Layer
u_i	- Fluctuating component of the velocity
u`	- Root Mean Square value of the fluctuating component of the velocity
u_{mean}	- Average streamwise component of the velocity
V	- Air velocity

x/c	- Non-dimensionalized distance from the leading edge of the wing to the chord. This horizontal distance is non-dimensionalized to the wing or model chord.
y/c	- Non-dimensionalized vertical distance on a wing airfoil shape. This vertical distance is non-dimensionalized to the wing or model chord

CHAPTER 1 - INTRODUCTION

The general aviation and commuter aircraft fleet represent 80% of all the aircraft flying. These aircraft are subject to icing encounters at increased intervals due to their flight profiles and high utilization. The pilots of these aircraft are trained to recognize marginal flight characteristics of the plane by stall indication systems (percentage of lift available before stall indicator) designed for clean airfoils. Current systems are inaccurate at best when an accretion of ice develops. Nowhere in the modern cockpit is there an instrument alerting the pilot of the slightest degradation of aircraft performance when ice is accreting. Added to this is the ever-increasing use of modern airfoils that are extremely sensitive to ice accretions. Therefore potential exists for an accident due to ice accretions to occur.

Ice can form on an aircraft when it flies into a cloud of super-cooled water droplets. Different types of ice can form depending on the surrounding conditions. If the temperature of the air is well below freezing and the Liquid Water Content (LWC) of the air is low, the water droplets will tend to freeze immediately to the aircraft. These ice shapes will tend to follow the shape of the object they freeze upon. On a wing, the ice will follow the shape of the leading edge. This type of ice is known as "Rime" ice and has a minimal effect on the performance of the aircraft. If the air temperature is near the freezing point and the LWC is high the water droplets will tend to not freeze entirely and flow around the wing. This type of freezing tends to form ice shapes with horns and ridges. This type of ice is called "Glaze" and can seriously affect the performance of an aircraft. There can also be an ice type called "Mixed" ice which occurs when the LWC fluctuates and the temperature is between well below freezing and the freezing point.[1]

There are standards that are followed for certification of anti-icing and de-icing systems. Typically many types of ice shapes are tested that are formed in two different lengths of time, they are the 22.5-minute ice shape and 45-minute ice shape. The 22.5-minute ice shape is used in analysis and certification to determine the performance loss in the event of an ice protection system failure. The 45-minute ice shape is used to determine the performance loss for an unprotected aerodynamic surface.[2] The Federal Aviation Administration (FAA) has regulations regarding the different types of icing conditions an aircraft is required to fly in to be certified for flight in icing conditions. The regulations are stated in the Federal Aviation Regulations (FAR's) Part 25, Appendix C; FAR Part 23 Section 23.1419; and FAR Part 25 Section 25.1419. In general, Part 23 and Part 25 of the FAR's govern the design and certification of General Aviation aircraft. Section 25.1419 and Section 23.1419 state generally the same rules for the certification of the aircraft. An aircraft must be controllable and stable with ice formations formed during conditions stated in these parts of the FAR's.

Many factors are involved with the degradation of performance of an aircraft due to ice accretion. The location of the ice on the aerodynamic surface is extremely important. Ice will cause the airflow to separate over a larger area of the surface at a lower angle of attack than normal. The location of the ice determines the amount of the surface that will be separated. Leading edge ice shapes will cause the flow to separate over the entire surface. Ridge ice, or ice located behind a deicing system, will cause the flow to separate behind the ridge and remain attached in front of the ridge. Another important factor is the thickness of the ice. The greater the thickness of the ice shape, the greater the performance degradation. A third factor is the height of the surface roughness of the ice shape. A rougher ice shape will remove more energy from the airflow and cause earlier separation of the flow around the aerodynamic surface and greater performance degradation.

Many systems have been developed to combat the formation of ice on an aircraft. Pneumatic de-ice boots have been used on the leading edge of aircraft to remove the ice after it has formed. Heating leading edges on aerodynamic surfaces serve the same purpose as the de-ice boots as well as preventing the ice to form in the first place. Alcohol mixtures are also used as an anti-icing device. The alcohol is allowed to seep from ports in the aircraft wing and prevent the formation of ice. These systems are typically used on or near the leading edge of an aerodynamic surface. It is not efficient to use these systems to de-ice the entire aircraft. Therefore it is possible to develop ice aft of the de-icing systems and on areas where it is impossible to install the anti-icing or de-icing systems. These systems are not designed to run continuously and will allow ice to form before removing it from the surface. De-icing and anti-icing equipment is expensive to install and operate and not all aircraft have this available to them. The combination of an aircraft having a de-icing system fail or not having such a system at all necessitates the need for a system that will provide information on the performance degradation of the aircraft with ice. The presence of this system will allow the pilot to maintain control of the aircraft in an icing situation.

Initial research conducted at Western Michigan University on a NACA 0018 wing has shown that by measuring select wing surface pressures, the stall margin of a wing can be determined in icing conditions.[3] The stall margin instrumentation provides a real time display of the aircraft's available lift by detecting even the smallest changes in stall margin. This would allow for immediate feedback to the pilot, even when the aircraft is on autopilot. Aircraft that are susceptible to tailplane stall and roll anomalies will benefit the most, allowing the pilot to take early action to avoid disaster. If forced to remain in the icing situation, this instrumentation will give the pilot direct knowledge of the performance changes to the aircraft.

An airplane's stall margin (SM) can be defined as the percentage of the airplane's lift coefficient (C_L) remaining to be used, as shown in equation (1). The normalized lift coefficient (C_{LN}) is defined in equation (2). When the stall margin is 100%, the aircraft has its entire lift coefficient available for use. When the stall margin is 0% the aircraft has none of its lift coefficient available and the aircraft has

reached stall. The opposite is true when discussing the normalized lift coefficient. A C_{LN} equal to 1 indicates that 100% of the lift coefficient has been used. A C_{LN} equal to 0 indicates that the entire lift coefficient is available for use.

$$(1) \quad SM = (1 - C_{LN}) \cdot 100\%$$

$$(2) \quad C_{LN} = \frac{C_L}{C_{Lmax}}$$

The stall margin utilize four surface pressures to determine the stall margin. The surface pressures are combined in a pseudo-pressure coefficient called Cp_x. Equation (3) details Cp_x and Figure 1 shows possible port locations for the pressures in Cp_x. C_{LN} is calibrated to Cp_x thereby providing a relationship between the change in maximum lift and measurable wing pressures. Through this method the Stall Margin is then known.

$$(3) \quad Cp_x = \frac{CP1 - CP2}{CP3 - CP4}$$

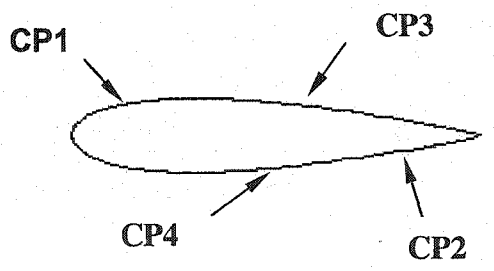

Figure 1 – Possible Pressure Port Locations

Currently available cockpit instrumentation systems display a normalized angle of attack, or require the pilot to manually adjust the airplane's approach speed based on flight manual data combined with the calculated aircraft weight and flap

configuration. The accuracy of these systems is dependent on calibrations performed for known configuration changes, such as wing flaps. Changes in the wing airfoil shape due to ice formation are not accounted for in the system calibrations and are errors. If an airplane accumulates significant ice, the actual stall margin will decrease with no indicated change in the cockpit. As the actual stall margin approaches zero the airplane will have a reduction in its performance and control margins. If the aircraft is being flown by an autopilot, these reduced margins most likely will go undetected by the flight crew. If the pilot and autopilot have accurate stall margin data the ice formation can be detected early allowing the crew to respond in a timely manner. The pressure system being developed at Western Michigan University can provide this information to the aircraft and pilot.

At the conclusion of the initial research conducted at WMU there were many questions that needed investigation. The initial test on the NACA 0018 was limited to a low Reynolds number of 600,000 due to model vibrations. The following questions were asked:

1) What are the effects of Reynolds number on the instrumentation?

2) Will the port locations change for other airfoil shapes?

3) Will the system work for other more severe ice shapes?

4) What is the instrumentation sensing on the wing that indicates the change in lift coefficient due to ice? (Why does it work?)

The work for this PhD Dissertation focuses on answering these questions.

CHAPTER 2 – LITERATURE REVIEW

Research in the field of aircraft icing has been conducted mainly due to the need for information on performance characteristics of aircraft in icing conditions. As more and more people began using air travel as their main mode of transportation, airlines needed to be able to fly in bad weather conditions. As the number of commuter flights increased, so did the number of accidents due to ice buildup on the aircraft. Anti-icing and De-icing systems were developed to increase the survivability of aircraft in icing conditions. Not much was known about the performance of an aircraft in icing conditions. As early as the 1938 researchers began to develop Anti-icing and De-icing systems and develop a knowledge base for the performance of aircraft in icing conditions. The two main motivators behind this research are the FAA and the National Aeronautics and Space Administration (NASA). The FAA and NASA have developed Aviation Safety Programs to educate pilots on the hazards of flying in icing conditions, and also to develop icing tolerant aircraft. Some of the most significant research and most related to this dissertation proposal have been conducted at NASA Glenn Research Center, Wichita State University and the University of Illinois at Urbana-Champaign.

2.1 AIRFOIL PERFORMANCE DEGRADATION (EXPERIMENTAL)

Airfoil performance degradation is measured mainly through the change in two quantities. The change in lift or lift coefficient describes the degradation in the ability of the wing to produce enough lift to keep the aircraft flying. Severe increases in stall speed are a direct result of the decrease in maximum lift coefficient. The second quantity is the change in drag or drag coefficient. Increases in drag significantly increase the power required to maintain the airspeed necessary for controlled flight. Most likely the earliest testing involving ice accretion was performed in 1938 by Gulick.[4] Gulick used surface roughness to simulate ice accretions. Decreases in maximum lift of 25% and an increase in drag of 90% were observed during this research.

2.1.1 Changes in Lift

One of the most recent works in documenting airfoil performance in icing conditions has been conducted by Papadakis *et al.*[2,5] at Wichita State University. In this work the effects of ice on a NACA 0011 airfoil were investigated. The ice shapes were simulated using a flat plate spoiler mounted toward the leading edge of the wing. The spoiler angle and height were varied throughout the test. The spoiler configuration is shown in Figure 2. The changes in C_L, C_D, C_M, and Cp due to the simulated ice shapes were documented. In some cases the C_L was observed to decrease as much as 70%. The C_M would change due to the change in pressure distribution around the airfoil. One of the most significant findings in this work was the change due to Reynolds number. The Reynolds number effects on the iced airfoil

were not significant for lift and drag, but there were significant changes in C_M, and Cp distribution due to the changes in Reynolds Number. This change in C_M and Cp distribution was attributed to the change in length of a separation bubble formed behind the simulated ice shape. As the Reynolds number would increase, the length of the bubble would also increase, thereby affecting the C_M and Cp distribution.

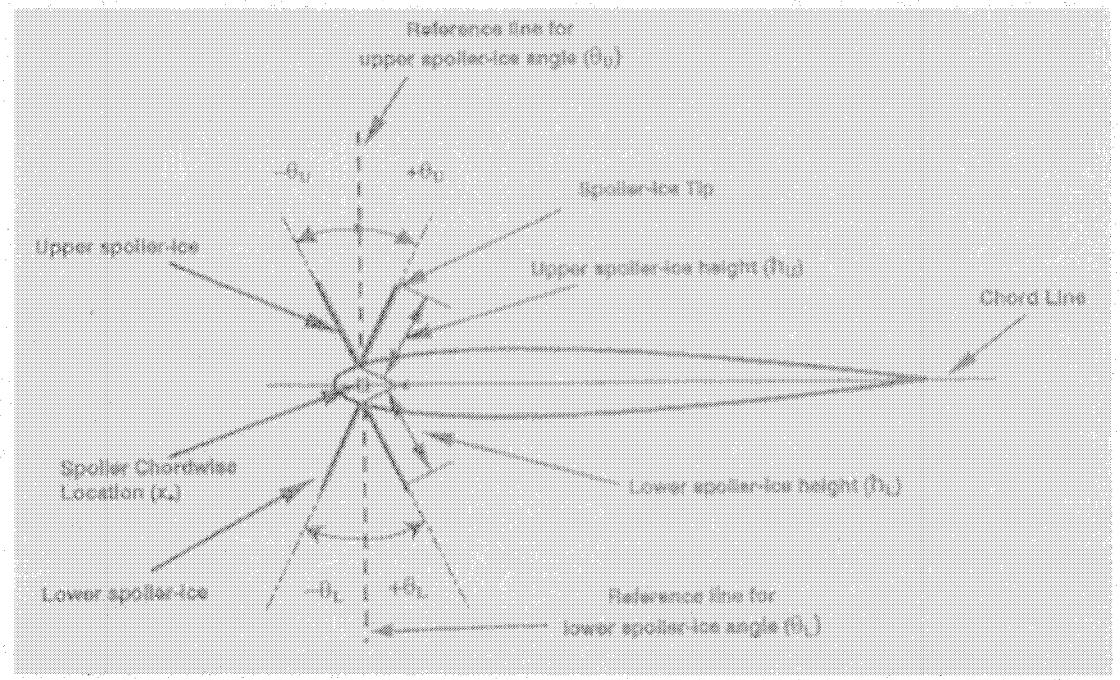

Figure 2 – Spoiler Ice Shapes[5]

Other work, similar in manner to the work conducted at Wichita State, has been conducted at the University of Illinois. Bragg *et al.*[6, 7, 8, 9] have conducted work mainly on a NLF-0414 airfoil and a NACA 23012m (modified) airfoil shape. The NLF-0414 airfoil is a Natural Laminar Flow airfoil and the 23012m airfoil is a typical airfoil found on general aviation and commuter type aircraft. In these tests, the ice shapes were simulated using quarter round and half round shapes mounted on the leading edge and progressively aft chord locations. The ice configurations are shown in Figure 3. Performance degradations were documented for multiple Reynolds numbers, angles of attack, ice shape heights, and ice shape locations. Similar effects were found by Bragg *et al.* that were found by Papadakis *et al.* As was expected, the maximum lift coefficient increased with Reynolds number for the clean airfoil, but for the iced airfoil the Reynolds number had less of an effect on the maximum lift coefficient. The tests were limited to three Reynolds numbers and according to Bragg *et al.* research the maximum lift coefficient would increase to a "critical" Reynolds number at which point there was not much change in the maximum lift coefficient. The tested "critical" Reynolds number for the NLF-0414 was 0.5×10^6. The tested

"critical" Reynolds number for the 23012m was 1.0x 10^6. The fact that the airfoil performance coefficients seem to be insensitive to Reynolds number allows the performance information to be applied to higher Reynolds numbers closer to full-scale aircraft Reynolds numbers. Other important factors to obtain from this research are the effect of ice shape height on the performance characteristics of the airfoil. As the height was increased for ice shapes located on the leading edge, there was a minimal change in maximum lift coefficient. The most significant changes came when the ice shape was moved to a 10% chord location. The ice shape height at this location became an important factor in the change of the maximum lift coefficient.

In 2001 Laflin and Papadakis[10] also tested an NLF-0414 wing using simulated ice shapes from plastic castings developed at the NASA Glenn Icing Research Tunnel. Tests were again conducted to document the changes in lift, drag, pitching moment, and hinge moment. Similar results of performance degradation were found.

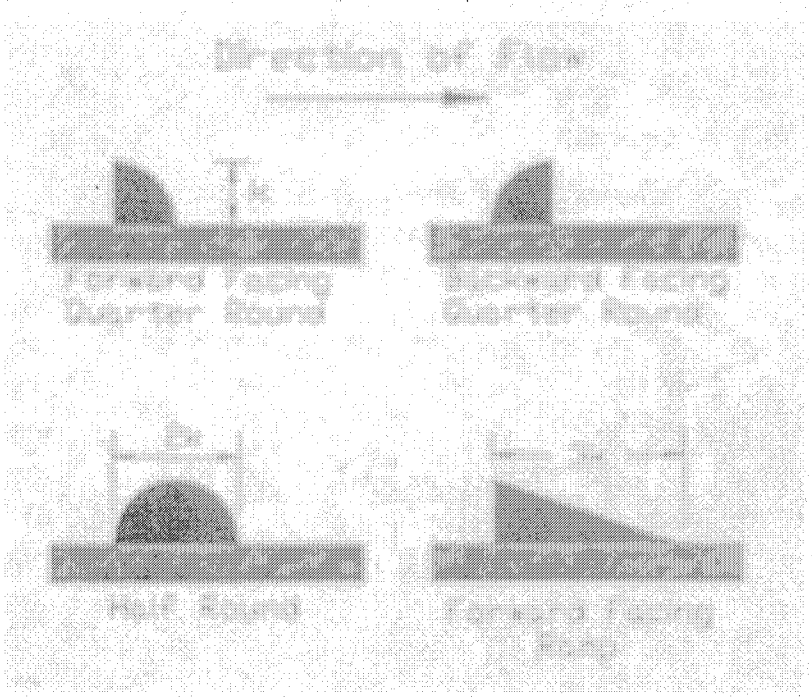

Figure 3 – Ice Shape Configurations[6]

Finite wing models were also tested by Khodadoust and Bragg.[11] Simulated horned leading edge ice shapes were attached to a finite wing. Significant decreases in lift were observed. Pressure distributions were measured at multiple spanwise locations to determine the influence of 3-D effects on the flow with a simulated ice shape. 3-D effects to downwash from wing tip vortices did not affect the pressure distributions until high angles of attack were reached. Large areas of separation were observed across the wing. At the wing root near the tunnel wall (simulating a wing

attached to a fuselage) the flow separation behind the ice shape was reduced due to the influence of the boundary layer on the tunnel wall.

2.1.2 Changes in Drag

Both Papadakis *et al.*[2, 5] and Bragg *et al.*[6, 7, 8, 9] document significant increases in drag with the spoiler and quarter round ice shapes. Earliest works to determine drag increases on iced airfoils were researched by Gray and Von Glahn [12, 13, 14]. In the 1950's Gray and Von Glahn measured the drag increases on six different airfoils. Based on information obtained from their research an empirical equation was developed to calculate drag increase with ice accretion. This equation utilized the relationship between angle of attack, airfoil chord, airfoil thickness, airfoil leading edge radius, air velocity, air temperature, time in icing conditions, liquid water content, and droplet impingement efficiency (% of droplets to impact airfoil surface) to determine the change in drag. This equation was accurate for the given airfoils. At the time of their research an empirical equation could not be developed for the change in lift due to lack of research data.

2.2 AIRFOIL PERFORMANCE DEGRADATION (COMPUTATIONAL)

In 1990 Kwon and Sankar[15] attempted to predict pressure distributions on an iced finite wing using computational methods. Using a 3-D Navier-Stokes solver a NACA 0012 wing was analyzed using smooth ice shapes. Computational chordwise pressure distributions were compared to experimental chordwise pressure distributions at multiple spanwise locations. Tests were conducted at angles of attack of 4 degrees and 8 degrees. The pressure distributions matched well at the lower 4 degree angle of attack. Deviations between the experimental and computational distributions began to occur at the higher 8 degree angle of attack due to the separated flow behind the ice shape. They were not able to accurately predict the flow near the stall region.

Around 1995 Cebeci, Roknaldin, and Carr[16, 17] were able to predict the maximum lift coefficient and post stall lift coefficients for mild ice shapes formed in the time span of 60 seconds. In 1997 Dompierre *et al.*[18] using a fully compressible Navier-Stokes code and unstructured meshes were able to predict the lift curve for a smooth iced NACA 0012 airfoil. The computational tests were conducted using a smooth ice shape and an ice shape with surface roughness. The lift curve was compared to an experimentally determined lift curve for an identical smooth ice shapes and the two curves correlated very well. The code would not completely converge for the rough ice shape. The comparison of the drag versus angle of attack did not match the experimental data for the smooth or the rough ice shape conditions.

Computational studies were then conducted to determine the effects of smoothing an ice shape on the lift and drag coefficients. Chung *et al.*[19] conducted tests on a NACA 23012 model to determine the effects of smoothing. To have a good comparison computational and experimental data were both collected. The results were that as the ice shape was changed from rough to smooth the maximum lift

coefficient would increase and the drag would decrease. The change seen was minimal at lower ranges of smoothing, but for extreme cases of smoothing the change was large.

Lee, Bragg *et al.*[20] also conducted computational tests on the quarter round and half round simulated ridge ice shapes and found good correlation between the experimental and computational data. The Navier-Stokes Unstructured 2D code developed at NASA Langley for multi-element airfoils was used for these calculations. The maximum converged angle of attack solutions corresponded with experimentally determined maximum lift coefficient angle of attack for the NACA 23012 modified airfoil. Kumar and Loth[21] also conducted tests on the NACA 23012 modified airfoil using the quarter round and a simulated ice shape. Good correlation between experimental and computational lift data was found. Pressure distributions also matched well.

Chung *et al.*[22] conducted computational test on an aircraft wing with a ridge ice shape. The work was part of an accident investigation involving a twin engine aircraft. A 2D and 3D Navier-Stokes code was used for the computations. A large difference between stall angles of attack was seen between the 2D and 3D calculations. The 3D code predicted stall angles 4 degrees higher than the 2D code. A large sensitivity to grid resolution was also observed during these tests.

2.3 SCALING EFFECTS

It is impossible to test full-scale models at all times, thus scaling effects are important to consider when conducting wind tunnel tests. The effects of scaling a clean (no-ice) model are fairly well understood. The matching of Reynolds number and/or Mach number between full-scale models and sub-scale models tends to ensure the acquisition of full-scale data, when testing sub-scale. However there may be times when Reynolds number and Mach number may be impossible to match. For clean (non-iced) models, this situation can be handled through the intentional tripping of boundary layers and other testing techniques.

For iced airfoils the matching of scale data to real life data is more of a challenge. Due to the complex nature of the flow structure around the ice shape, the sub-scale data may not always match full-scale data. Geometric scaling of the ice shapes may not always produce a scaled flow structure. The most recent work in this area has been conducted by Papadakis *et al.*[23] through use of simulated ice shapes provided through the use of the LEWICE 2.0 software, developed at NASA Glenn Research Center. Papadakis *et al.*[23] conducted multiple tests on a NACA 63_A213 airfoil to compare the change in performance and flow characteristics between full-scale and sub-scale models. Three models were used. The first model had a chord of 57 inches, the second had a chord of 24 inches, and the third had a chord of 4 inches. Reynolds number effects on the maximum lift coefficients were found to be insignificant for the 57-inch model and relatively small for the 24 inch and 4 inch models. The pressure distribution and moment coefficient were most effected by the change in Reynolds number. The maximum pressure coefficients tended to be lower, for the smaller scale models, even if the Reynolds number was matched between the

scales. The pressure distribution tended to change due to the effects of the geometric scaling. This was attributed to the change in length of the separation bubble region observed behind the ice shapes. Even with a matched Reynolds number, the separation bubble tended to elongate with smaller scale airfoils and ice shapes. This in effect changed the load distribution on the airfoil, which is directly linked to the change in pitching moment coefficient. The effects of scaling in iced airfoil situations, and how to correctly scale a model to obtain full-scale data is not fully understood at this time and needs to be studied further.

2.4 DOCUMENTING THE FLOW FIELD AROUND AN ICED AIRFOIL

2.4.1 Separation Bubble

The dominating flow structure in the flowfield around an iced airfoil is the separation bubble that occurs behind a "Glaze" or horned ice shape. The separation bubble is similar to the separated region that occurs near the leading edge on a clean airfoil at low Reynolds numbers. Much work has been done in this area to develop ways to determine the length and location of the separation bubble. Mueller *et al.*[24], at the University of Notre Dame, documents methods used to measure the flowfield characteristics in the non-iced laminar separated bubble region. Figure 4, reproduced from Mueller *et al.*[24], clearly shows the flow structure in this region.

Research on documenting the structure of the separation bubble, caused by ice shapes, has been conducted by Bragg, Khodadoust and Gurbacki.[25, 26] Methods similar to that of Mueller were used to document the flow behind the ice shape. Four main methods are documented in the aforementioned works.

The first method uses the airfoil pressure distribution to determine the separation and reattachment point of the bubble. For the laminar flow bubble, an inviscid pressure distribution is determined and compared to the viscous pressure distribution. The point at which the viscous distribution diverges from the inviscous solution is the separation point. The point at which the viscous distribution converges back with the inviscous distribution is the reattachment point. In the case of an iced airfoil, the clean pressure distribution is compared to the iced pressure distribution. This method is regarded by some researches as somewhat inaccurate and only works for a few cases.[25, 26]

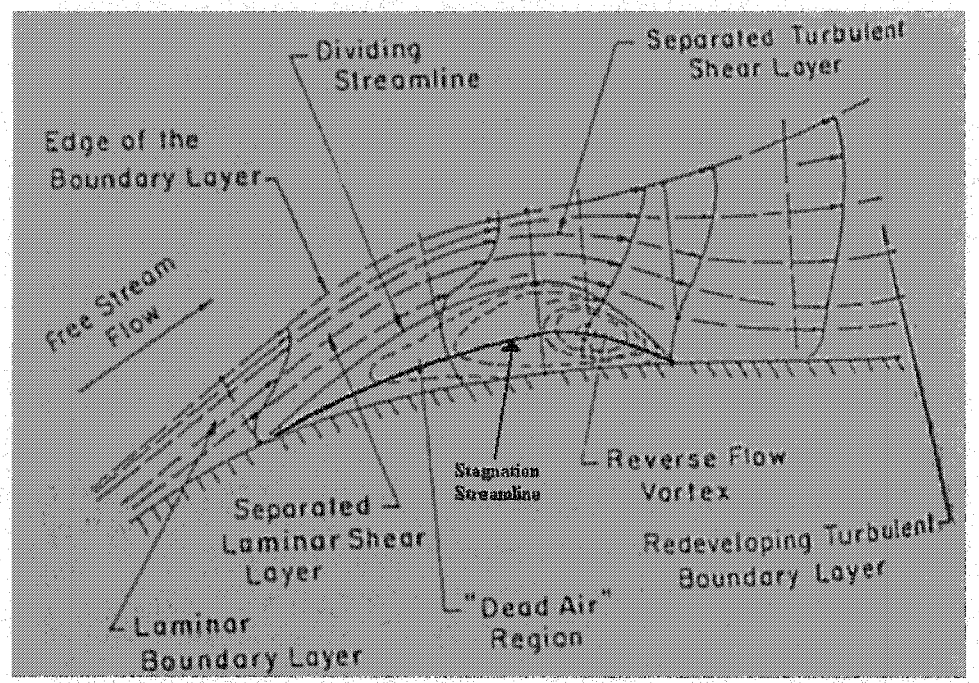

Figure 4 – Flow Structure near a Separation Bubble[24]

The second method used is an oil flow visualization technique. A light film of oil is placed on a wind tunnel model and the air is blown over the model. The oil will tend to pool at the separation and reattachment point of the bubble. The oil pools due to the fact that on either side of these points the flow is in opposite directions and the flow in between stagnates. The reverse flow is developed inside the bubble.[25, 26]

The third and fourth methods use the velocity profile measurements at various chord locations in the separated region. The velocity profile was obtained either through Hotwire measurements or Laser Doppler Velocimetry (LDV). The LDV is determined to be more accurate because the flow direction can be obtained using LDV. Only with a 2 or 3 component hotwire anemometry system will the flow direction be ascertained. Error may be introduced into the calculations by using a single component velocity from a hotwire system. The velocity profile is used to determine the dividing streamline, shown in Figure 4, which will indicate the location of the bubble. The streamline is determined using Equation 4. This equation integrates the velocity profile above and below the mean flow stagnation streamline, Figure 4, until the mass of the fluid flowing in the reverse direction below the stagnation streamline is equal to that flowing in the forward direction above the stagnation streamline. This works for constant density flows. The stagnation streamline is the location at which the mean flow or stream wise velocity is equal to zero. The velocity direction at the stagnation streamline is perpendicular to the stagnation streamline.[25, 26]

(4) $$\int_0^{y_{sep}/c} \frac{u}{U_e} d\left(\frac{y}{c}\right) \cong 0$$

The fourth method uses the velocity profile to determine the boundary layer displacement thickness and momentum thickness. Equations 5 and 6 show the equations used to determine these thicknesses.

(5) Displacement Thickness $$\frac{\delta_1}{c} = \int_0^{\delta/c} \left(1 - \frac{u}{U_e}\right) d\left(\frac{y}{c}\right)$$

(6) Momentum Thickness $$\frac{\delta_2}{c} = \int_0^{\delta/c} \left|\frac{u}{U_e}\right| \left(1 - \frac{u}{U_e}\right) d\left(\frac{y}{c}\right)$$

The momentum thickness will provide a graph of the thickness versus the non-dimensional chord location. In this graph there will be trends that will indicate the location of the separation point and the location of the reattachment point. The displacement thickness can only provide the location of the separation point by determining the location of the first local maximum. Figures 5 and 6, reproduced from *Bragg et al.*[26], provide a good representation of these two graphs. The momentum thickness graph indicates the separation point by the first local maximum and the reattachment point by a second local maximum.

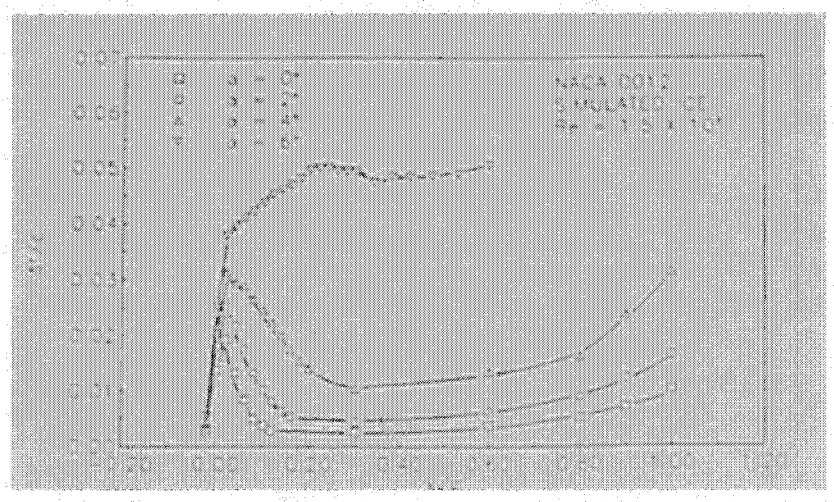

Figure 5 – Boundary Layer Displacement Thickness Sample Graph[26]

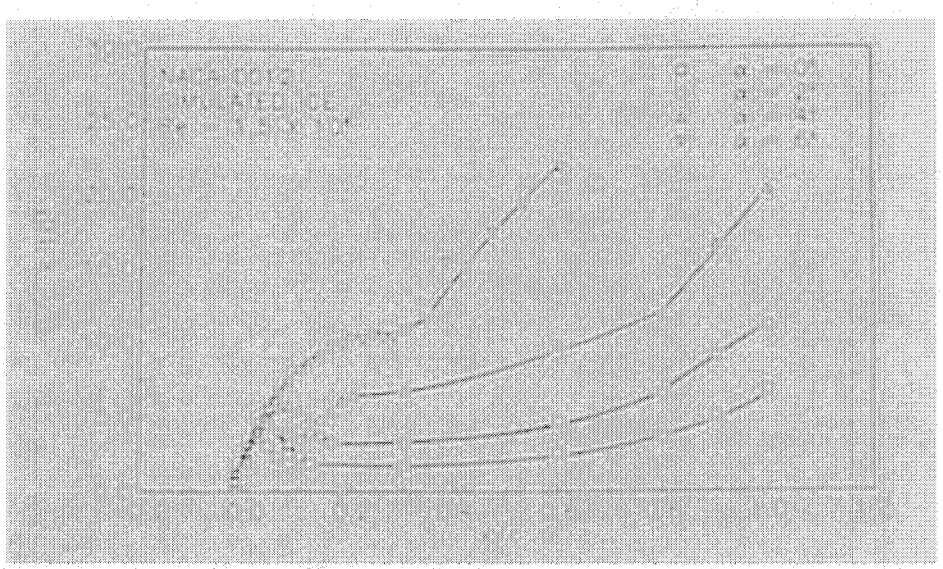

Figure 6 – Boundary Layer Momentum Thickness Sample Graph[26]

2.4.2 Stalled Wing

Another important aspect of the flowfield around an iced or non-iced airfoil is the fluctuating airflow caused by flow separation of a stalled airfoil. When an airfoil stalls, vortices are shed that produce vorticity (or rotation) in the flow. This is referred to as the separated region of flow in which the air reverses direction. This rotation causes fluctuations in the pressure distribution. Time histories of pressure distributions on a stalled wing were researched in detail by Yon and Katz[27]. The change from a smooth pressure distribution to a fluctuating pressure distribution is important for predicting the stall angle of attack for an iced airfoil.

2.4.3 Surface Roughness Effects

Many ice shapes can be seen as large scale surface roughness on an airfoil. Much research has been conducted on the effects of surface roughness on the flow over an aerodynamic surface. Kerho, Cummings and Bragg[28, 29, 30, 31, 32] have conducted much research in this area as part of Kerho's dissertation and subsequent publications. This research was conducted with simulated roughness elements on or near the leading edge of the wing. Typically the height of the roughness element was 1 millimeter or less. The roughness would initiate the transition from laminar to turbulent flow. On some ice shapes there tends to be a smooth region followed by a rough region. The rough region is thought to occur near or in the region of transition from laminar to turbulent flow. This region tends to increase heat transfer and cause water to freeze quicker on the surface of the wing. This causes a region of larger surface roughness and further degradation of the airfoil performance. Many wind tunnel tests are conducted with smooth ice shapes even though the surface roughness

is known to exist. It is important to consider the effects of this surface roughness. Kerho, Cummings and Bragg documented the effects of the surface roughness. In this research it was found that the addition of roughness to a clean airfoil decreased the maximum lift coefficient which is directly related to a change in the pressure distribution. Levels of turbulence intensity on the order of 10% were found toward the trailing edge of the clean airfoil. With the addition of surface roughness the turbulence intensity levels increased aft of the location of the surface roughness. The turbulence intensity increase widened the bands of turbulence intensity toward the trailing edge of the airfoil. The roughness elements were shown to induce transition, but at no time was there a fully developed turbulent boundary layer in the region of the roughness elements. The surface roughness was typically located in the favorable pressure gradient region on the airfoil. Favorable pressure gradients typically increase the Reynolds number required for transition to a fully developed turbulent boundary layer as is well documented by Driest and Blumer.[33] The roughness elements may also need to protrude further from the airfoil to create the turbulent boundary layer. Based on these observations it will be important in the future to investigate the effects of surface roughness on simulated ice shapes related to the operation of the stall margin instrumentation.

2.5 CURRENT INSTRUMENTATION IN DEVELOPMENT

Two systems are currently in development to produce instrumentation that will determine the degradation in lift under icing conditions and display this knowledge to the pilot in the cockpit. The first system is being worked on by Bragg *et al.*[34] at the University of Illinois. The second system is being developed by Hoadley and Pederson[3] at Western Michigan University.

2.5.1 University of Illinois

The first system being worked on by Bragg *et al.* senses the change in flap/elevator hinge moment due to the accretion of ice. The system has to take into account many parameters, including the hinge moment, and the many parameters used by Gray and Von Glahn[12]. These parameters are continuously monitored and run through a neural network to determine the output lift degradation. The system is still under development and is fairly complicated. Real time indication of stall margin is not present at this time.

2.5.2 Western Michigan University

Hoadley and Pederson[3] are developing the second instrumentation system. This system uses four pressures measured around the airfoil to relate a pseudo-pressure coefficient to the normalized lift coefficient. This system was first developed by Hoadley[35, 36] in the early 1980's to indicate stall margin change to the pilot due to

flap deflections and angle of attack changes. The technology has now been applied to iced aircraft situations. The system can indicate the stall margin, ±10%, to the pilot regardless of what ice shape is on the leading edge.

The system developed at WMU for use in icing conditions uses four surface pressures, measured aft of the ice formation, from which the aircraft's normalized lift coefficient (C_{LN}) is determined. The pressure port locations are selected such that the calibration algorithm remains nearly constant as the leading edge ice shape and thickness change. For the initial research a 2-D airfoil pressure model was used to obtain the surface pressure distribution for a range of angles of attack and ice formations. Analysis of the data has identified port locations that provide C_{LN} data within 11% of the actual value, with and without ice. The initial data was collected using an airfoil approximating a NACA 0018, as this model was readily available. A software package, LEWICE 2.0, was obtained from NASA Glenn Research Center and was used to predict four ice shapes. These shapes were cut from a foam block, using a hot wire, and attached to the model leading edge for testing.

2.5.2.1 Experimental Setup

A 12 inch chord pressure model, which approximated an NACA 0018 airfoil, was adapted for the WMU Advanced Design Wind Tunnel (ADWT). The model spanned the entire 42.5 inch test section. This was done to eliminate 3-D effects on the wing thereby simulating 2-D flow. The model had twenty pressure ports on the upper wing surface and twenty ports on the lower wing surface.

The wind tunnel at WMU is not capable of producing ice, thus another method had to be developed to predict and model the ice shapes. For this purpose a computational ice simulation software package, LEWICE 2.0, developed at NASA Glenn Research Center, was used.[37] This software uses computational methods to predict the ice shape that forms on a surface. This shape is based on the angle of attack, temperature, airspeed, water droplet size, liquid water content and time in the icing situation. Figure 7 shows the different shapes used in this test. Each ice shape was formed using the same airspeed, droplet size and angle of attack, while varying the temperature and duration in the icing conditions. These parameters were used to simulate an aircraft in a cruise flight configuration. Both glaze and rime ice shapes were modeled; however, configuration (1) was not tested due to model vibration problems. For the baseline wing configuration, and configurations (2), (3), and (4), surface pressure data were collected over a range of angles of attack. The ports under the ice formation were not used, as they may not be available under actual icing conditions.

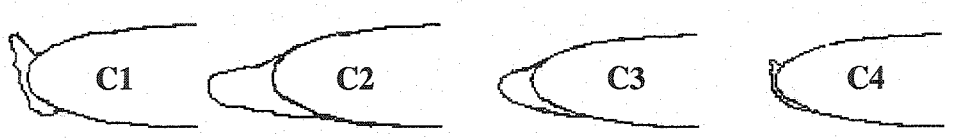

Figure 7 – Computationally Determined Ice Shapes[3]

To determine C_{LN}, the stall angle of attack for each ice configuration needed to be known. The pressure model produced too great a load for the available wind tunnel balance and the pressure tubing would have interfered with the balance. Thus the stall angle of attack could not be determined from force data. Tufts, placed on the wing upper surface at several chord locations, were observed to determine at what angle of attack the flow separated. For this series of experiments, a flow separation at 50% of the chord was considered to be stalled. By knowing the stall angle of attack, the C_{LN} could be determined for each angle of attack and ice formation tested. The stall angles of attack for each configuration are listed in Table 1.

	Stall Angle of Attack (deg)
No Ice	9
Configuration 2	4.8
Configuration 3	5
Configuration 4	6

Table 1 – Stall Angles of Attack[3]

A non-trivial Cp_x was computed for each combination of the pressure ports not located under the ice formation. To qualify for consideration, the relationship between Cp_x and C_{LN}, between a C_{LN} of 0.5 and 1.0, was examined. This range of C_{LN} represents the normal landing and takeoff values. The slope of the C_{LN} versus Cp_x curve was required to be greater than a minimum threshold to ensure sufficient sensitivity to changes in C_{LN}. The port sets that met this criterion were compared against the other ice shapes and the baseline data.

2.5.2.2 Experimental Results

This analysis yielded a set of port locations that maintained nearly the same relationship, regardless of ice configuration. The x/c locations for this set of ports are listed below.

CP1 – Upper Surface x/c = 0.22 CP2 – Lower Surface x/c = 0.68
CP3 – Upper Surface x/c = 0.41 CP4 – Lower Surface x/c = 0.41

As described in equation (7), the pressures measured at these ports are combined to give Cp_x.

$$(7) \qquad Cp_x = \frac{CP1 - CP2}{CP3 - CP4}$$

Figure 8 shows the C_{LN} vs. Cp_x relationship, for this set of ports. The relationship is shown for the no ice baseline and ice configurations (2), (3), and (4), which are labeled C2R4, C3R2, and C4R1, respectively.

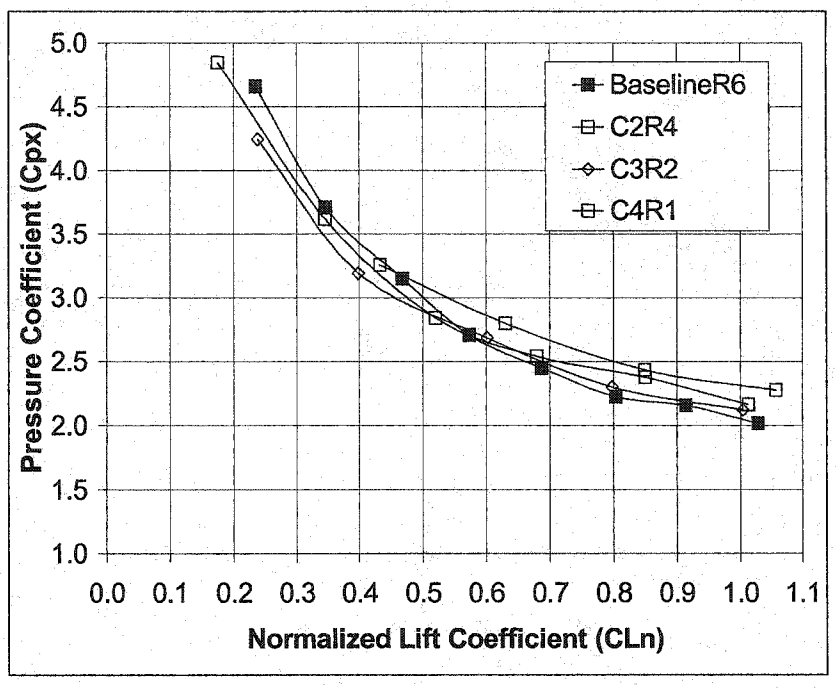

Figure 8 – Cp_x Versus C_{LN} for the Selected Port Locations[3]

2.5.2.3 Instrumentation Evaluation

The ice and no ice curves coincide fairly well at the higher C_{LN} conditions. A C_{LN} of 0.6 to 1.0 is typically seen in approach to landing and landing flare flight regimes. The advantage of using this system is better seen by comparing the C_{LN} displayed to the pilot using the pressure instrumentation to a typical C_{LN} displayed to the pilot using an angle of attack sensor. The angle of attack sensor cannot sense the change in wing performance due to the ice configurations and therefore indicated the same C_{LN} regardless of ice buildup. To best understand this comparison, the graph in Figure 9 must be studied.

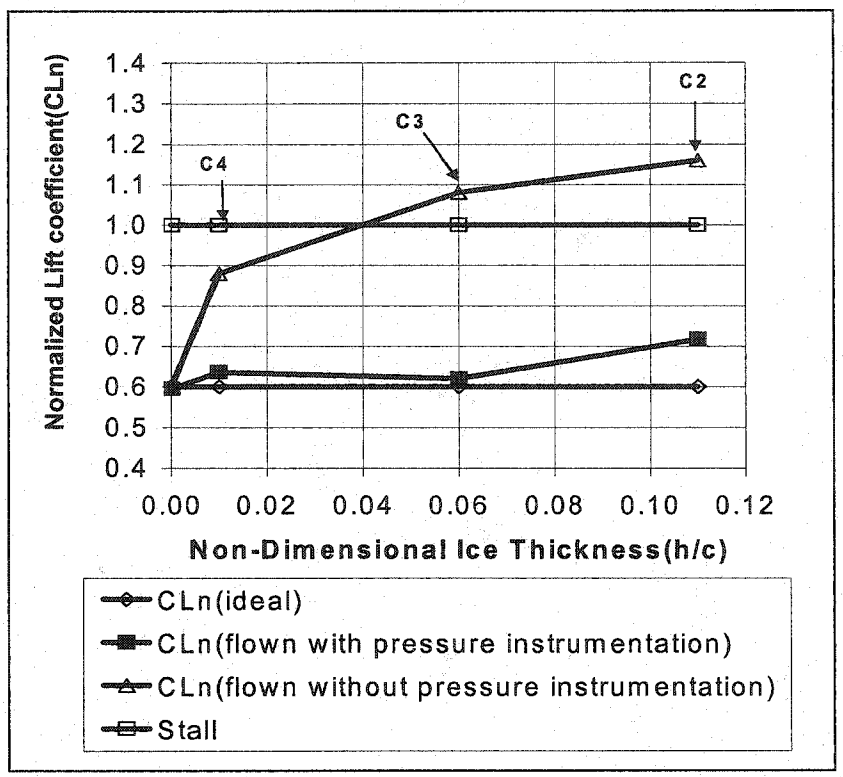

Figure 9 – Comparison for an Approach Flown with an Indicated C_{LN}=0.6[3]

Figure 9 uses the data gathered from the NACA 0018 wind tunnel test. A C_{LN} equal to 1.0 indicates a 100% use of lift coefficient or a stalled aircraft. A C_{LN} = 0.6 is a typical approach to landing C_{LN}. This is equal to the typical approach to landing at an airspeed of 1.3 times the aircraft stall speed in the no ice or clean configuration. With no ice on the wing at an h/c = 0 the angle of attack (AOA) and pressure instrumentation will both indicate a C_{LN} = 0.6. If there was ice on the wing similar to ice configuration 4, the AOA system will still indicate a C_{LN} = 0.6, while the actual stall margin will have risen to a C_{LN} = 0.88 (close to stall). If the pressure system had been used, the pilot would have seen the C_{LN} rising toward 0.88 and would have known to lower the angle of attack and increase airspeed. Doing so would allow the pilot to maintained an indicated C_{LN} = 0.6, which would have corresponded to an actual C_{LN} = 0.64. Now consider an ice shape similar to configuration 3. The AOA system will still indicate a C_{LN} = 0.6, while the actual stall margin will have risen to a C_{LN} = 1.08 (stalled). If the pressure system was used, the pilot would have seen the C_{LN} rising toward 1.08 and would have known to lower the angle of attack and

increase airspeed. Doing so would allow the pilot to maintained an indicated C_{LN} = 0.6, which would have corresponded to an actual C_{LN} = 0.63. This would have allowed the pilot to maintain control of the aircraft. Even with the error in C_{LN} from the pressure instrumentation shown in Figure 9, the pilot would still have maintained an approach C_{LN} of 0.72 or less. From these tests it was concluded that this system could indeed work, but further research needed to be conducted to validate the system and understand the mechanism behind the ice port selection.

CHAPTER 3 - EXPERIMENTAL SETUP

3.1 WMU SUBSONIC WIND TUNNEL

The subsonic wind tunnel at Western Michigan University is a closed loop tunnel. The tunnel can obtain a maximum calibrated airspeed of 250 ft/sec. The tunnel has a test section measuring 96 inches in length, 42.5 inches in width and 32.5 inches in height. The test section is shown in Figures 10 and 11.

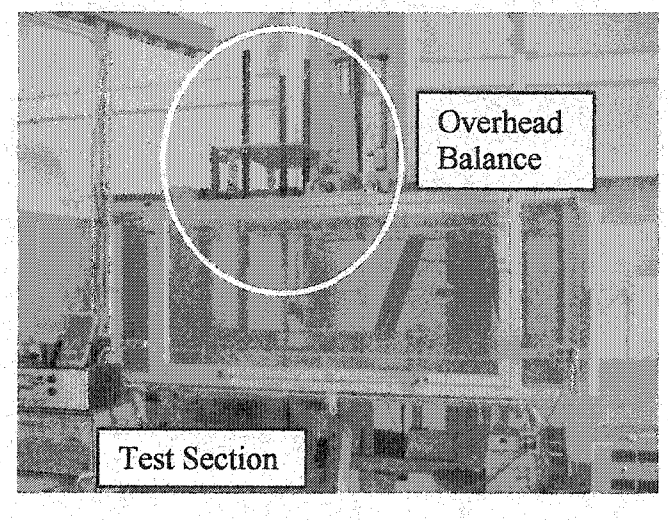

Figure 10 – ADWT Test Section with overhead balance

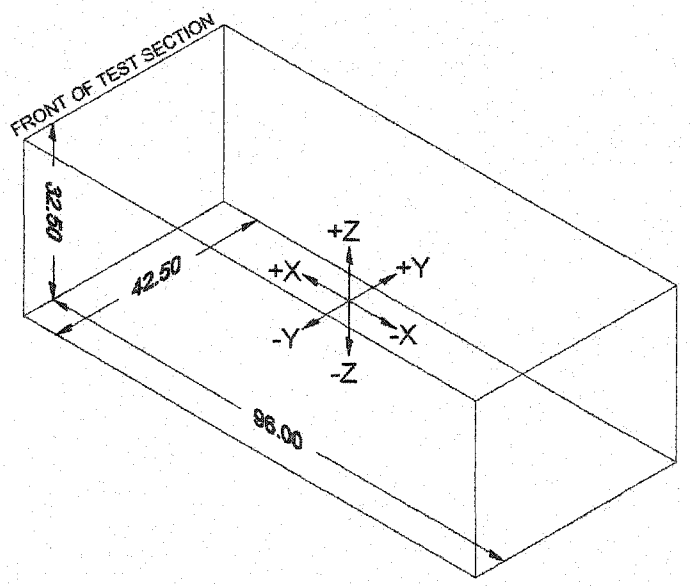

Figure 11 – Test Section Coordinate System and Dimensions

The background turbulence intensity in the test section has been documented using hotwire anemometry. The turbulence intensity is a measure of the velocity fluctuations in the streamwise direction of the flow. The lower the turbulence intensity levels in the tunnel the better the flow quality in the test section. Typically a good quality wind tunnel is at or near a turbulence intensity of 0.1%. Turbulence levels are shown in Figures 12 and 13. The levels in the center of the test section are at 0.5%.

All data collection and motion control is controlled through a Labview program located on a computer in the control room. An arm is located on the top of the tunnel which can traverse the y-z plane in the center of the test section. The tunnel temperature is measured using a thermocouple located on the lower end of the y-z probe. During pressure and force measurements the y-z probe is removed from the tunnel with the exception of the lower two inches of the arm. The tunnel dynamic pressure is controlled by the speed of the fan. The dynamic pressure is measured using two pitot-static probes located near the front of the test section on the side walls. The dynamic pressure is read through a pressure transducer which was calibrated using a water manometer. The barometric pressure is read through a mercury barometer located on the wall of the control and is manually entered into the Labview control program. The tunnel Reynolds number is calculated from these measured values.

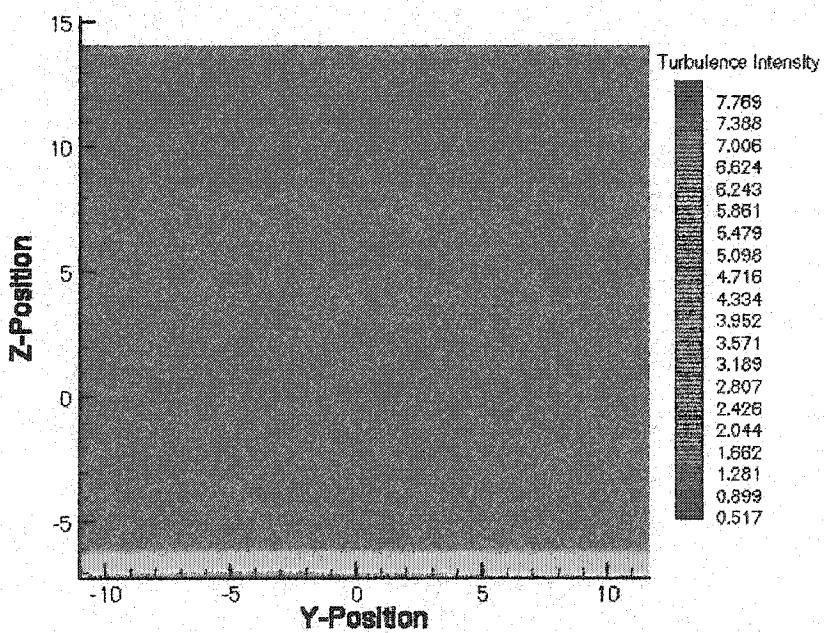

Figure 12 – Test Section Turbulence Intensity, Re ~ 1,000,000

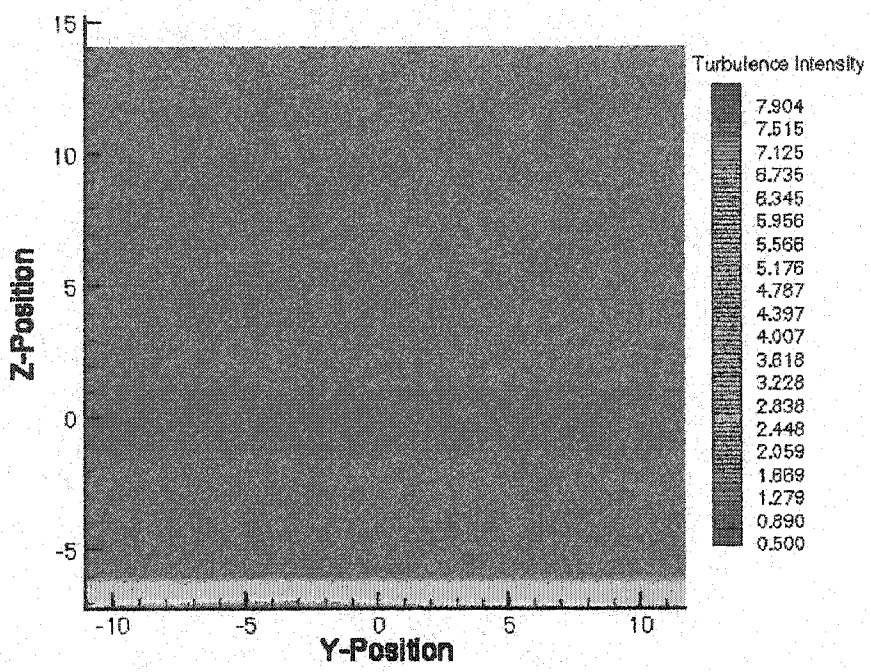

Figure 13 – Test Section Turbulence Intensity, Re ~ 1,300,000

3.2 OVERHEAD BALANCE

The tunnel has multiple balance systems. The balance system used to obtain the force data in these experiments is mounted on top of the test section and is shown in Figure 10. The balance extends three sting mounts into the test section. The three mounts run vertically and are attached to the lower surface of the model. Two of the mounts are attached near the leading edge of the model and the third mount is attached near the trailing edge. The balance can measure vertical or lift loads up to 1500 lbf and horizontal or drag loads up to 500 lbf. The balance has an uncertainty of $\pm$ 0.5 lbs. The balance is designed to have a downward force and thus the wing is mounted inverted in the test section to produce a downward lift force. At this point in time it is not possible for the balance to measure pitching moments. This balance was used to gather the force data needed for this research.

3.3 HOTWIRE INSTRUMENTATION

The tunnel is equipped with TSI Model 1056 constant temperature hotwire anemometry instrumentation. The hotwire measures tunnel velocity and turbulence intensity. The tunnel velocity is a time averaged mean of 100 samples from the

hotwire. Turbulence intensity is a measure of the fluctuation in tunnel mean velocity and is calculated using equations 8 and 9 where u_i are the individual velocity measurements.

$$u' = \sqrt{\frac{\sum u_i^2}{\frac{i=0 to N}{N}}} \tag{8}$$

$$\text{Turbulence Intensity} = 100 \times \frac{u'}{u_{mean}} \tag{9}$$

A hotwire is a temperature sensor. As air flows over the hotwire, heat is removed and the temperature of the wire changes which in turn alters the hotwire resistance. To maintain a constant temperature, the current flowing through the hotwire is adjusted which in turn changes the voltage across the hotwire. The voltage is read and is calibrated to the tunnel velocity. This instrumentation utilizes a single wire probe to measure streamwise or x-direction velocity and turbulence levels within the tunnel. The single wire sensor is attached to an arm on the computer controlled y-z probe. The probe must be manually moved in the x-direction. The hotwire is calibrated prior to every test. The wire is calibrated to the tunnel velocity using the wind tunnel pitot-static probes and pressure sensor. The temperature of the probe is calculated and the tunnel temperature at calibration is recorded. Since the hotwire adjusts to changes in temperature, or heat transfer, it is sensitive to changes in tunnel airspeed and changes in tunnel ambient temperature. The WMU wind tunnel is a closed loop wind tunnel which has half of the tunnel located outside of the laboratory and half of the tunnel inside the laboratory. This research was conducted through the winter months and as a consequence the tunnel temperature varied from 10 degrees Fahrenheit in the morning hours to 60 degrees Fahrenheit after 6 hours of operation. This large change in temperature caused drifts in the hotwire calibration. The tunnel temperature was measured during every test and a correction factor was applied to the signal voltage of the hotwire. The equation for the correction factor suggested by TSI is shown in equation 10.

$$Voltage_{corrected} = Voltage_{uncorrected} \times \frac{Temp_{wire} - Temp_{tunnel}}{Temp_{wire} - Temp_{tunnel\_at\_calibration}} \tag{10}$$

The correction works well for small changes in tunnel temperature, but the correction fails for large changes of ten degrees Fahrenheit or more. The result of this is a drift in velocity measurements. The probe was calibrated often, however the

velocity measurements cannot be considered reliable. Velocity drifts of 10 ft/sec or more were common in this testing. This can lead to a large drift in the reference tunnel velocity and therefore a large error in the velocity measurements taken around the pressure model. A 10 ft/sec change in a mean flow of 100 ft/sec is a drift of 10% which is far to large to consider the data to be accurate. However, turbulence intensity measurements are reliable in reference to the temperature change. A fluctuation of 1 ft/sec in a 100 ft / sec flow is equivalent to a 1% turbulence intensity. A 1 ft / sec fluctuation in a 110 ft / sec flow is equivalent to a 0.9% turbulence intensity. Thus a drift of 10 ft / sec causes a small change in turbulence intensity, but not a large change when being compared to the levels seen in the flow around the pressure model. Another characteristic of a single wire probe is that turbulence levels greater than 20% cannot be accurately obtained using hotwire probes. The hotwire must be aligned to the mean flow and turbulence levels of 20% or higher indicates a change in direction of the flow, possibly reversed flow. The angle of the flow causes the air to accelerate between the probe arms shown in Figure 14, causing an error in the velocity reading.[38] Turbulence levels grater than 20% were seen in the separated areas of flow behind the horned ice shapes. Thus the turbulence intensity measurements taken around the clean and iced wings are a qualitative look at the turbulence contours of the separated flow around the wing.

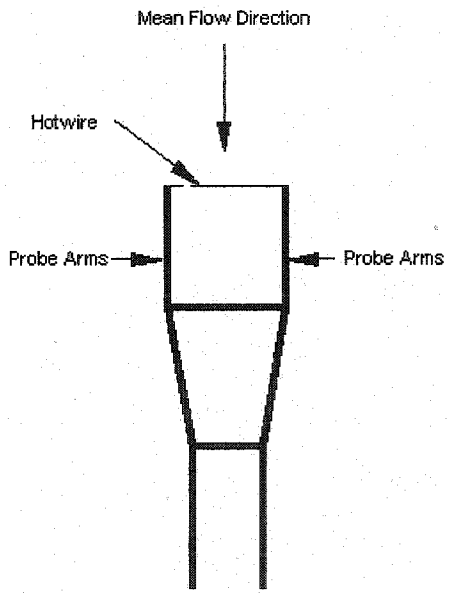

Figure 14 – Hotwire Schematic

3.4 HIGH SPEED VIDEO AND SMOKE WIRE

The tunnel is equipped with a high speed video camera and smoke wire system. The camera and smoke wire were used to provide flow visualization around the wing and ice shapes. The camera is capable of recording 2000 frames per second. The smoke wire is mounted toward the front of the test section and is utilized with the horizontally mounted force model. The smoke produces streamlines of smoke that travel downstream around the surface of the model. The smoke wire must operate at tunnel airspeeds of 30 feet per second or less to prevent rapid dissipation of the smoke streamlines. This tunnel airspeed is approximately equal to a tunnel Reynolds number of 100,000 when operating the smoke wire.

3.5 PRESSURE INSTRUMENTATION

The pressure instrumentation used in these experiments is a Scanivalve system. The instrumentation has one differential pressure transducer and a mechanical rotating mechanism to switch between each pressure port. The Scanivalve system can measure up to 48 pressures at one time. The pressure model has 87 ports and thus two separate runs were needed to obtain all 87 pressure measurements. The Scanivalve system is setup such that the pressure readings obtained are in the form of a pressure coefficient. The differential pressure transducer is referenced to the tunnel static pressure. This allows the pressure readings obtained to be (Port Pressure – Static Pressure). The tunnel dynamic pressure is also measured in this same manner (Total Pressure – Static Pressure). A standard pressure coefficient is then determined from these readings. By calculating a pressure coefficient immediately, any drift that occurred is constant over that set of data and will therefore cancel out of the pressure coefficient equation shown in equation 11. Using the Scanivalve system in this manner eliminates any error due to a zero shift. The system is essentially self zeroing.

$$(11) \qquad Cp = \frac{\text{Port Pressure} - \text{Static Pressure}}{\text{Total Pressure} - \text{Static Pressure}} = \frac{\text{Port Pressure} - \text{Static Pressure}}{\text{Dynamic Pressue}}$$

3.6 NACA 23012 MODELS

The NACA 23012 airfoil shape was chosen because it is a common shape used in general aviation aircraft and there is a good amount of experimental data describing the characteristics of this airfoil shape. There is also the possibility of future flight test research on a twin engine Beech Baron that uses the NACA 23012 airfoil for its main wings. Two NACA 23012 models were constructed for the wind tunnel tests. Pressure and force data was needed to determine the Cp_x and C_{LN}. The force model has a span if 42.5 inches, a constant chord of 14 inches and an aspect ratio of 3. This model was mounted horizontally in the test section and spanned the entire test section to eliminate wingtip vortices and simulate 2D flow. At maximum angle of attack the force model blocks 10% of the test section. The pressure model has a span of 32.5 inches, a constant chord of 14 inches and an aspect ratio of 2.3. This model was mounted vertically in the test section and spanned the entire test section to simulate 2D flow. The pressure model blocks 8% of the test section at maximum angle of attack. The pressure model has 87 pressure ports. 43 ports are on the upper surface and 43 ports are on the lower surface with one port on the leading edge. The ports extend from an x/c location of 0% to 89%. The port distribution is shown in Figure 15. The ports toward the leading edge are separated chordwise by 0.125 inches and the aft port locations are separated by 0.5 inches. All ports are separated spanwise by 0.25 inches. The pressure ports are located at the half span location to take advantage of the most uniform flow in the test section. The pressure model was mounted on a computer controlled yaw table to change the angle of attack. Pressure data was taken every one degree, ranging from 0 degrees to the positive stall angle of attack. The pressure model mounted in the test section is shown in Figure 16.

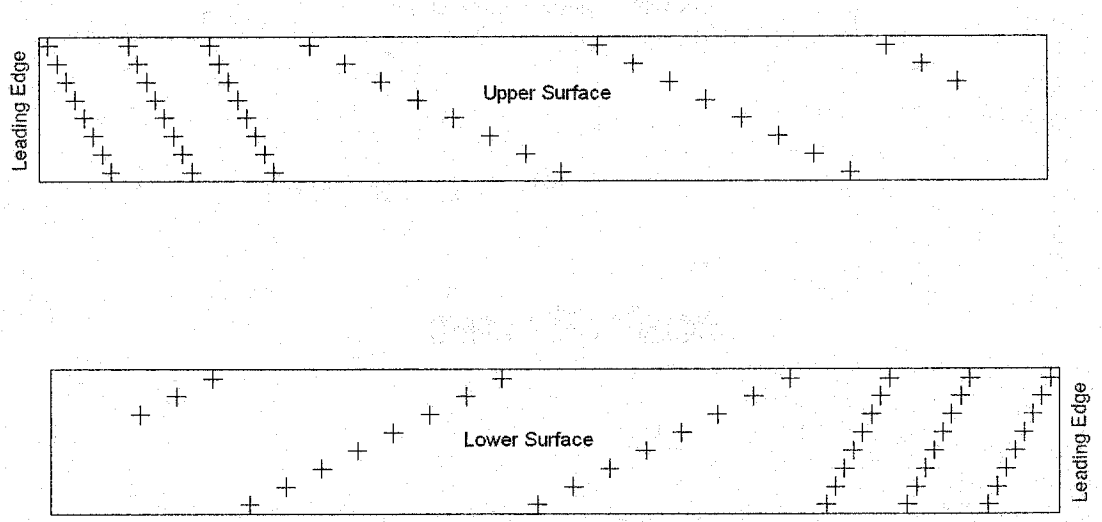

Figure 15 – Port Locations for the Pressure Model

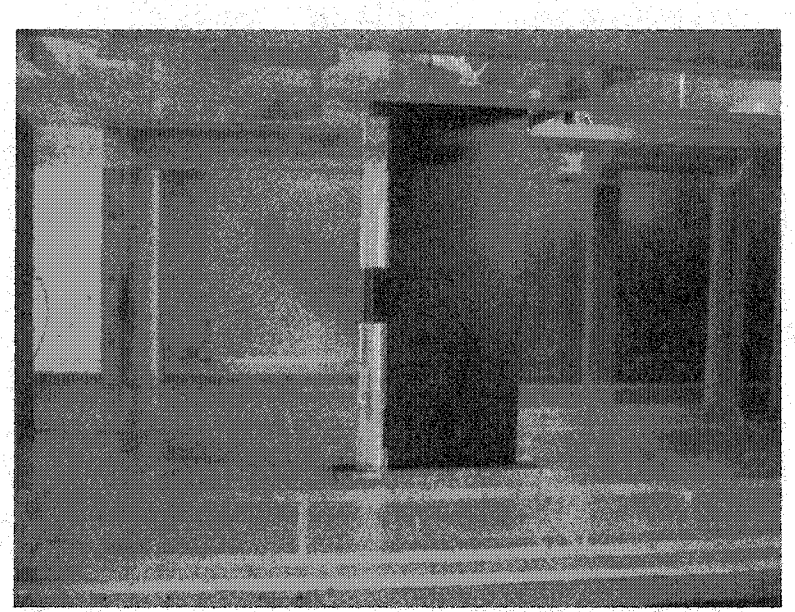

Figure 16 – Pressure Model in the Test Section

3.7 SIMULATED ICE SHAPES

The WMU subsonic tunnel is not an icing tunnel, thus simulated ice shapes were used in these experiments. The ice shapes were determined using the LEWICE 2.0 software from NASA Glenn. The flight input parameters were determined using typical flight conditions for a twin engine Beech Baron. The airspeeds, altitudes, and angles of attack in Table 3 were chosen to model the operations of a twin engine Beech Baron aircraft, shown in Figure 17, which utilizes a NACA 23012 airfoil section for its wing. The altitudes of 6000 ft and 10000 ft were chosen as common cruising altitudes for this aircraft. The angles of attack were calculated using the known parameters listed in Table 2 and Equations 12 and 13.

(12) $$\alpha = \frac{C_{Lcruise} - C_{L0}}{C_{L\alpha}}$$

(13) $$C_{Lcruise} = \frac{Gross\_Weight}{Q \cdot S}$$

Figure 17 – Beech Baron 58

Cruise Speeds (TAS At 5,200 LB)				
Maximum Cruise Power 25 In. Hg (Or Full Throttle) @ 2,500 RPM				
6,000 FT 202 KTS (233 MPH)				
8,000 FT 200 KTS (230 MPH)				
10,000 FT 198 KTS (228 MPH)				
Normal Cruise Power 23 In. Hg (Or Full Throttle) @ 2,300 RPM				
6,000 FT 190 KTS (219 MPH)				
8,000 FT 192 KTS (221 MPH)				
10,000 FT 189 KTS (217 MPH)				
Maximum Range Power 21 In. Hg (Or Full Throttle) @ 2,100 RPM				
6,000 FT 159 KTS (183 MPH)				
8,000 FT 164 KTS (189 MPH)				
10,000 FT 167 KTS (192 MPH)				
Weights				
Maximum Ramp Weight 5,524 LB				
Maximum Take-Off Weight 5,500 LB				
Maximum Landing Weight 5,400 LB				
Wing Area And Loadings				
Wing Area 199.2 SQ FT				
Wing Loading 27.6 LB / SQ FT				
Dimensions				
Wing Span 37 FT 10 IN				
Length 29 FT 10 IN				
Height 9 FT 9 IN				

Table 2 – Beech Baron 58 Specifications

The meteorological input parameters were determined from typical icing conditions described in the Federal Aviation Regulations (FAR) Parts 23.1419 and 25.1419. Typically in certification flight times in icing conditions of 22.5 minutes and 45 minutes are used. The 22.5-minute ice shape is used in analysis and certification to determine the performance loss in the event of an ice protection system failure. The 45-minute ice shape is used to determine the performance loss for an unprotected aerodynamic surface. A range of input parameters were chosen from these conditions and four ice shapes were developed. The input parameters are shown in Table 3. The ice shapes developed from these parameters are shown in Figure 18. The ice shapes were laser cut from half inch thick acrylic. The individual slices were bonded together to form a 2-D representation of the ice shape that spanned the leading edge of each model. The ice shapes were attached to the model using tape. Surface roughness was not added to the ice shape. Configuration 2 is the most severe ice shape and is formed in the 45 minute time period. Configuration 1 used the same conditions as Configuration 2 and was formed in 22.5 minutes. Configuration 3 is the mildest ice shape. Configuration 4 is similar to Configuration 3 with moderate horn shapes beginning to protrude from the leading edge. Using these shapes the force and pressure data was collected.

Config	Time (min)	V (kts)	Cruise AOA (deg)	Altitude (m)	LWC (g/cu. Meter)
23012C1	22.5	200	0.5	3048	0.3
23012C2	45	200	0.5	3048	0.3
23012C3	45	200	0.5	3048	0.25
23012C4	45	160	1.7	1830	0.3

Config	MVD DPD (microns)	Chord (m)	Temp Infinity (deg C)	Press Infinity (N/m^2)	
23012C1	50	1.6	-10	69990.8	
23012C2	50	1.6	-10	69990.8	
23012C3	50	1.6	-22.2	69990.8	
23012C4	50	1.6	-14.4	81482.7	

Table 3 – LEWICE 2.0 Input Parameters

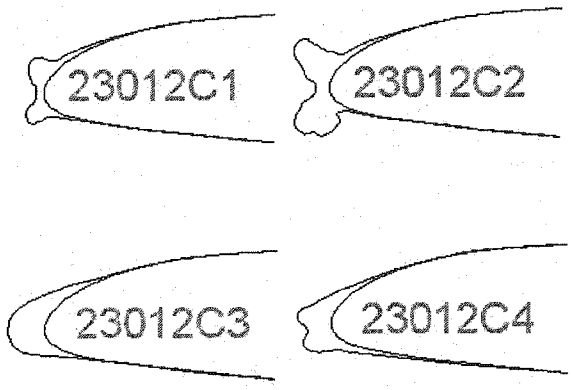

Figure 18 – Simulated Ice Shapes

CHAPTER 4 – FORCE DATA, PRESSURE DATA AND NACA 23012 PORT LOCATIONS

4.1 CLEAN WING FORCE DATA

Tests were first conducted on the NACA 23012 force and pressure models for the clean wing configuration. These tests were conducted at Reynolds numbers of 700,000; 1,000,000; 1,300,000 and 1,600,000. Lift data at a Reynolds number of 700,000 was compared to data taken by Ashden, Lindberg and Marwitz[40, 41, 42] at Reynolds number of 550,000. The Ashenden *et al.* [40, 41, 42] data matches the Re ~ 700,000 force data very well. This provides a good comparison between experimental wind tunnel data taken from multiple wind tunnels. All of the C_L data obtained from the force model was also compared to C_L data obtained from numerical integration of the pressure data. The C_L data was also compared to lift data obtained from the Software Aeronautics program called Sub2D. Sub2D uses panel methods to calculate the lift coefficients and pressure distributions. Figure 19 shows the C_L versus α data and Figure 20 shows the C_L versus C_D data for the clean wing at each Reynolds number. The comparison of C_L versus α data is shown in Figures 21, 22, 23 and 24. These comparisons indicate that valid data is being obtained from the WMU wind tunnel.

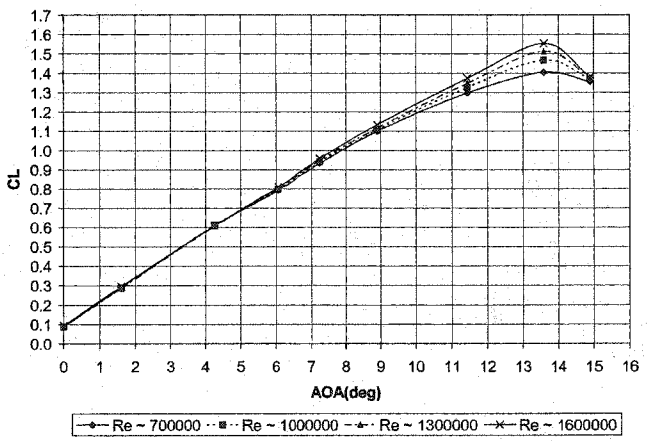

Figure 19 – CL vs α for Clean Configuration

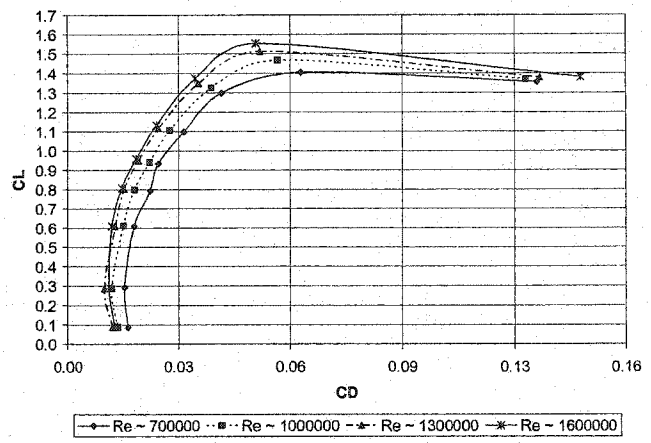

Figure 20 – CL vs CD for Clean Configuration

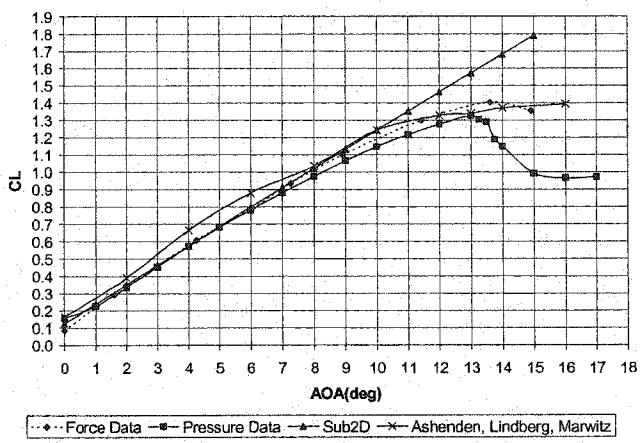

Figure 21 – CL vs α comparison, Re ~ 700,000

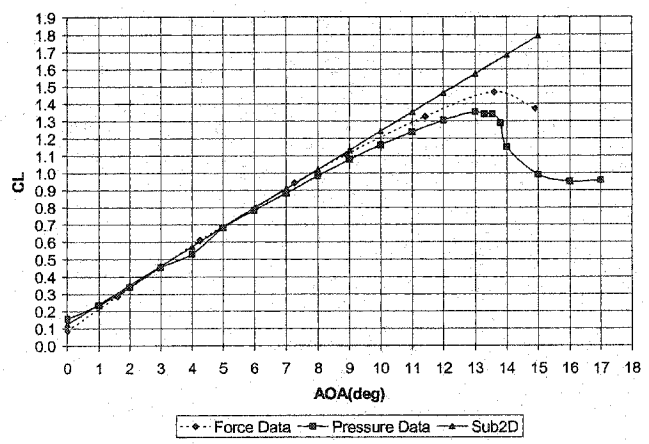

Figure 22 – CL vs α comparison, Re ~ 1,000,000

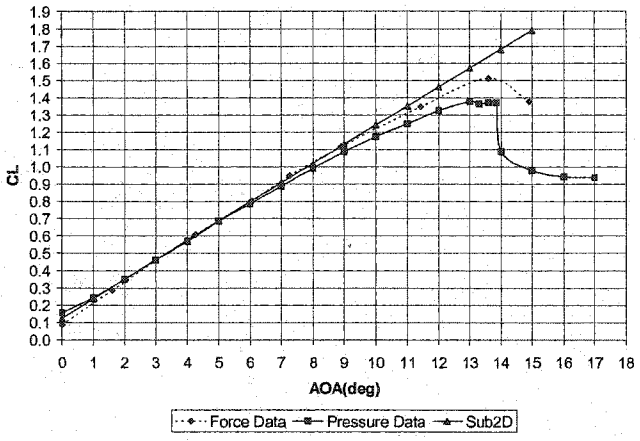

Figure 23 – CL vs α comparison, Re ~ 1,300,000

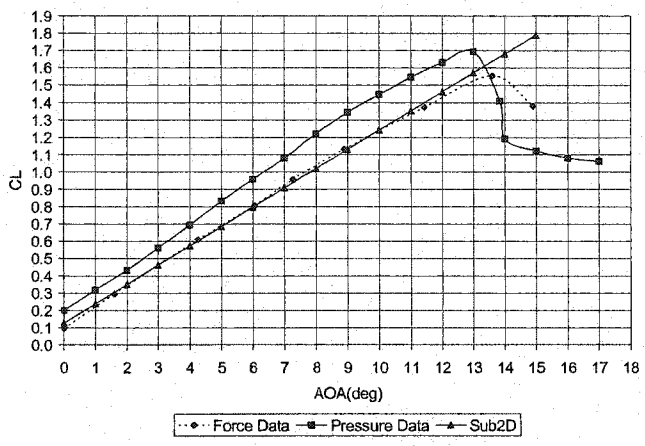

Figure 24 – CL vs α comparison, Re ~ 1,600,000

In all of these figures, the force data is in good agreement with the Sub2D at angles of attack from 0 degrees to 10 degrees. Sub2D does not calculate the C_L loss at stall and therefore cannot be compared to the experimental data at stall. The pressure data matches the force data well with the exception of Reynolds number of 1,600,000 and at C_{Lmax}. At a Reynolds number of 1,600,000 the Sub2D and force data match, but the pressure data is significantly different. The shift in the pressure lift curve was investigated to determine if the shift was related to the instrumentation or to the actual pressure distribution around the model. Through careful analysis of the data it was determined that the amplifier in the Scanivalve system produced a voltage higher than the limits available in the data acquisition system. This caused the instrumentation to saturate and produce an artificially low dynamic pressure measurement. The dynamic pressure is in the denominator of the pressure coefficient and an artificially low measurement will produce an artificially high pressure coefficient. Through integration, the lift coefficient will also be artificially high. Due to these limits of the

instrumentation the data taken at a Reynolds number of 1,600,000 must be disregarded for the calculations involving Cp_x and C_{LN}. In the lower three Reynolds numbers the pressure data under predicts the force data C_{Lmax} by 0.1 in all cases. A portion of the shift in C_{Lmax} can be attributed to the difference in tunnel blockage between the force and pressure models. Rae and Pope[39] blockage correction factors were applied the force and pressure data to determine the effect of solid and wake blockage effects. The blockage corrections are a series of correction factors based on the model and test section dimensions. Solid blockage corrects for an acceleration of the flow around the model due to test section blockage. The solid blockage creates an increase in velocity over the wing that would not normally be present. The wake blockage corrects for an increase in velocity around the model due to the presence of the model wake. Any model will have a wake which contains air flowing at a lower velocity than the surrounding airflow. In order to satisfy continuity the mass or volumetric flow rate must be constant throughout the test section. The presence of tunnel walls, force the airflow outside of the wake to be higher than what it would be in a normal flight situation. The equations used for the blockage corrections are shown in equations 14, 15, 16 and 17. Comparison of the corrected C_L data is shown in Figures 25, 26, and 27.

(14) $$C_{L\_corrected} = C_{L\_uncorrected}(1-2\varepsilon)$$

(15) $$\varepsilon = \varepsilon_{solid\_blockage} + \varepsilon_{wake\_blockage}$$

(16) $$\varepsilon_{wake\_blockage} = \frac{chord \times C_{D\_uncorrected}}{2 \times test\_section\_height}$$

(17) $$\varepsilon_{solid\_blockage} = \frac{0.7 \times thickness \times chord \times wingspan}{test\_section\_area^{3/2}}$$

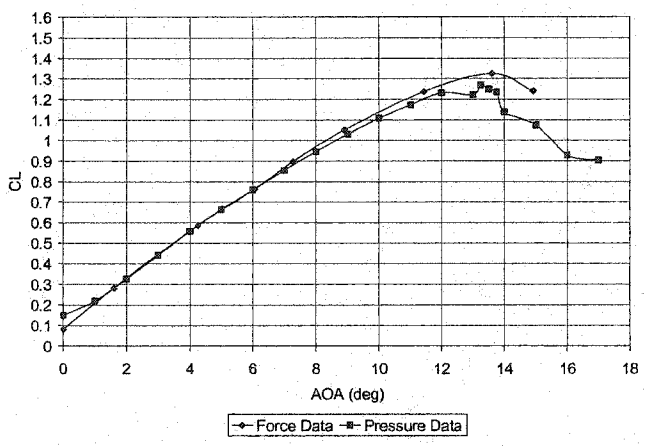

Figure 25 – Blockage Correction CL vs. α comparison, Re ~ 700,000

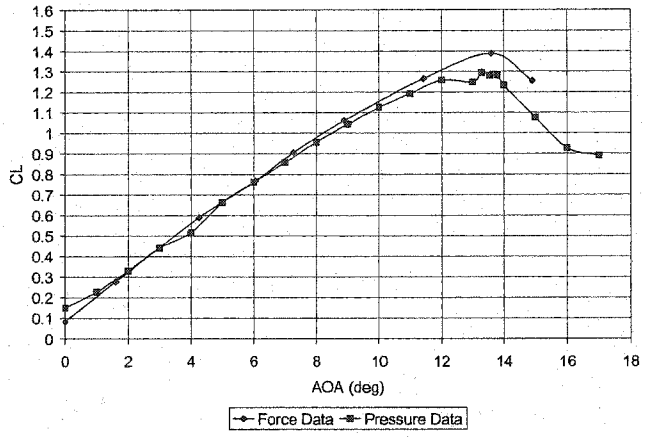

Figure 26 – Blockage Correction CL vs α comparison, Re ~ 1,000,000

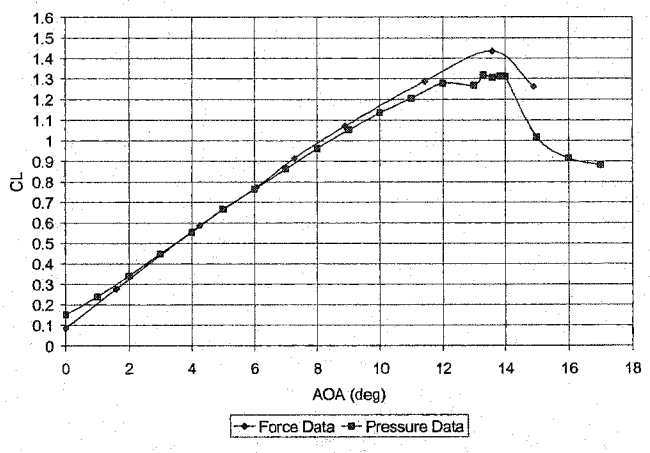

Figure 27 – Blockage Correction CL vs α comparison, Re ~ 1,300,000

The blockage corrections work best at the lower Reynolds number. The pressure and force data C_{Lmax} nearly match at a Reynolds number of 700,000. The difference in C_{Lmax} is still present for the other Reynolds numbers, although it is not as high as the uncorrected curves. In comparison of the pressure and force data for the application to the stall margin instrumentation, the difference in C_{Lmax} will be a consistent error and will allow the instrumentation to still be validated. Using the force data C_{Lmax} will cause the instrumentation to under predict the C_{LN} value for the pressure data. A comparison of the difference in C_{LN} is shown in Figure 28. For this example the pressure data uses a C_{Lmax} of 1.3 and the force data a C_{Lmax} of 1.4. A difference of 0.09 in C_{LN} is present at the near stall regions.

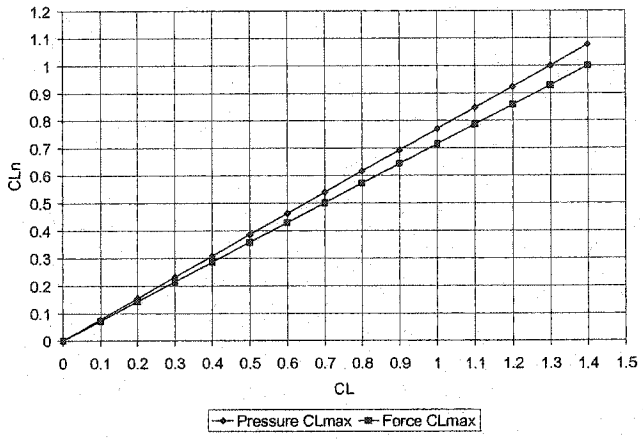

Figure 28 – C_{LN} versus C_{Lmax} Comparison

Tunnel blockage corrections were not applied to the data during the Cp_x versus C_{LN} comparisons for two reasons. The first is that the blockage correction is a correction applied through a multiplication of the uncorrected C_L and the blockage correction factors shown in equation 14. In calculation of C_{LN}, from the corrected data, the blockage correction factor will cancel out of the equation. The second reason is that it is not known whether the correction factor is accurate with leading edge ice on the model.

4.2 ICED WING FORCE DATA

The models were tested with the four leading edge ice shapes. The C_L versus α data for each Reynolds number is shown in Figures 29, 30, and 31. The C_L versus C_D data is shown in Figures 32, 33, and 34. C_{Lmax} for the iced wings remains the same for all Reynolds numbers. This data indicates that the wings are past the critical Reynolds number discussed by Bragg *et al.*[6, 7, 8, 9]. When comparing the iced wing data between Reynolds numbers, the C_L versus α data is essentially the same. The degradation in lift is also clearly indicated in this data. C_{Lmax} for the clean wing can be determined clearly, but for the iced wing the value of C_{Lmax} is somewhat ambiguous.

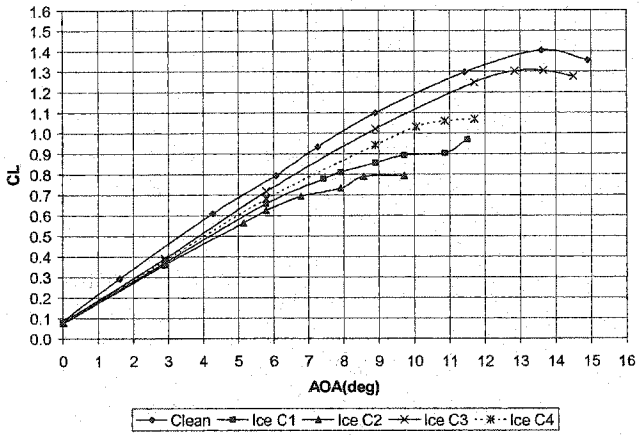

Figure 29 – CL vs. α, Re ~ 700,000

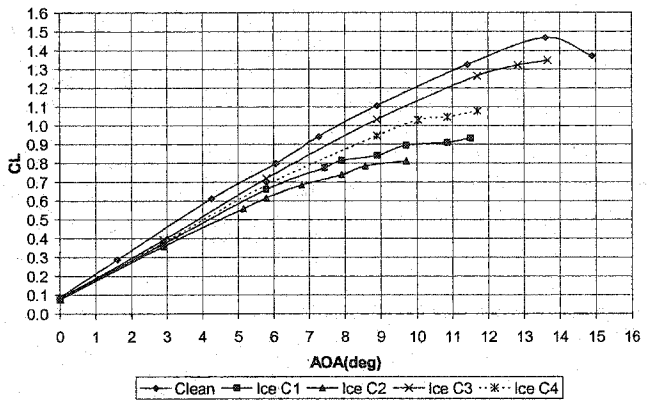

Figure 30 – CL vs. α, Re ~ 1,000,000

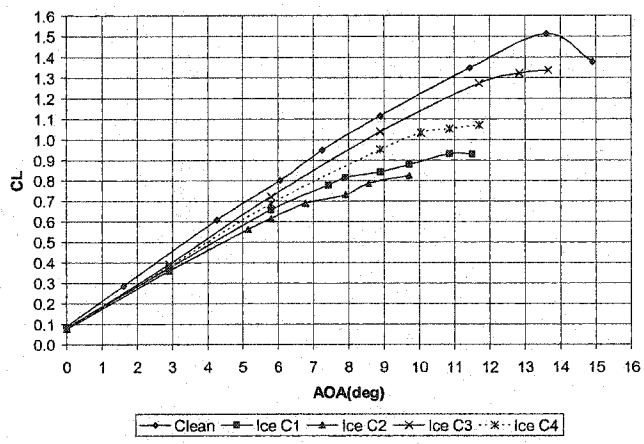

Figure 31 – CL vs. α, Re ~ 1,300,000

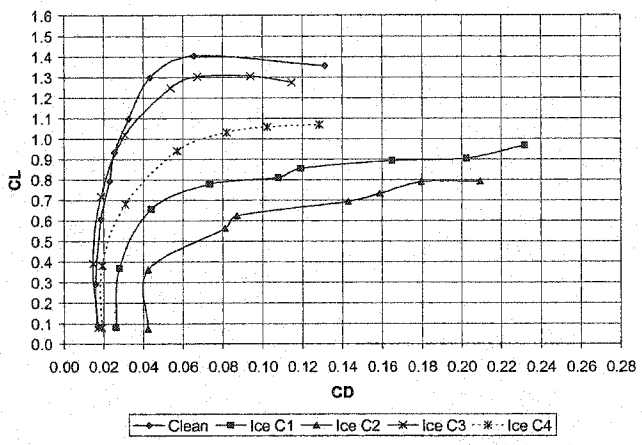

Figure 32 – CL vs. CD, Re ~ 700,000

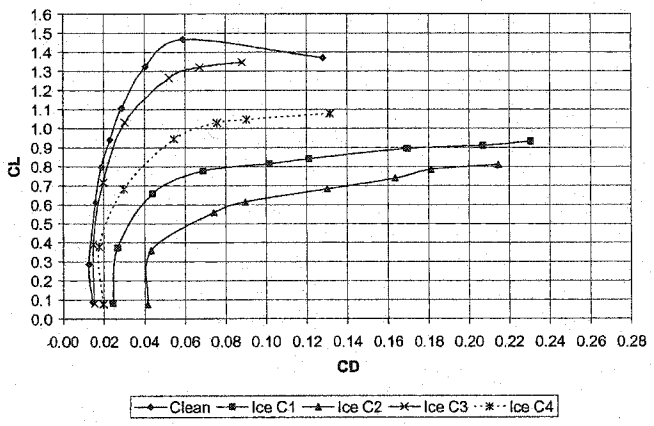

Figure 33 – CL vs. CD, Re ~ 1,000,000

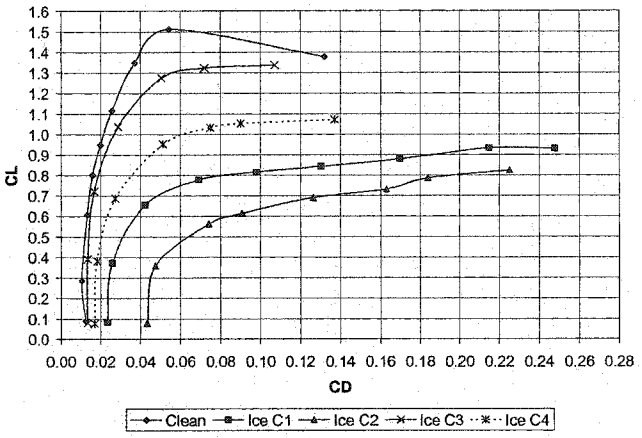

Figure 34 – CL vs. CD, Re ~ 1,300,000

To determine C_{Lmax} for the iced wings for use in the calculation of C_{LN}, a combination of four observations were used. The C_L versus α data were analyzed to determine the point of inflection in each curve. The C_L at the point of inflection was then compared to the C_L versus C_D data to determine if this was the location at which the slope of the curve approached zero, indicating a stalled wing (large increase in drag for small increase in lift). The pressure data at the angle of attack at which this occurred was analyzed to determine if this was the angle at which the pressure coefficients began to fluctuate from the smooth attached flow condition. An example of the pressure comparison can be seen in Figures 35, 36, and 37. The figures show consecutive angles of attack for the clean and ice C1 pressure distributions at a Reynolds number of 1,300,000. The C1 pressure distribution begins as a smooth distribution and tends to match the clean pressure distribution. As the angle of attack increases the C1 distribution fluctuates on the upper surface trailing edge of the airfoil. This fluctuation signifies separated flow and a stalled wing. This flow separation matches the point at which the stall angle determined from the force data occurs. To further check the stall angle of attack determined from the force data, the fluctuating component of the pressure distribution was observed. When collecting the data for the pressure distribution 100 readings were taken for every data point. To obtain the Cp value at each point this data was averaged. The root mean square (RMS) of the 100 Cp readings was also calculated. The mean was subtracted from the RMS values to determine the fluctuating component of the Cp distribution. An example of the upper surface pressure fluctuations is shown in Figures 38, 39, and 40. These figures again compare the stall for ice configuration C1. The stall angle was set as the angle at which the fluctuating Cp distribution significantly deviated from the clean attached flow angle of attack fluctuating Cp distribution. The stall angle of attack matched through all four methods and the C_L at this angle of attack was taken to be the C_{Lmax} for that particular ice shape. Table 4 shows the C_{Lmax} values for each ice shape.

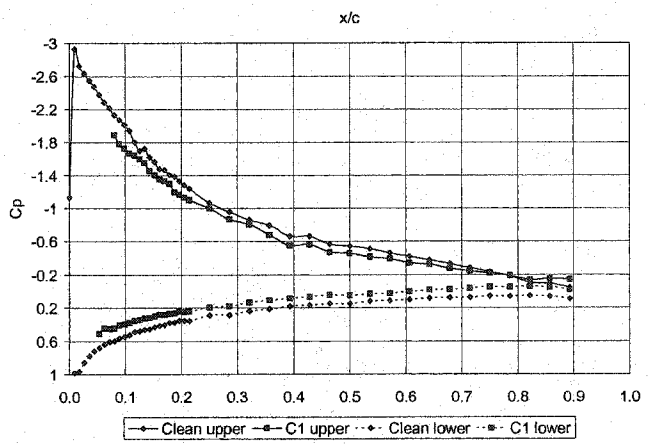

Figure 35 – Pressure Distribution; Re ~ 1,300,000; AOA 8 deg; Ice C1

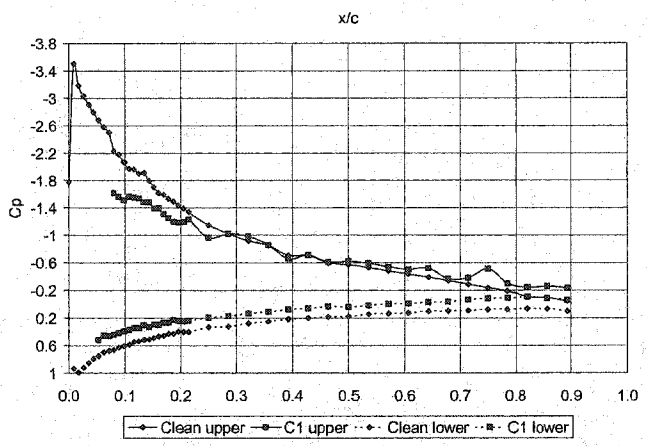

Figure 36 – Pressure Distribution; Re ~ 1,300,000; AOA 9 deg; Ice C1

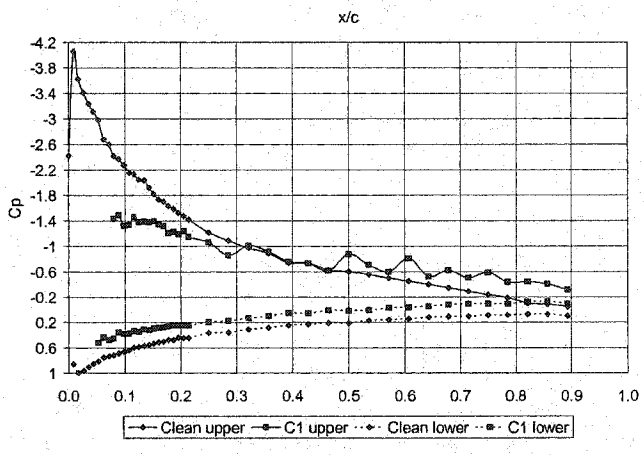

Figure 37 – Pressure Distribution; Re ~ 1,300,000; AOA 10 deg; Ice C1

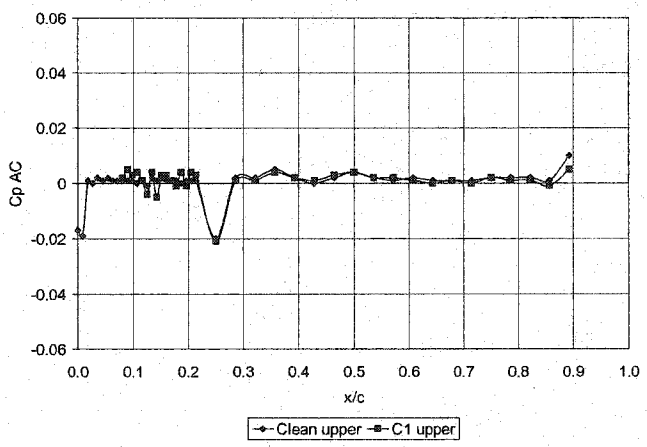

Figure 38 – Fluctuating Cp Distribution; Re ~ 1,300,000; AOA 7 deg; Ice C1

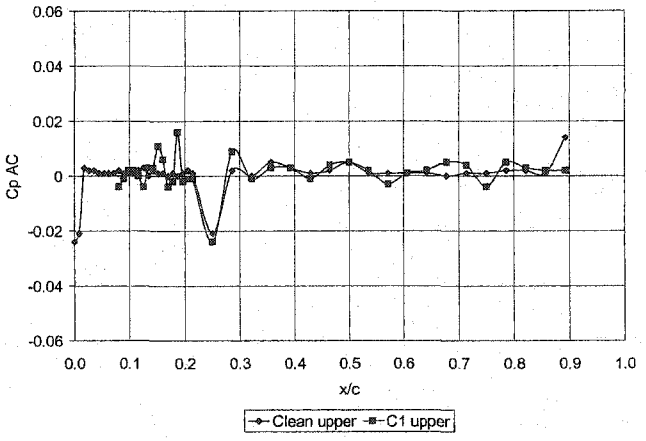

Figure 39 – Fluctuating Cp Distribution; Re ~ 1,300,000; AOA 8 deg; Ice C1

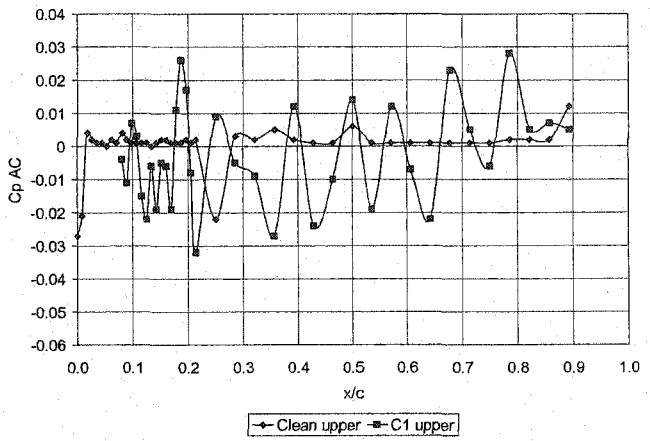

Figure 40 – Fluctuating Cp Distribution; Re ~ 1,300,000; AOA 9 deg; Ice C1

Configuration	C_{Lmax} Re~700000	C_{Lmax} Re~1000000	C_{Lmax} Re~1300000
Clean	1.4	1.469	1.5
C1	0.88	0.85	0.85
C2	0.7	0.75	0.72
C3	1.3	1.35	1.338
C4	1.08	1.05	1.055

Table 4 – C_{Lmax} Data

4.3 CLEAN AND ICED WING PRESSURE DATA

Pressure data for the clean and iced configurations was taken every one degree beginning at zero degrees angle of attack and ranging past stall. Detailed figures for the pressure data are shown in the Appendix A for all three Reynolds numbers. The fluctuating Cp distribution data is shown in Appendix B.

4.4 PORT LOCATIONS

A program was developed in Microsoft Excel using Visual Basic to analyze the pressure and C_{LN} data. The program was setup to look at every possible combination of four ports used in the Cp_x equation. A calibration algorithm was developed between Cp_x and C_{LN} for each ice configuration and the clean configuration. The clean and iced calibration algorithms were compared to determine which set of port locations produced an identical curve for both cases. There were three conditions for a set of ports to be accepted. The first condition is that the slopes of the curve between a C_{LN} = 1.0 and a CLN = 0.5 be within 5% of each other. The second condition is that the intercept of this curve also match within 5%. The third condition is that the Cp_x values at C_{LN} equal to 0.6, 0.7, 0.8 and 0.9 are within 5% of each other. The set of ports from this analysis were then cross referenced between each ice configuration to determine which set was present in all cases. One set of ports was found to work for the C1, C3 and C4 ice configurations. A set of ports that was accurate for all four configurations was not found. The severity of the horned ice shape C2 produced a change in the pressure distribution for a given C_{LN} that was much too different from the other configurations to allow a single set of ports to be found. The port locations for the C1, C3, and C4 configurations are as follows:

CP1 – Upper Surface x/c = 0.46
CP2 – Lower Surface x/c = 0.89
CP3 – Lower Surface x/c = 0.14
CP4 – Lower Surface x/c = 0.64

Figures 41, 42, and 43 show the relationships between Cp_x and C_{LN} for each Reynolds number. Data for ice C2 is included in these figures to show the deviation from the typical linear curve for the Cp_x versus C_{LN}. Clean, C1, C3, and C4 conditions are linear curves lying nearly on top of each other. The C2 configuration is the curve that fluctuates throughout the range of C_{LN}'s. The range of C_{LN} shown in these figures is 0.40 to 1.00. This is the range at which an aircraft will fly during takeoff, in the airport pattern and an approach to landing which are the most critical phases of flight. This is also the most likely time for ice to accumulate on the aircraft. This is the point at which most accidents due to aircraft icing occur and would be the critical time for use of this instrumentation. The curves deviate significantly from each other for C_{LN} values of 0.0 to 0.4. There is little to no deviation in Figures 41,

42, and 43 due to changes in Reynolds number. The Reynolds number effects are discussed further in the next chapter.

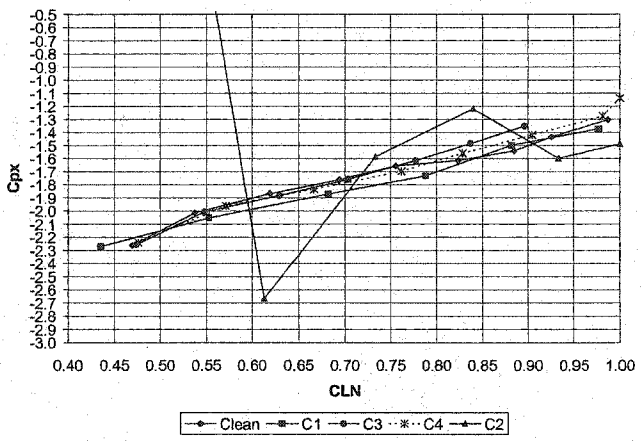

Figure 41 – Cp_x vs. C_{LN}, Re ~ 700,000

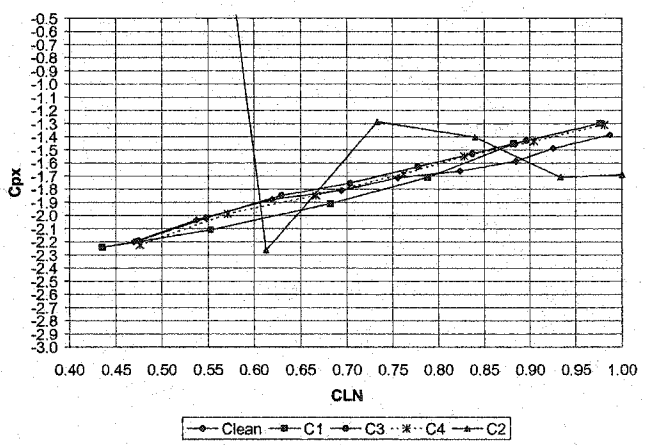

Figure 42 – Cp_x vs. C_{LN}, Re ~ 1,000,000

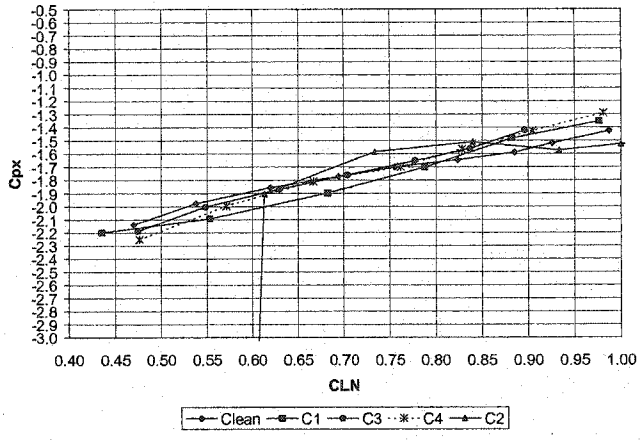

Figure 43 – Cp_x vs. C_{LN}, Re ~ 1,300,000

To implement this system on an aircraft the clean curve must be used for the algorithm relating Cp_x to C_{LN}. Tables 5, 6, and 7 compare the C_{LN} that would be displayed to a pilot from the clean configuration algorithm to the actual C_{LN}. These tables give a clearer picture of the error in these port locations from the ice configuration curves not matching the clean configuration curve exactly. A negative value in the percent difference from clean column indicates an under prediction and a positive value indicates an over prediction. Information for C2 is not included for these tables; the deviation can be seen in the previous Cp_x versus C_{LN} figures.

Clean	C1 Actual	C1 % Diff from Clean	C3 Actual	C3 % Diff from Clean	C4 Actual	C4 % Diff from Clean
0.5	0.50	0%	0.51	-1%	0.51	-1%
0.6	0.67	-7%	0.62	-2%	0.62	-2%
0.7	0.78	-8%	0.71	-1%	0.73	-3%
0.8	0.84	-4%	0.76	4%	0.80	0%
0.9	0.88	2%	0.84	6%	0.86	4%

Table 5 – C_{LN} Comparison, Re ~ 700,000

Clean	C1 Actual	C1 % Diff from Clean	C3 Actual	C3 % Diff from Clean	C4 Actual	C4 % Diff from Clean
0.5	0.54	-4%	0.5	0%	0.52	-2%
0.6	0.69	-9%	0.6	0%	0.63	-3%
0.7	0.74	-4%	0.67	3%	0.70	0%
0.8	0.80	0%	0.74	6%	0.76	4%
0.9	0.85	5%	0.83	7%	0.83	7%

Table 6 – C_{LN} Comparison, Re ~ 1,000,000

Clean	C1 Actual	C1 % Diff from Clean	C3 Actual	C3 % Diff from Clean	C4 Actual	C4 % Diff from Clean
0.5	0.57	-7%	0.53	-3%	0.55	-5%
0.6	0.70	-10%	0.62	-2%	0.63	-3%
0.7	0.76	-6%	0.70	0%	0.70	0%
0.8	0.81	-1%	0.76	4%	0.76	4%
0.9	0.85	5%	0.84	6%	0.84	6%

Table 7 – C_{LN} Comparison, Re ~ 1,300,000

These tables indicate that a clean calibration curve will predict the actual C_{LN} within 10% at the worst case and within 5% a large percentage of the time. To gain a better understanding of the advantages of implementing a system such as this, the C_{LN} values for the Stall Margin Instrumentation for use in icing conditions must be compared to instrumentation without compensation for icing conditions. Consider five aircraft on final approach to landing. The first aircraft has a clean wing. The second aircraft has accreted ice in the shape of configuration C3. The third aircraft has accreted ice in the shape of configuration C4. The fourth aircraft has accreted ice in the shape of configuration C1. The fifth aircraft has accreted ice in the shape of configuration C2 (most severe situation).These aircraft are flying at or near 1.3 times the stall speed, a typical approach speed. This is equivalent to a C_{LN} = 0.6 or 60%. Table 8 illustrates what the pressure based Stall Margin (ice compensating) system would indicate, what an angle of attack based (no ice compensation) system would indicate and what the actual C_{LN} would be. This table assumes the aircraft remains at the same lift coefficient for each condition. The only change between aircraft is the decrease in C_{Lmax} due to the ice accretion. The actual C_{LN} is determined using force

data from the wind tunnel tests. The Angle of Attack based system would always indicate a C_{LN} of 60% even though the aircraft is approaching stall with the different leading edge ice shapes. With the pressure based system the C_{LN} would adjust as the aircraft was on final approach to landing. The pilot would have an indication that the aircraft is approaching stall as he/she sets up for a normal approach to landing. Knowing this information the pilot would be able to take corrective action by lowering the nose of the aircraft and maintaining a higher airspeed in the approach to landing phase.

	C_{LN} Angle of Attack Based System	C_{LN} Pressure Based System	C_{LN} Actual	Notes
Clean	60%	60%	60%	
C3	60%	67%	67%	
C4	60%	92%	85%	near stall
C1	60%	100%	105%	stalled
C2	60%	100%	125%	stalled

Table 8 – Instrumentation Comparison, Re ~ 1,300,000

4.5 UNCERTAINTY ANALYSIS

A standard uncertainty analysis was performed on the Cp_x data to determine the accuracy of the data taken for analysis. Pressure readings were taken 100 times per port location for each data point. The Cp values used for the Cp_x calculation are an average of these 100 readings. For the uncertainty analysis a weighting factor of 3 standard deviations, determined from the 100 readings, was used. A percent uncertainty was determined for every data point and for all three Reynolds numbers. The results from these calculations are shown in Figures 44, 45 and 46. The highest Reynolds number has the lowest uncertainty due to the higher magnitude surface pressures at higher airspeeds. The percent uncertainty is also lower for less severe ice shapes. The more severe the ice shape, the more the pressure fluctuated across the surface of the wing causing a larger standard deviation. Ice C2 produces the largest fluctuation in uncertainty. The fluctuation can be attributed to the large horn causing flow separation and higher turbulence levels across the entire surface of the wing. The flow separation causes large pressure fluctuations that make it difficult to determine proper port locations for C2. The slope of the Cp_x versus C_{LN} graphs is nearly one (Figures 41, 42, and 43), therefore an uncertainty of 1% in Cp_x equates to a fluctuation in C_{LN} of 1%. At a Reynolds number of 700,000 the uncertainty is at a level equal to the % difference from clean calculations shown in Table 5. This makes

it difficult to determine if the difference in C_{LN} is due to the port location or the uncertainty of the data. However in the case of the Reynolds number of 1,000,000 and 1,300,000 the uncertainty falls below the % difference from clean values shown in Tables 6 and 7. Therefore the change in C_{LN} can be attributed to the ice shape and not the uncertainty in the data. This indicates that the port locations do not produce a 100% accurate indication of the C_{LN} between the clean and iced configurations. However, as was stated earlier the calibration would remain within 5% of the actual C_{LN} for a large percentage of the situations. The pressure based stall margin instrumentation has been validated for another airfoil shape. The system maintains accuracy within 10% of the actual stall margin with the exception of the most severe 45 minute ice shape. This shape would be a worst case scenario and the pilot would see the stall margin system adjusting as the ice was forming on the aircraft.

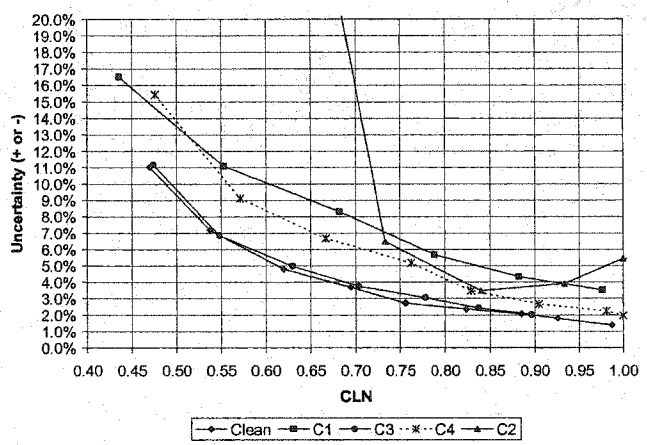

Figure 44 – % Uncertainty vs. C_{LN}, Re ~ 700,000

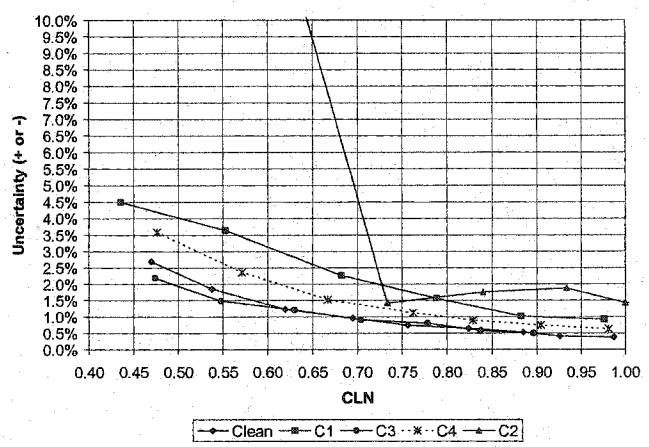

Figure 45 – % Uncertainty vs. C_{LN}, Re ~ 1,000,000

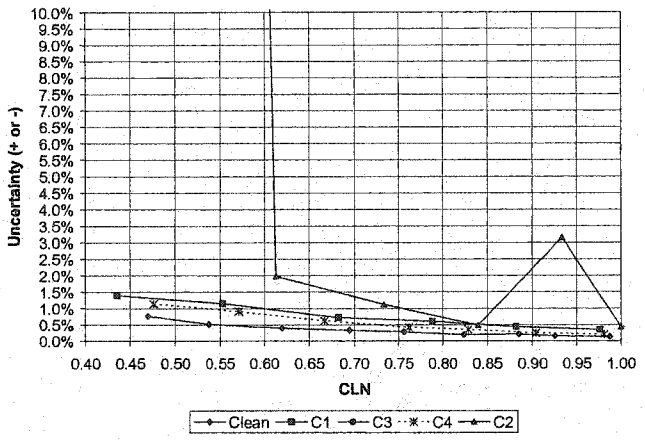

Figure 46 – % Uncertainty vs. C_{LN}, Re ~ 1,300,000

CHAPTER 5 – REYNOLDS NUMBER COMPARISON

5.1 FORCE DATA COMPARISON

It is important to compare the changes in C_L versus α and C_L versus C_D between Reynolds numbers. The iced airfoils reach a critical Reynolds number at which point there is no further increase in C_{Lmax}. A constant C_{Lmax} removes a variable in the process of determining port locations for each ice shape. The C_L versus α data is shown in Figures 47, 48, 49 and 50. There is little to no change in the lift curves between Reynolds numbers for each ice shape. The C_L versus C_D is shown in Figures 51, 52, 53, and 54. There is little to no change in these curves between Reynolds numbers for each ice shape. The critical Reynolds number is below 700,000 in this case.

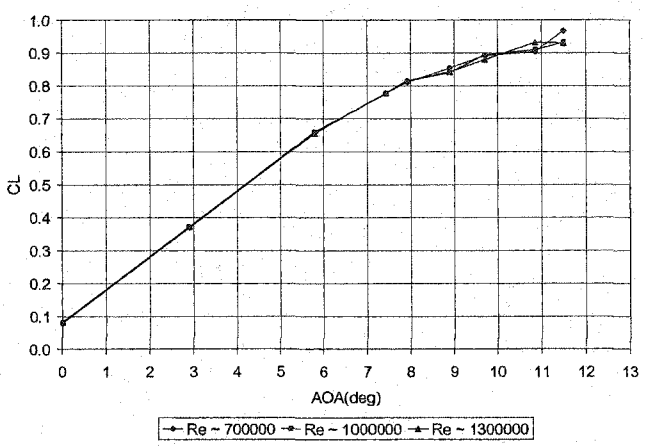

Figure 47 – C_L vs. α Reynolds Number Comparison for Ice C1

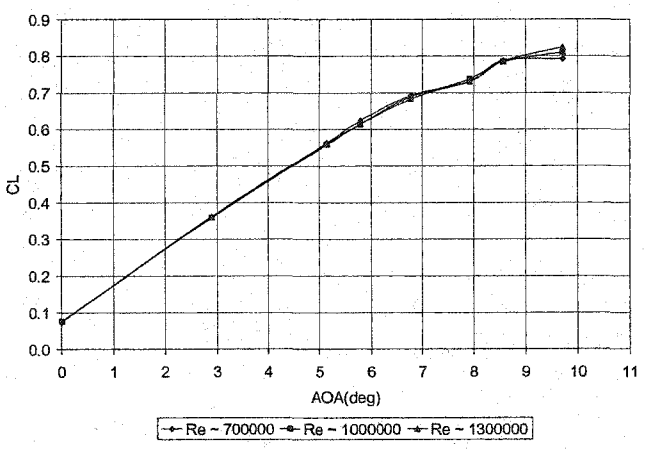

Figure 48 – C_L vs. α Reynolds Number Comparison for Ice C2

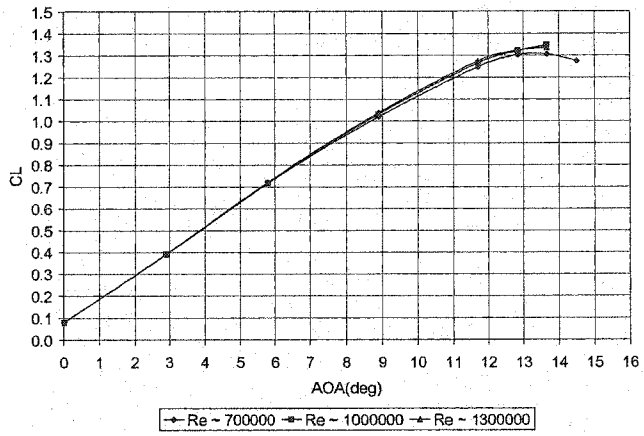

Figure 49 – C_L vs. α Reynolds Number Comparison for Ice C3

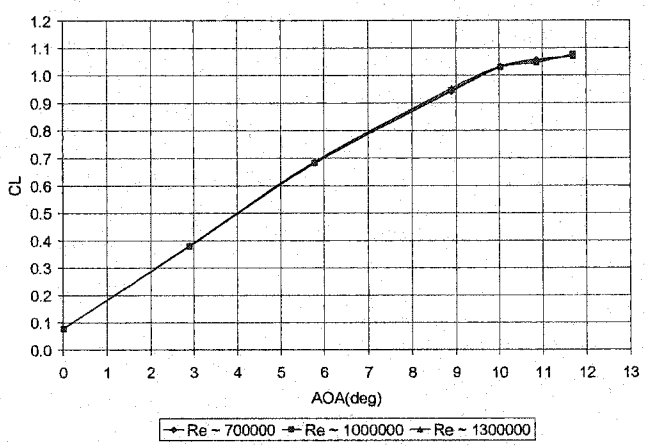

Figure 50 – C_L vs. α Reynolds Number Comparison for Ice C4

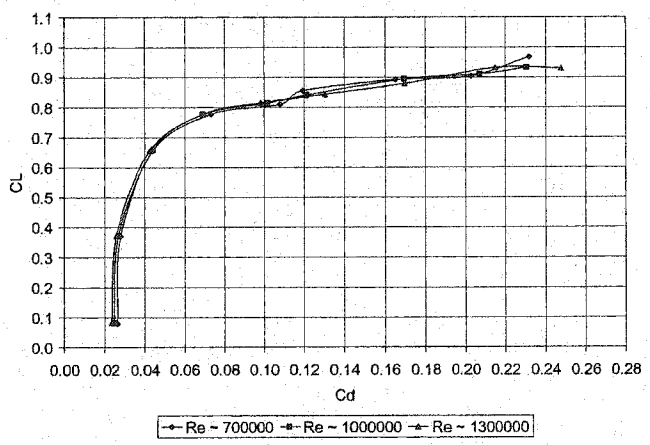

Figure 51 – C_L vs. C_D Reynolds Number Comparison for Ice C1

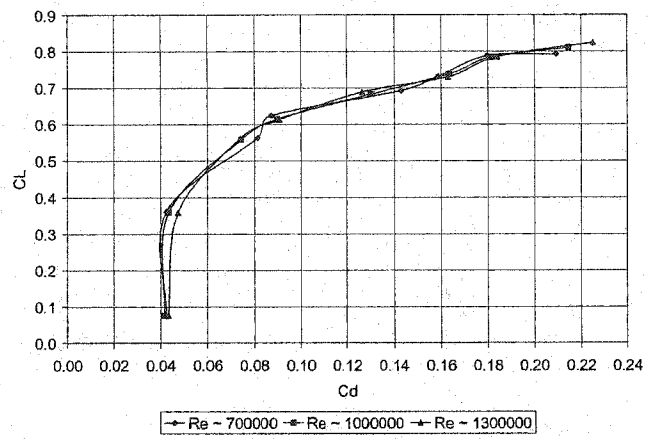

Figure 52 – C_L vs. C_D Reynolds Number Comparison for Ice C2

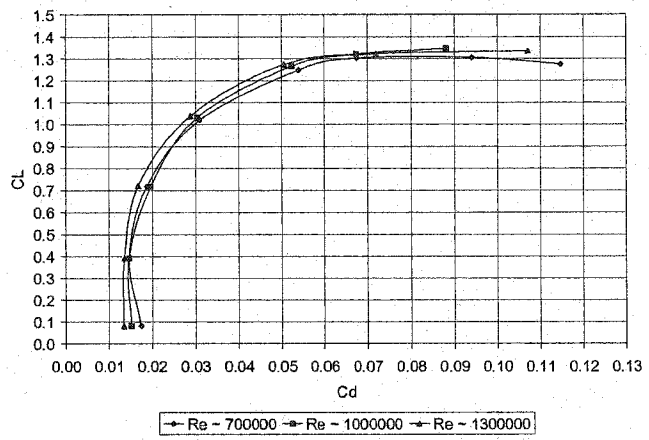

Figure 53 – C_L vs. C_D Reynolds Number Comparison for Ice C3

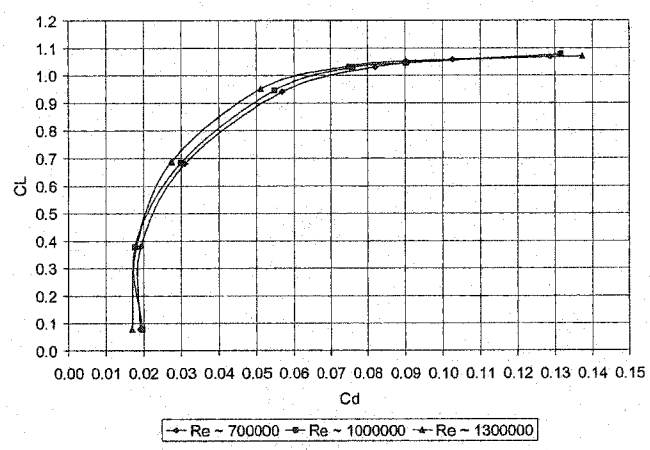

Figure 54 – C_L vs. C_D Reynolds Number Comparison for Ice C4

5.2 PRESSURE DATA COMPARISON

It is also important to compare the pressure distributions for each ice shape between Reynolds numbers. If it can be shown that the distribution does not significantly change, then the Cp_x versus C_{LN} relationship is constant for every Reynolds number. This will eliminate the need to search multiple Reynolds numbers for the correct set of port locations which would significantly decrease development time for each airfoil shape. The pressure distributions are compared for each ice shape across three angles of attack. A sample of the comparison is shown for the clean configuration and ice configuration C1 in Figures 55, 56, 57 and 58. Angles of attack were chosen for a mid range C_{LN} and a near stall C_{LN}. These angles of attack are near the boundaries of the working region for the port configurations. The angles of attack are different for each ice shape. All four ice shapes and clean configuration are compared in Appendix C. The comparison for the three Reynolds numbers indicates that there is little to no change in the pressure distribution with the exception of Ice configuration C2 and near stall angles of attack. There are small fluctuations in the pressure distributions near stall which is to be expected with the onset of flow separation. There are minor fluctuations throughout the pressure distributions of ice configuration C2 due to the horned nature of this ice shape. With a combination of constant lift curve slopes and constant pressure distributions the port location search can be narrowed to one Reynolds number.

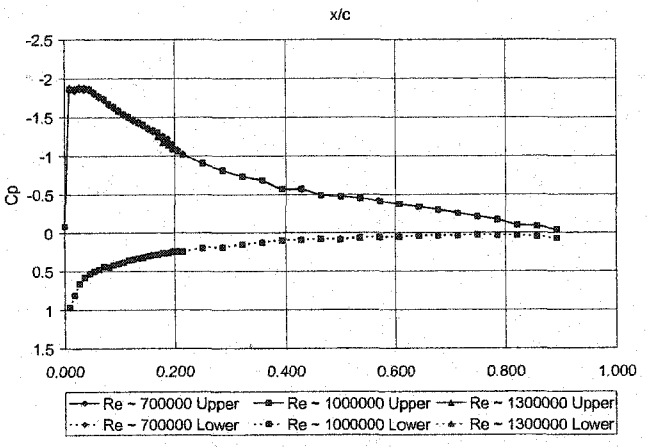

Figure 55 – Cp vs. x/c Reynolds Comparison for Clean AOA 6 Degrees

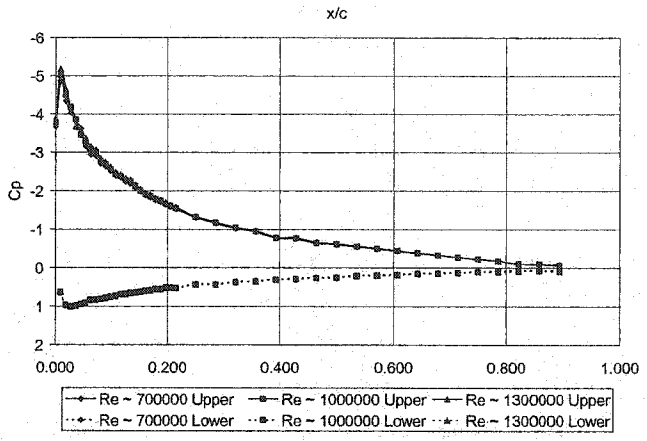

Figure 56 – Cp vs. x/c Reynolds Comparison for Clean AOA 12 Degrees

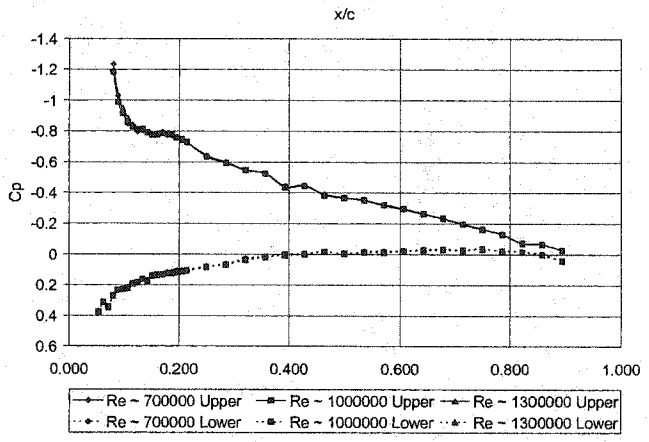

Figure 57 – Cp vs. x/c Reynolds Comparison for C1 AOA 4 Degrees

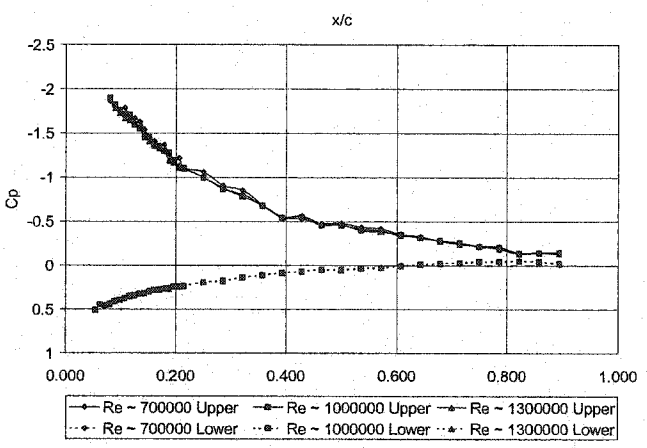

Figure 58 – Cp vs. x/c Reynolds Comparison for C1 AOA 8 Degrees

5.3 STALL MARGIN PORT COMPARISON

The individual pressure coefficient versus C_{LN} for each port in the Cp_x equation has also been analyzed to determine if there is a change in distribution between Reynolds numbers. A sample of this comparison is shown for the clean configuration and the C1 ice configuration in Figures 59, 60, 61 and 62. All four ice shapes and the clean configuration are compared in Appendix D. For the range of C_{LN}'s in which the stall margin instrumentation is working there is some change in the pressure distribution between Reynolds numbers for the clean configuration. This is to be expected, with the change in clean C_{Lmax} comes a change in the pressure distribution. For the range of C_{LN}'s in which the stall margin instrumentation is working there is no change in the pressure distributions for the ice configurations with the exception of ice C2. For C2 there is a large change in Cp1 and Cp4.

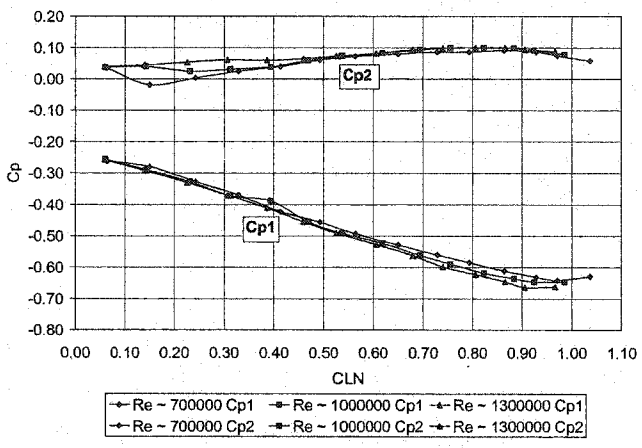

Figure 59 – Cp vs. C_{LN} Reynolds Comparison for Clean ports Cp1 and Cp2

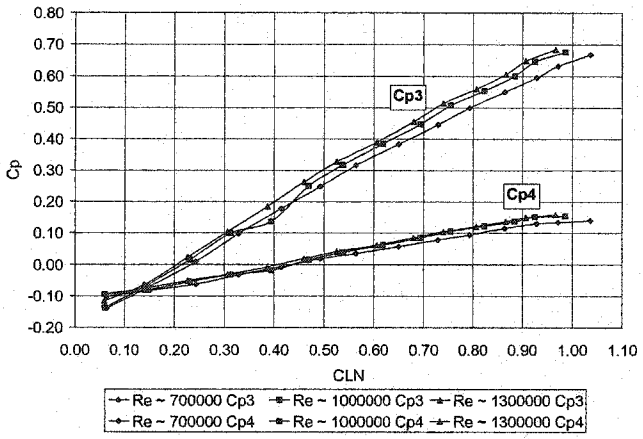

Figure 60 – Cp vs. C_{LN} Reynolds Comparison for Clean ports Cp3 and Cp4

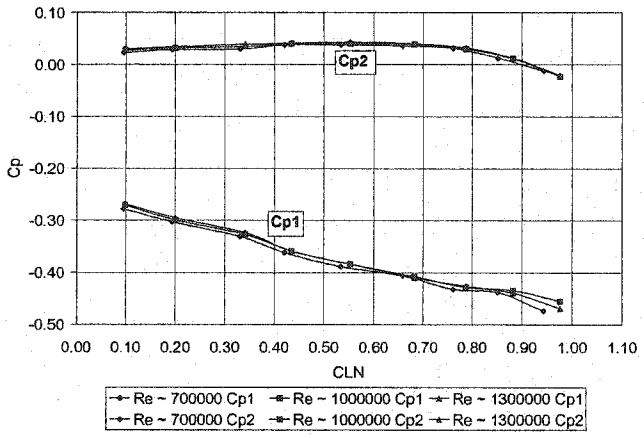

Figure 61 – Cp vs. C_{LN} Reynolds Comparison for Ice C1 ports Cp1 and Cp2

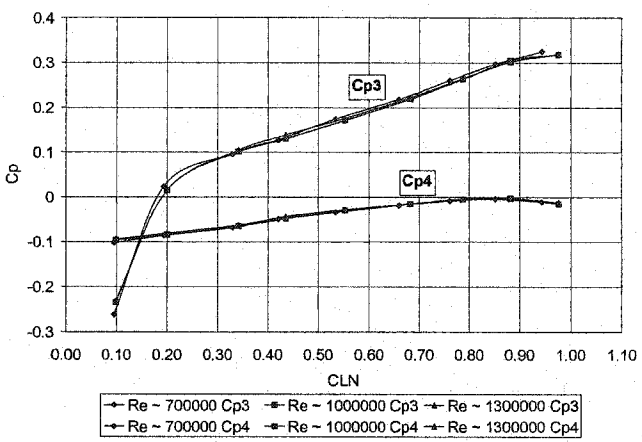

Figure 62 – Cp vs. C_{LN} Reynolds Comparison for Ice C1 ports Cp3 and Cp4

CHAPTER 6 – FLOW VISUALIZATION AND HOTWIRE MEASUREMENTS

6.1 SMOKE WIRE FLOW VISUALIZATION

Smoke wire flow visualization was implemented to gain a better understanding of the flow characteristics occurring around the ice shape and airfoil. A smoke wire was placed in the test section to produce streamlines around the airfoil between the vertical sting mounts. The camera was set up to be focused on the smoke at a point in front of the leading edge ice shape. Pictures were taken at 250 frames per second. The full capability of 2000 frames per second was not used, 250 frames per second was used to capture enough light to clearly see the smoke streamlines. To properly observe the streamlines the entire wing could not be included in the frame. The forward 60% of the wing is viewed. Pictures were captured at four different angles of attack for the clean and ice configurations. The camera setup in relation to the test section is shown in Figure 63. The test was conducted at a Reynolds Number of 100,000.

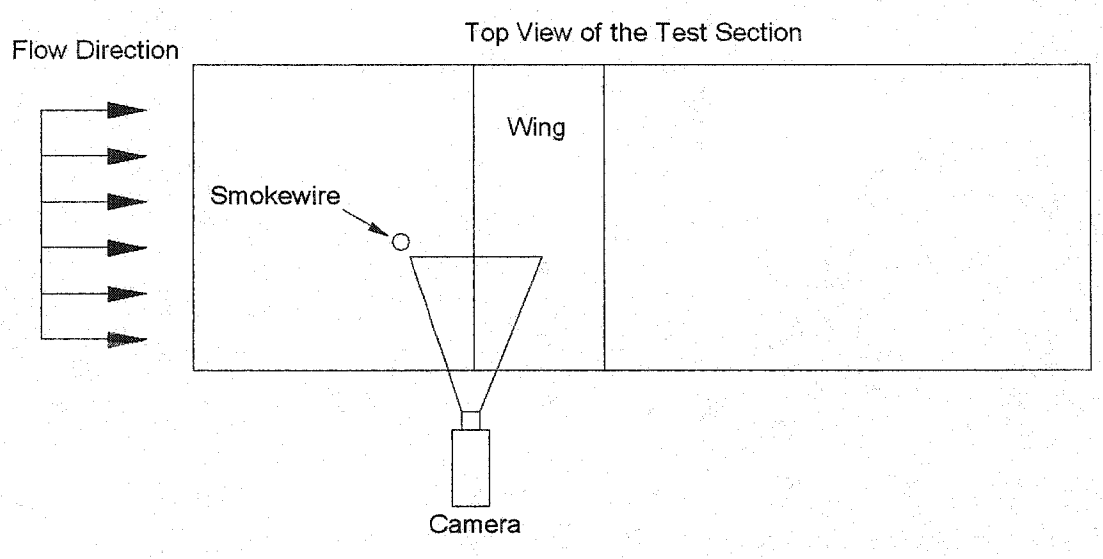

Figure 63 – Smoke Wire Flow Visualization Setup

The camera must be focused on the plane in which the smoke will travel thru. This causes the wing boundary at the edge of the test section to be blurred in each frame. It is difficult to determine the proper boundary of the airfoil section. Reference points were taken off the leading edge ice shape to properly determine the location of the airfoil. Samples of the smoke wire flow visualization at an angle of attack of 4 degrees are shown in Figures 64 thru 68. Angles of attack of 0 degrees, 4 degrees, 8 degrees, 12 degrees and 13.5 degrees are shown in Appendix E.

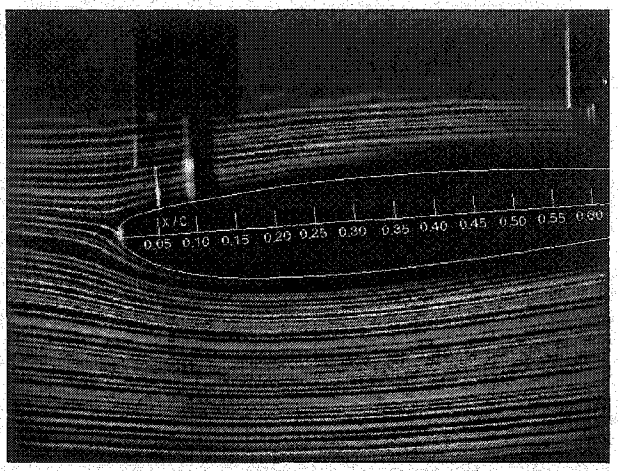

Figure 64 – Clean AOA 4 degrees

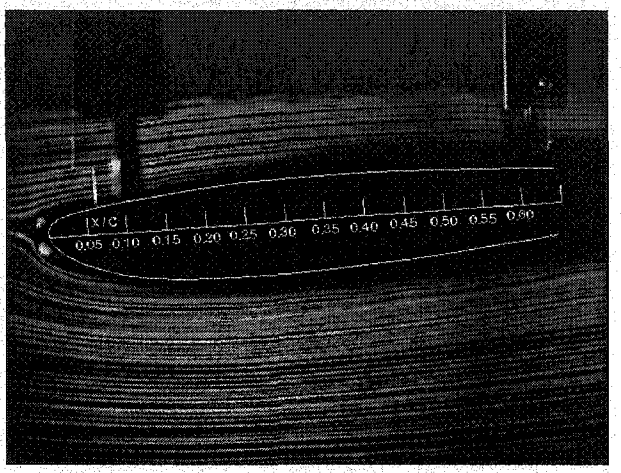

Figure 65 – C1 AOA 4 degrees

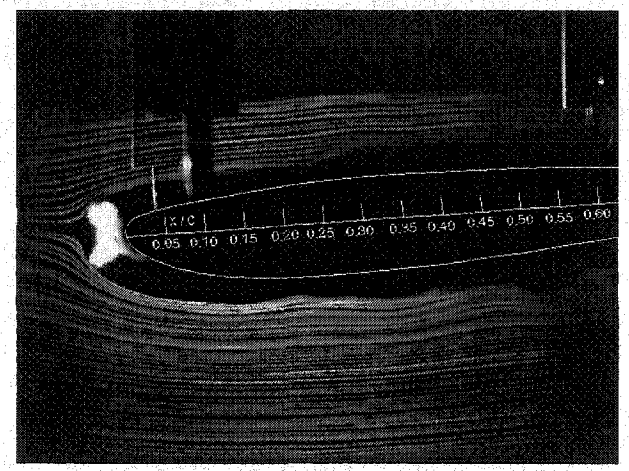

Figure 66 – C2 AOA 4 degrees

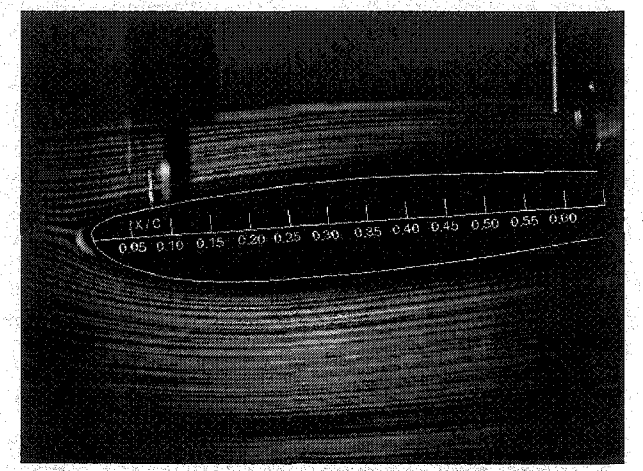

Figure 67 – C3 AOA 4 degrees

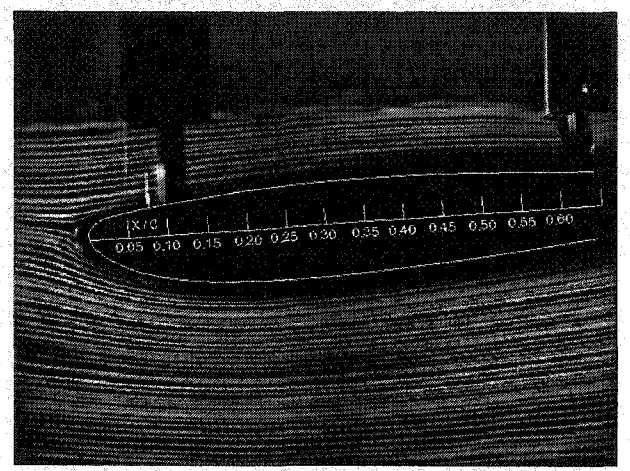

Figure 68 – C4 AOA 4 degrees

It is difficult to determine the location of any separation bubbles located behind the ice shapes. The smoke was unable to be carried into the reverse flow regions to properly document the region of reversed flow. However, the streamlines clearly show fluctuations in the airflow. Configuration C2 immediately has fluctuations in the streamlines at 0 degrees angle of attack with severe fluctuations beginning at an angle of attack of 4 degrees. The separation bubble can be observed behind the C2 configuration on the upper and lower surface of the airfoil and is represented by the black region void of smoke behind the ice shape shown in Figure 66. The length of the bubble is unobtainable with this method. A smaller separation bubble is present behind the C1 configuration. This bubble is not nearly as severe as the C2 configuration. C3 exhibits similar flow characteristics as the clean wing. Separation bubbles behind the ice shapes are not present on the C3 and C4 configurations at any angle of attack. The mild ice shape acts as an extension of the clean wing. Onset of separation begins at 12 degrees for the C3 configuration and is not present at the angle for the clean configuration. Full separation is clearly indicated

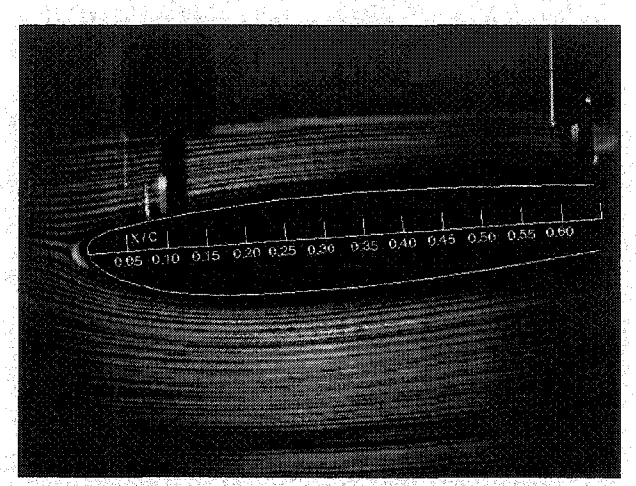

Figure 67 – C3 AOA 4 degrees

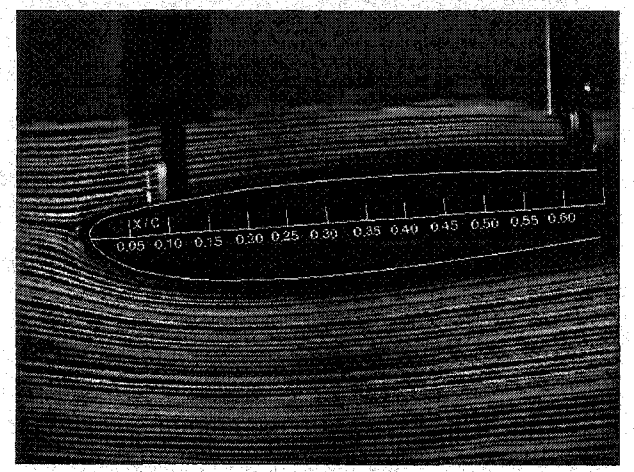

Figure 68 – C4 AOA 4 degrees

It is difficult to determine the location of any separation bubbles located behind the ice shapes. The smoke was unable to be carried into the reverse flow regions to properly document the region of reversed flow. However, the streamlines clearly show fluctuations in the airflow. Configuration C2 immediately has fluctuations in the streamlines at 0 degrees angle of attack with severe fluctuations beginning at an angle of attack of 4 degrees. The separation bubble can be observed behind the C2 configuration on the upper and lower surface of the airfoil and is represented by the black region void of smoke behind the ice shape shown in Figure 66. The length of the bubble is unobtainable with this method. A smaller separation bubble is present behind the C1 configuration. This bubble is not nearly as severe as the C2 configuration. C3 exhibits similar flow characteristics as the clean wing. Separation bubbles behind the ice shapes are not present on the C3 and C4 configurations at any angle of attack. The mild ice shape acts as an extension of the clean wing. Onset of separation begins at 12 degrees for the C3 configuration and is not present at the angle for the clean configuration. Full separation is clearly indicated

at 13.5 degrees for both configurations. Even with the slight horned nature of the C4 configuration, C4 exhibits characteristics similar to that of C3. This can also be seen in the pressure distributions for each configuration. Hotwire anemometry was used to obtain a clearer picture of the separated regions of flow not observed through the smoke wire visualization.

6.2 HOTWIRE TURBULENCE INTENSITY MEASUREMENTS

Turbulence intensity measurements were taken in line surveys perpendicular to the chord line at angles of attack of 0 degrees, 2 degrees and 4 degrees. The angle of attack was limited by the hotwire probe vibration. Flow separation behind the ice shape caused the hotwire to vibrate and produce erroneous data at angles of attack higher than the 4 degrees. The readings were taken at x/c locations of -3.5%, 0%, 3.5%, 7%, 10.5%, 14%, 17.5%, 21%, 24.5%, 28%, 31.5%, 35%, 38.5%, 42%, 50%, 57%, 71%, 85%, and 96%. The movement of the probe was limited by the capabilities of the y-z probe. The probe had a minimum movement of 0.1 inches. Measurements were taken at a Reynolds number of 1,300,000. The location of each data point is shown in Figure 69. The number of readings and locations were held constant throughout each run with the exception of the data points near the leading edge ice shapes. Movement was restricted in this area due to the presence of the ice shapes. The turbulence intensity contour plots are shown in Figures 70 thru 84.

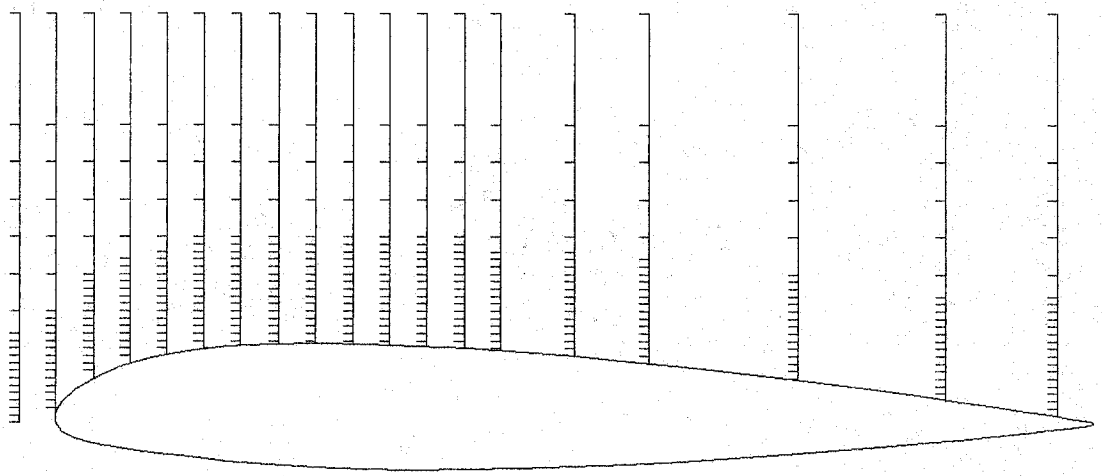

Figure 69 – Hotwire Measurement Locations

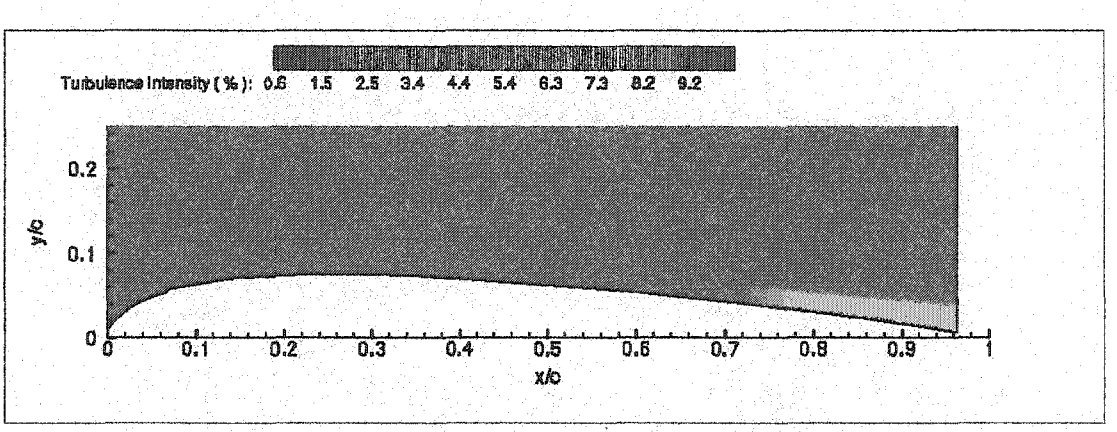

Figure 70 – Clean, Turbulence Intensity, Re ~ 1,300,000, AOA 0 Degrees

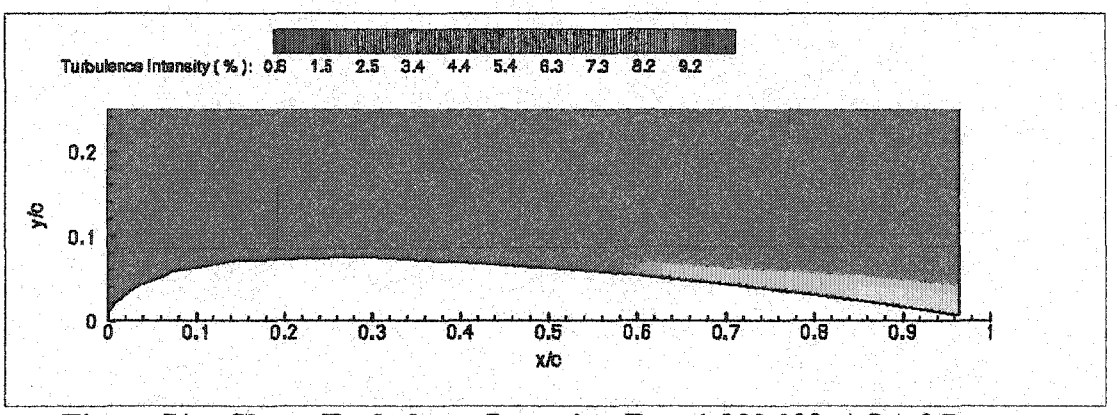

Figure 71 – Clean, Turbulence Intensity, Re ~ 1,300,000, AOA 2 Degrees

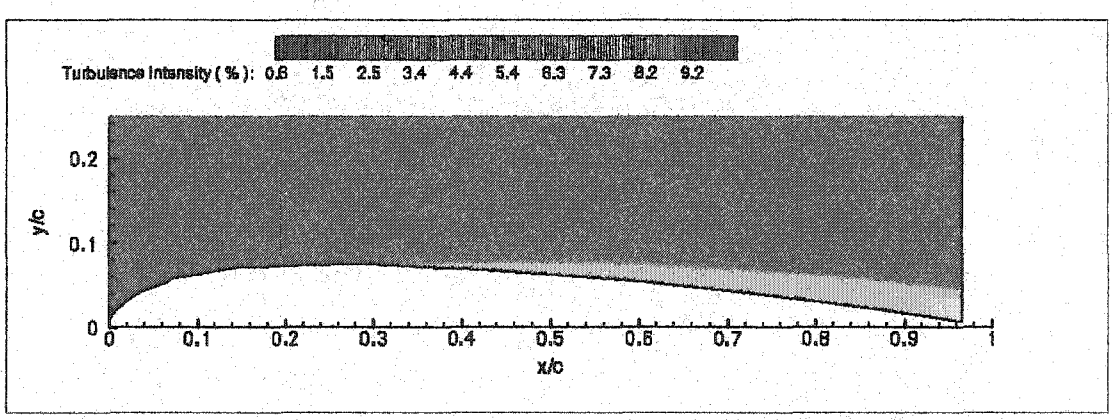

Figure 72 – Clean, Turbulence Intensity, Re ~ 1,300,000, AOA 4 Degrees

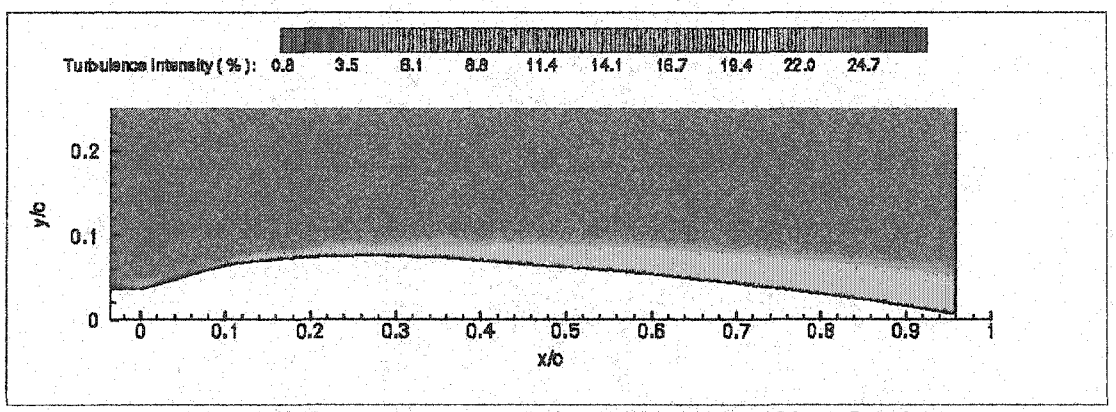

Figure 73 – C1, Turbulence Intensity, Re ~ 1,300,000, AOA 0 Degrees

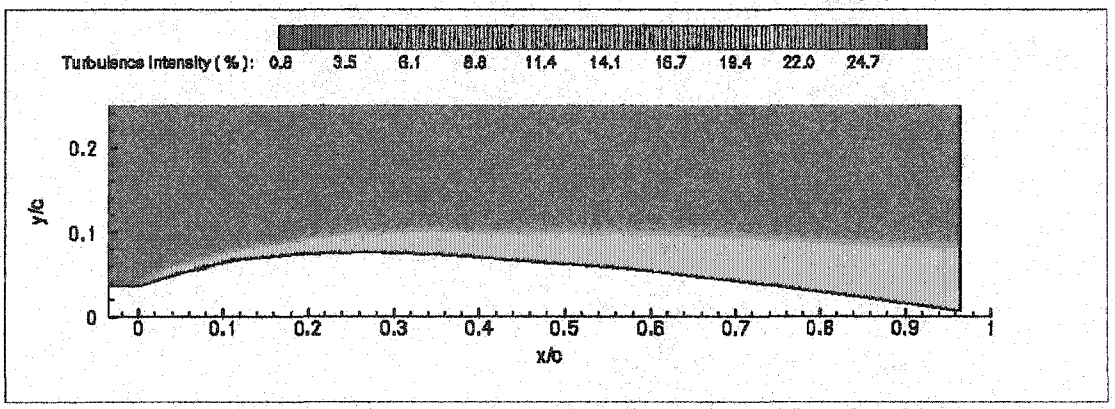

Figure 74 – C1, Turbulence Intensity, Re ~ 1,300,000, AOA 2 Degrees

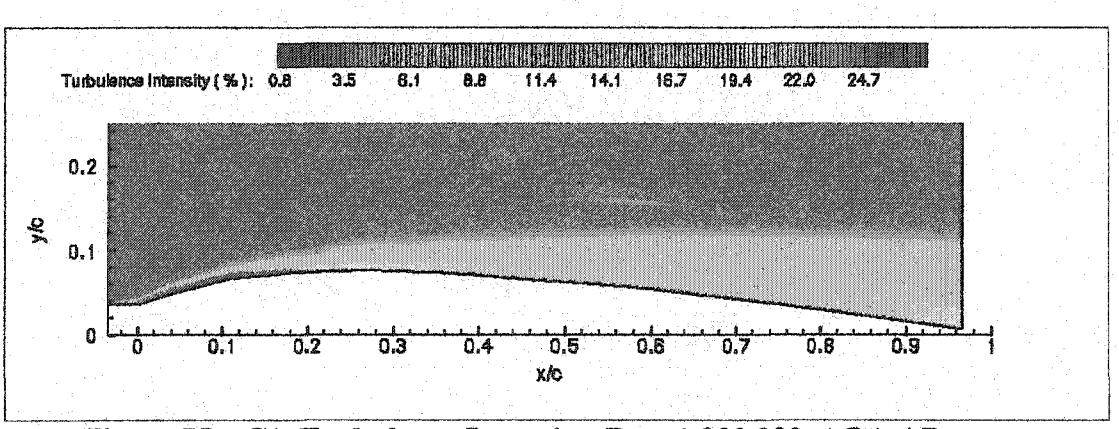

Figure 75 – C1, Turbulence Intensity, Re ~ 1,300,000, AOA 4 Degrees

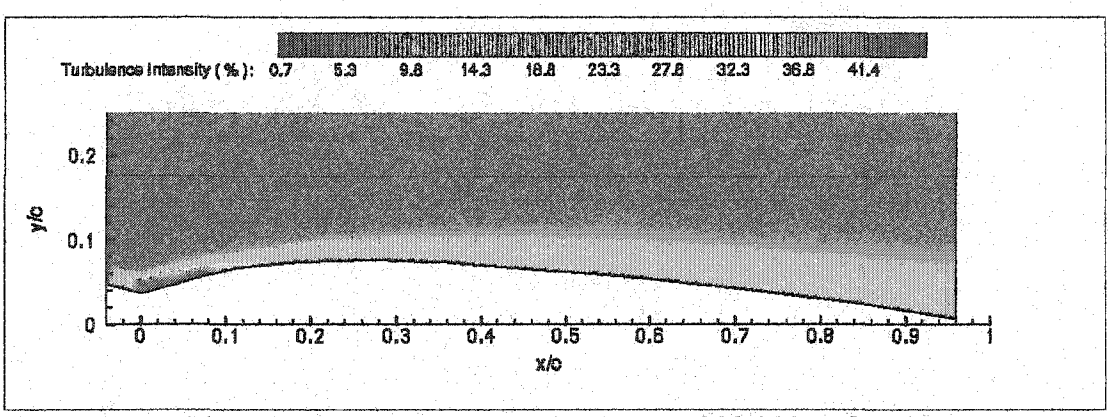

Figure 76 – C2, Turbulence Intensity, Re ~ 1,300,000, AOA 0 Degrees

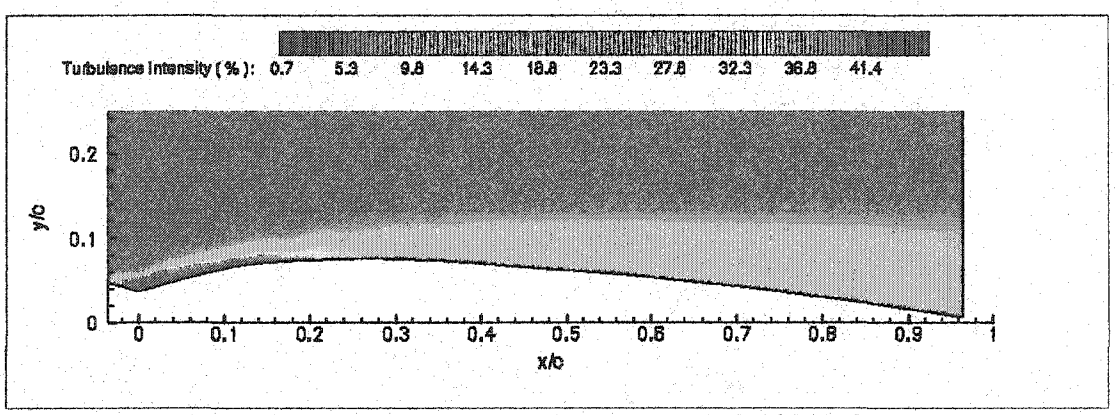

Figure 77 – C2, Turbulence Intensity, Re ~ 1,300,000, AOA 2 Degrees

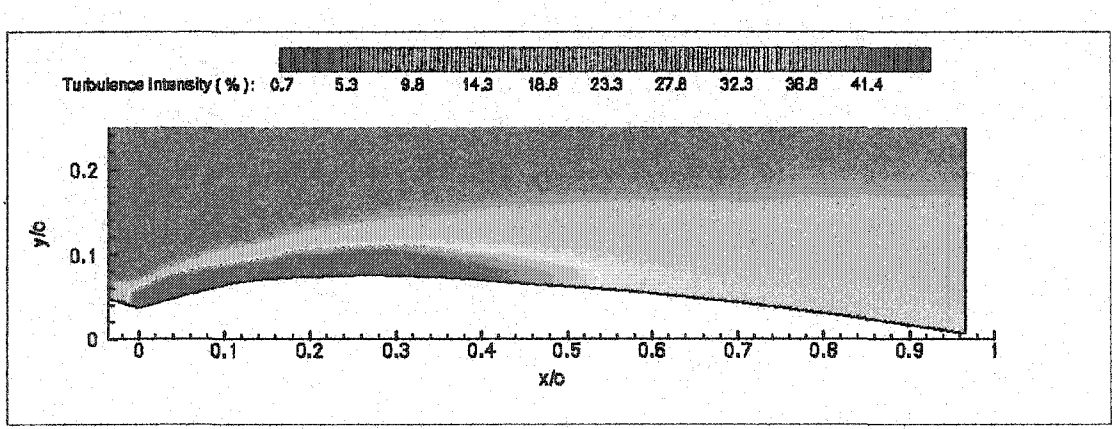

Figure 78 – C2, Turbulence Intensity, Re ~ 1,300,000, AOA 4 Degrees

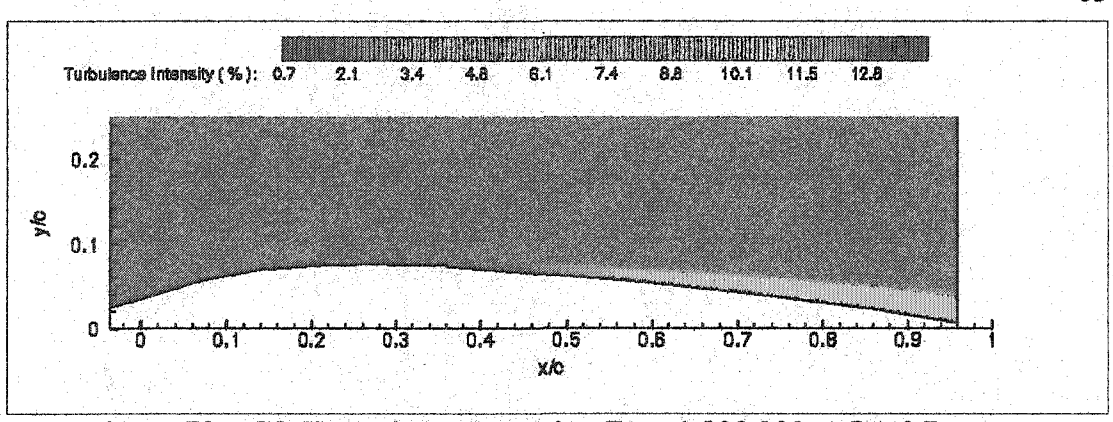

Figure 79 – C3, Turbulence Intensity, Re ~ 1,300,000, AOA 0 Degrees

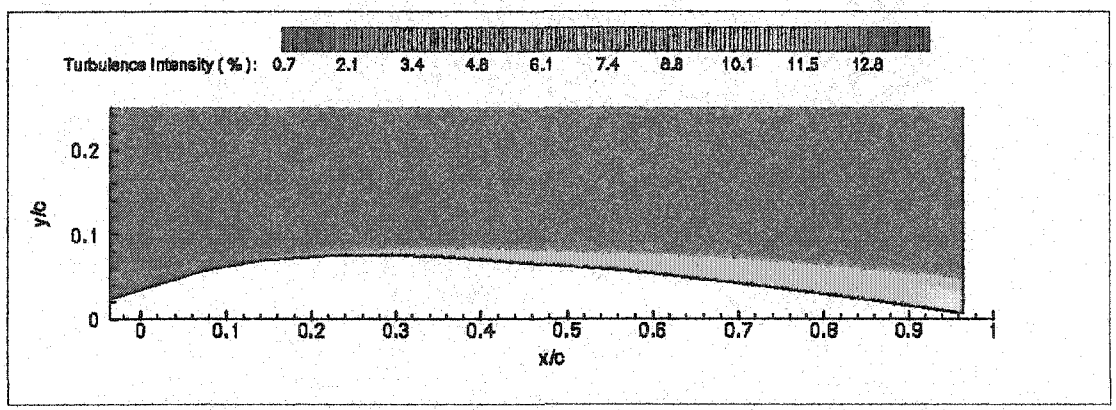

Figure 80 – C3, Turbulence Intensity, Re ~ 1,300,000, AOA 2 Degrees

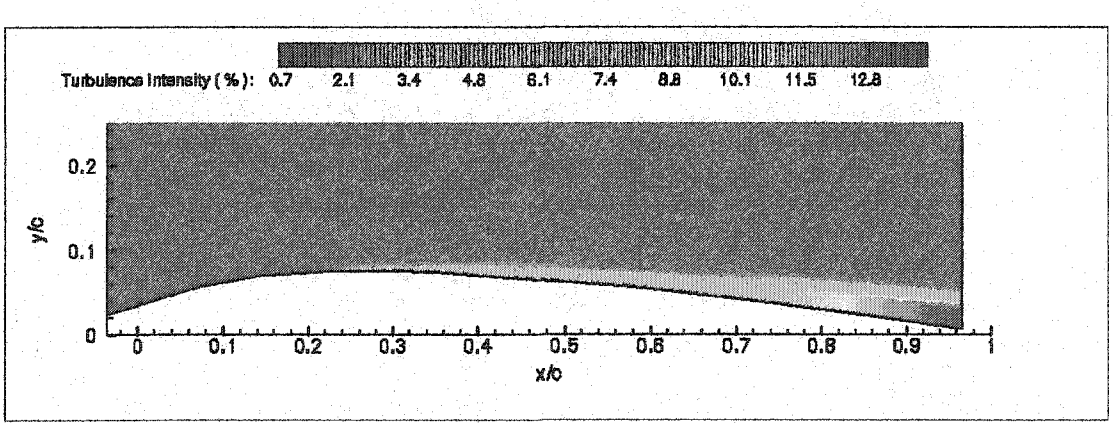

Figure 81 – C3, Turbulence Intensity, Re ~ 1,300,000, AOA 4 Degrees

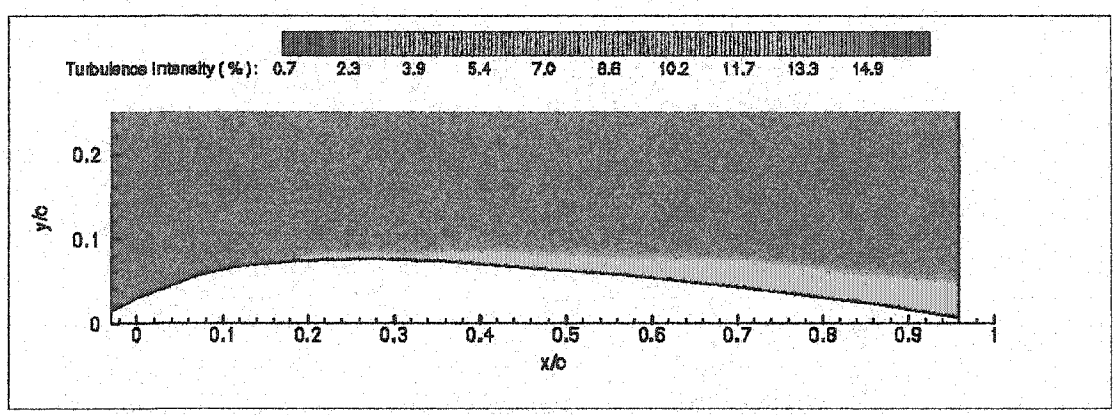

Figure 82 – C4, Turbulence Intensity, Re ~ 1,300,000, AOA 0 Degrees

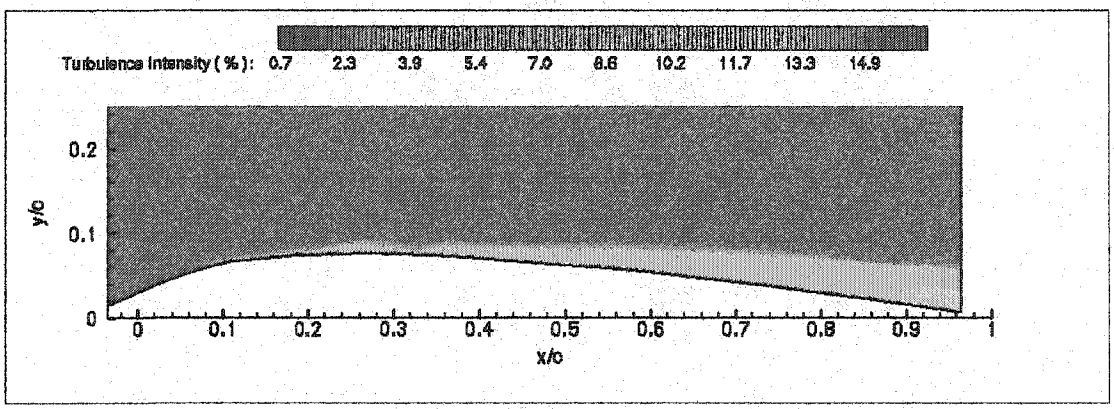

Figure 83 – C4, Turbulence Intensity, Re ~ 1,300,000, AOA 2 Degrees

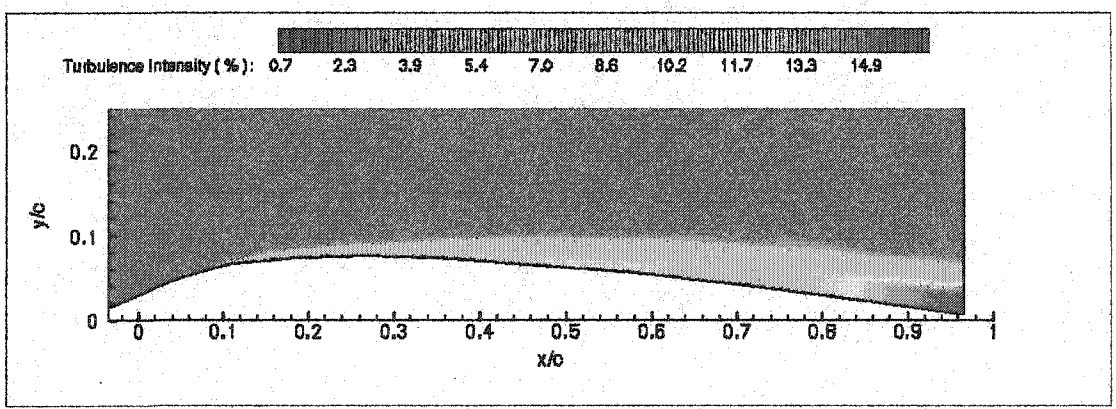

Figure 84 – C4, Turbulence Intensity, Re ~ 1,300,000, AOA 4 Degrees

A separation bubble or region of reversed flow is clearly present for ice C2 shown in Figures 76, 77 and 78. The bubble is characterized by the region of turbulence intensity on the order of 40% or higher. The bubble extends from behind the ice shape to 10% of the chord for zero degrees angle of attack. The bubble continues to lengthen in a non-linear relationship with increase in angle of attack. The bubble extends to 50% of the chord for an angle of attack of four degrees. The stall angle of attack for ice C2 is 7 degrees. The majority of the separated flow for ice C2 is a result of the horned ice shape and not from separated flow moving forward from the trailing edge. A separation bubble is not present for the clean, ice C3 and ice C4 configurations. The flow is characterized by an increase in the thickness and magnitude of the turbulent region at the trailing edge with increase in angle of attack. The clean configuration has a maximum turbulence intensity near 7%. Ice C3 has a maximum turbulence intensity near 13%. Ice C4 has a maximum turbulence intensity near 15%. The turbulence intensity levels are increasing with the severity of the ice shape. Ice C1 exhibits flow characteristics similar to the clean, C3 and C4 configurations. A separation bubble is not present to the extent that the bubble was present for ice C2. A small bubble may be present just behind the ice shape which can be better observed in the smoke wire flow visualization. A bubble (or smokeless region) appears to be present behind the ice shape extending to 4% of the chord. The limits of the hotwire probe movement caused this bubble to be missed in the turbulence intensity measurements. The bubble on Ice C1 does not appear to move as quickly as the bubble behind Ice C2 causing the flow separation to be dominated by trailing edge separation rather than separation caused by the ice shape. Therefore the Ice C1 wing exhibits characteristics which are more related to flow characteristics of the clean, C3 and C4 configurations. The maximum turbulence level for Ice C1 near the trailing edge is near 17%. Levels of higher turbulence are present near the leading edge behind the ice shape, but are limited to a very thin layer near the surface of the wing. The large difference in flow characteristics for the Ice C2 provides an indication as to why the port locations for the other three ice shapes will not work for Ice C2. The flow characteristics must be similar for the Stall Margin Instrumentation to work correctly. This is discussed further in Chapter 7.

CHAPTER 7 – STALL MARGIN SYSTEM ANALYSIS

An objective of this research was to further understand the stall margin system and develop it for use on other airfoil shapes. To accomplish this, the locations of the ports and their relationship to the surrounding flow characteristics must be examined. The port locations must also be compared to previous locations for other airfoil shapes. The research conducted on the NACA 0018 wing will provide a limited comparison. The NACA 0018 test was designed to discover the port locations and therefore was limited to pressure data at lower Reynolds numbers.[3]

7.1 PORT PRESSURE

The stall margin system is based on a calibration remaining constant for every ice shape. There must be a common shift due to the ice formation. The C_{LN} is related to Cp_x through a calibration equation. Cp_x measures the shift in pressure due to the ice shape on the leading edge of the wing. The Cp_x equation possesses specific characteristics that allow this to happen. The use of four pressures allows the instrumentation to work independent of altitude or airspeed. The derivation of this is shown in equations 18, 19 and 20. Dynamic Pressure and Static Pressure will both cancel out of these equations allowing the individual port pressures to remain in the form of a numerator and denominator.

$$(18)\quad Cp_x = \frac{CP1 - CP2}{CP3 - CP4}$$

$$(19)\quad Cp_x = \frac{\frac{P1 - Pstatic}{Q} - \frac{P2 - Pstatic}{Q}}{\frac{P3 - Pstatic}{Q} - \frac{P4 - Pstatic}{Q}}$$

$$(20)\quad Cp_x = \frac{P1 - P2}{P3 - P4} = \frac{Cp_{\text{numerator}}}{Cp_{\text{denominator}}}$$

There is a change in the pressure distribution due to the ice shape. This change causes a shift of the delta pressures for the numerator and denominator. For the original or clean calibration to work, the shift in the numerator and denominator must be equal to each other. Thereby canceling each other and producing the same value for Cp_x that would be seen for the clean wing case. The shift must be a constant factor

of multiplication to be removed from equation 20. The multiplication factors are represented by M1 and M2 in equation 21. For every ice shape and every C_{LN}, M1 and M2 must be equal for the system to be prefect. The error in prediction of C_{LN} is present because M1 and M2 are not always equal.

$$(21)\quad Cp_x = \frac{M1 \cdot Cp_{\text{numerator}}}{M2 \cdot Cp_{\text{denominator}}}$$

Figures 85 and 86 show Cp_N and Cp_D for the port locations discussed in Chapter 4.

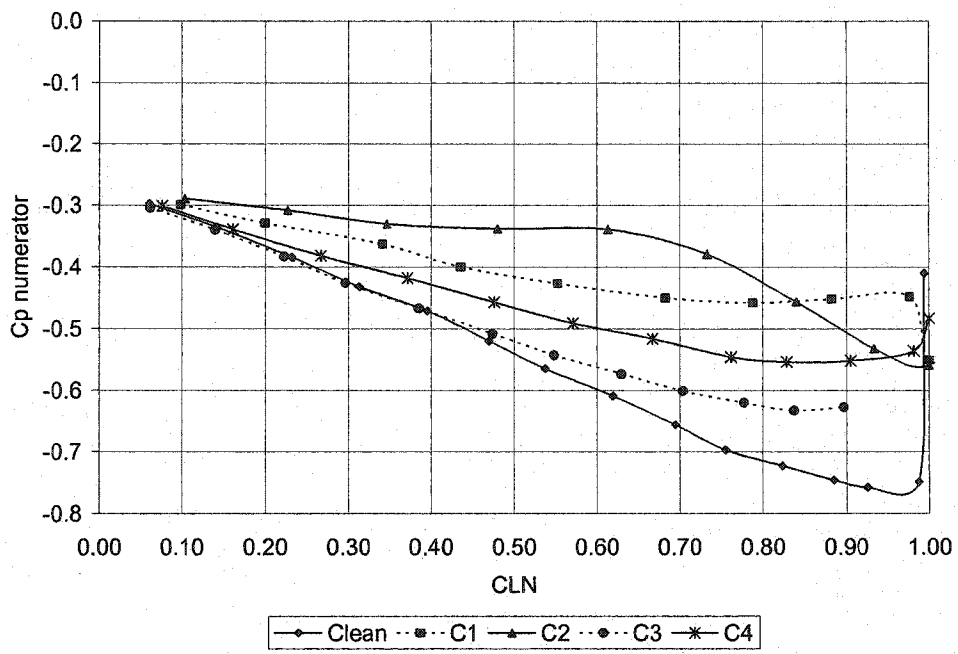

Figure 85 – Cp_N versus C_{LN}, Re ~ 1,300,000

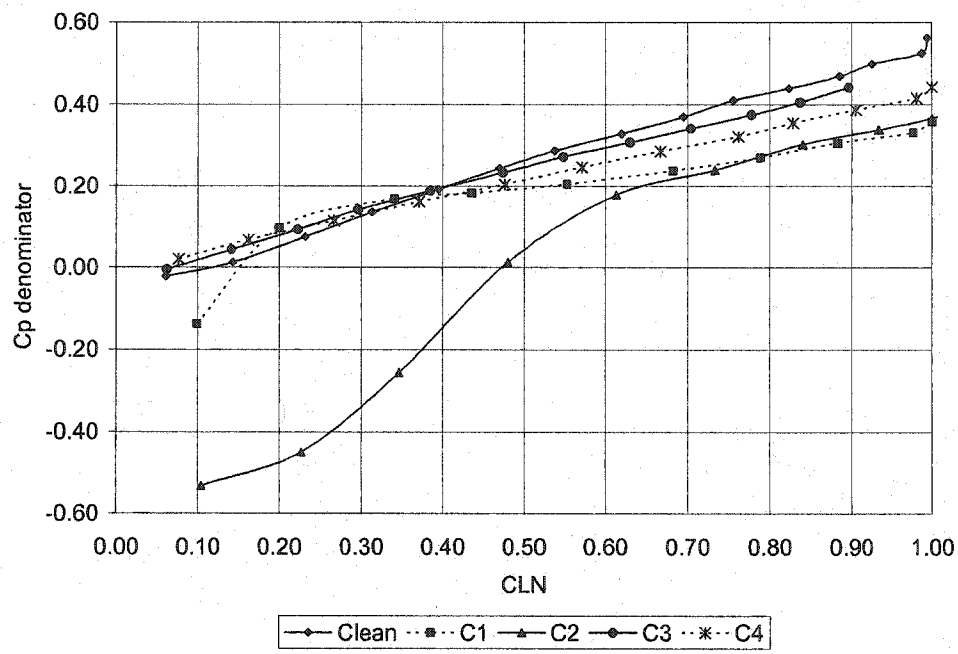

Figure 86 – Cp_D versus C_{LN}, Re ~ 1,300,000

The data lines in each figure have a set order to them. Beginning with the clean configuration in Figure 85 the order of the data lines is Clean, C3, C4, C1 and C2. In Figure 86 the order is Clean, C3, C4, C1 and C2. This order must match to produce the constant shift required to cancel M1 and M2. Notice also that the order in which the data lines deviate from clean is from the mildest ice shape (or closest to clean configuration) to the most severe. Tables 9, 10, 11, and 12 examine the relationship between the Clean and Ice configurations in more detail through calculation of M1, M2 and the Ratio between M1 and M2.

CLN	Clean - N	C1 - N	M1	Clean - D	C1 - D	M2	Ratio
0.5	-0.54	-0.42	1.29	0.26	0.19	1.37	0.94
0.6	-0.60	-0.44	1.36	0.32	0.22	1.49	0.92
0.7	-0.66	-0.45	1.47	0.37	0.24	1.54	0.95
0.8	-0.71	-0.46	1.54	0.43	0.27	1.59	0.97

Table 9 – Clean to Ice C1 Comparison for M1 and M2, Re ~ 1,300,000

CLN	Clean - N	C2 - N	M1	Clean - D	C2 - D	M2	Ratio
0.5	-0.54	-0.34	1.59	0.26	0.01	26.00	0.06
0.6	-0.60	-0.34	1.76	0.32	0.17	1.88	0.94
0.7	-0.66	-0.36	1.83	0.37	0.22	1.64	1.11
0.8	-0.71	-0.42	1.69	0.43	0.28	1.54	1.10

Table 10 – Clean to Ice C2 Comparison for M1 and M2, Re ~ 1,300,000

CLN	Clean - N	C3 - N	M1	Clean - D	C3 - D	M2	Ratio
0.5	-0.54	-0.52	1.04	0.26	0.24	1.06	0.98
0.6	-0.60	-0.56	1.07	0.32	0.29	1.08	0.99
0.7	-0.66	-0.60	1.10	0.37	0.34	1.09	1.01
0.8	-0.71	-0.62	1.15	0.43	0.38	1.12	1.03

Table 11 – Clean to Ice C3 Comparison for M1 and M2, Re ~ 1,300,000

CLN	Clean - N	C4 - N	M1	Clean - D	C4 - D	M2	Ratio
0.5	-0.54	-0.46	1.17	0.26	0.21	1.21	0.97
0.6	-0.60	-0.50	1.20	0.32	0.26	1.23	0.98
0.7	-0.66	-0.52	1.27	0.37	0.30	1.23	1.03
0.8	-0.71	-0.55	1.29	0.43	0.34	1.26	1.02

Table 12 – Clean to Ice C4 Comparison for M1 and M2, Re ~ 1,300,000

For M1 and M2 to be removed from the equation the ratio must be equal to one. Any deviation from one is an error that will appear in the final curves shown in Figures 41, 42 and 43. Configurations C3 and C4 match really well and are within 3% of one for the M1 and M2 ratio. This equates into little to no deviation from the clean curves. Configuration C1 deviates slightly more from clean. The largest deviation for C1 is 7%, which equates into a larger error from the clean configuration. Configuration C2 deviates significantly as can be seen in the large non-linear nature of the Cp_N and Cp_D curves in Figures 85 and 86. To further understand the deviation for ice configuration C2 the individual port pressure coefficients versus C_{LN} must be examined. These relationships are shown in Figures 87, 88, 89 and 90.

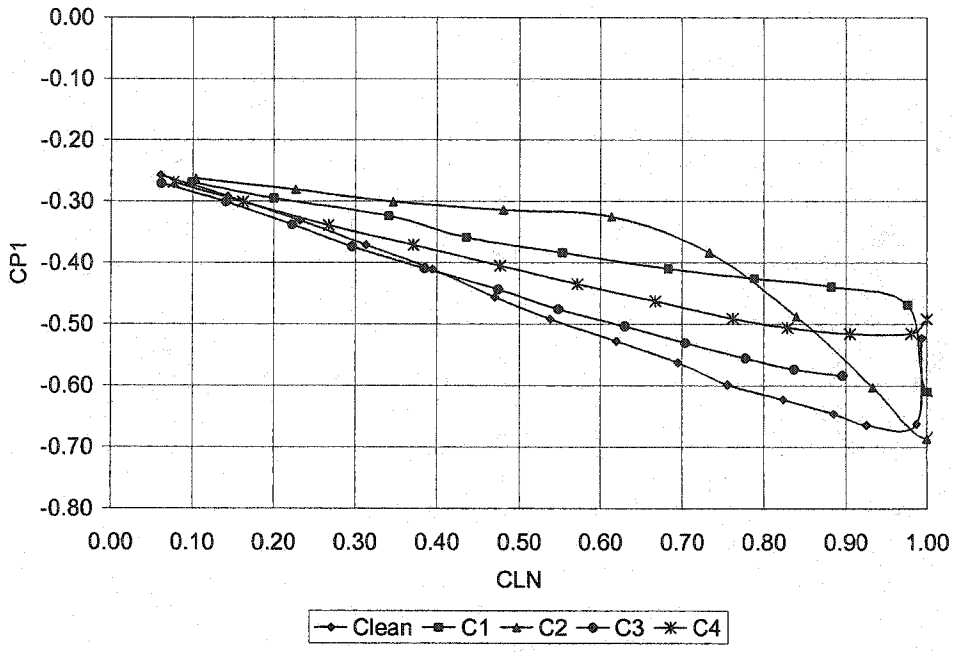

Figure 87 – CP1 versus C_{LN}, Re ~ 1,300,000

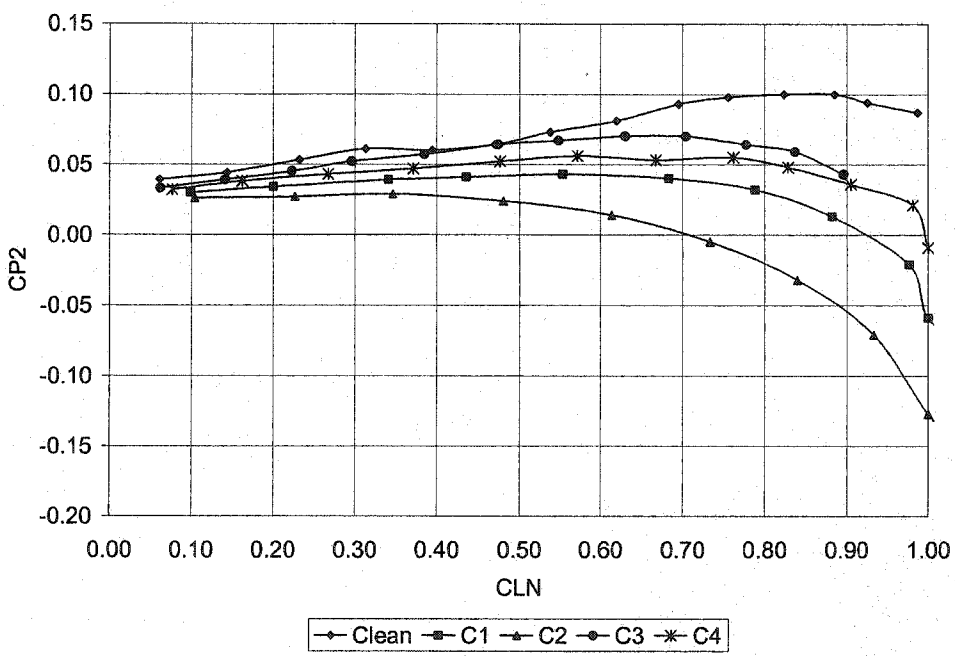

Figure 88 – CP2 versus C_{LN}, Re ~ 1,300,000

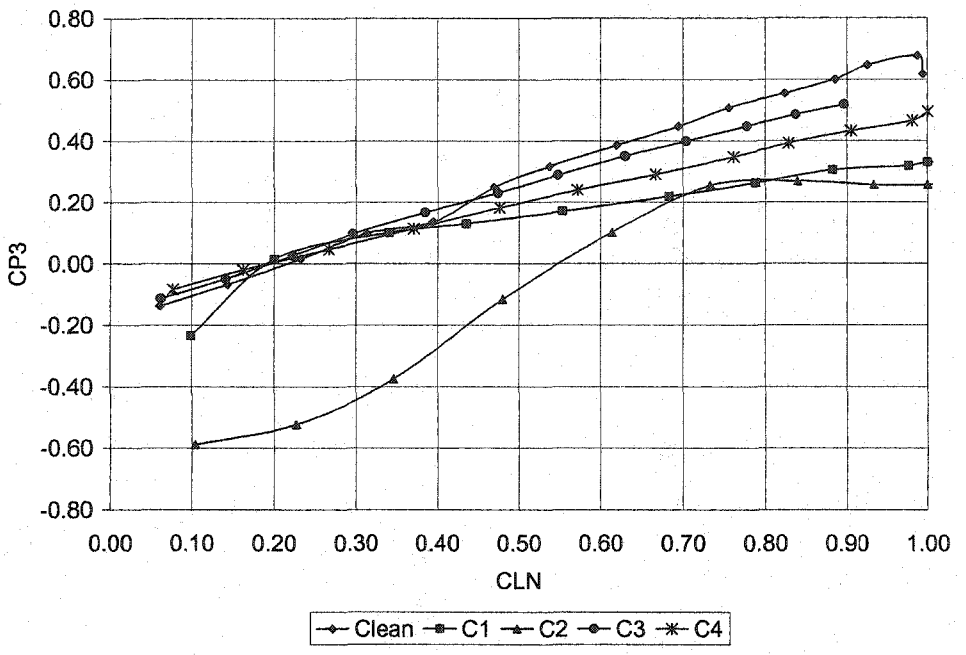

Figure 89 – CP3 versus C_{LN}, Re ~ 1,300,000

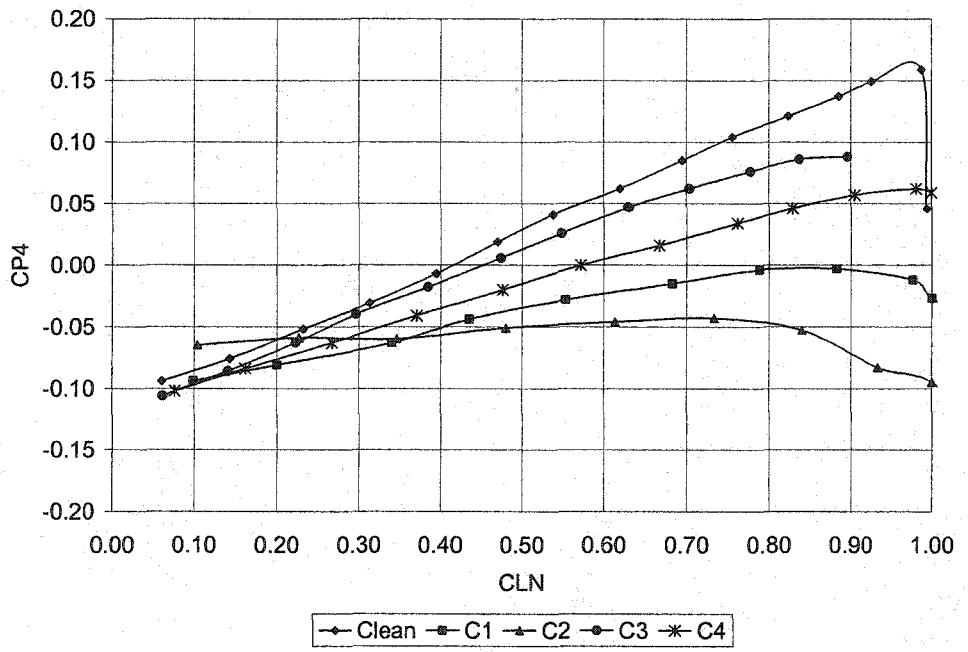

Figure 90 – CP4 versus C_{LN}, Re ~ 1,300,000

Recall that the port locations from Chapter 4 that allow the stall margin to work properly for the NACA 23012 airfoil are:

CP1 – Upper Surface x/c = 0.46
CP2 – Lower Surface x/c = 0.89
CP3 – Lower Surface x/c = 0.14
CP4 – Lower Surface x/c = 0.64

Ports CP2 and CP4

CP2 and CP4 are nearer to the trailing edge of the airfoil than CP1 and CP2. CP2 and CP4 shown in Figures 88 and 90 shows an orderly arrangement to the Cp curves similar to that found in the Cp_N and Cp_D figures. The shift that appears in Cp_N and Cp_D must occur in the individual port curves for it to appear in the Cp_N and Cp_D curves. The following order applies to both, beginning with the Clean configuration; Clean, C3, C4, C1 and C2.

Port CP1

Port CP1 has the proper order and shift for the Clean, C3, C4 and C1 configurations. There is a deviation for Ice C2. Ice C2 appears to work for a C_{LN} range from 0% to 60%. The C_{LN} of 60% corresponds directly to the angle of attack at which the separation bubble passes over port CP1. When the separation bubble passes over this port the pressure drops sharply and no longer follows the trend for the pressure seen outside of separation bubble.

Port CP3

A similar occurrence is found for CP3 located at 14% on the lower surface. The proper order and shift is present for the Clean, C3, C4 and C1 configurations. A separation bubble occurs behind the lower horn on Ice C2 which can be seen in Appendix E (smoke flow visualization) Figures 271 thru 275. The pressure curve for Ice C2 drops significantly at the lower range of C_{LN}'s. The Cp value is nearly the same as seen for port CP1 in the separation bubble. The lower surface separation bubble is present at the ranges of C_{LN}'s corresponding to the large deviation in Cp. However, the pressure curve appears to return to the proper Cp values for the C_{LN} range from 85% to 100%. This corresponds to the C_{LN}'s at which the separation bubble is no longer influencing this port. From these observations it is evident that the ports must remain out of the influence of any separation bubble. This is difficult to avoid for the 45 minute severely horned ice shapes.

7.2 PORT LOCATION

The location of the ports is important to the operation of the stall margin system. The ports must be located such that M1 and M2 are removed from the Cp_x equation. The port locations must also be a significant distance from each other to produce a proper delta pressure for Cp_N and Cp_D which will produce the proper slope for the calibration curve. The largest pressure difference will be produced in the numerator by locating a port near the minimum pressure point on the upper surface and a port on the lower surface. To produce a denominator with a magnitude near zero port locations must be chosen on the same surface or near the trailing edge of the airfoil. The ports must be a significant distance apart to avoid the possibility of a denominator Cp of zero. This will produce a divide by zero error in any calibration.

The slope of the calibration curve is also important. A larger numerator and smaller denominator will produce a large slope for the Cp_x versus C_{LN} calibration curve. A slope approaching zero will not allow the C_{LN} to be calculated from a Cp_x value with any accuracy. A single value of Cp_x may produce a large number of C_{LN} values. An example of this is shown in Figure 91. A slope approaching infinity will produce only one C_{LN} for a large number of Cp_x values. A slope in a range from one to four will produce the optimum calibration curve. This slope is enough to dampen out the effects of any instrumentation error and is possible to obtain with the delta pressures available in an airfoil pressure distribution. The slope for the calibration curve for this instrumentation is near one.

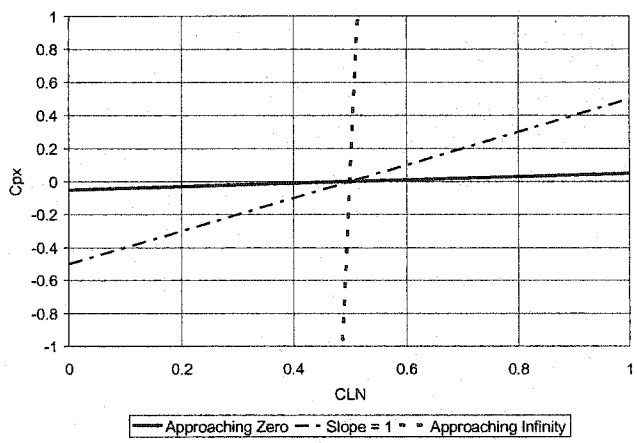

Figure 91 – Slope Comparison Example

The ports for the NACA 23012 follow the rules stated above CP1 and CP2 produce a large difference in pressure by utilizing apart on the upper surface near the leading edge and a lower surface port near the trailing edge. CP3 and CP4 produce a small denominator allowing the proper slope to be obtained for the calibration curve.

7.3 COMPARISON TO THE NACA 0018 PORT LOCATIONS

The locations for the NACA 0018 are:
CP1 – Upper Surface x/c = 0.22
CP2 – Lower Surface x/c = 0.68
CP3 – Upper Surface x/c = 0.41
CP4 – Lower Surface x/c = 0.41

The locations for the NACA 23012 as stated earlier are:
CP1 – Upper Surface x/c = 0.46
CP2 – Lower Surface x/c = 0.89
CP3 – Lower Surface x/c = 0.14
CP4 – Lower Surface x/c = 0.64

There are similarities and differences between these two sets of port locations. The numerators for both sets utilize a lower surface aft port subtracted from an upper surface forward port. Both denominators utilize ports near each other to produce a small denominator magnitude for the proper calibration curve slope. However the NACA 0018 has CP3 on the upper surface rather than the lower surface. It is suspected that the difference in port locations may be a result of the ice shapes used for the 0018 test. The test was limited to milder ice shapes with minor horns not nearly as severe as the 23012 test. The shapes can be seen in Figure 7. The 0018 test was limited because the model was structurally unstable with the separated flow produced by the severely horned ice shapes. Without the large horns there was not as large an influence from the separation bubble on the pressure distribution. Sets of port locations were found for Ice C3 and C4 on the 23012 wing that were nearer to the set found in the 0018 test. These sets of ports produced a non-linear Cp_x versus C_{LN} calibration curve as is seen in Figure 8 for the 0018 test. With a structurally sound 0018 model and with horned ice shapes it is suspected that the port locations will move from the locations found in the initial 0018 test.

7.4 CAMBER AND THICKNESS RELATIONSHIP TO THE ICED AIRFOIL

The camber and thickness of an airfoil play an important role in lift production. The camber is a measure of the halfway point between the upper and lower surface of an airfoil. If there is 0% camber then the camber line and the chord line are the same line. The chord line is a straight line connecting the leading edge and trailing edge of the airfoil. If there is a positive camber there is an arc to the camber line and it is above the chord line. An increase in camber serves to offset the zero degree angle of attack lift coefficient. A 0% camber or symmetrical airfoil will have a lift coefficient equal to zero at zero degrees angle of attack. A positively cambered airfoil will have a positive offset for the lift coefficient at zero degrees angle of attack. The positive offset will cause a positive adjustment to occur in the maximum lift coefficient of the wing. The thickness of the wing also changes the

maximum lift coefficient. For the 5-digit 23000 series airfoils an increase in thickness will decrease the maximum lift coefficient and will also decrease the slope of the lift curve as is documented by the text "Theory of Wing Sections".[43] However, a change in thickness will not produce an offset at the zero degree angle of attack lift coefficient like an increase in camber will. The maximum lift coefficient decrease with increase in thickness can be seen for the 5-digit 23000 series airfoils in Table 13.

Airfoil	C_{Lmax}
23012	1.6
23015	1.5
23018	1.4
23021	1.3

Table 13 – 23000 series C_{Lmax} at Re ~ 3,000,000

The shift in maximum lift coefficient for the clean and iced configurations is similar to a shift in maximum lift coefficient due to a change in airfoil thickness. Figure 92 again shows the lift curve for the clean and iced configurations. There is no shift in the zero degree angle of attack lift coefficient similar to a change in airfoil thickness. There is also a change in the maximum lift coefficient again similar to what is seen with a change in thickness and there is a decrease in lift curve slope with a decrease in maximum lift coefficient. A decrease in lift coefficient is associated with a decrease in area between the upper and lower surface pressure distributions. To gain a better understanding of this relationship the pressure distributions for the clean and iced configurations at a C_{LN} of 0.6 and the pressure distributions for NACA 23012, 23015 and 23018 airfoils at a C_{LN} of 0.6 are compared. In the NACA 5-digit airfoil series the last two digits represent the thickness of the airfoil as a percent of chord. Thus a 12 located in the last two digits represents a 12% thick airfoil. Figures 93 and 95 show the clean and iced pressure distribution and Figures 94 and 96 show the 23000 series pressure distribution.

For the clean and iced configurations, pressure curves tend to follow the same order as do the 5-digit series pressure curves. For the upper surface iced airfoil the order is Clean, C3, C4, C1 and C2 which is in order of decreasing C_{Lmax}. Near the leading edge of the airfoil the 5-digit series upper surface has the order 23012, 23015, 23018 which is again in the order of decreasing C_{Lmax}. The upper surface pressure distributions for the 5-digit series cross and reverse order near the mid chord locations, but the pressure values are nearly constant across thicknesses at this point. The clean and iced configuration lower surface pressure distributions again match the decreasing C_{Lmax} order of the 5-digit series lower surface pressure distributions for chord locations of 0% to 90%. It is important to note that the pressure distribution orders are similar for the decreasing maximum lift coefficient and not thickness

change. The addition of an ice shape on the leading edge of the wing decreases the percentage thickness of the airfoil by increasing the chord length. For the 5-digit 23000 series airfoil the decrease in C_{Lmax} is associated with an increase in thickness. The iced pressure distributions have incremental shifts in pressure which are similar to a shift in pressure distribution due to a change in thickness. The area between the upper and lower surface pressure distributions is decreasing incrementally with increase in the severity of the ice shape. An incremental shift occurs over the entire airfoil for the clean to iced situations. The stall margin system uses the four port locations to measure this shift in pressure distribution. The pressure shift not being constant across the entire airfoil causes the location of the ports to be important. If the pressure distribution was a constant percentage increase across the entire airfoil there would be more sets of port locations that properly cancel M1 and M2.

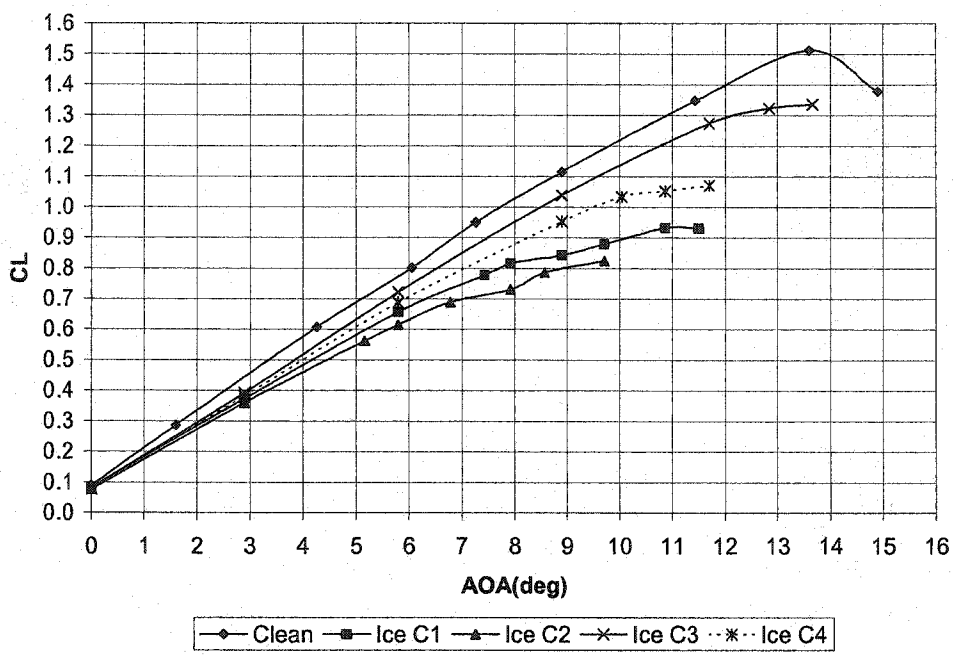

Figure 92 – CL vs α comparison , Re ~ 1,300,000

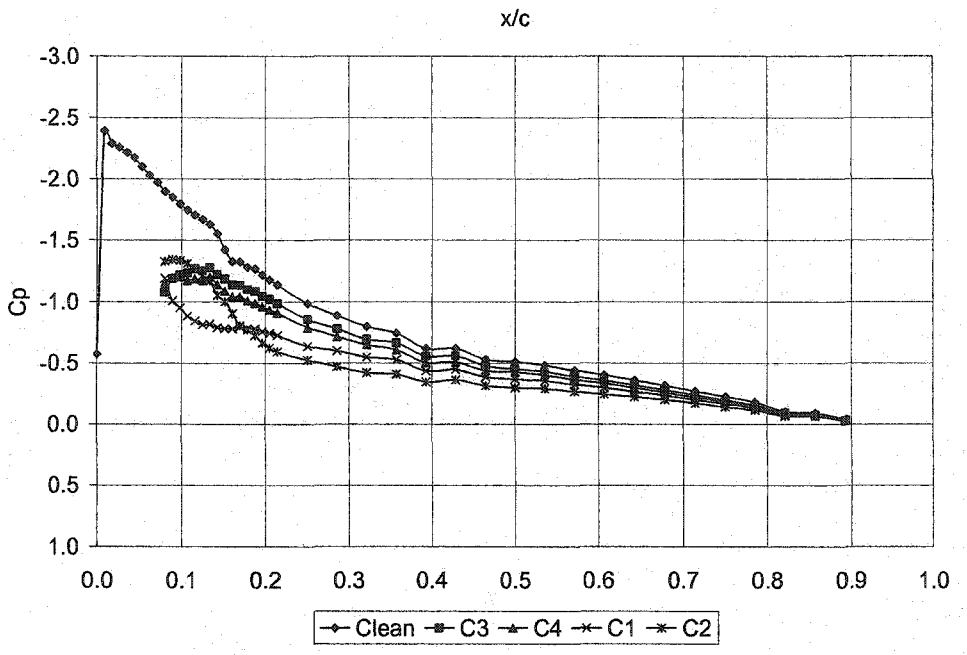

Figure 93 – Pressure Distribution C_{LN} = 0.6, Upper Surface, Re ~ 1,300,000

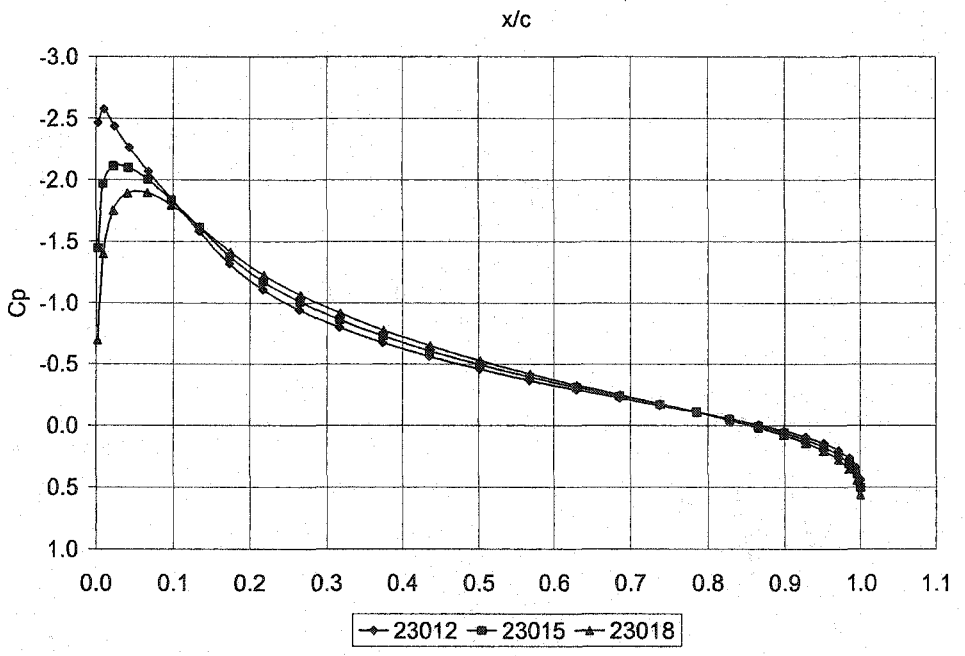

Figure 94 – 23000 Series Pressure Distribution C_{LN} = 0.6, Upper Surface, Re ~ 1,300,000

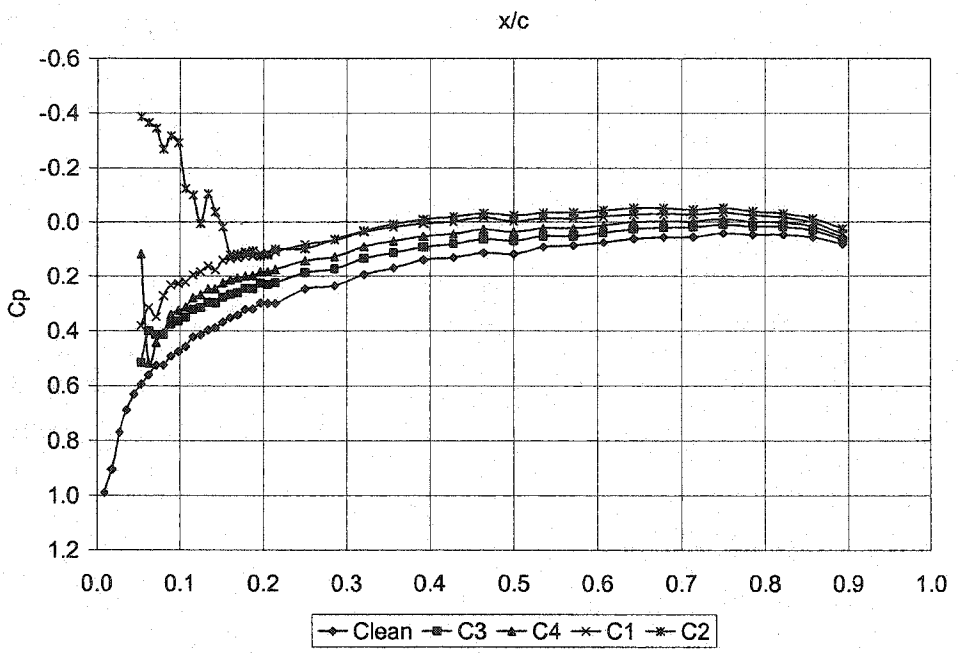

Figure 95 – Pressure Distribution C_{LN} = 0.6, Lower Surface, Re ~ 1,300,000

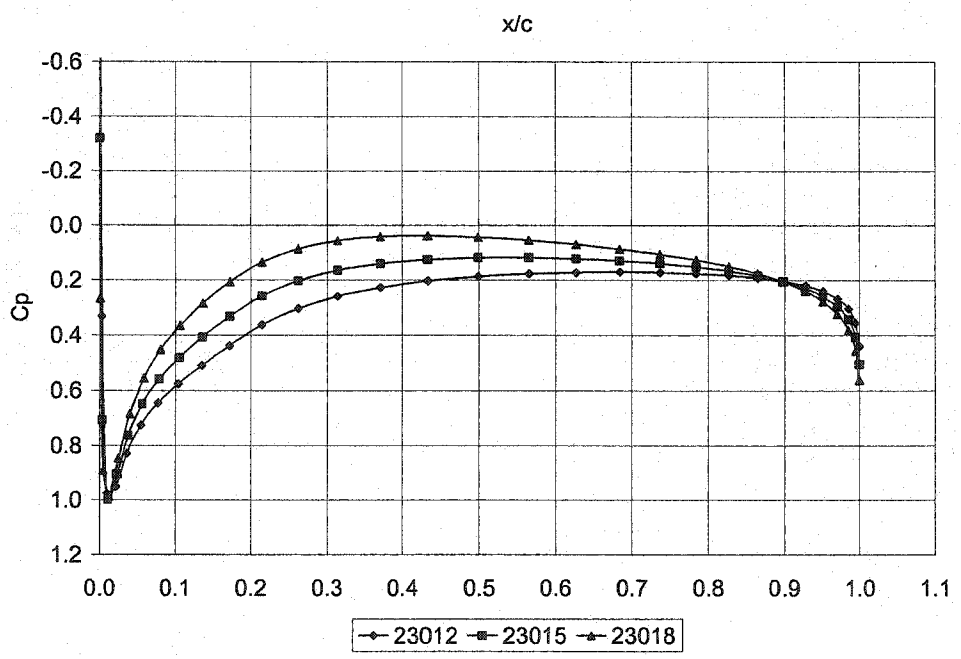

Figure 96 – 23000 Series Pressure Distribution C_{LN} = 0.6, Lower Surface, Re ~ 1,300,000

CHAPTER 8 – AVERAGE CALIBRATION CURVE

The calibration curve originally required to implement this instrumentation is calculated using the data from a clean airfoil calibration. The idea being that once a set of port locations was found for one airfoil shape they would work for all other airfoil shapes. The ports could therefore be installed and calibrated without the use of simulated ice shapes. A calibration in this manner would produce a system that can accurately predict the stall margin within 10% and 5% a large amount of the time as is shown in Tables 5, 6 and 7. From the current research it has been shown that the port locations will be different for each airfoil shape. Because of this characteristic it is necessary to test ice shapes on every airfoil shape. This will produce multiple Cp_x versus C_{LN} curves for the clean and ice configurations as is shown in Figures 41, 42 and 43. Since it is known that simulated ice shapes will be needed for every airfoil an average calibration of the clean and three representative ice shapes can be taken as the relationship between Cp_x and C_{LN}. This will decrease the overall error. It will however introduce error into the clean calibration. To compare the error involved with an average calibration curve the C_{LN} for the average calibration curve will be compared to the clean and iced configurations. The average calibration curves are shown in Figures 97, 98 and 99.

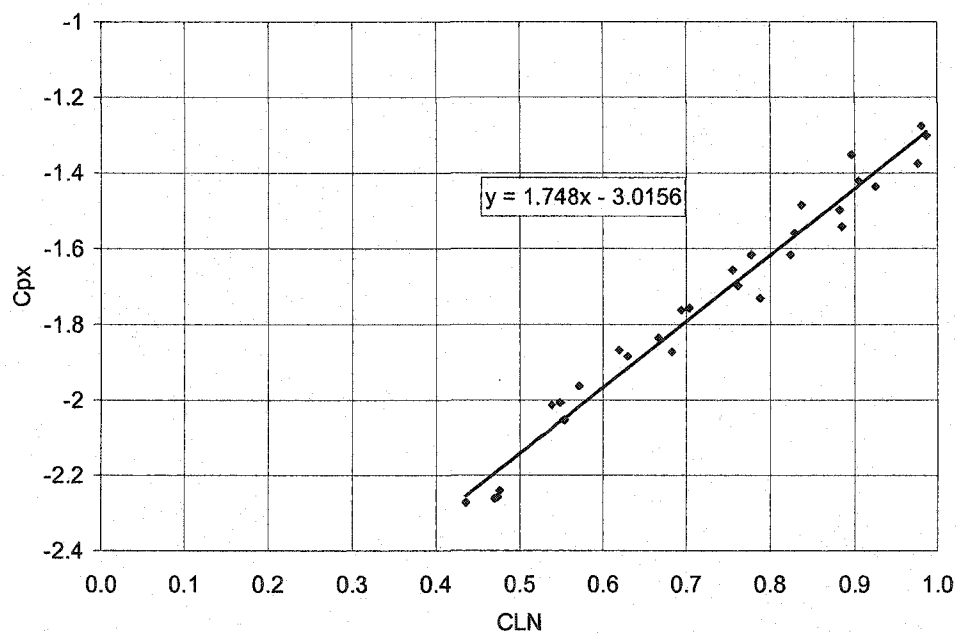

Figure 97 – Average Calibration Curve, Re ~ 700,000

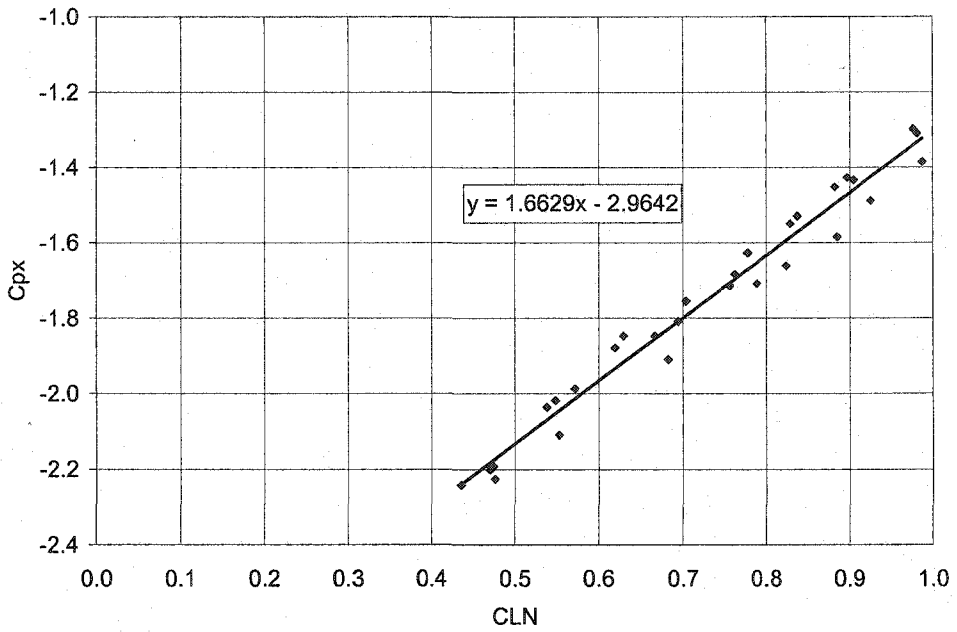

Figure 98 – Average Calibration Curve, Re ~ 1,000,000

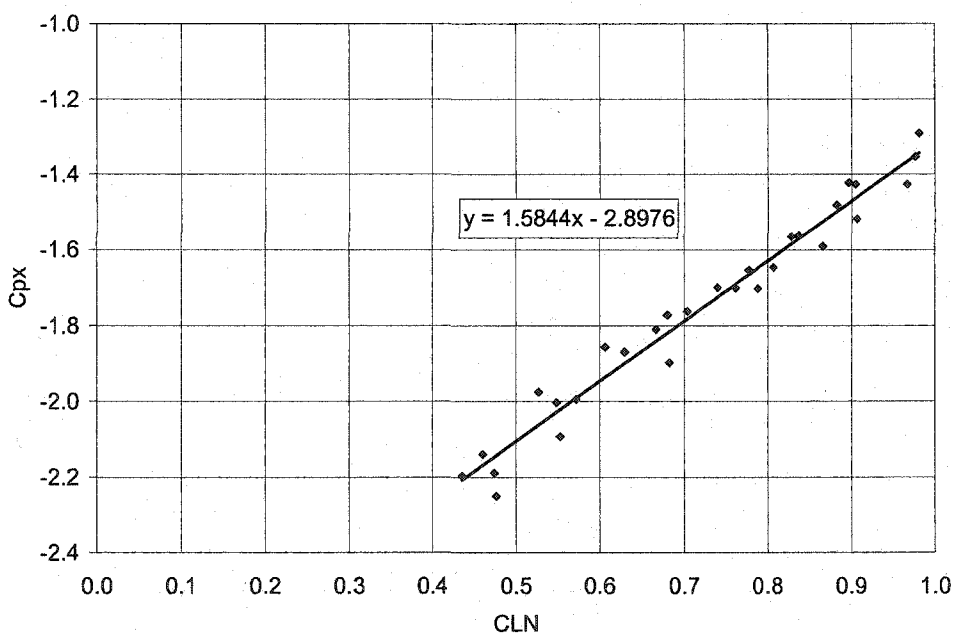

Figure 99 – Average Calibration Curve, Re ~ 1,300,000

Tables 14, 15 and 16 show the comparison of the normalized lift coefficients. A negative value in the % difference column indicates an under prediction and a positive value indicates and over prediction. Using this method the error is greatly reduced. For the Clean and Ice C1, C3 and C4 configurations the C_{LN} can be accurately predicted within 5% and within 3% for a large amount of the time. This is a large improvement over the NACA 0018 calibration curves and the clean calibration curves for the NACA 23012.

CLN Avg Cal	CLN Clean	Clean % Diff from Avg	CLN C1 Actual	C1 % Diff from Avg	CLN C3 Actual	C3 % Diff from Avg	CLN C4 Actual	C4 % Diff from Avg
0.5	0.50	0%	0.50	0%	0.51	-1%	0.51	-1%
0.6	0.56	4%	0.62	-2%	0.56	4%	0.56	4%
0.7	0.67	3%	0.74	-4%	0.68	2%	0.70	0%
0.8	0.80	0%	0.83	-3%	0.77	3%	0.80	0%
0.9	0.92	-2%	0.92	-2%	0.85	5%	0.90	0%

Table 14 – Average Calibration C_{LN} Comparison, Re ~ 700,000

CLN Avg Cal	CLN Clean	Clean % Diff from Avg	CLN C1 Actual	C1 % Diff from Avg	CLN C3 Actual	C3 % Diff from Avg	CLN C4 Actual	C4 % Diff from Avg
0.5	0.50	0%	0.55	-5%	0.50	0%	0.52	-2%
0.6	0.57	3%	0.65	-5%	0.57	3%	0.58	2%
0.7	0.70	0%	0.74	-4%	0.67	3%	0.70	0%
0.8	0.85	-5%	0.82	-2%	0.77	3%	0.78	2%
0.9	0.95	-5%	0.87	3%	0.87	3%	0.87	3%

Table 15 – Average Calibration C_{LN} Comparison, Re ~ 1,000,000

CLN Avg Cal	CLN Clean	Clean % Diff from Avg	CLN C1 Actual	C1 % Diff from Avg	CLN C3 Actual	C3 % Diff from Avg	CLN C4 Actual	C4 % Diff from Avg
0.5	0.47	3%	0.55	-5%	0.51	-1%	0.53	-3%
0.6	0.55	5%	0.65	-5%	0.59	1%	0.60	0%
0.7	0.66	4%	0.75	-5%	0.69	1%	0.69	1%
0.8	0.84	-4%	0.83	-3%	0.80	0%	0.80	0%
0.9	0.95	-5%	0.90	0%	0.88	2%	0.88	2%

Table 16 – Average Calibration C_{LN} Comparison, Re ~ 1,300,000

CHAPTER 9 – SUMMARY, CONCLUSIONS AND FUTURE RESEARCH

9.1 SUMMARY AND CONCLUSIONS

This research was conducted to answer the following questions about the Stall Margin Instrumentation under development at Western Michigan University.

1) What are the effects of Reynolds number on the instrumentation?

2) Will the port locations work for other airfoil shapes?

3) Will the system work for other more severe ice shapes?

4) What is the instrumentation sensing on the wing that indicates the change in lift coefficient due to ice? (Why does it work?)

To answer these questions NACA 23012 pressure and force models were built to determine the relationship between the normalized lift coefficient and the pseudo-pressure coefficient. Four simulated ice shapes were developed using LEWICE 2.0. Inputs for LEWICE were obtained from parameters established from the Federal Aviation Regulations and the flight characteristics of a Beech Baron. Pressure and Force data was analyzed from angle of attacks ranging between 0 degrees and stall. All possible port locations were analyzed using a Visual Basic program and one set of four port locations was found that could accurately predict the normalized lift coefficient with ice shapes on the leading edge of the wing. The set of port locations for the NACA 23012 is:

CP1 – Upper Surface x/c = 0.46
CP2 – Lower Surface x/c = 0.89
CP3 – Lower Surface x/c = 0.14
CP4 – Lower Surface x/c = 0.64

Using an average calibration for the clean and ice configurations the normalized lift coefficient can be accurately predicted within 5%. For ice configuration C2 a set of port locations could not be found. The separation bubble produced by the severely horned ice shape altered the pressure distribution such that it interfered with the port locations that worked well for the clean, C1, C3 and C4 configurations. Further analysis of the flowfield using smoke wire visualization and hotwire anemometry was conducted to obtain a picture of the flowfield. Through the smoke wire images and the contour plots of turbulence intensity from the hotwire, it was observed that ice C2 was the only ice configuration with a significant separation bubble. The individual port pressure coefficients were then examined to determine the

effects of the ice on the pressure distribution. It was determined that the movement of the separation bubble behind Ice C2 corresponded with the deviation of ports CP1 and CP3 from the desired Cp distribution. When in the region of the separation bubble both ports tended toward a Cp equal to -0.6. Ice C1 produced a separation bubble of smaller proportions than what was produced by Ice C2. It has been shown that the stall margin instrumentation encounters problems with the large separation bubbles behind severely horned ice shapes. In real applications of this instrumentation the severely horned ice shapes build slowly and the change in stall margin can be seen before reaching the 45 minute ice shape. Ice C2 is so severe that the aircraft would not have the capabilities to climb or maintain level flight. At that point the aircraft would be in a controlled crash situation and the stall margin system would be of little assistance.

The stall margin system was then analyzed to determine what the instrumentation was truly sensing. It was determine through observations of clean airfoils with changes in thickness, that the ice shape was producing similar effects that a change in thickness would produce. An increase in thickness for the 5-digit series of airfoils decreased maximum lift coefficient. An addition of ice to the leading edge from a moderately smooth ice shape to severely horned ice shape also decreased the maximum lift coefficient. The pressure distributions had an incremental decrease in magnitude with decrease in C_{Lmax} or an increase in ice severity. The stall margin system is sensing the incremental shift in the pressure distribution produced by the ice shape.

The results were also analyzed to determine the effects of Reynolds number on the instrumentation. Through analysis of the lift curves and pressure distributions it was determined that the airfoil was past its critical Reynolds number. The lift curves and pressure distributions had little to no change with change in Reynolds number for the range tested. This allows one Reynolds number to be used for further development of this instrumentation.

In conclusion, the Stall Margin Instrumentation was validated for another airfoil shape. The system worked for more severely horned ice shapes with the exception of severely horned ice shapes produced using a 45 minute flight time. There was little to no effect from changes in Reynolds number. The system is measuring a shift in pressure distribution similar to the shift seen with a change in thickness.

9.2 FUTURE RESEARCH

There are many aspects of this instrumentation that must be researched further before it can be fully implemented. It is recommended that further research be conducted in the following areas:

1) Determine the relationship between a change in camber, a change in thickness and the port locations for the instrumentation. A test possibly using a NACA 2412 for camber change and a NACA 23012 for thickness change would provide a great deal of insight into the change of port locations for change in camber and thickness.

2) The effects of surface roughness on the pressure distribution must also be determined. Typically ice shapes will range from a smooth shape to a rough ice shape. The effects on the port locations must be determined before this instrumentation can be installed on certified aircraft.

3) The effects of flaps on the iced stall margin instrumentation must also be investigated. A flap deflection is effectively a change in airfoil camber and will certainly effect the port locations.

4) Negative angles of attack must be investigated.

5) The interface between the pilot and the instrumentation must also be developed. The possibility of having a display for the tailplane surface and the wing will need to be examined. The integration of this instrumentation into an autopilot system will need to be developed. This would best be accomplished through the use of simulators.

6) The instrumentation must also be installed on an actual aircraft and fully flight tested. De-icing of the ports will need to be addressed in this flight testing. A flowing system to allow for water separation will need to be developed for this instrumentation to be implemented.

7) The effects of ridge ice on the instrumentation must also be investigated. Ridge ice typically forms from water runback produced by the de-icing equipment and is an important consideration for flight in icing conditions.

There are many years of research left before this instrumentation can be installed on certified aircraft.

REFERENCES

[1]Winkler, J., Bragg, M., "Local Flowfield Large Distributed Roughness in the Initial Ice Accretion Process," AIAA 1996-0868, AIAA 34th Aerospace Sciences Meeting and Exhibit, Reno, NV, January 15-18, 1996.

[2]Papadakis, M., Alanstan, S., Seltman, M., "Experimental Study of Simulated Ice Shapes on a NACA 0011 Airfoil," AIAA 1999-0096, AIAA 37th Aerospace Sciences Meeting and Exhibit, Reno, NV, January 11-14, 1999.

[3]Hoadley, A., Pederson, E., "Prediction of Airfoil Stall in Icing Conditions Using Wing surface Pressures," *Journal of Aircraft* Vol. 39, No. 2, March 2002, pp. 326 – 330.

[4]Gulick, B. G. "Effects of Simulated Ice Formation on the Aerodynamic Characteristics of an Airfoil," NACA WR L-292, May 1938

[5]Papadakis,M., Alanstan, S., Wong, S., "Aerodynamic Characteristics of a Symmetric NACA Section with Simulated Ice Shapes," AIAA 2000-0098, AIAA 38th Aerospace Sciences Meeting and Exhibit, Reno, NV, January 10-13, 2000.

[6]Lee, S., Kim, H., Bragg, M., "Investigation of Factors that Influence Iced-Airfoil Aerodynamics," AIAA 2000-0099, AIAA 38th Aerospace Sciences Meeting and Exhibit, Reno, NV, January 10-13, 2000.

[7]Lee, S., Bragg, M., "Effects of Simulated-Spanwise Ice Shapes on Airfoils: Experimental Investigation," AIAA 1999-0092, AIAA 37th Aerospace Sciences Meeting and Exhibit, Reno, NV, January 11-14, 1999.

[8]Jackson, D., Bragg, M., "Aerodynamic Performance of an NLF Airfoil with Simulated Ice," AIAA 1999-0373, AIAA 37th Aerospace Sciences Meeting and Exhibit, Reno, NV, January 11-14, 1999.

[9]Kim, H., Bragg, M., "Effects of Leading-Edge Ice Accretion Geometry on Airfoil Performance," AIAA 1999-3150, AIAA 37th Aerospace Sciences Meeting and Exhibit, Reno, NV, January 11-14, 1999.

[10]Laflin, B., Papadakis, M., "Experimental Investigation of Simulated Ice Accretions on a Natural Laminar Flow Airfoil," AIAA 2001-0088, AIAA 39th Aerospace Sciences Meeting and Exhibit, Reno, NV, January 8-11, 2001.

[11]Khodadoust, A., Bragg, M., "Aerodynamics of a Finite Wing with Simulated Ice," *Journal of Aircraft* Vol. 32, No. 1, Jan-Feb, 1995, pp. 137-144

[12]Gray, V. "Prediction of Aerodynamic Penalties Caused by Ice Formations on Various Airfoils," NASA TN D-2166, 1964

[13] Gray, V., Von Glahn, U. "Effect of Ice and Frost Formations on Drag of NACA 65_1-212 Airfoil for Various Modes of Thermal Ice Protection," NACA TN 2962, 1953

[14] Gray, V., Von Glahn, U. "Aerodynamic Effects Caused by Icing of an Unswept NACA 65A004 Airfoil," NACA TN 4151, 1958

[15]Kwon, O., Sankar, L., "Numerical Study of the Effects of Icing on Finite Wing Aerodynamics," AIAA 90-0757, AIAA 28th Aerospace Sciences Meeting and Exhibit, Jan 8-11, 1990, Reno, NV

[16]Cebeci, T., Roknaldin, F., Carr, L.W., "Prediction of Stall and Post-Stall Behavior of Airfoils at Low and High Reynolds Numbers," AIAA 93-3502, January 1993

[17]Cebeci, T., "Effect of Ice on Airfoil Stall at High Reynolds Numbers," *AIAA Journal* Vol. 33, No. 7, 1995, pp. 1351-1352

[18]Dompierre, J., Cronin, D., Bourgault, Y., Baruzzi, G., Habashi, W., Wagner, G., "Numerical Simulation of Performance Degradation of Ice Contaminated Airfoils," AIAA 97-2235

[19]Chung, J., Reehorst, A., Choo, Y., Potapczuk, M., "Effect of Airfoil Ice Shape Smoothing on the Aerodynamic Performance," AIAA 98-3242

[20]Lee, S., Dunn, T., Gurbacki, H., Bragg, M., Loth, E., "An Experimental and Computational Investigation of Spanwise-Step-Ice Shapes on Airfoil Aerodynamics," AIAA 98-0490, AIAA 36th Aerospace Sciences Meeting and Exhibit, Reno, NV, January 12-15, 1998.

[21]Kumar, S., Loth, E., "Aerodynamic Simulations of Airfoils with Upper-Surface Ice-Shapes," *Journal of Aircraft* Vol. 38, No. 2, March-April 2001, pp. 285-295

[22]Chung, J., Choo, Y., Reehorst, A., Potapczuk, M., Slater, J., "Navier-Stokes Analysis of the Flowfield Characteristics of an Ice Contaminated Aircraft Wing," AIAA 99-0375, AIAA 37th Aerospace Sciences Meeting and Exhibit, Reno, NV, January 11-14, 1999.

[23]Papadakis, M., Laflin, B., Youssef, G., Ratvasky, T., "Aerodynamic Scaling Experiments with Simulated Ice Accretions," AIAA 2001-0833, AIAA 39th Aerospace Sciences Meeting and Exhibit, Reno, NV, January 8-11, 2001.

[24]Fitzgerald, E., Mueller, T., "Measurements in a Separation Bubble on an Airfoil Using Laser Velocimetry," *AIAA Journal* Vol. 28, No. 4, April 1990, pp. 584 – 592.

[25]Gurbacki, H., Bragg, M., "Unsteady Aerodynamic Measurements of an Iced Airfoil," AIAA 2002-0241, AIAA 40th Aerospace Sciences Meeting and Exhibit, Reno, NV, January 14-17, 2002.

[26]Bragg, M., Khodadoust, A., "Measurements in a Leading-Edge Separation Bubble due to a Simulated Airfoil Ice Accretion," *AIAA Journal* Vol. 30, No. 6, June 1992, pp. 1462 – 1467.

[27]Yon, S., Katz, J., "Study of the Unsteady Flow Features on a Stalled Wing," *AIAA Journal* Vol. 36, No. 3, March 1998, pp. 305-312

[28]Kerho, M. "Effect of Large Distributed Roughness Near an Airfoil Leading Edge on Boundary-Layer Development and Transition," PhD Dissertation, The University of Illinois Urbana-Champaign, Urbana-Champaign, Illinois, 1992

[29]Bragg, M., Kerho, M., Cummings, M., "Effect of Initial Ice Roughness on Airfoil Aerodynamics," AIAA 94-0800, AIAA 32nd Aerospace Sciences Meeting and Exhibit, Jan 10-13, 1994 , Reno, NV

[30]Bragg, M., Kerho, M., Cummings, M., "Airfoil Boundary Layer due to Large Leading Edge Roughness," AIAA 95-0536, AIAA 33rd Aerospace Sciences Meeting and Exhibit, Jan 9-12, 1995, Reno, NV

[31]Bragg, M., Cummings, M., Lee, S., Henze, C., "Boundary-Layer and Heat-Transfer Measurements on an Airfoil with Simulated Ice Roughness," AIAA 96-0866, AIAA 34th Aerospace Sciences Meeting and Exhibit, Reno, NV, January 15-18, 1996

[32]Kerho, M., Bragg, M., "Airfoil Boundary-Layer Development and Transition with Large Leading-Edge Roughness," *AIAA Journal* Vol. 35, No. 1, January 1997, pp.75-84

[33]Driest, E., Blumer, C., "Boundary Layer Transition: Freestream Turbulence and Pressure Gradient Effects," *AIAA Journal* Vol. 1, No. 6, June 1963, pp. 1303-1306

[34]Gurbacki, H., Bragg, M., "Sensing Aircraft Icing Effects by Unsteady Flap Hinge-Moment Measurement," *Journal of Aircraft* Vol. 38, No. 3, May 2001, pp. 575 – 577.

[35]Hoadley, A., "Conversion of Wing Surface Pressures into Normalized Lift Coefficient," 1979 SAE Transactions.

[36]Hoadley, A., "Normalized Coefficient of Lift Indicator," US Patent No. 4,235,104.

[37]Wright, "User Manual for the NASA Glenn Ice Accretion Code LEWICE," NASA/CR-1999-209409.

[38]Merati, P., Adrian, R.J., "Directional Sensitivity of Single and Multiple Sensor Probes," TSI Quarterly, Vol. X, Issue 2, April-June 1984, pp. 3-12

[39]Rae, W. H., Pope, A., *Low-Speed Wind Tunnel Testing*, John Wiley & Sons, 1984.

[40]Ashenden, R., Lindberg, W., Marwitz, J., "Two-Dimensional NACA 23012 Airfoil Performance Degradation by Super Cooled Cloud, Drizzle, and Rain Drop Icing," AIAA 96-0870.

[41]Ashenden, R., Lindberg, W., Marwitz, J., Hoxie, B., "Airfoil Performance Degradation by Supercooled Cloud Drizzle, and Rain Drop Icing," *Journal of Aircraft* Vol. 33, No. 6, Nov-Dec 1996, pp. 1040-1046

[42]Ashenden, R., Lindberg, W., Marwitz, J., "Two-Dimensional Airfoil Performance Degradation Because of Simulated Freezing Drizzle," Journal of Aircraft, Vol. 35, No.6, November-December 1998.

[43]Abbot, I. H., Von Doenhoff, A., "Theory of Wing Sections" Dover Publications Inc, New York 1959

APPENDIX A – PRESSURE DISTRIBUTIONS

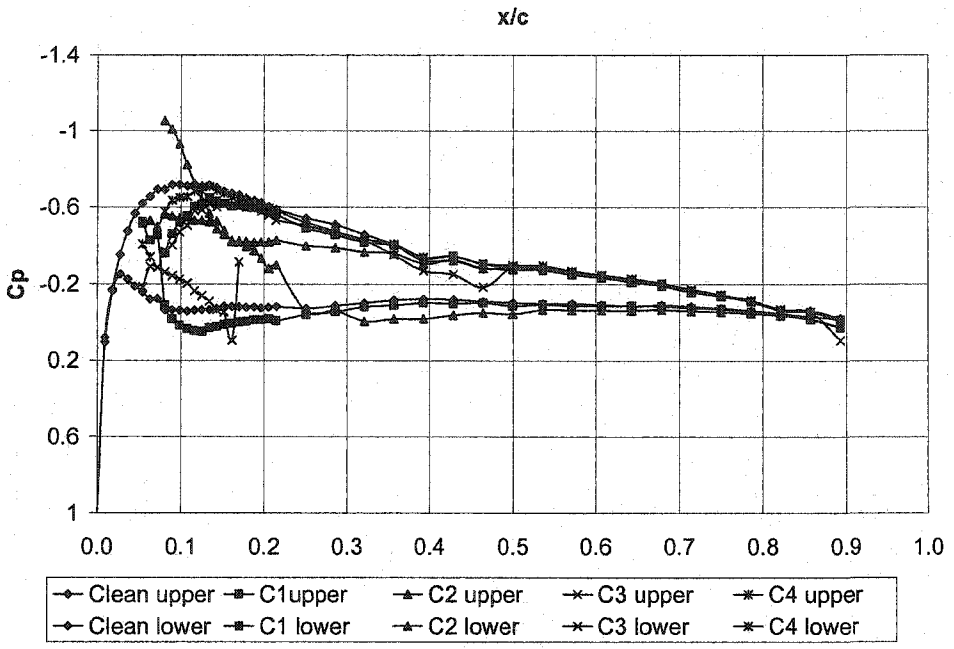

Figure 100 – Cp vs. x/c, Re ~ 700,000, AOA = 1 deg

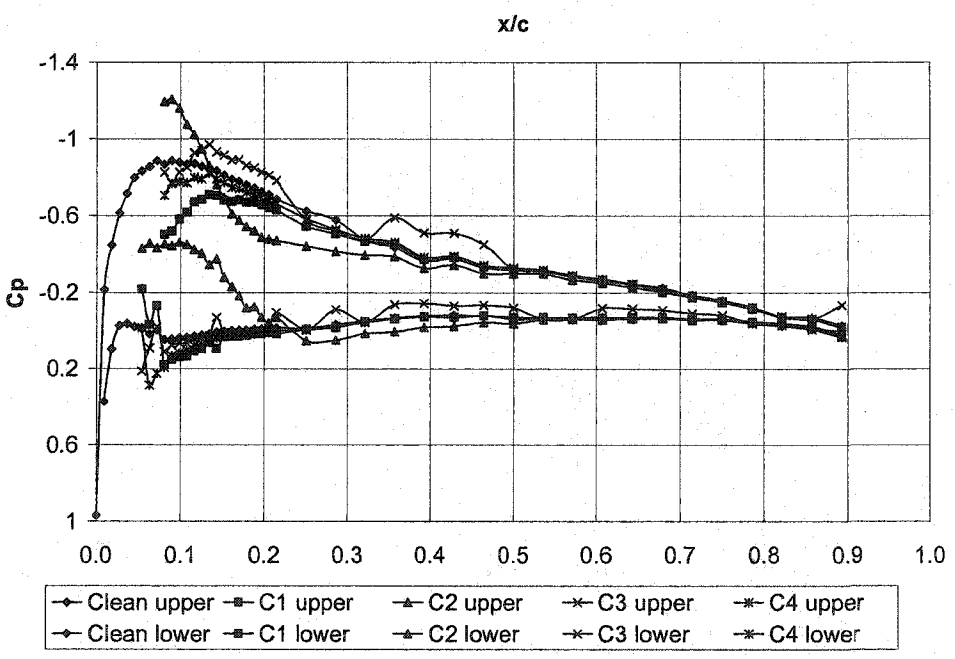

Figure 101 – Cp vs. x/c, Re ~ 700,000, AOA = 2 deg

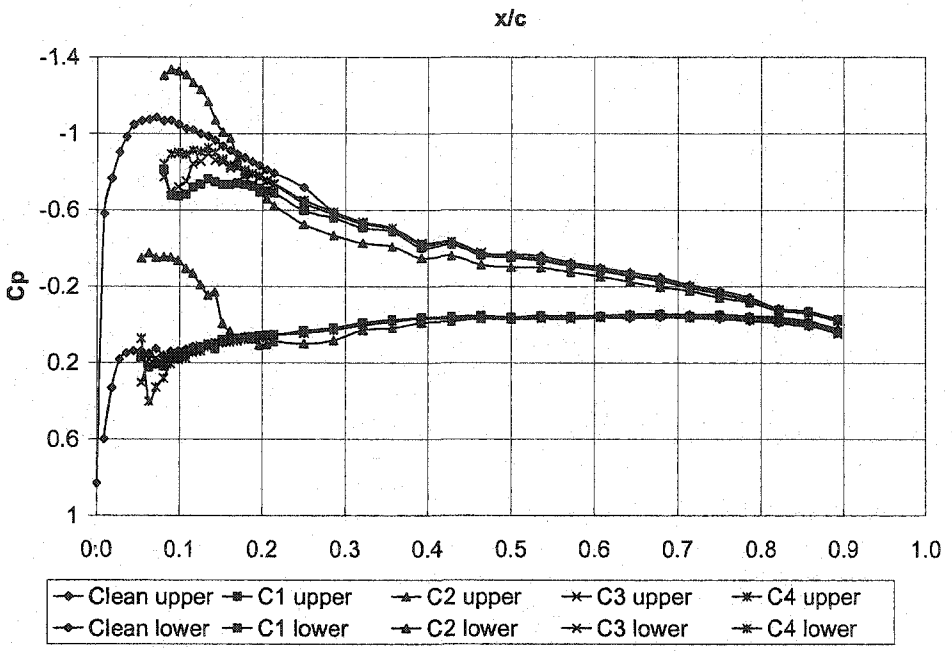

Figure 102 – Cp vs. x/c, Re ~ 700,000, AOA = 3 deg

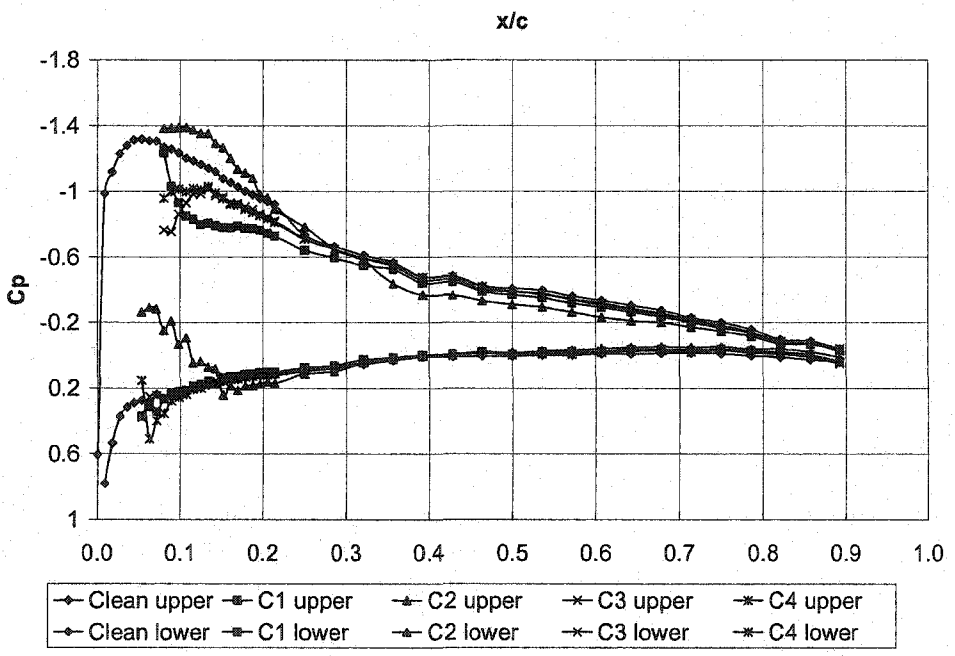

Figure 103 – Cp vs. x/c, Re ~ 700,000, AOA = 4 deg

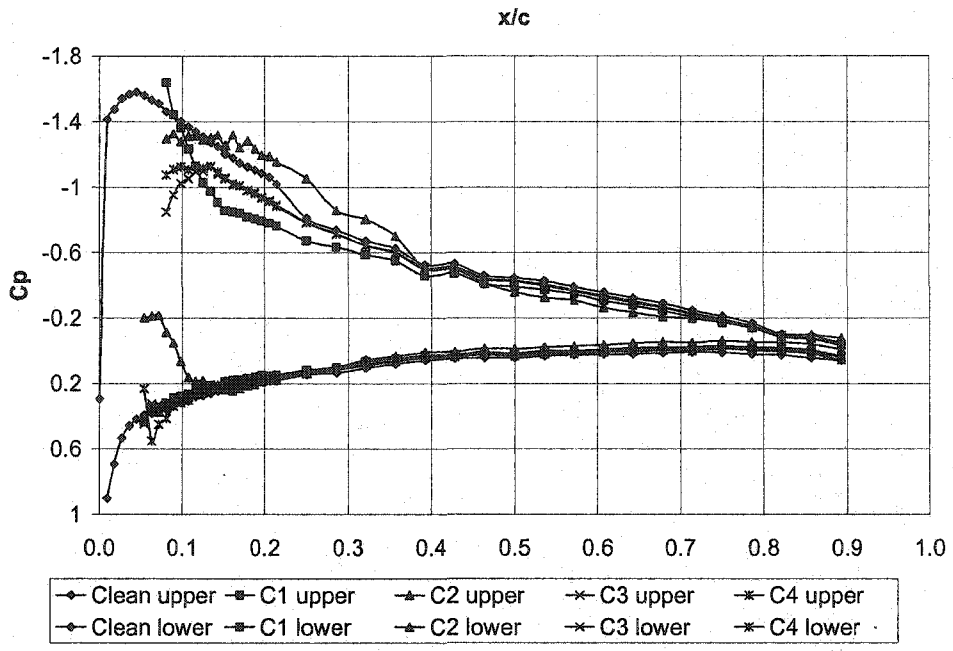

Figure 104 – Cp vs. x/c, Re ~ 700,000, AOA = 5 deg

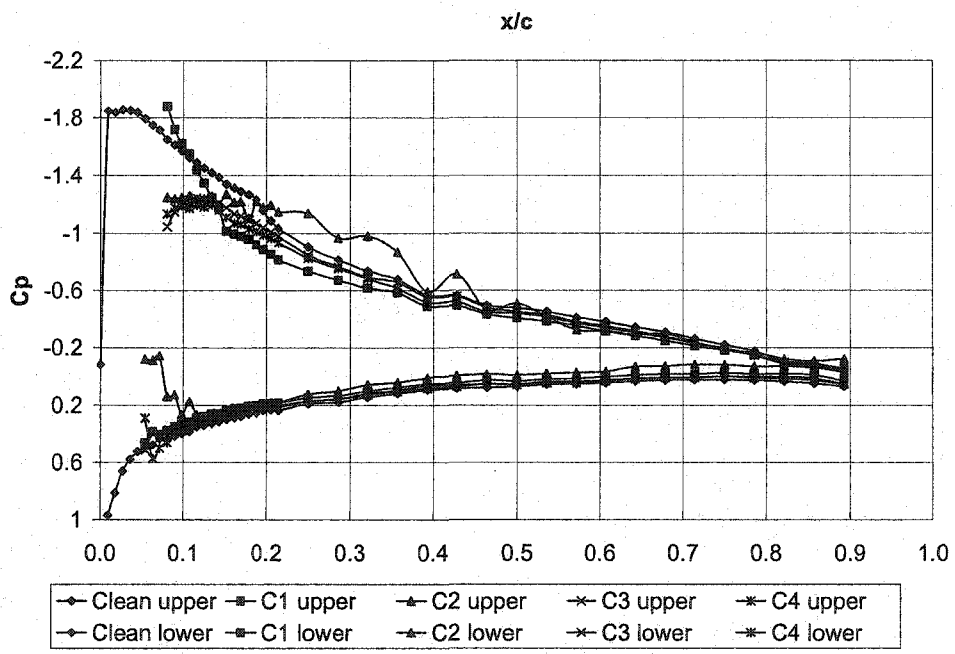

Figure 105 – Cp vs. x/c, Re ~ 700,000, AOA = 6 deg

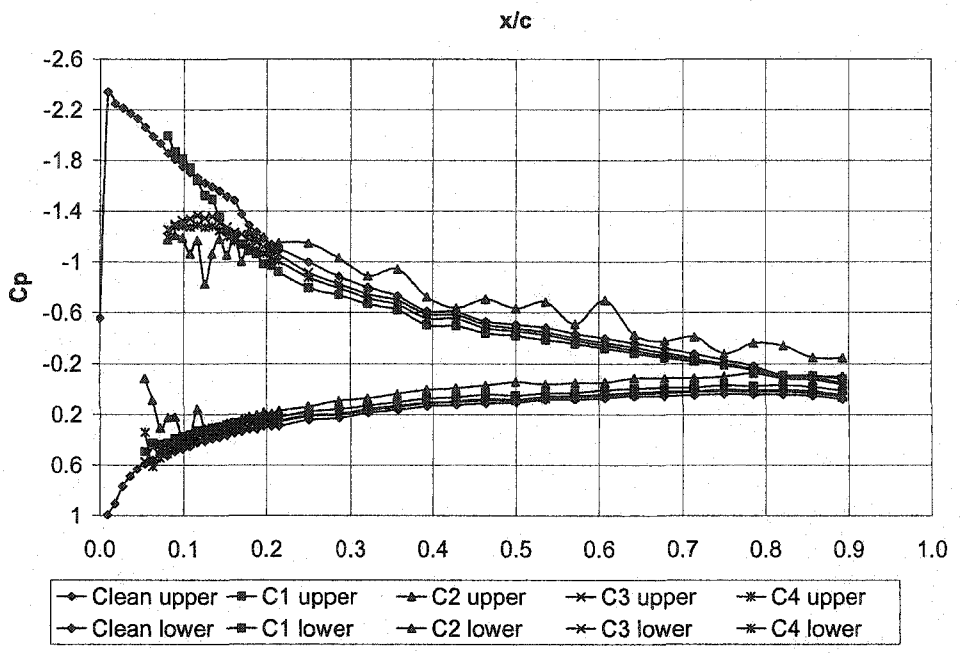

Figure 106 – Cp vs. x/c, Re ~ 700,000, AOA = 7 deg

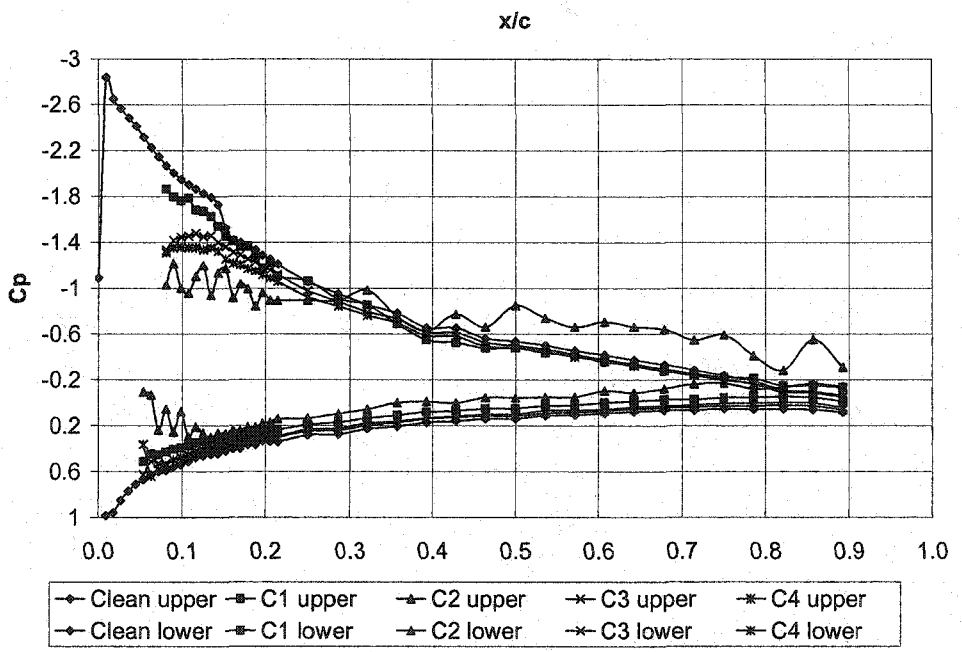

Figure 107 – Cp vs. x/c, Re ~ 700,000, AOA = 8 deg

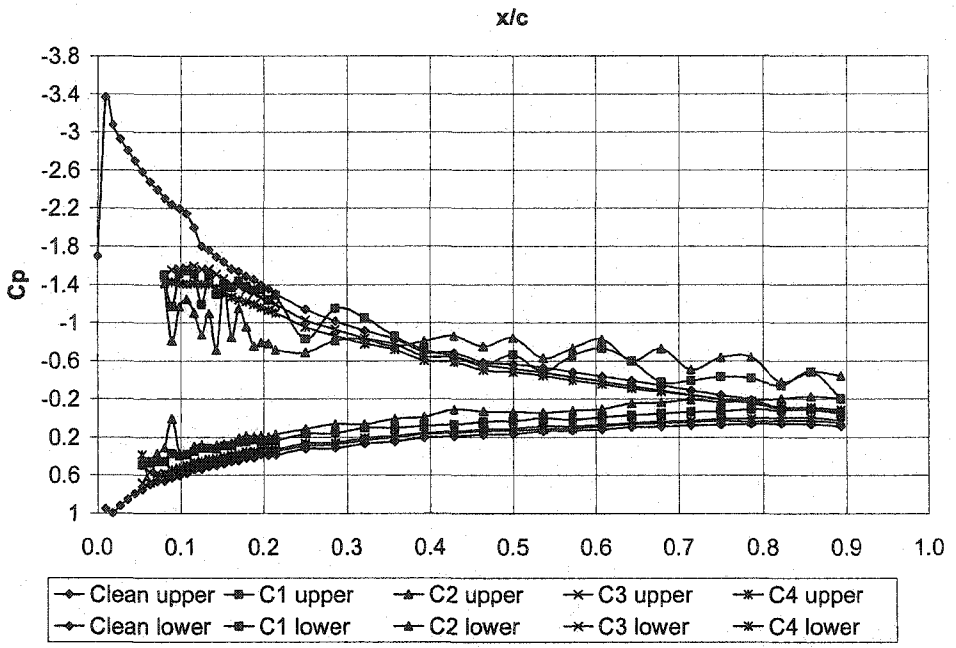

Figure 108 – Cp vs. x/c, Re ~ 700,000, AOA = 9 deg

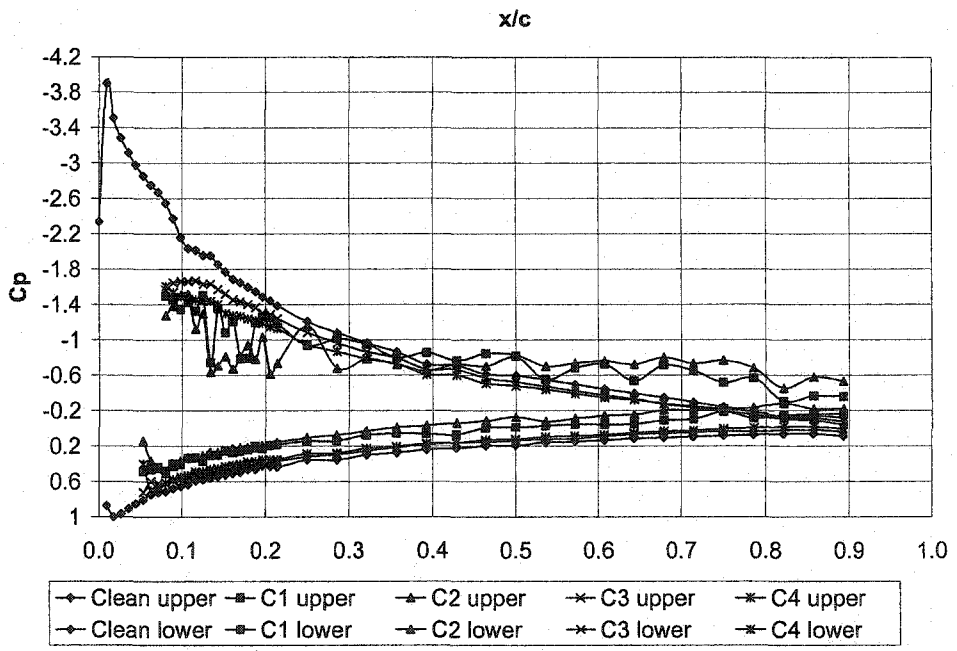

Figure 109 – Cp vs. x/c, Re ~ 700,000, AOA = 10 deg

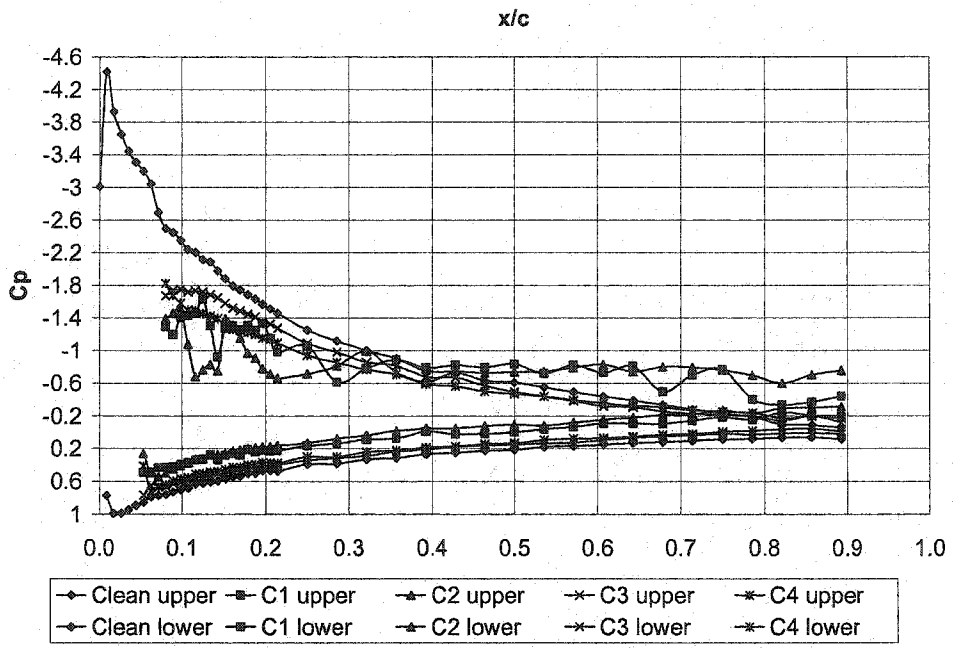

Figure 110 – Cp vs. x/c, Re ~ 700,000, AOA = 11 deg

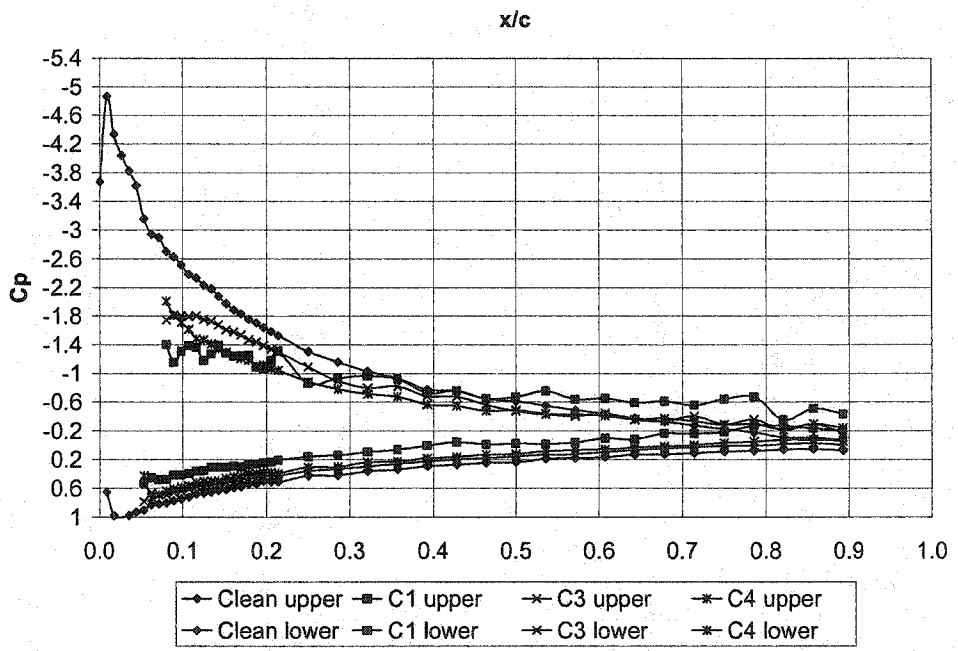

Figure 111 – Cp vs. x/c, Re ~ 700,000, AOA = 12 deg

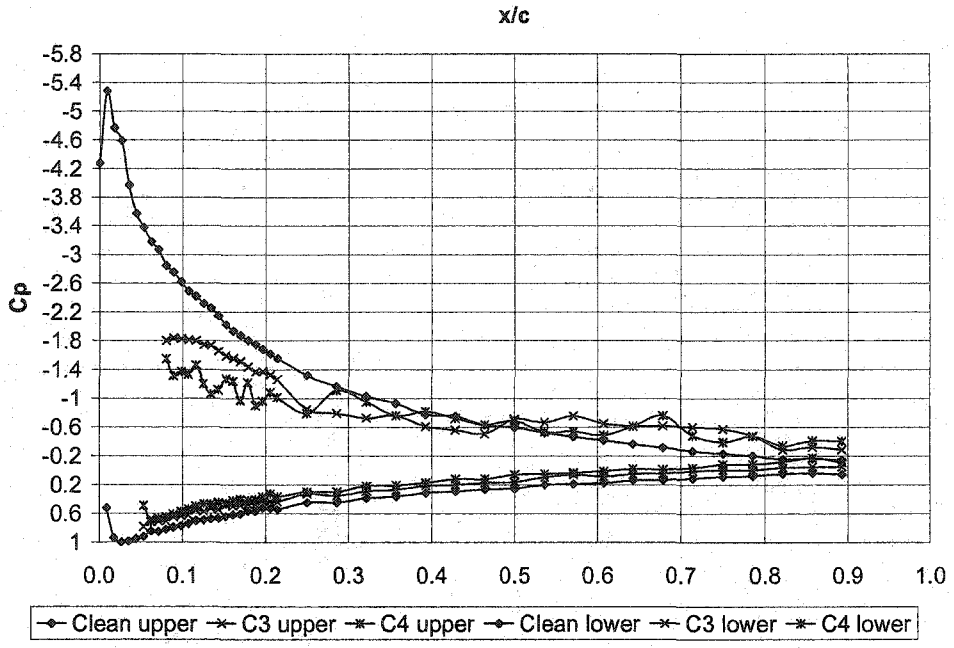

Figure 112 – Cp vs. x/c, Re ~ 700,000, AOA = 13 deg

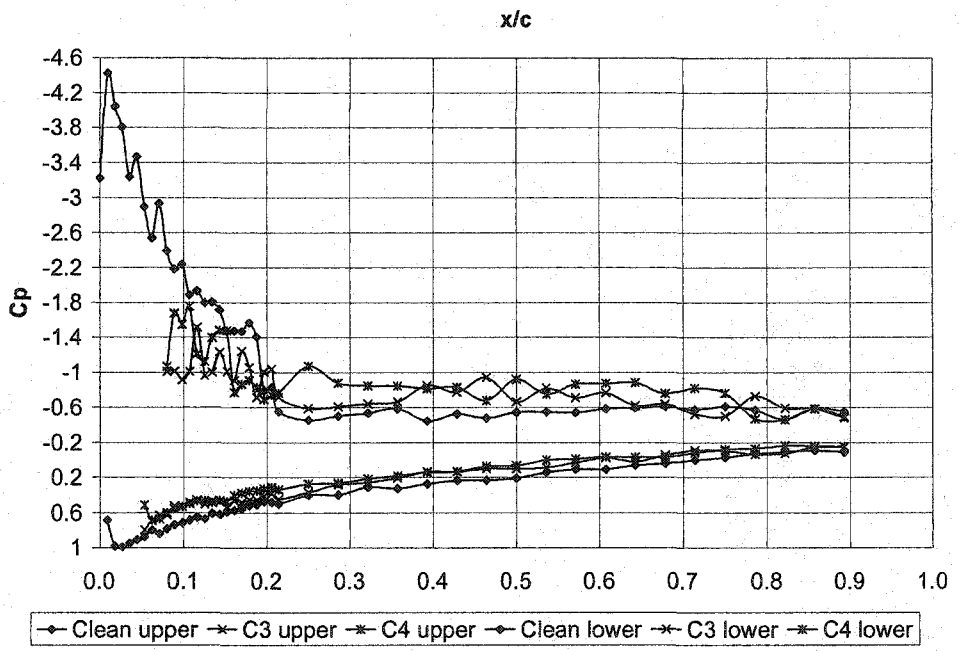

Figure 113 – Cp vs. x/c, Re ~ 700,000, AOA = 14 deg

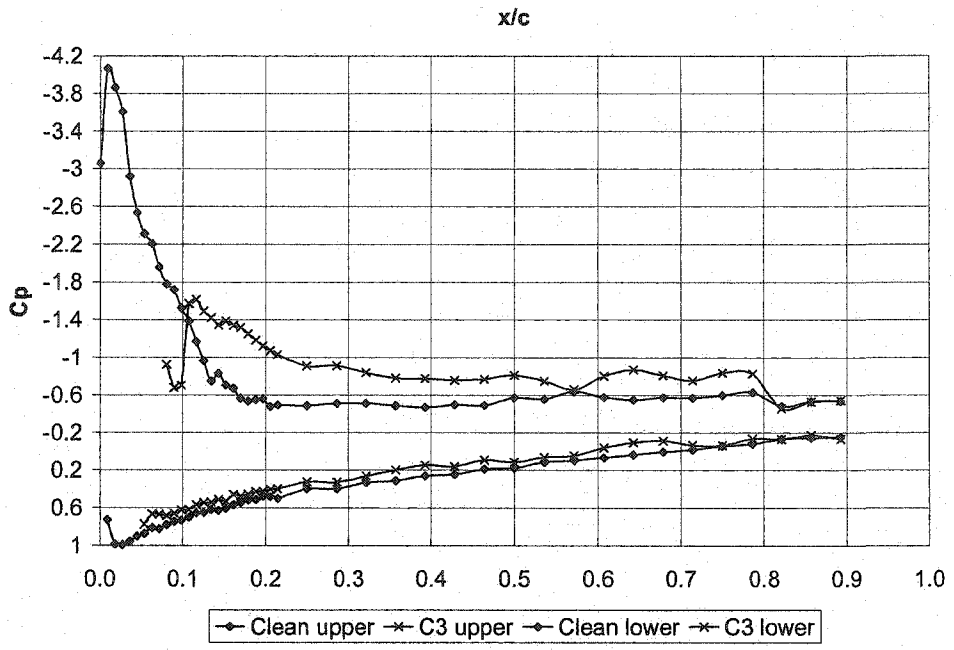

Figure 114 – Cp vs. x/c, Re ~ 700,000, AOA = 15 deg

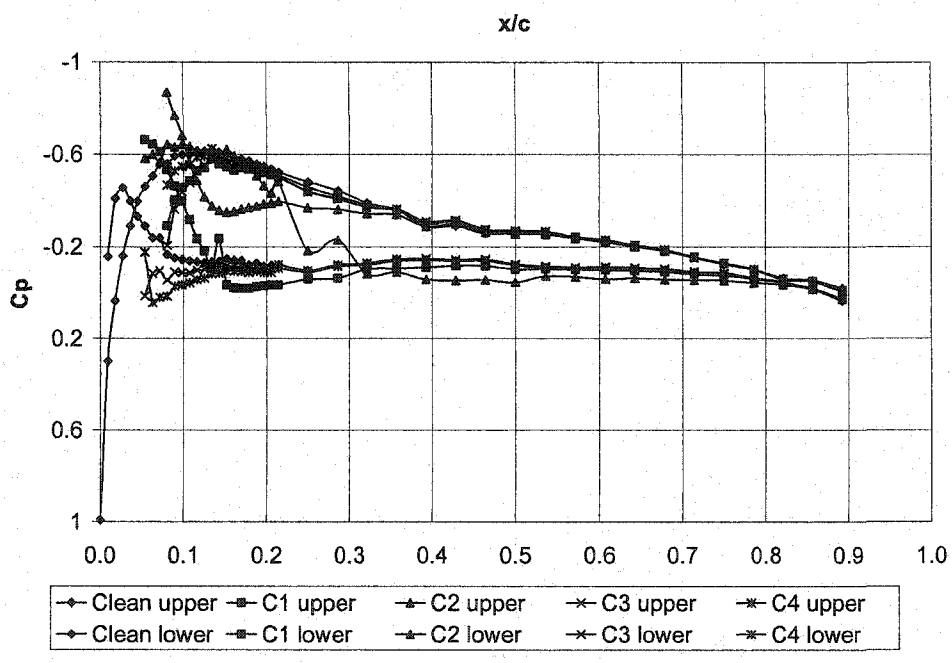

Figure 115 – Cp vs. x/c, Re ~ 1,000,000, AOA = 0 deg

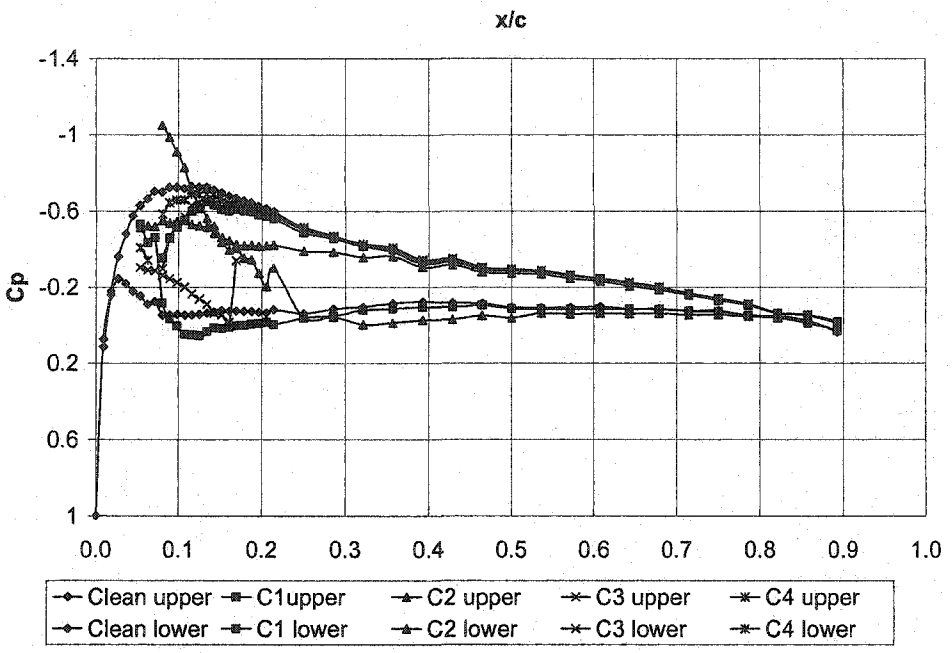

Figure 116 – Cp vs. x/c, Re ~ 1,000,000, AOA = 1 deg

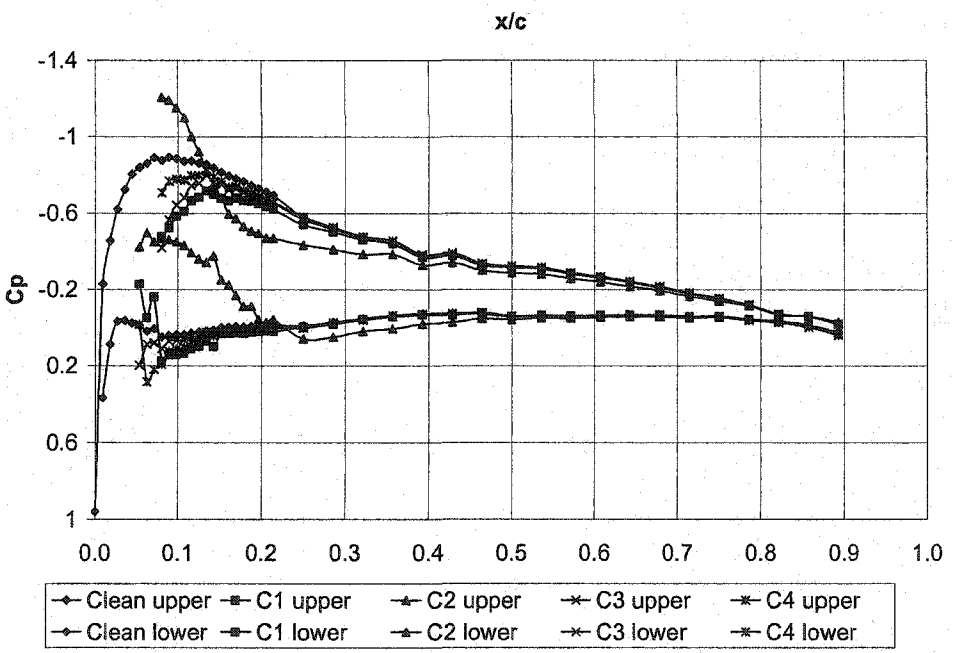

Figure 117 – Cp vs. x/c, Re ~ 1,000,000, AOA = 2 deg

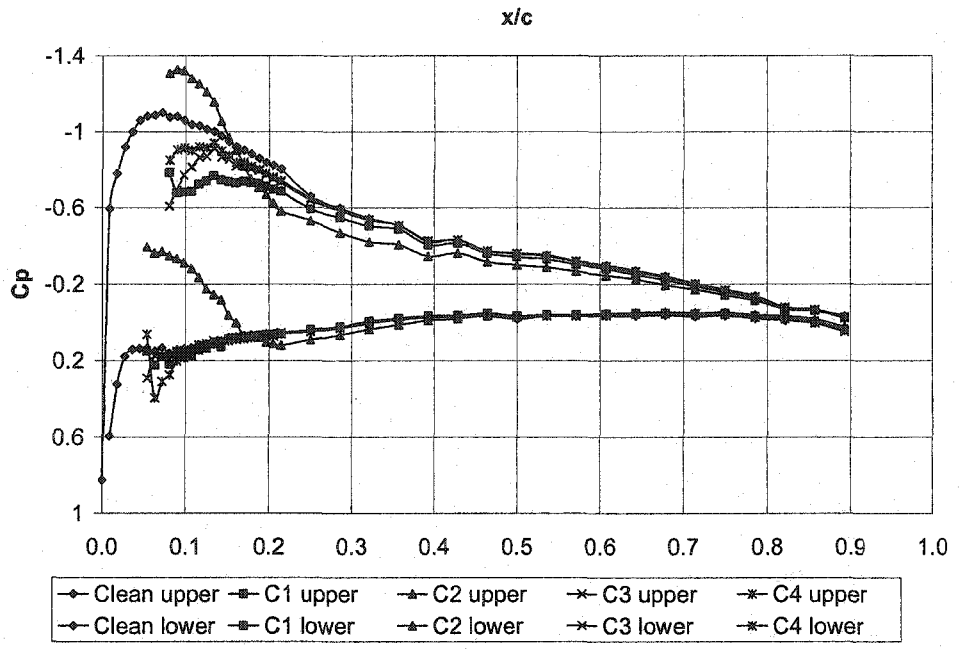

Figure 118 – Cp vs. x/c, Re ~ 1,000,000, AOA = 3 deg

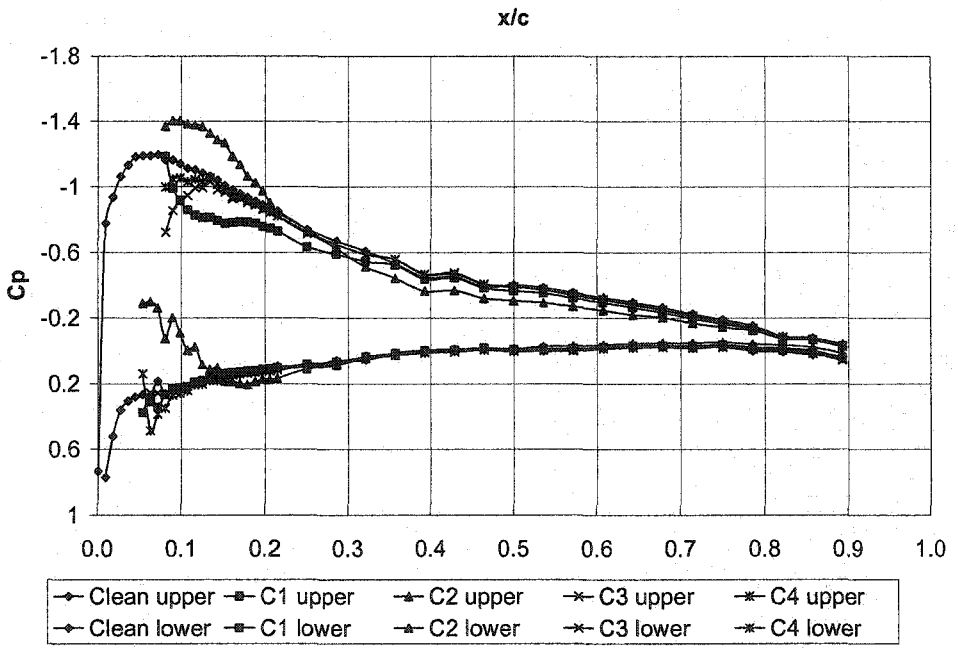

Figure 119 – Cp vs. x/c, Re ~ 1,000,000, AOA = 4 deg

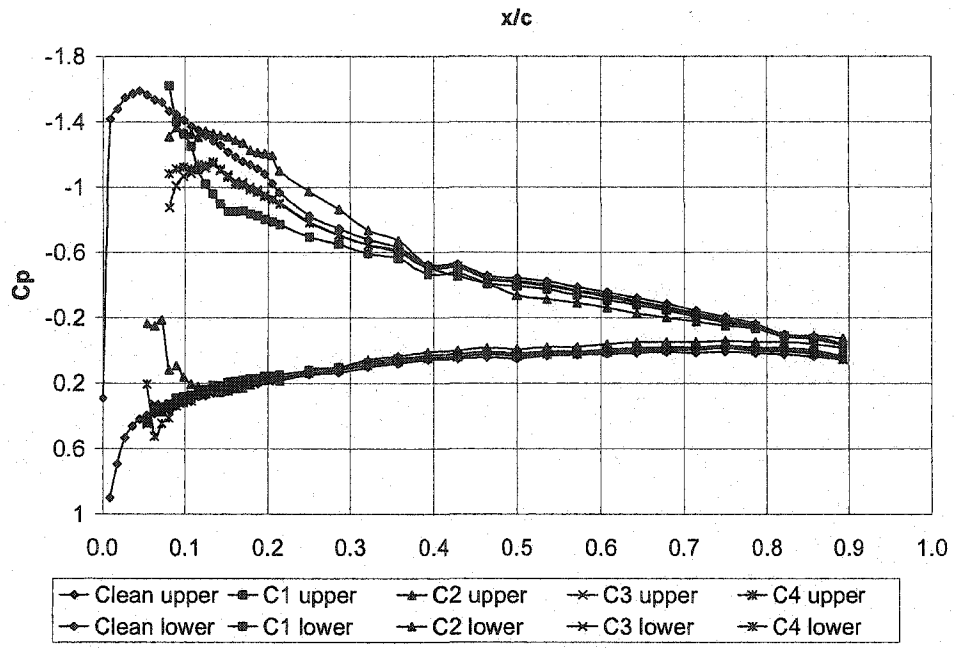

Figure 120 – Cp vs. x/c, Re ~ 1,000,000, AOA = 5 deg

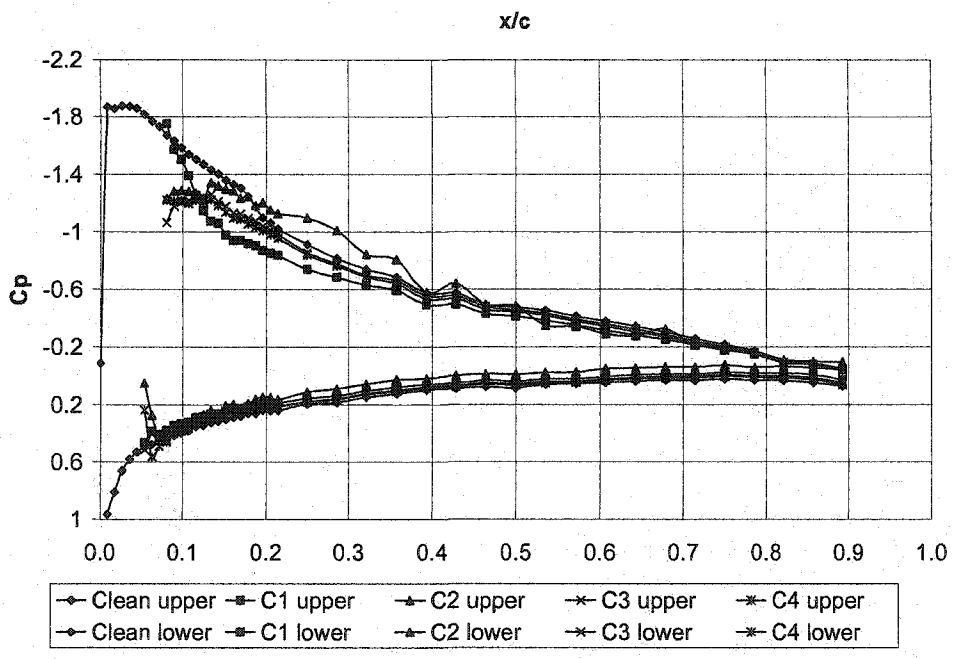

Figure 121 – Cp vs. x/c, Re ~ 1,000,000, AOA = 6 deg

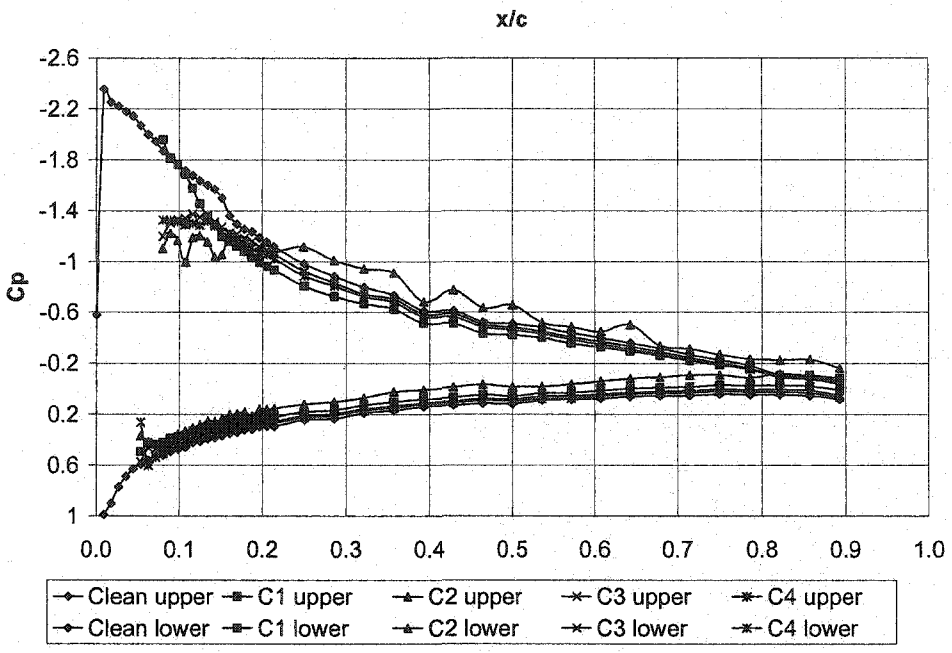

Figure 122 – Cp vs. x/c, Re ~ 1,000,000, AOA = 7 deg

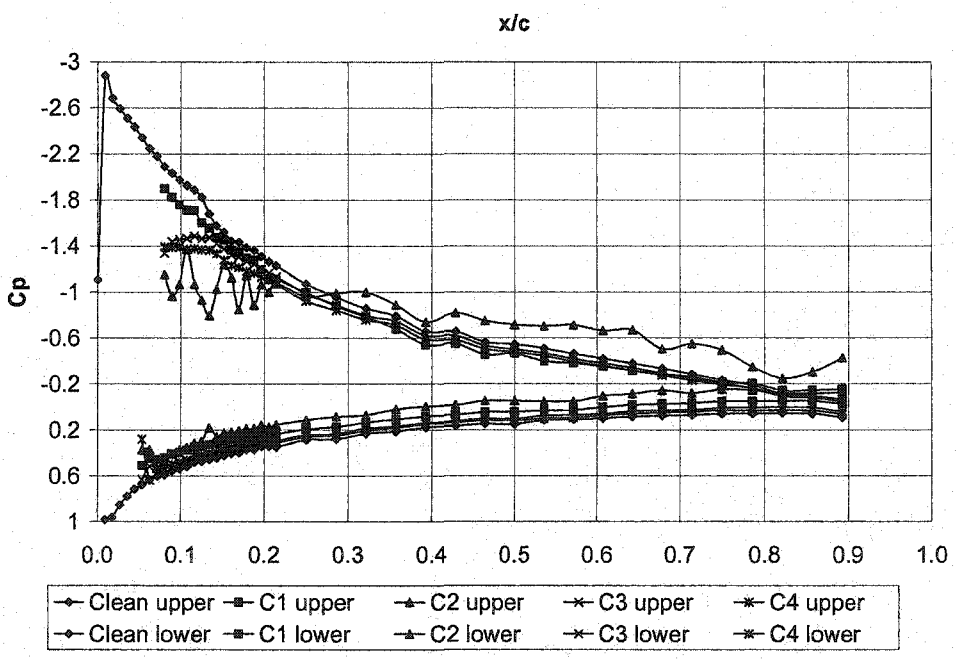

Figure 123 – Cp vs. x/c, Re ~ 1,000,000, AOA = 8 deg

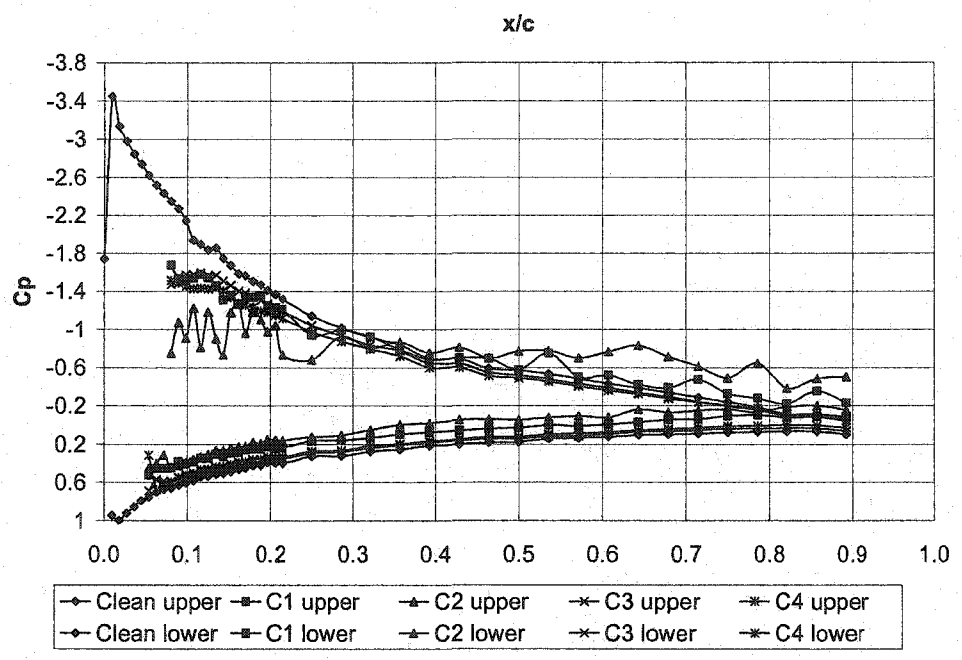

Figure 124 – Cp vs. x/c, Re ~ 1,000,000, AOA = 9 deg

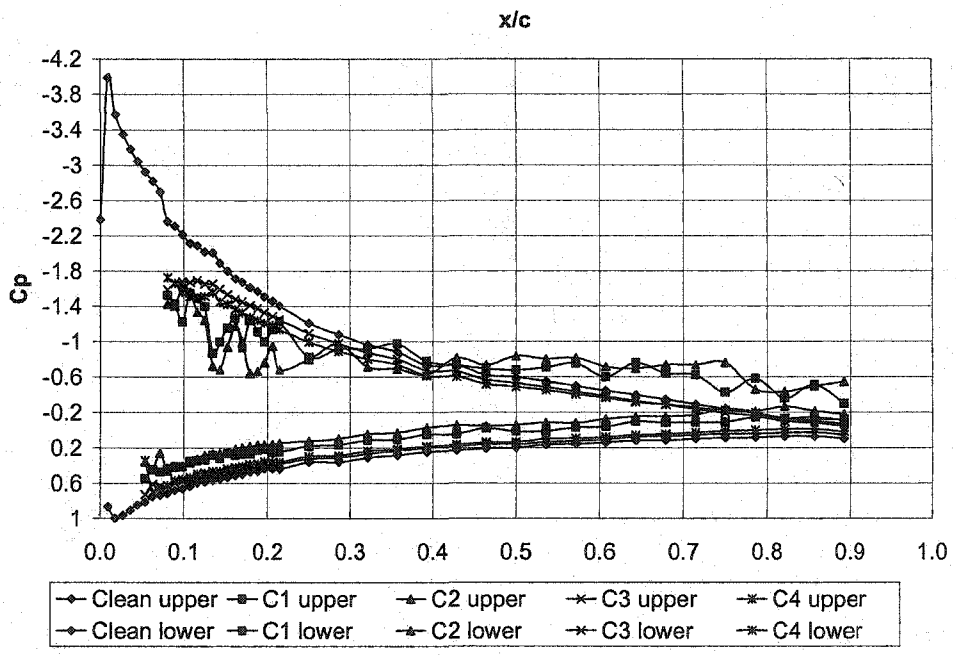

Figure 125 – Cp vs. x/c, Re ~ 1,000,000, AOA = 10 deg

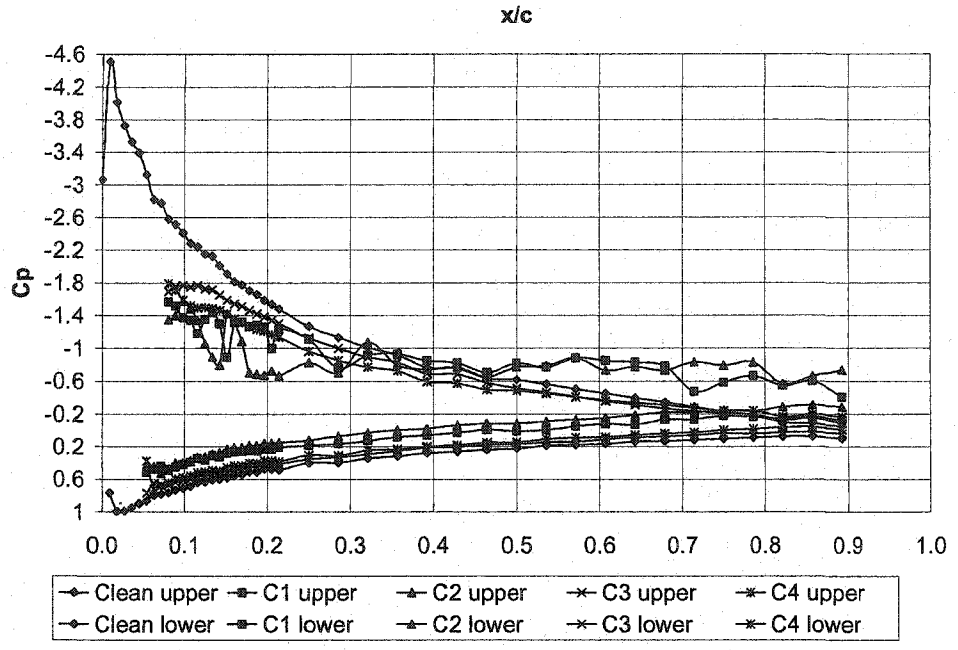

Figure 126 – Cp vs. x/c, Re ~ 1,000,000, AOA = 11 deg

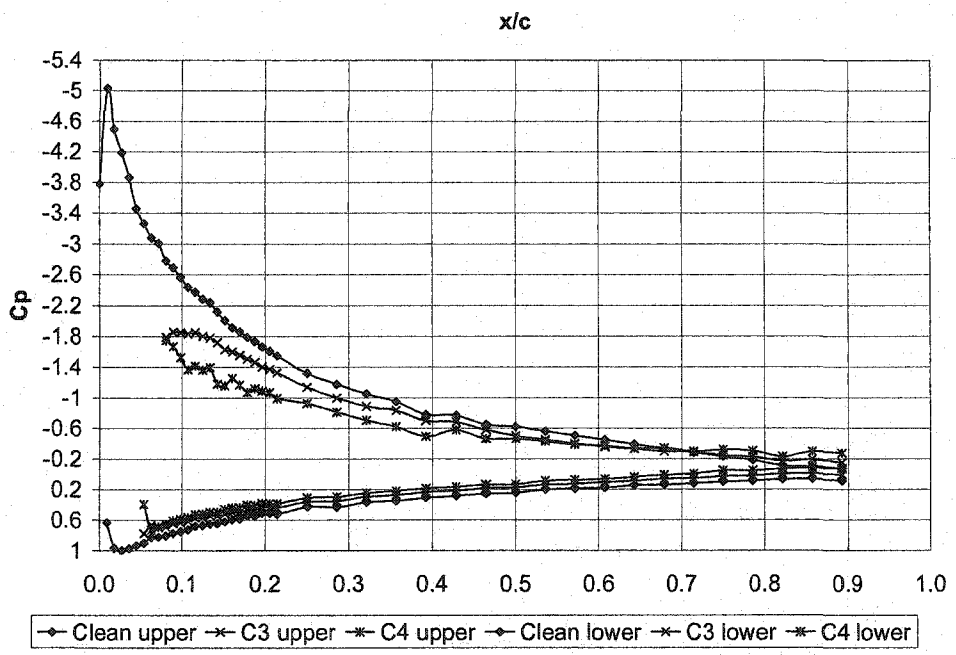

Figure 127 – Cp vs. x/c, Re ~ 1,000,000, AOA = 12 deg

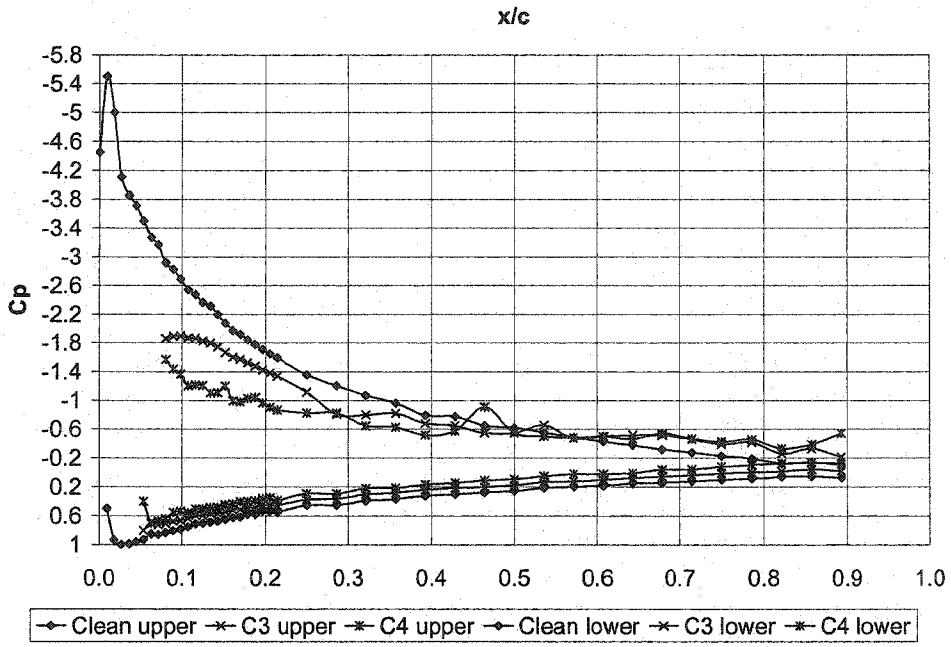

Figure 128 – Cp vs. x/c, Re ~ 1,000,000, AOA = 13 deg

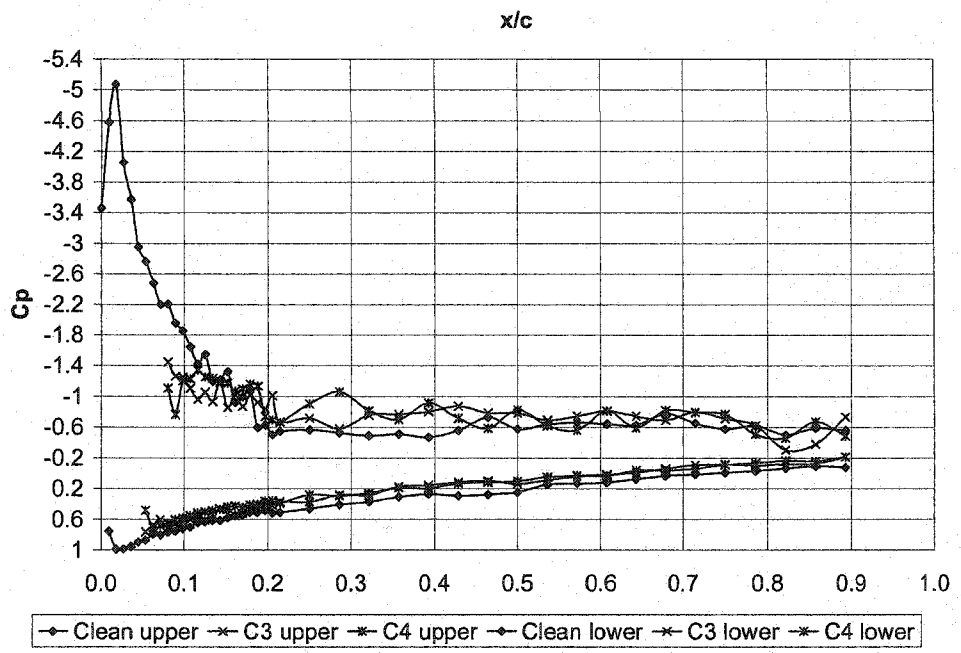

Figure 129 – Cp vs. x/c, Re ~ 1,000,000, AOA = 14 deg

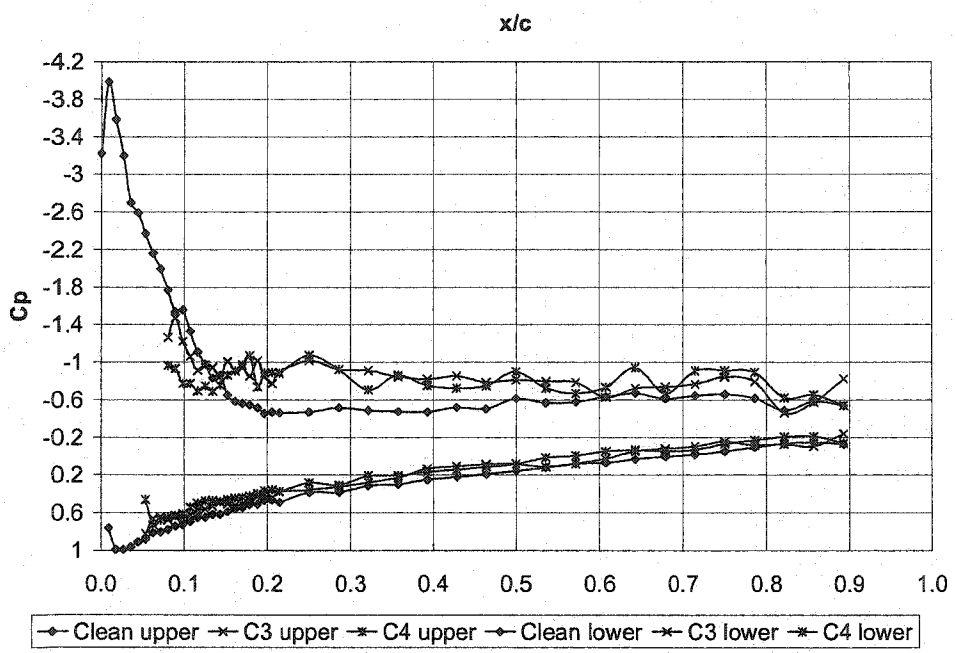

Figure 130 – Cp vs. x/c, Re ~ 1,000,000, AOA = 15 deg

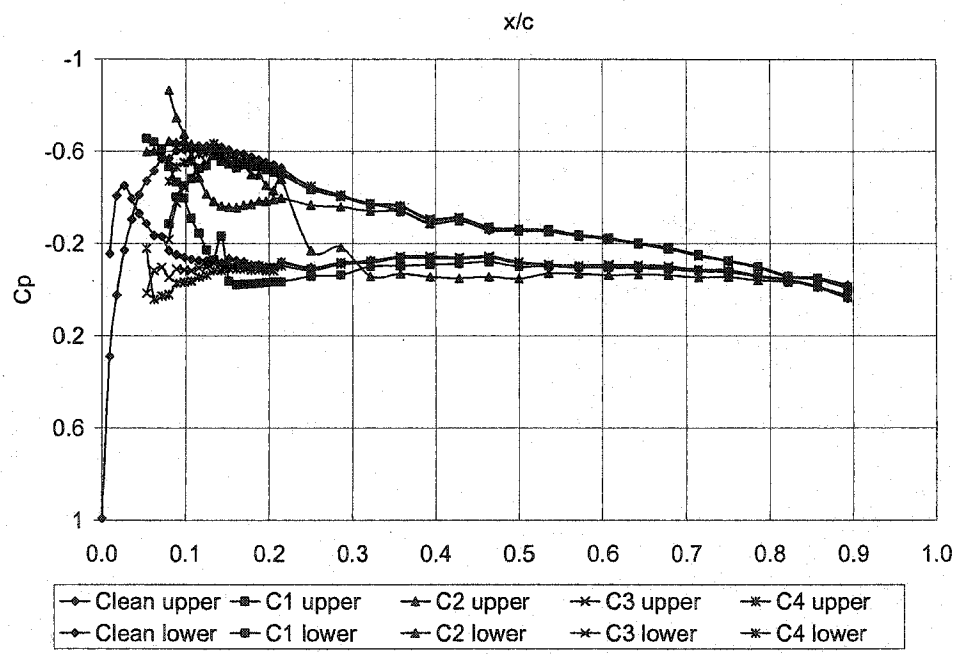

Figure 131 – Cp vs. x/c, Re ~ 1,300,000, AOA = 0 deg

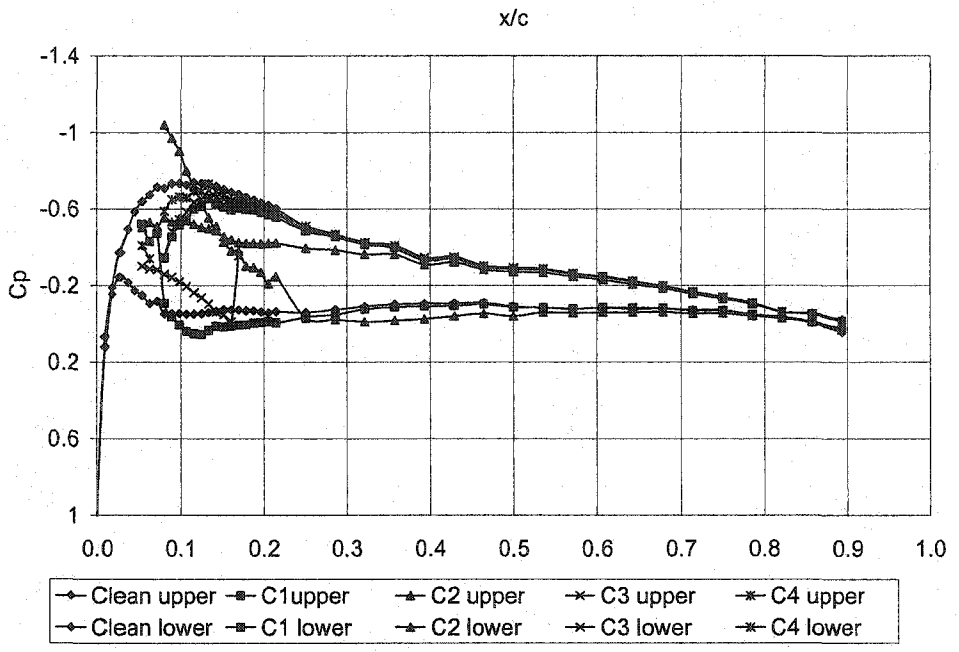

Figure 132 – Cp vs. x/c, Re ~ 1,300,000, AOA = 1 deg

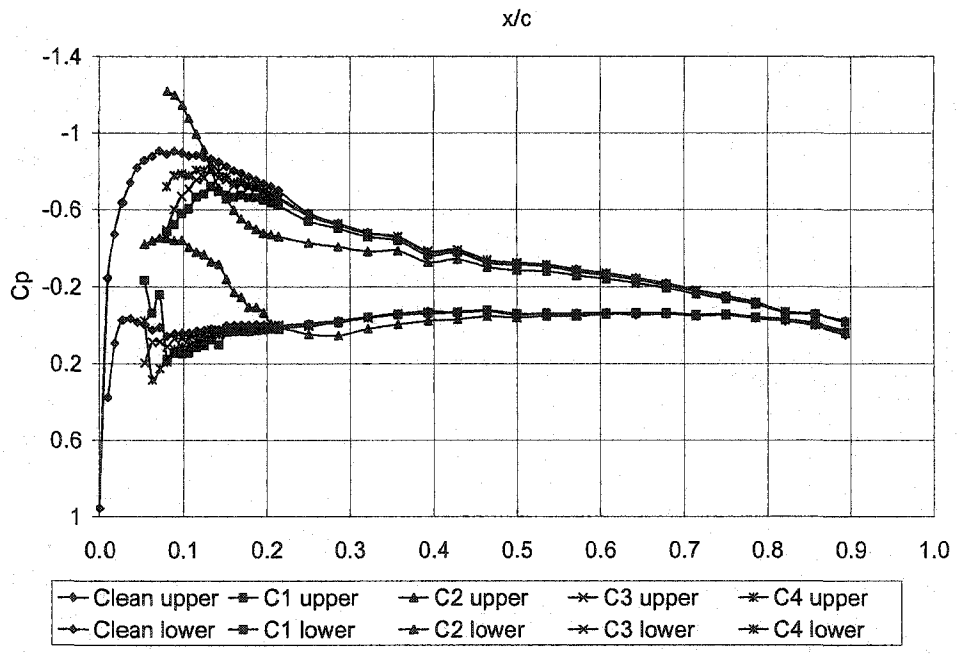

Figure 133 – Cp vs. x/c, Re ~ 1,300,000, AOA = 2 deg

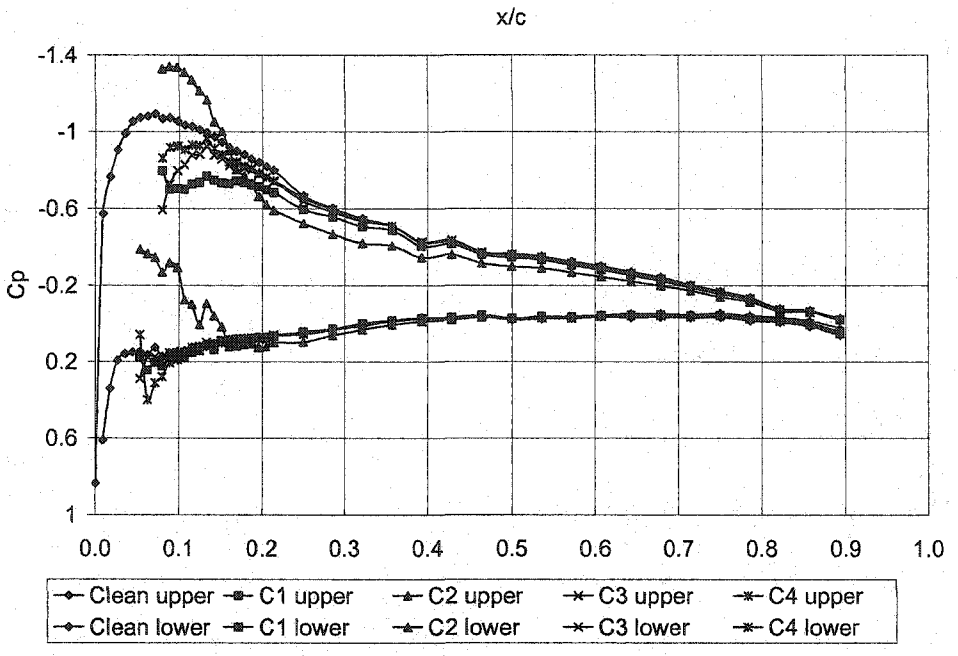

Figure 134 – Cp vs. x/c, Re ~ 1,300,000, AOA = 3 deg

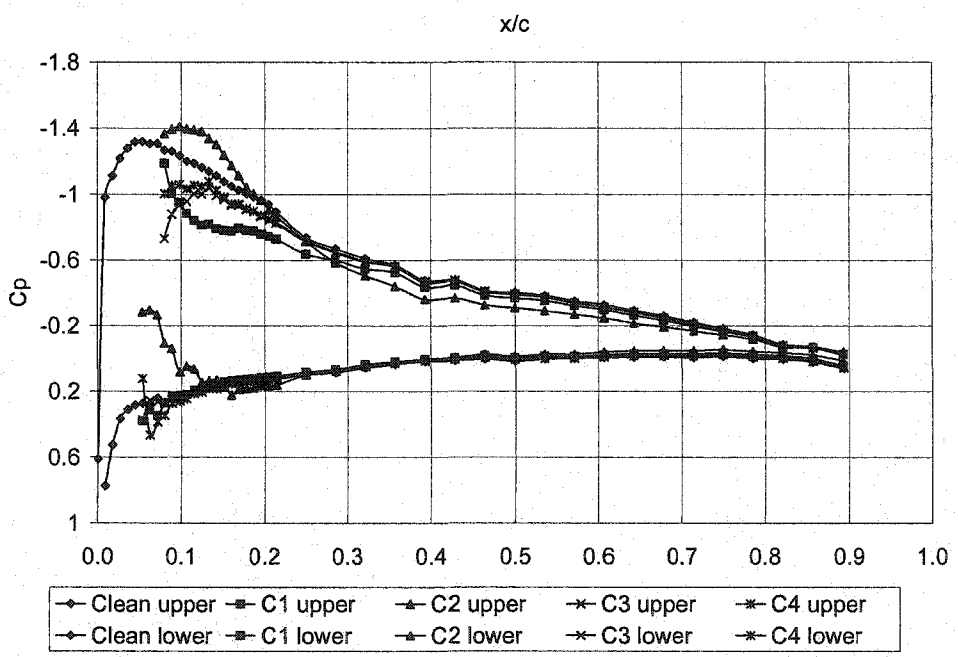

Figure 135 – Cp vs. x/c, Re ~ 1,300,000, AOA = 4 deg

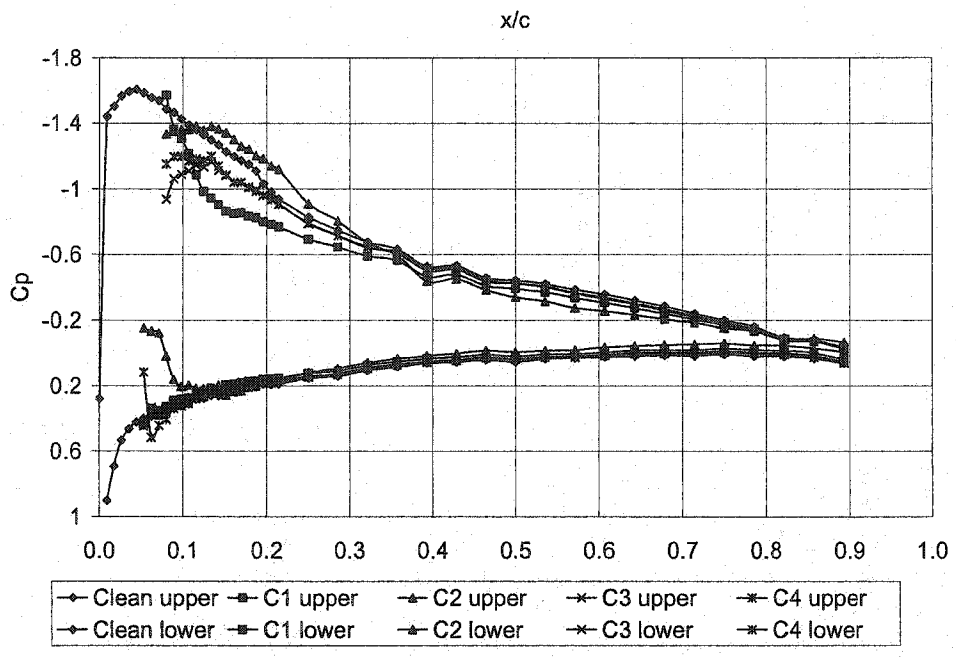

Figure 136 – Cp vs. x/c, Re ~ 1,300,000, AOA = 5 deg

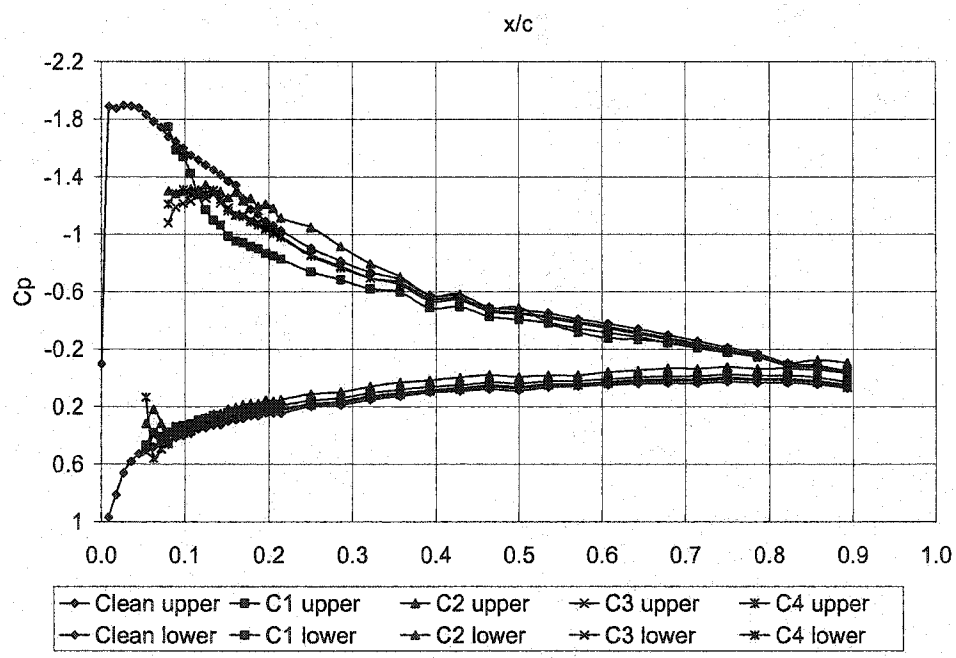

Figure 137 – Cp vs. x/c, Re ~ 1,300,000, AOA = 6 deg

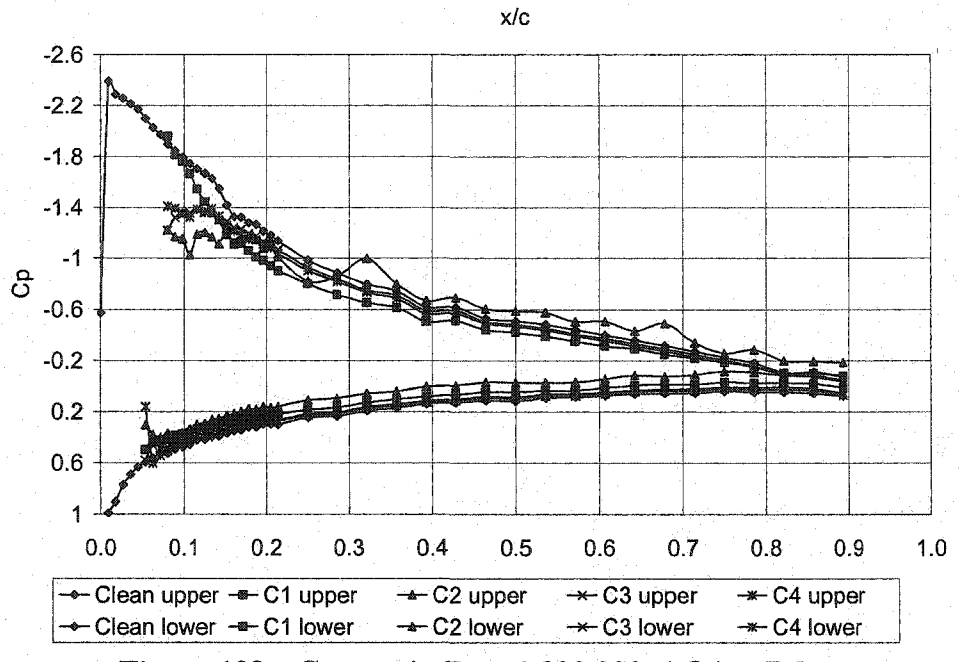

Figure 138 – Cp vs. x/c, Re ~ 1,300,000, AOA = 7 deg

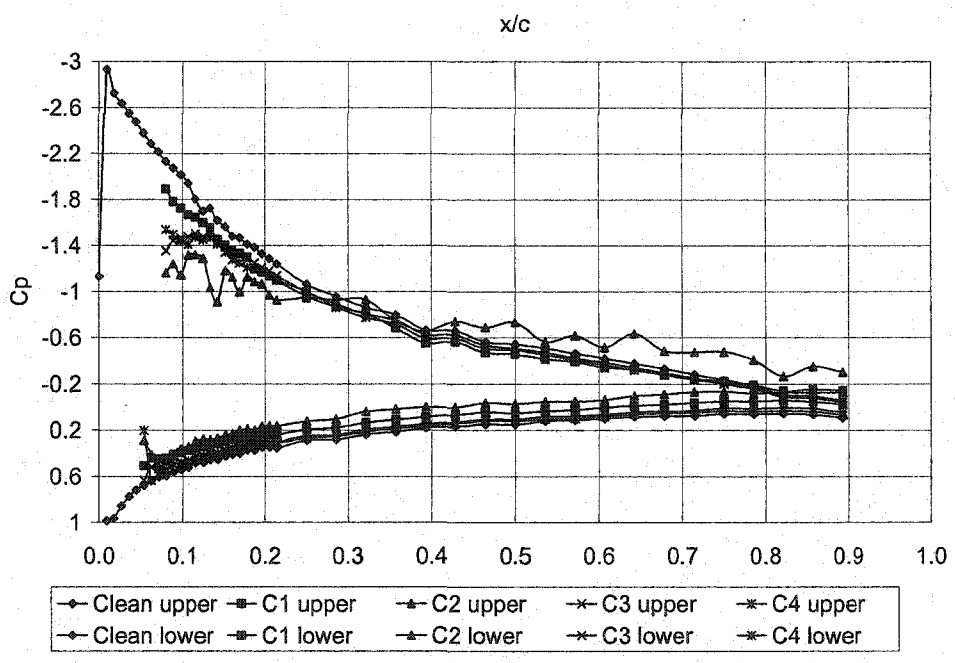

Figure 139 – Cp vs. x/c, Re ~ 1,300,000, AOA = 8 deg

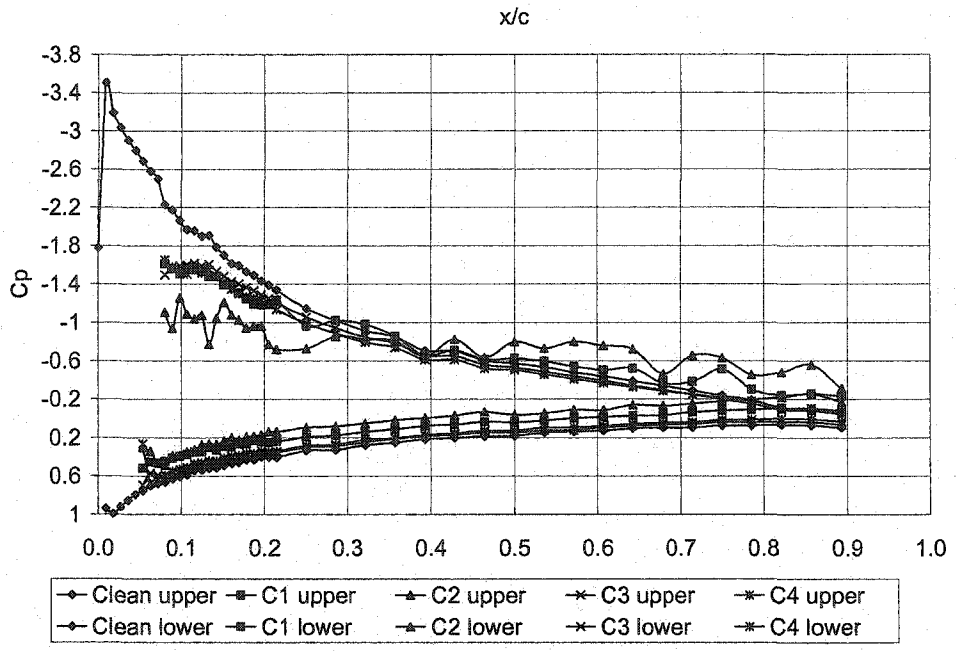

Figure 140 – Cp vs. x/c, Re ~ 1,300,000, AOA = 9 deg

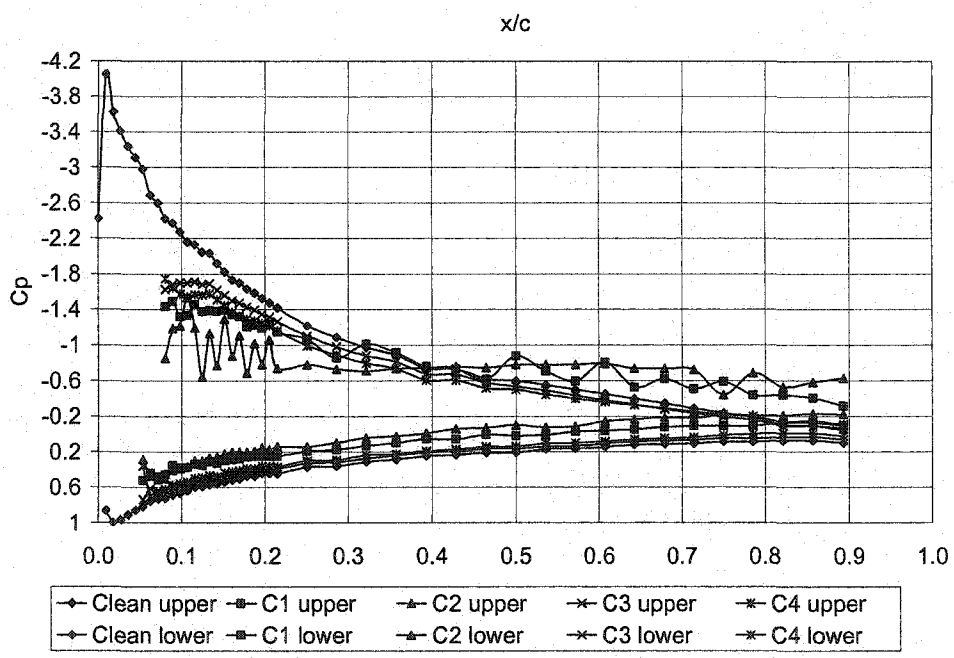

Figure 141 – Cp vs. x/c, Re ~ 1,300,000, AOA = 10 deg

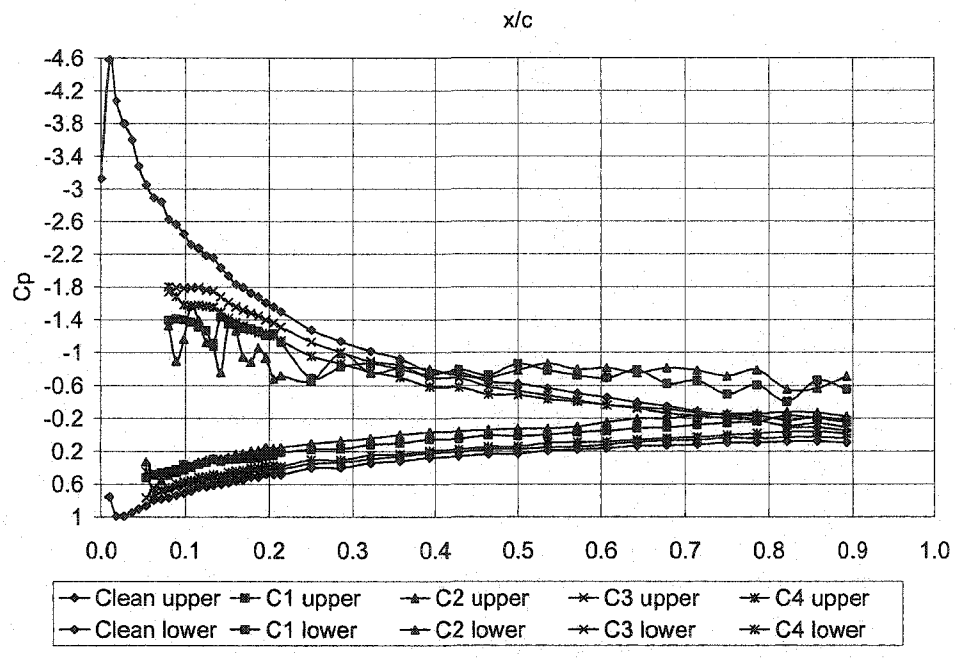

Figure 142 – Cp vs. x/c, Re ~ 1,300,000, AOA = 11 deg

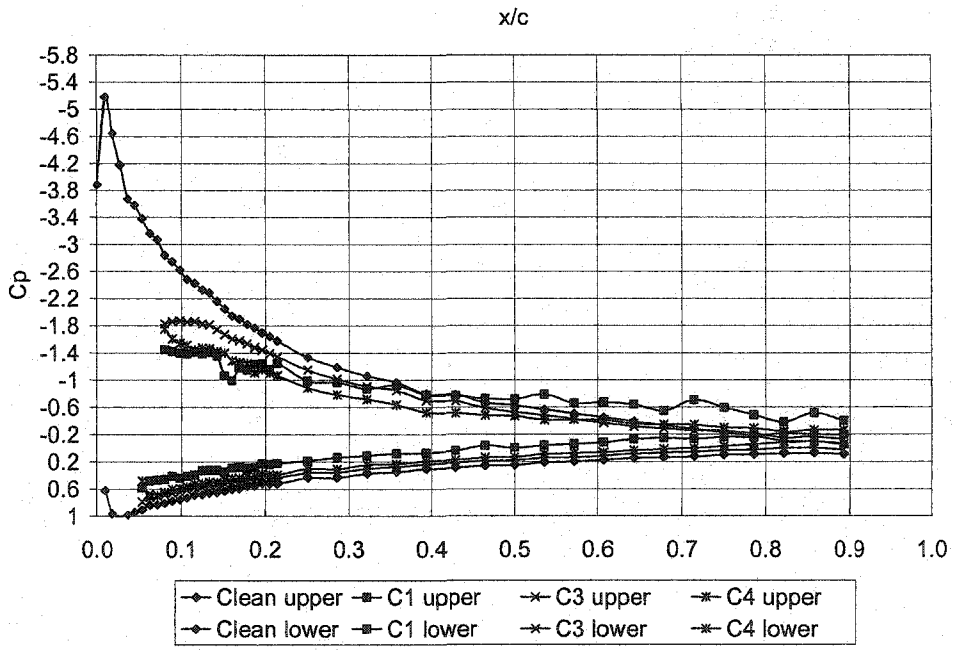

Figure 143 – Cp vs. x/c, Re ~ 1,300,000, AOA = 12 deg

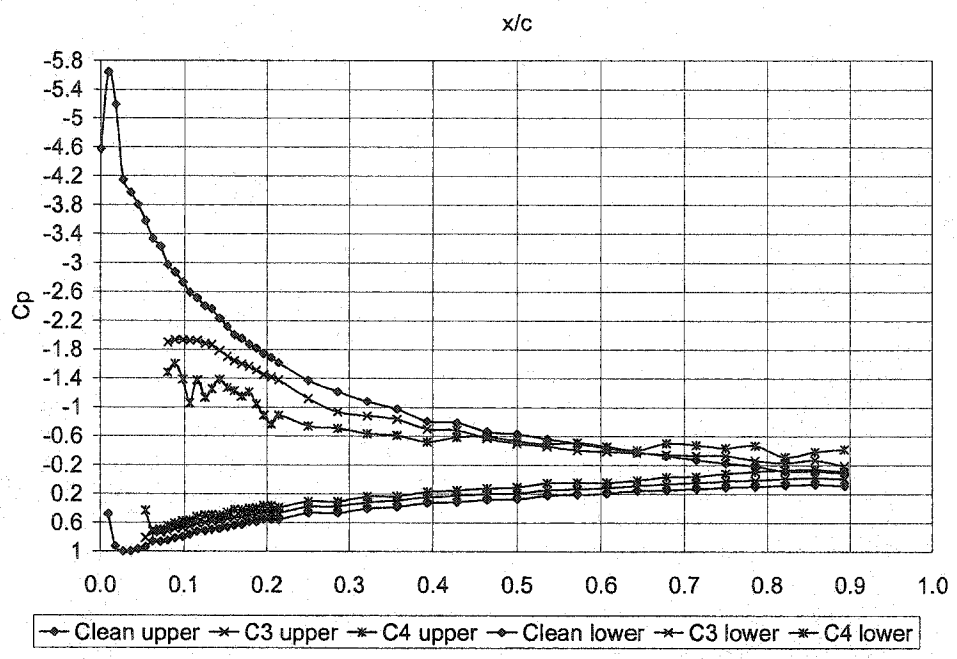

Figure 144 – Cp vs. x/c, Re ~ 1,300,000, AOA = 13 deg

APPENDIX B – FLUCTUATING CP DISTRIBUTIONS

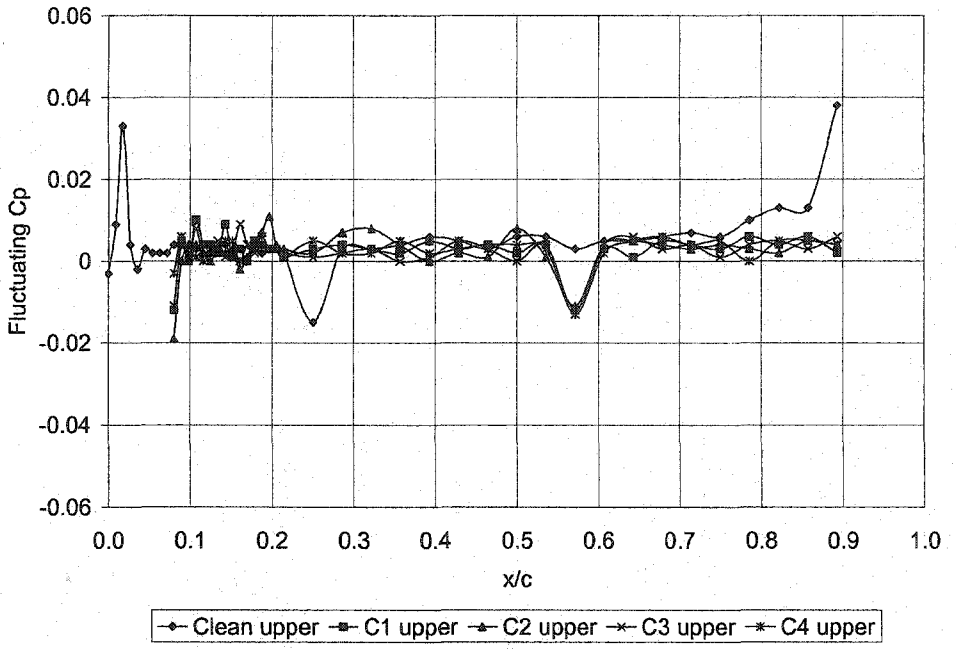

Figure 145 – Fluctuating Cp Dist., Re~700000, α = 0 deg, Upper Surface

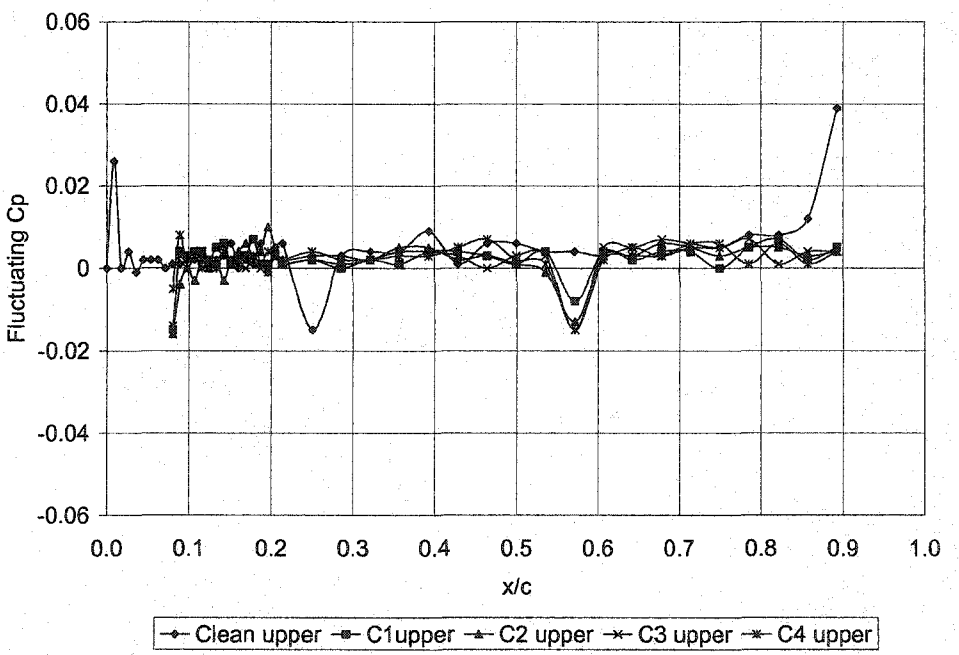

Figure 146 – Fluctuating Cp Dist., Re~700000, α = 1 deg, Upper Surface

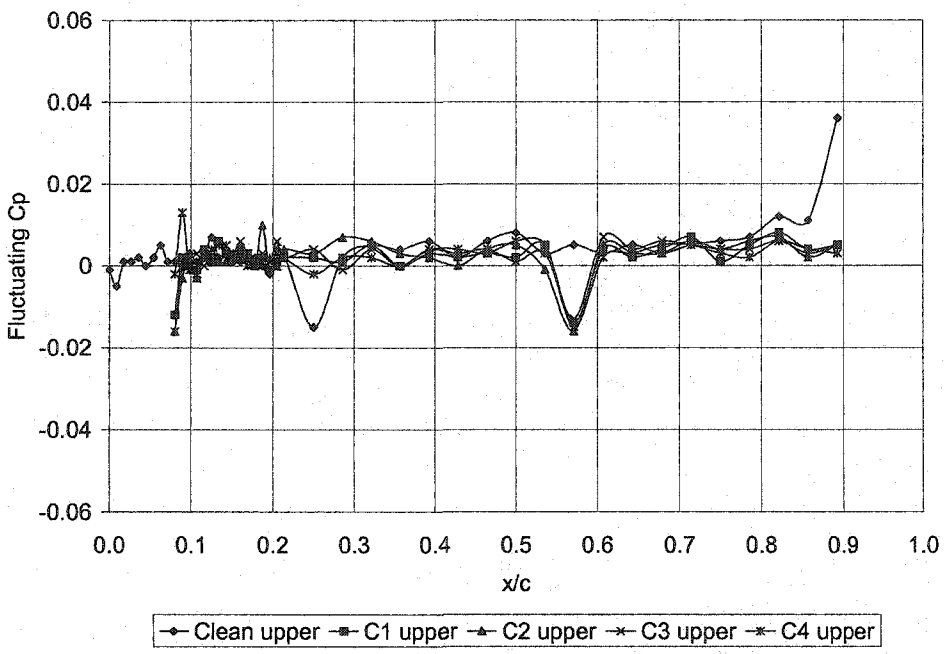

Figure 147 – Fluctuating Cp Dist., Re~700000, α = 2 deg, Upper Surface

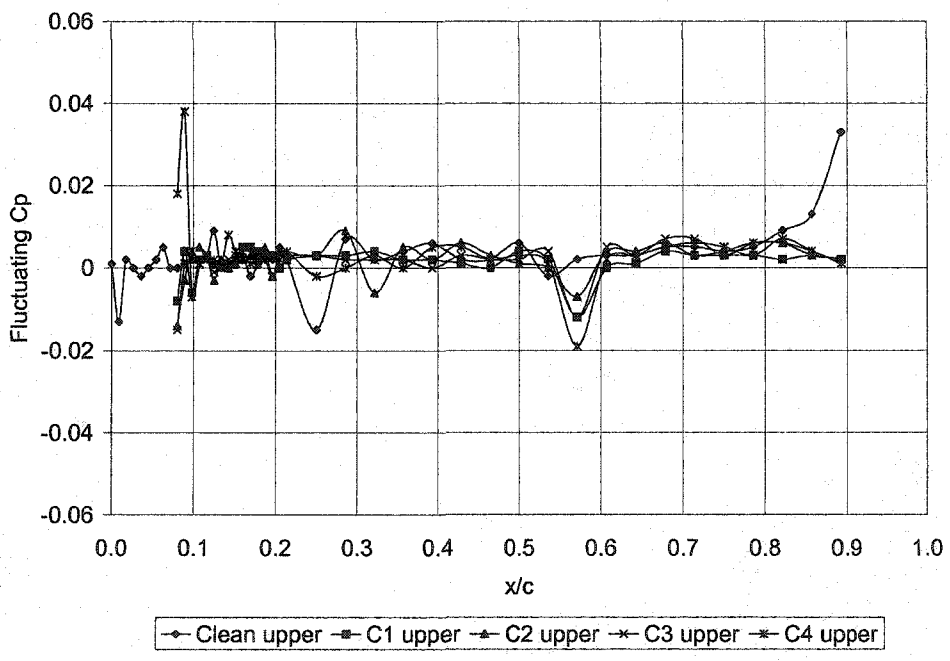

Figure 148 – Fluctuating Cp Dist., Re~700000, α = 3 deg, Upper Surface

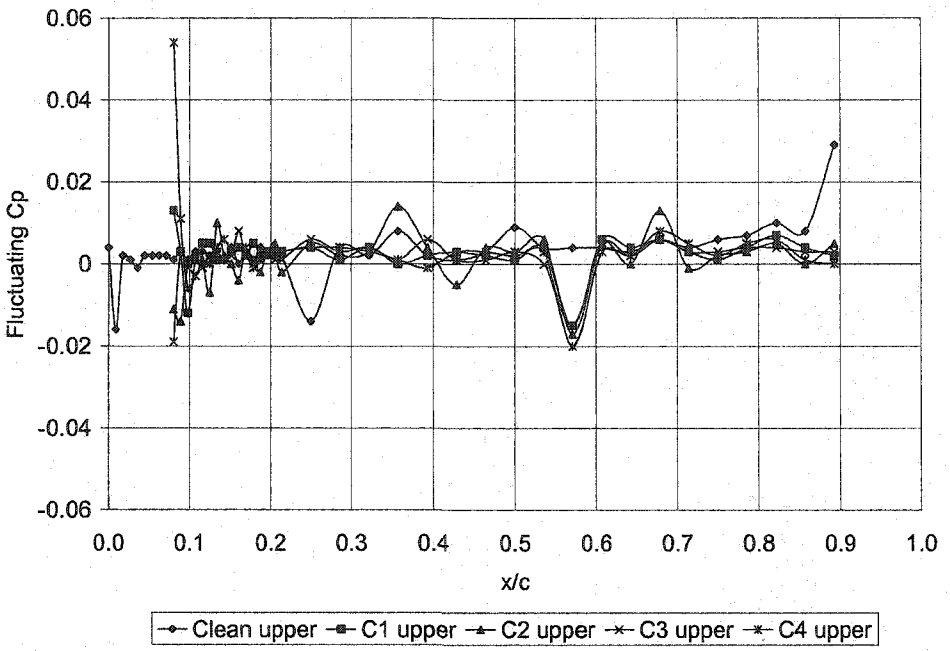

Figure 149 – Fluctuating Cp Dist., Re~700000, α = 4 deg, Upper Surface

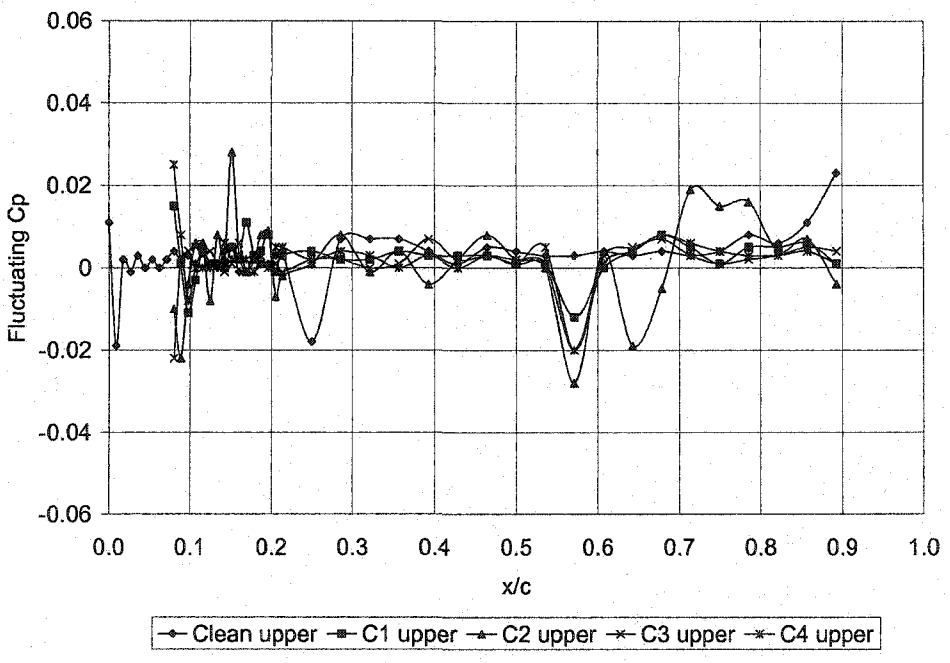

Figure 150 – Fluctuating Cp Dist., Re~700000, α = 5 deg, Upper Surface

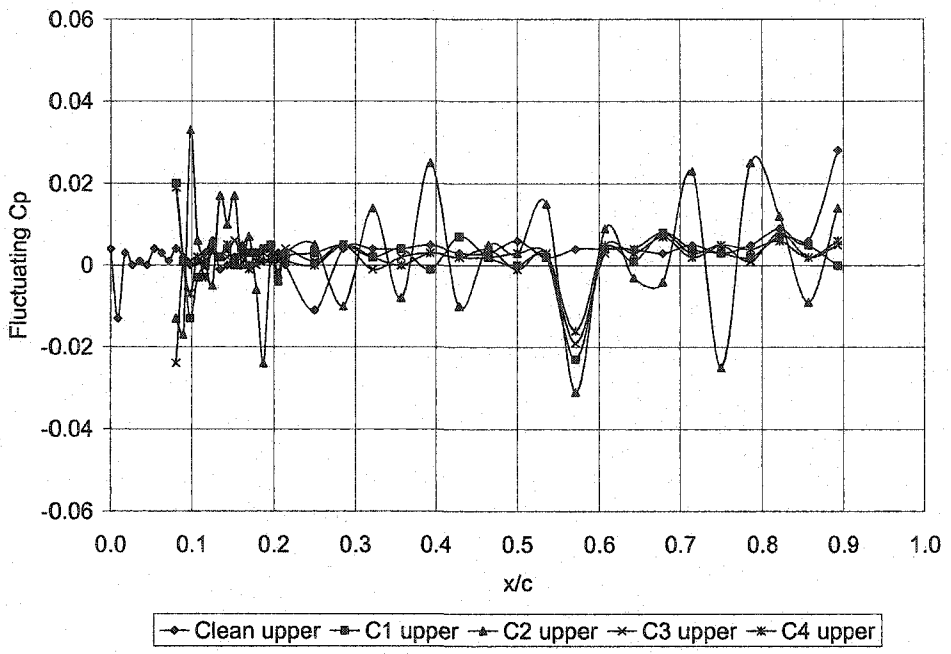

Figure 151 – Fluctuating Cp Dist., Re~700000, α = 6 deg, Upper Surface

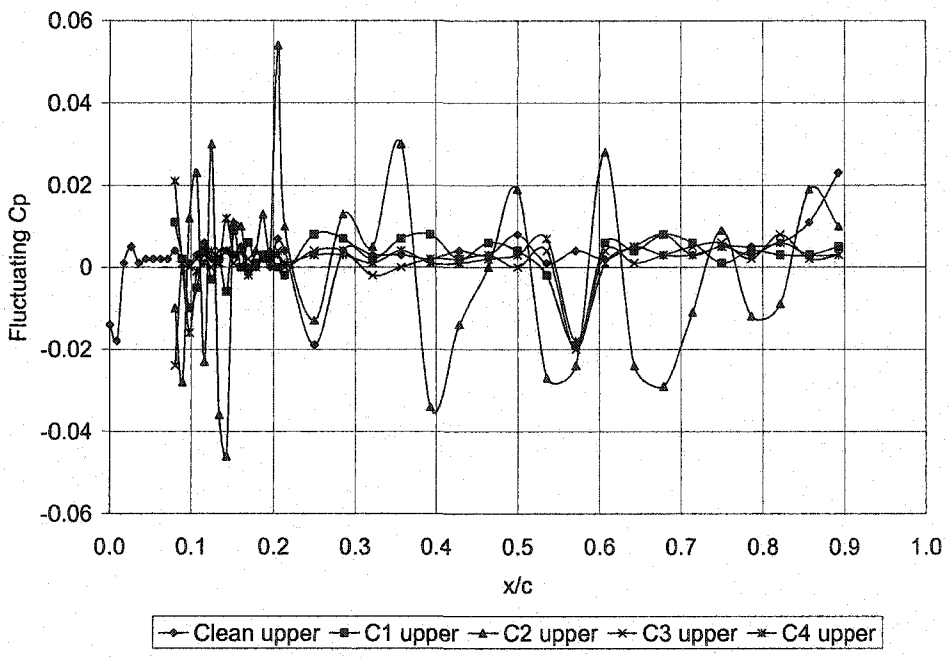

Figure 152 – Fluctuating Cp Dist., Re~700000, α = 7 deg, Upper Surface

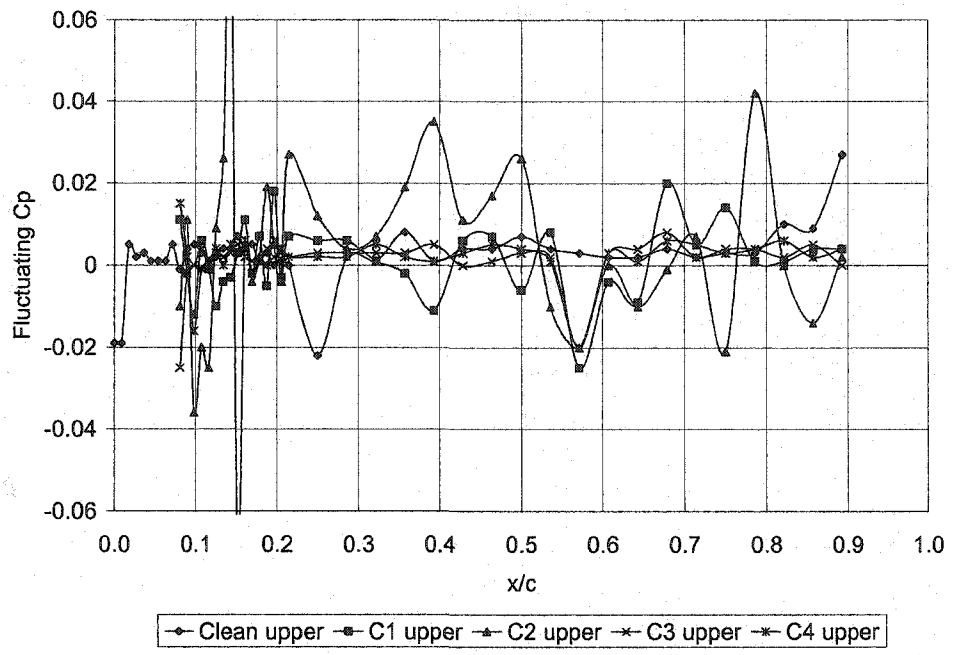

Figure 153 – Fluctuating Cp Dist., Re~700000, α = 8 deg, Upper Surface

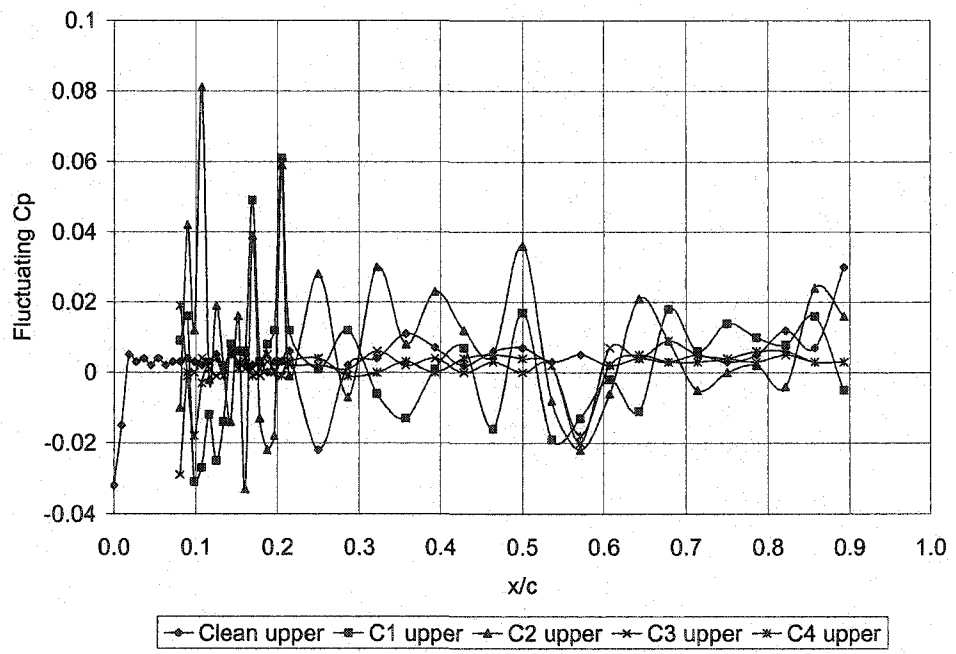

Figure 154 – Fluctuating Cp Dist., Re~700000, α = 9 deg, Upper Surface

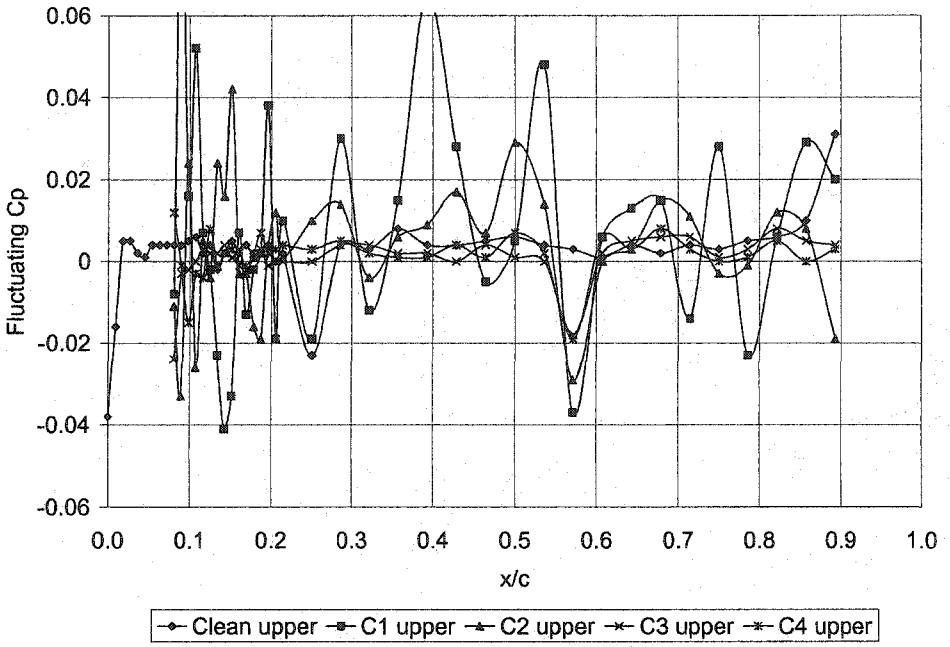

Figure 155 – Fluctuating Cp Dist., Re~700000, α = 10 deg, Upper Surface

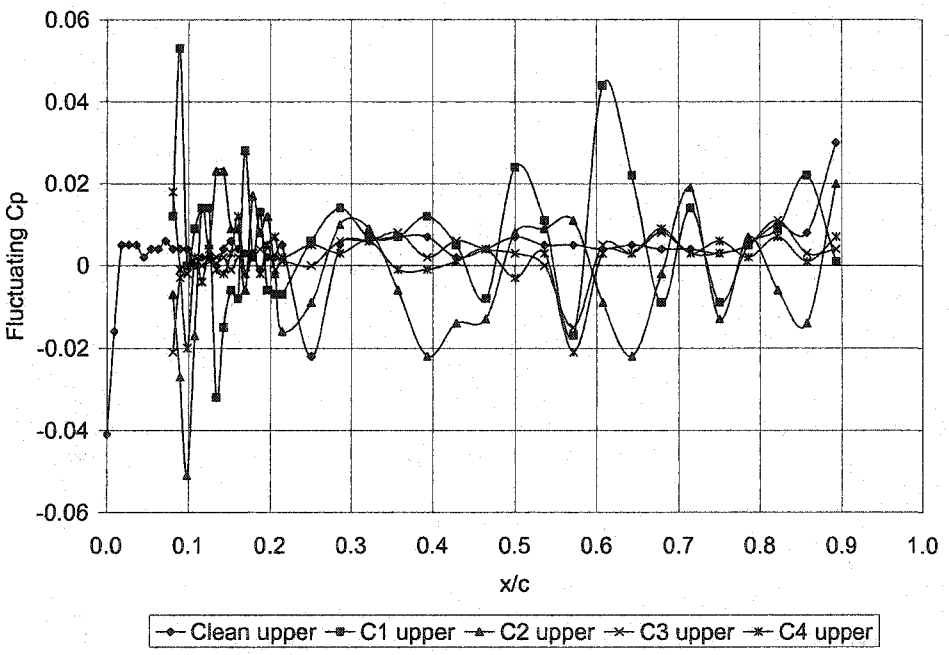

Figure 156 – Fluctuating Cp Dist., Re~700000, α = 11 deg, Upper Surface

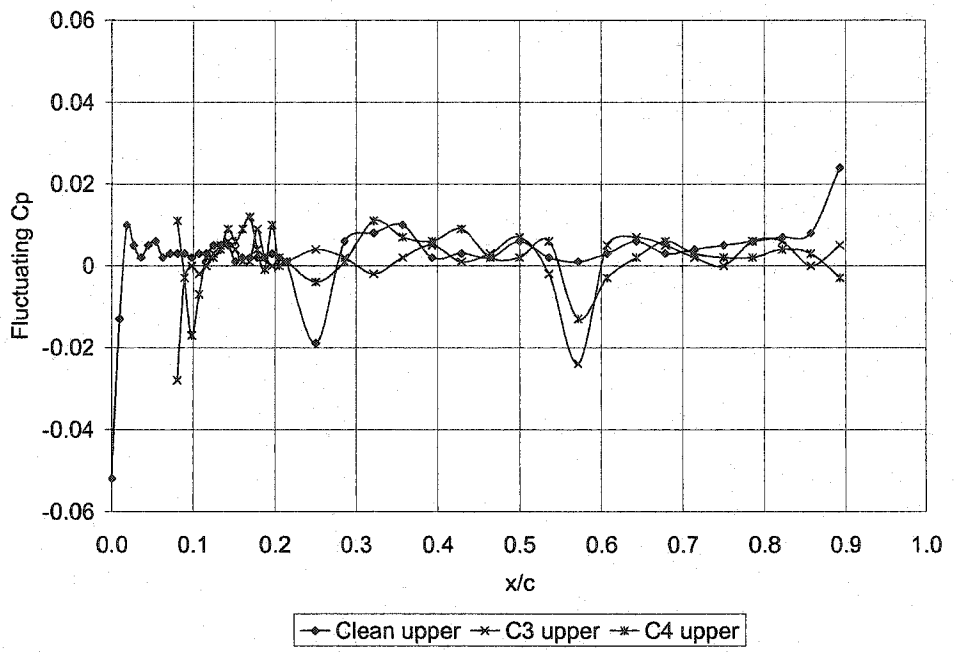

Figure 157 – Fluctuating Cp Dist., Re~700000, α = 12 deg, Upper Surface

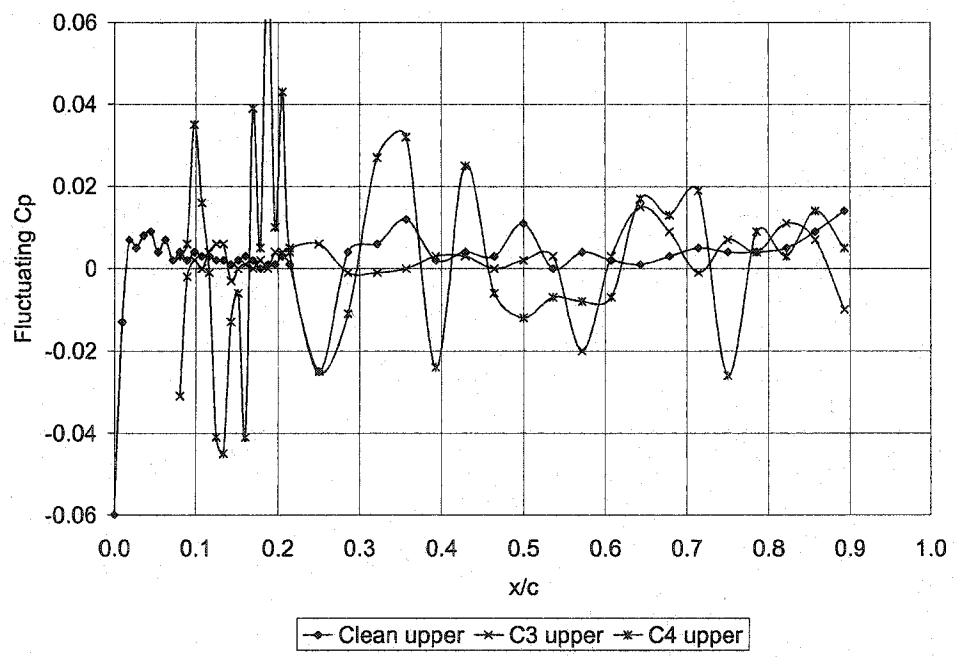

Figure 158 – Fluctuating Cp Dist., Re~700000, α = 13 deg, Upper Surface

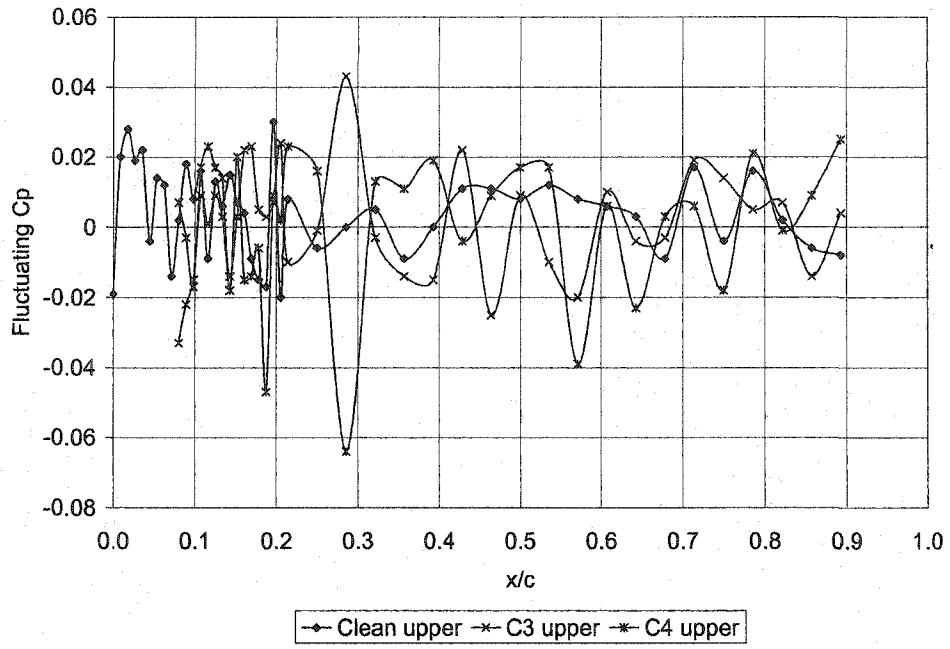

Figure 159 – Fluctuating Cp Dist., Re~700000, α = 14 deg, Upper Surface

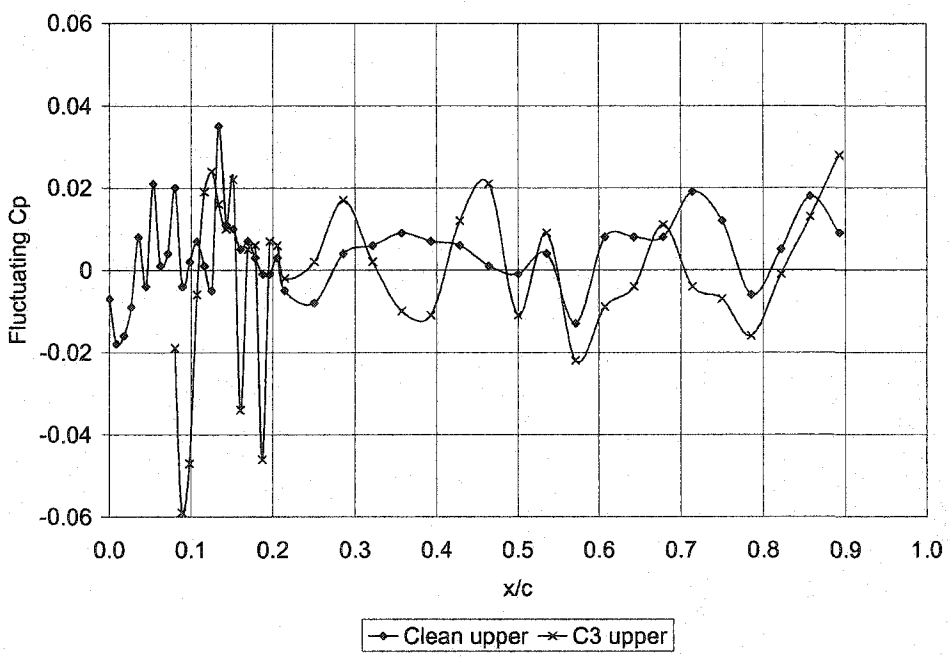

Figure 160 – Fluctuating Cp Dist., Re~700000, α = 15 deg, Upper Surface

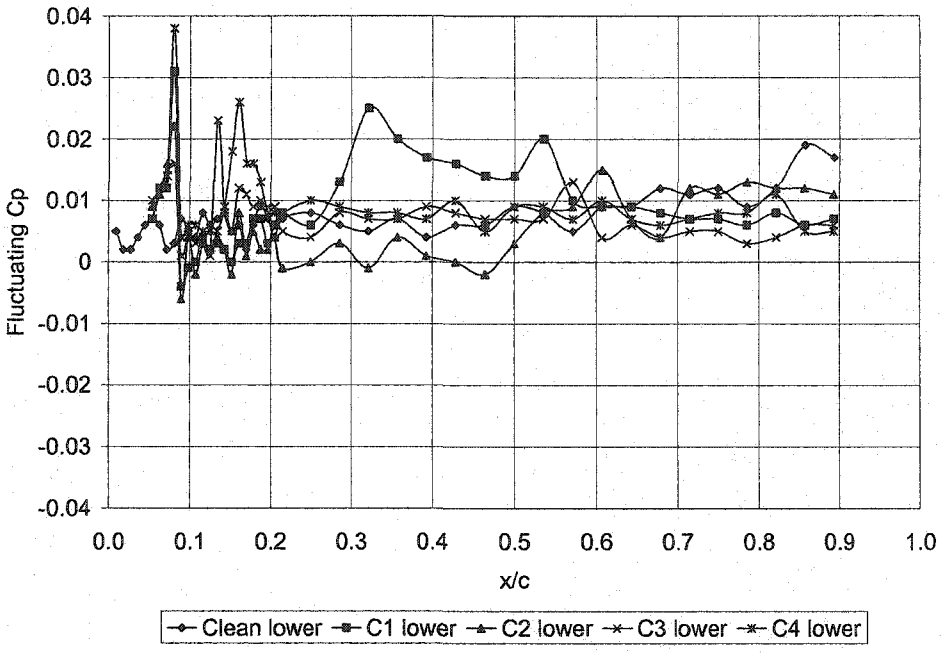

Figure 161 – Fluctuating Cp Dist., Re~700000, α = 0 deg, Lower Surface

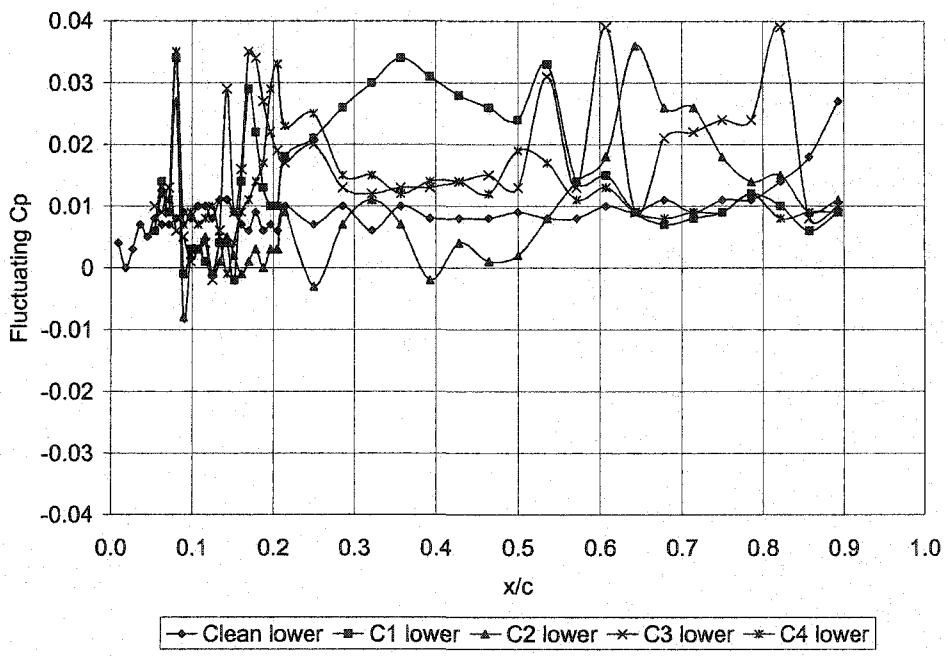

Figure 162 – Fluctuating Cp Dist., Re~700000, α = 1 deg, Lower Surface

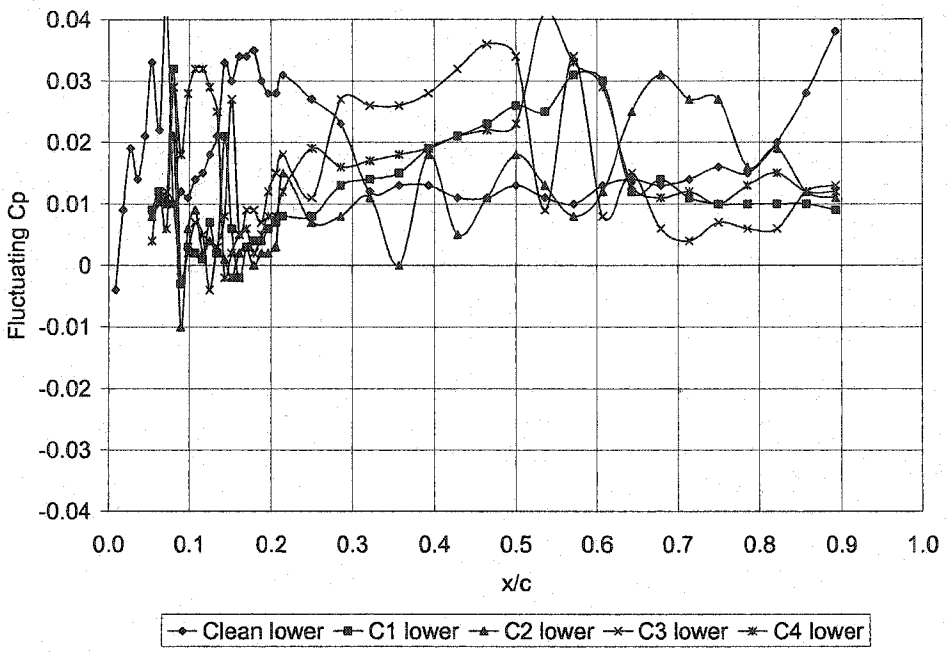

Figure 163 – Fluctuating Cp Dist., Re~700000, α = 2 deg, Lower Surface

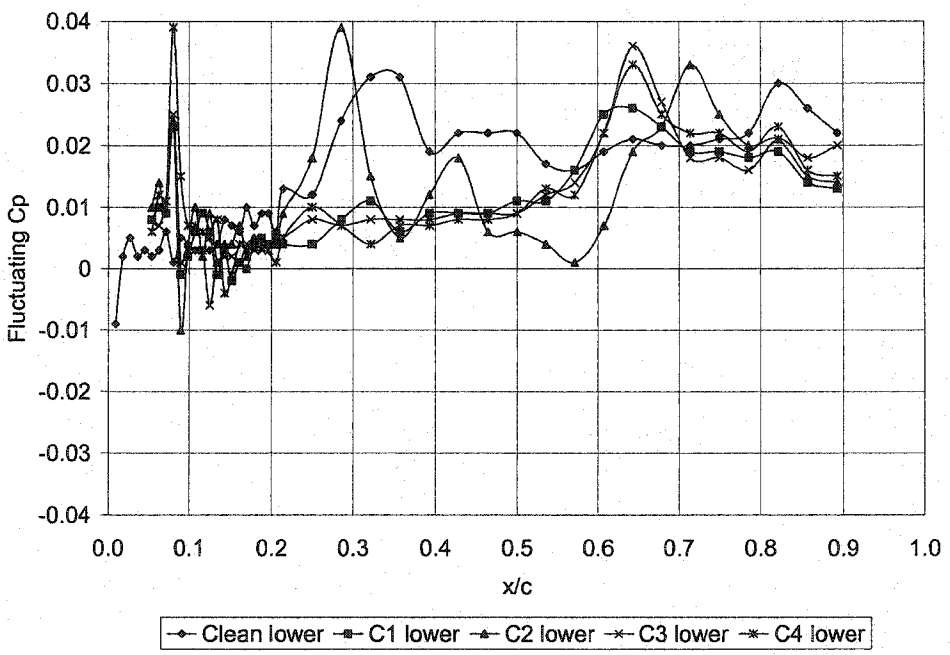

Figure 164 – Fluctuating Cp Dist., Re~700000, α = 3 deg, Lower Surface

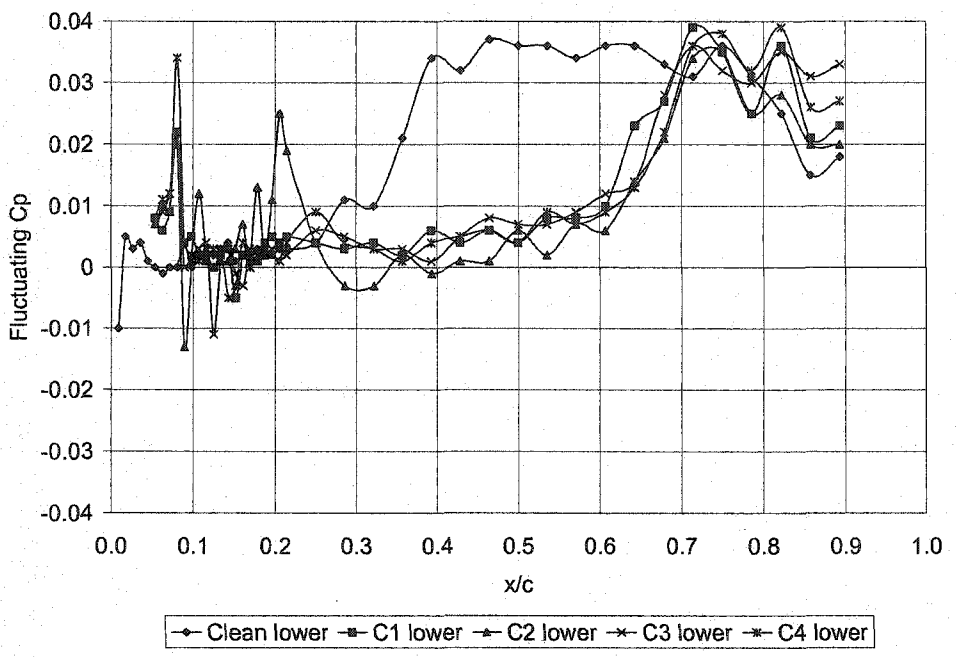

Figure 165 – Fluctuating Cp Dist., Re~700000, α = 4 deg, Lower Surface

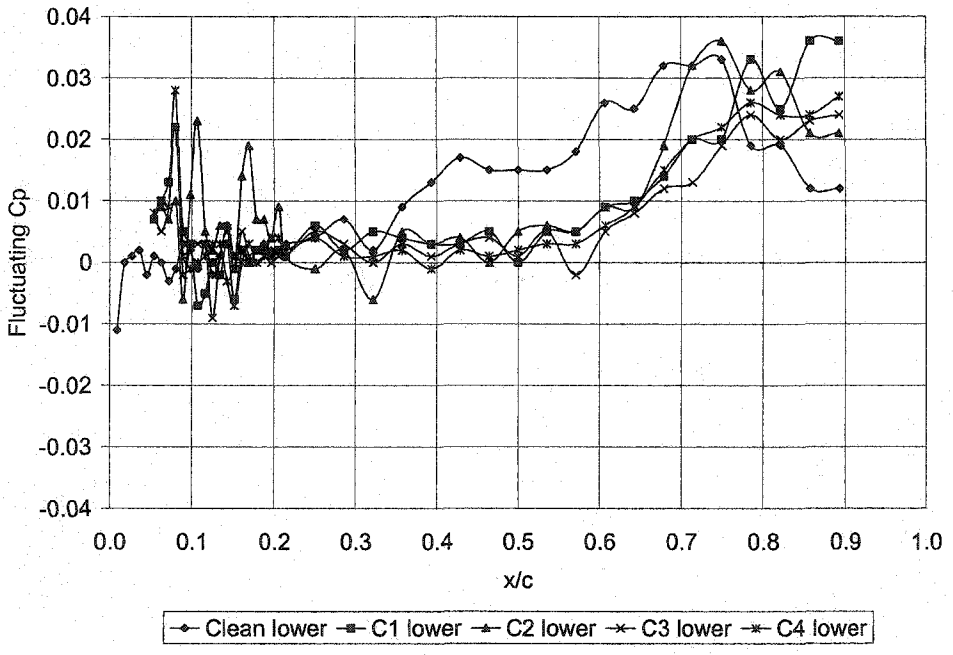

Figure 166 – Fluctuating Cp Dist., Re~700000, α = 5 deg, Lower Surface

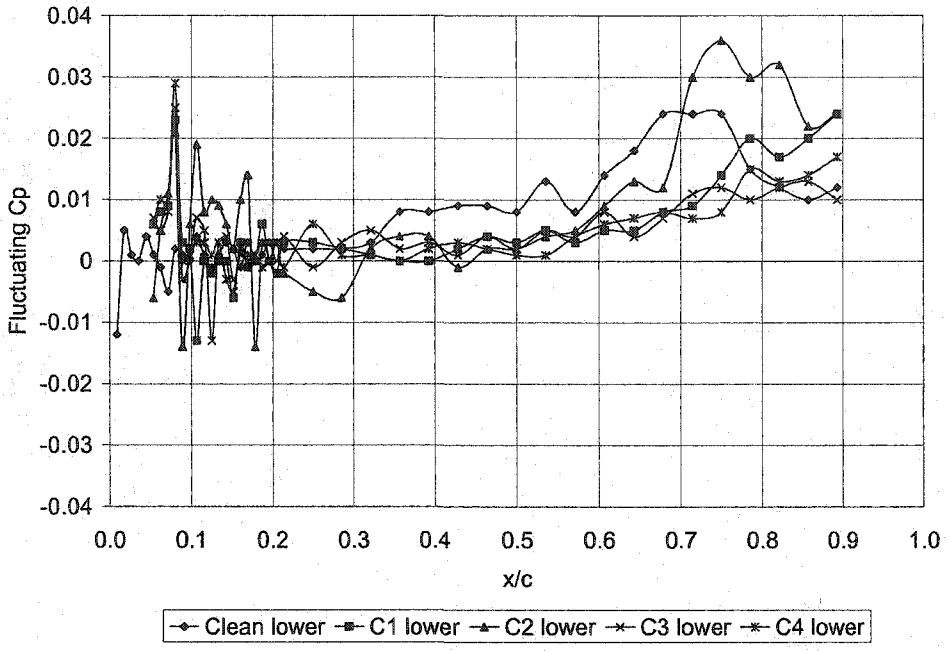

Figure 167 – Fluctuating Cp Dist., Re~700000, α = 6 deg, Lower Surface

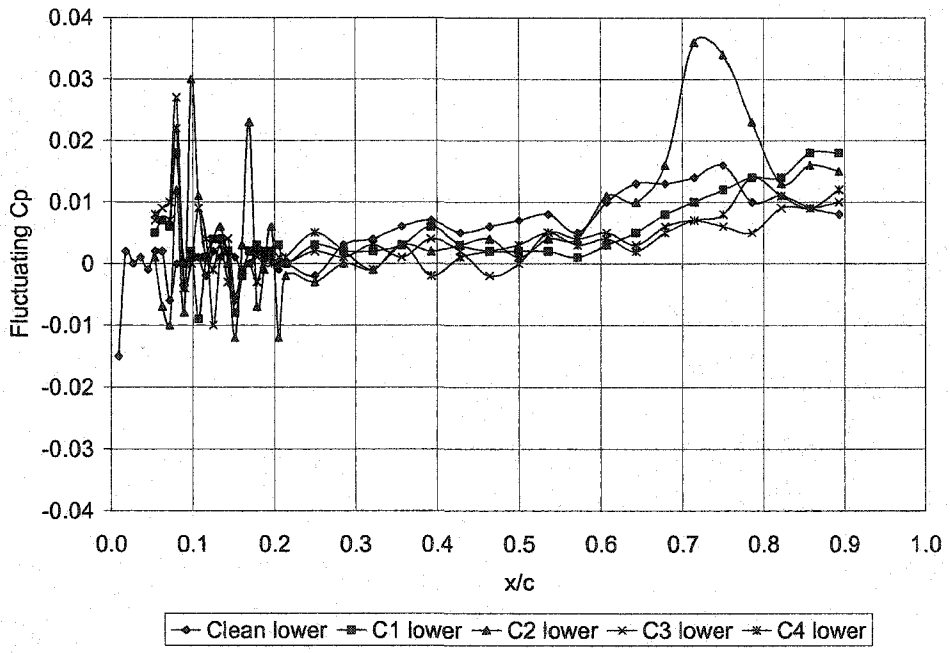

Figure 168 – Fluctuating Cp Dist., Re~700000, α = 7 deg, Lower Surface

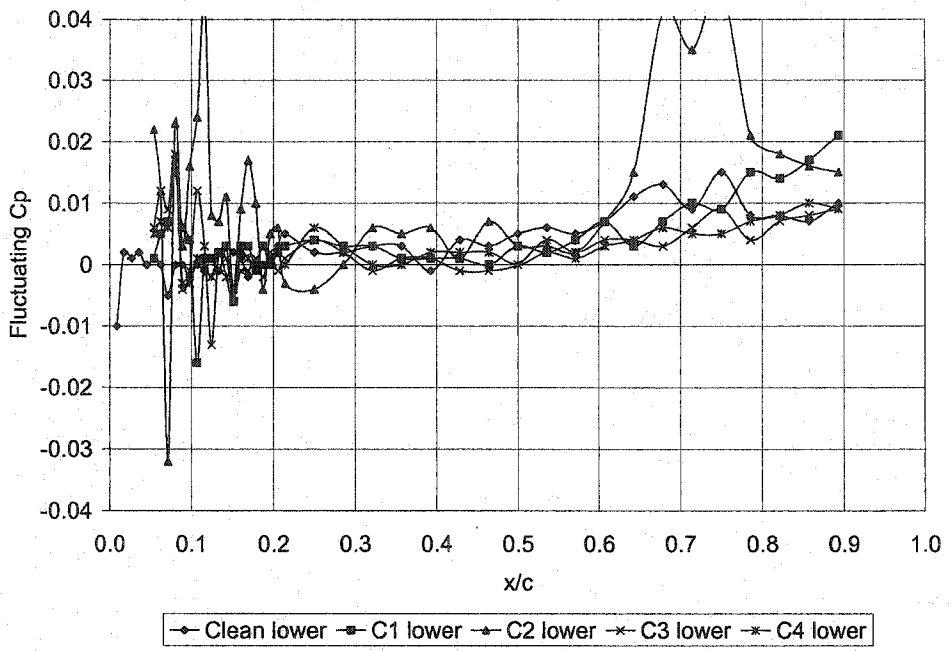

Figure 169 – Fluctuating Cp Dist., Re~700000, α = 8 deg, Lower Surface

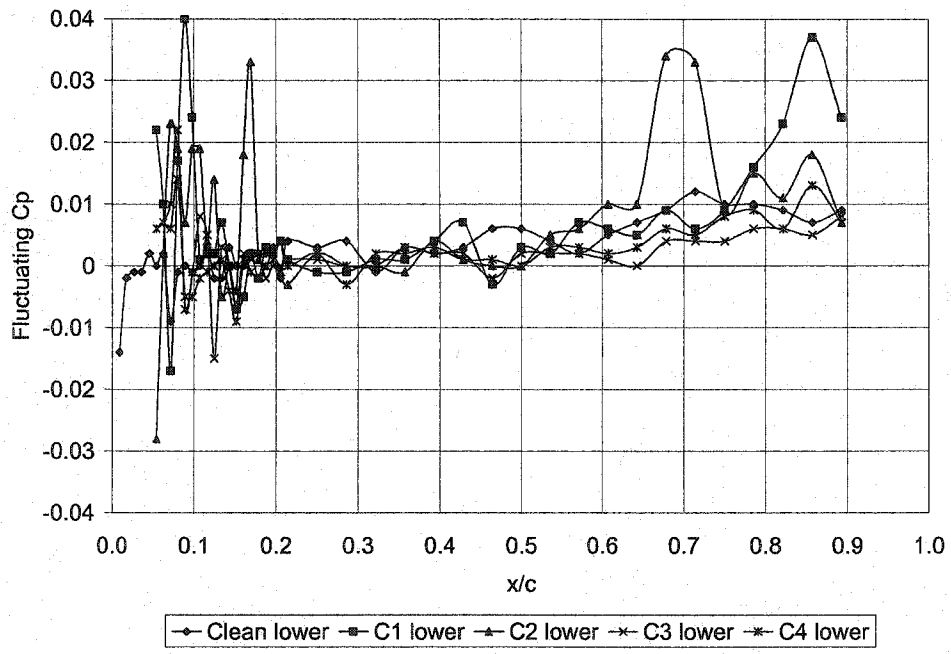

Figure 170 – Fluctuating Cp Dist., Re~700000, α = 9 deg, Lower Surface

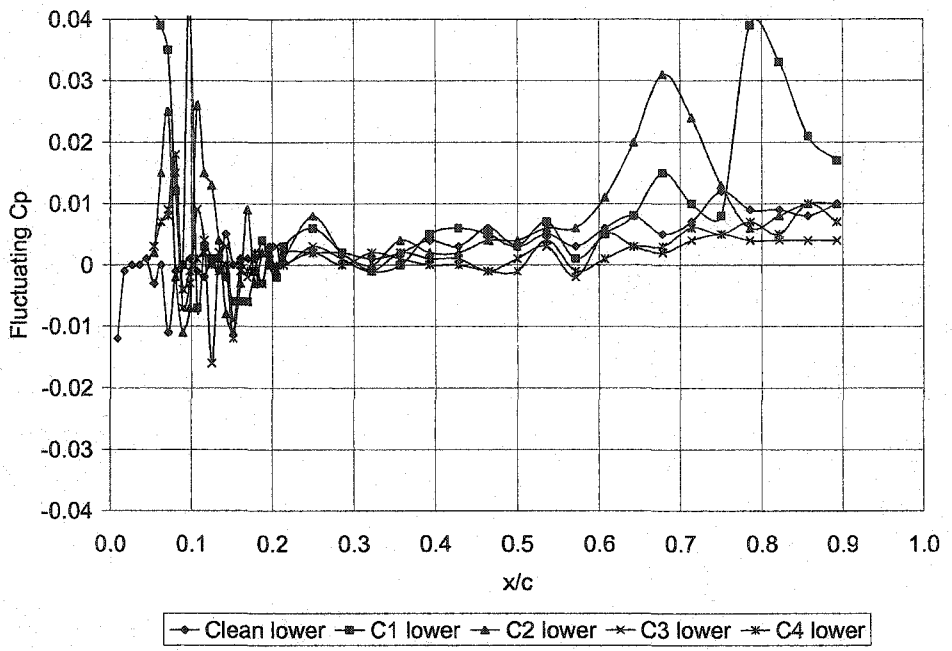

Figure 171 – Fluctuating Cp Dist., Re~700000, α = 10 deg, Lower Surface

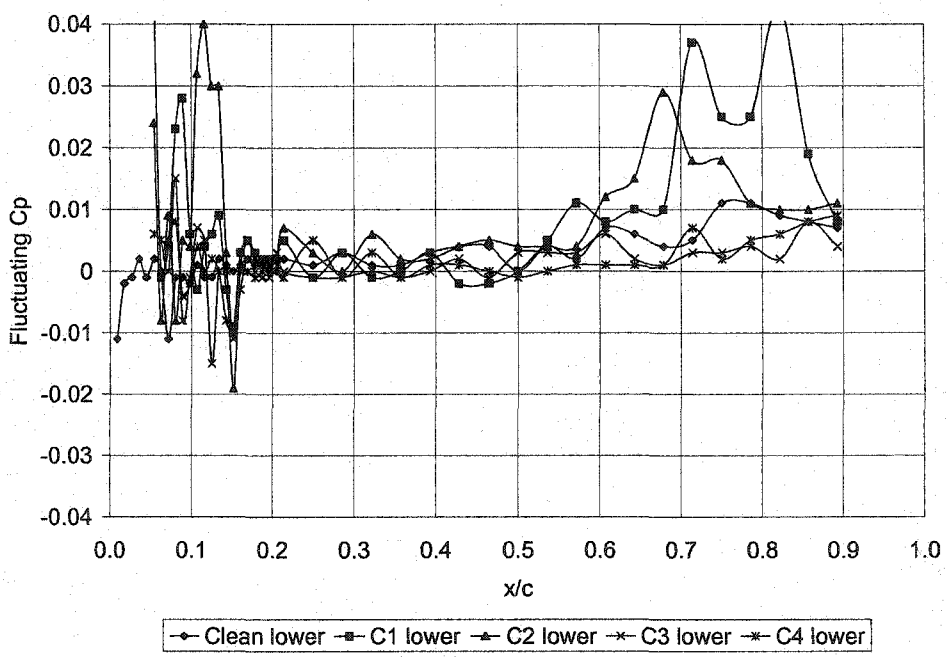

Figure 172 – Fluctuating Cp Dist., Re~700000, α = 11 deg, Lower Surface

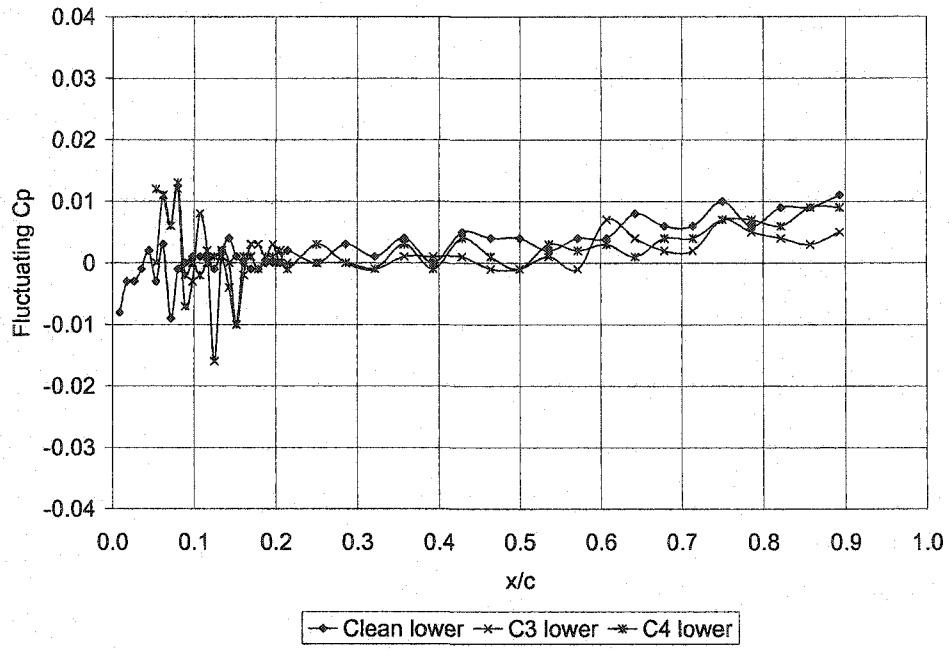

Figure 173 – Fluctuating Cp Dist., Re~700000, α = 12 deg, Lower Surface

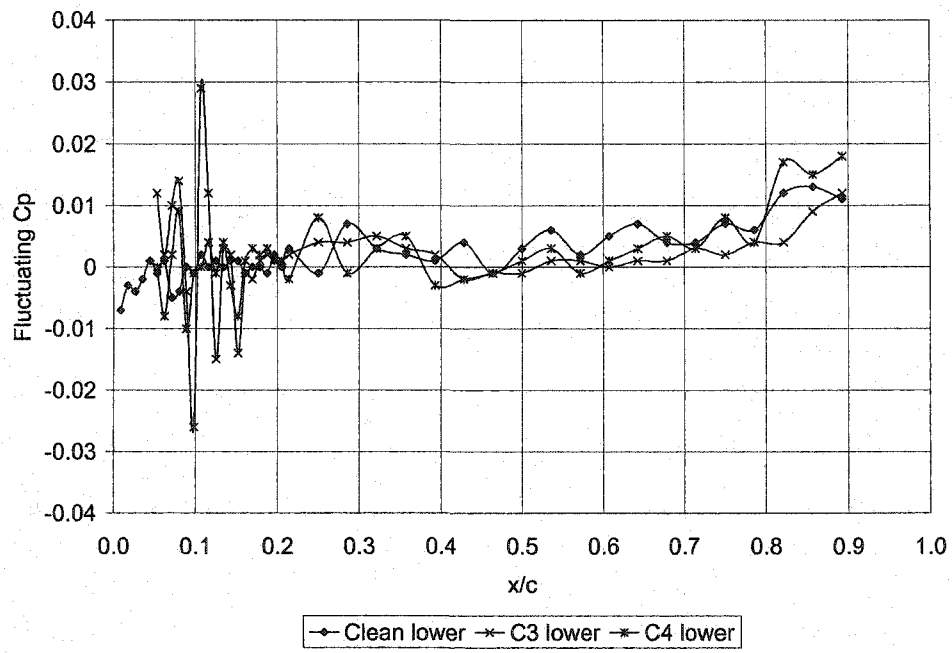

Figure 174 – Fluctuating Cp Dist., Re~700000, α = 13 deg, Lower Surface

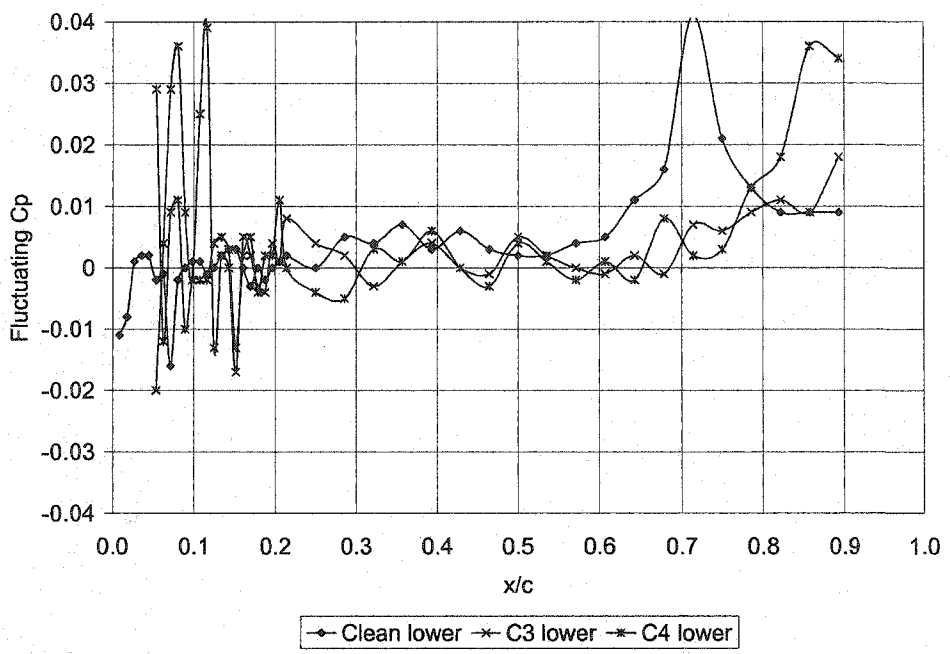

Figure 175 – Fluctuating Cp Dist., Re~700000, α = 14 deg, Lower Surface

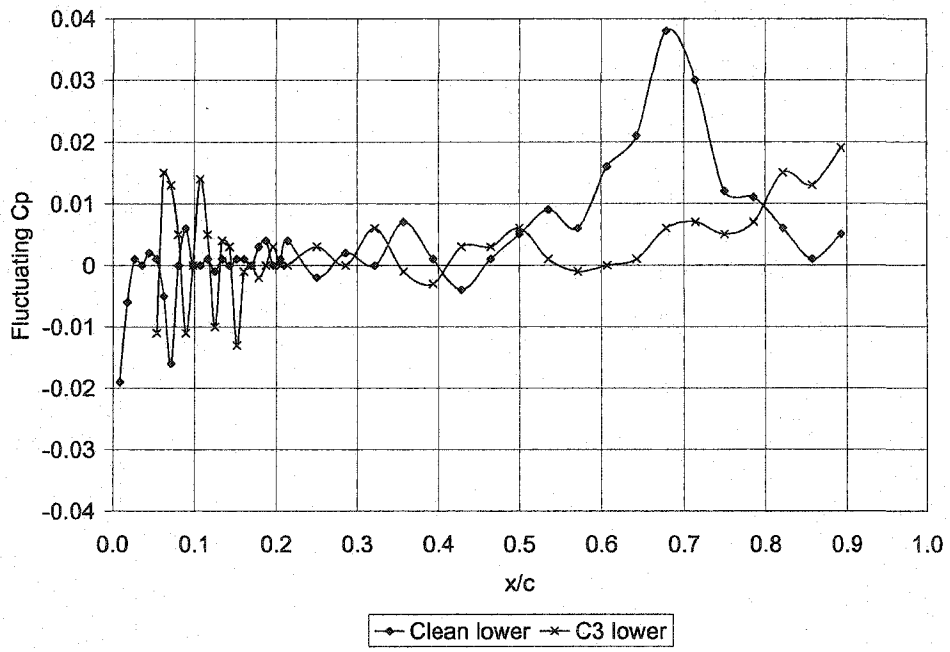

Figure 176 – Fluctuating Cp Dist., Re~700000, α = 15 deg, Lower Surface

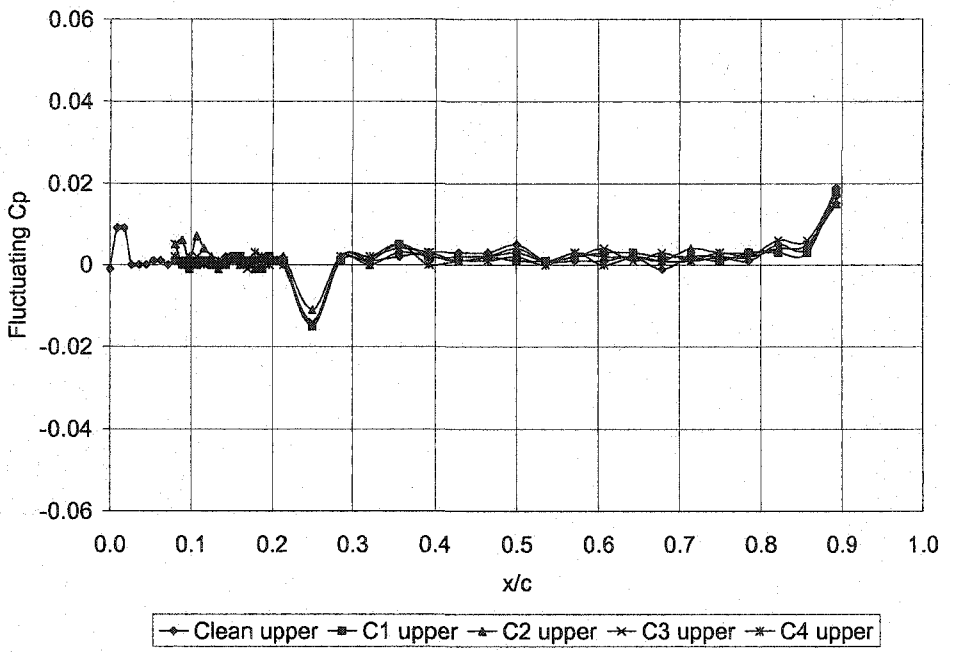

Figure 177 – Fluctuating Cp Dist., Re~1000000, α = 0 deg, Upper Surface

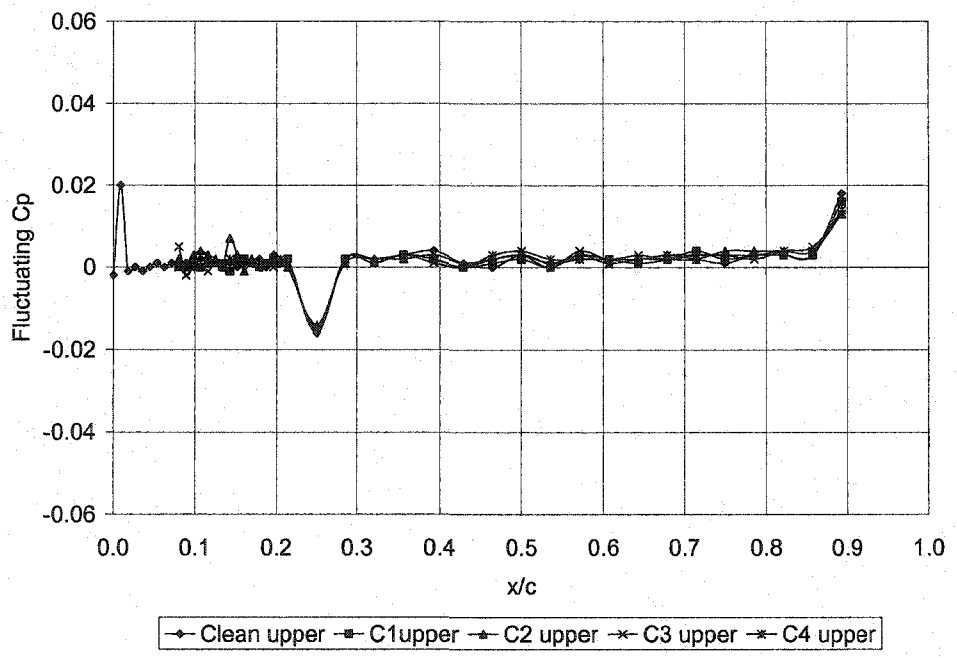

Figure 178 – Fluctuating Cp Dist., Re~1000000, α = 1 deg, Upper Surface

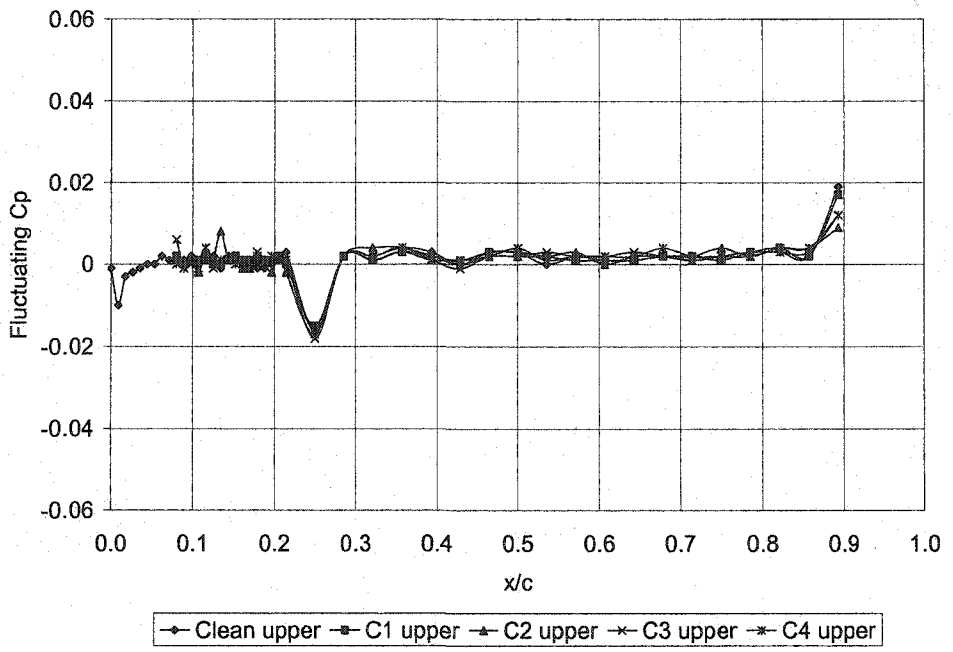

Figure 179 – Fluctuating Cp Dist., Re~1000000, α = 2 deg, Upper Surface

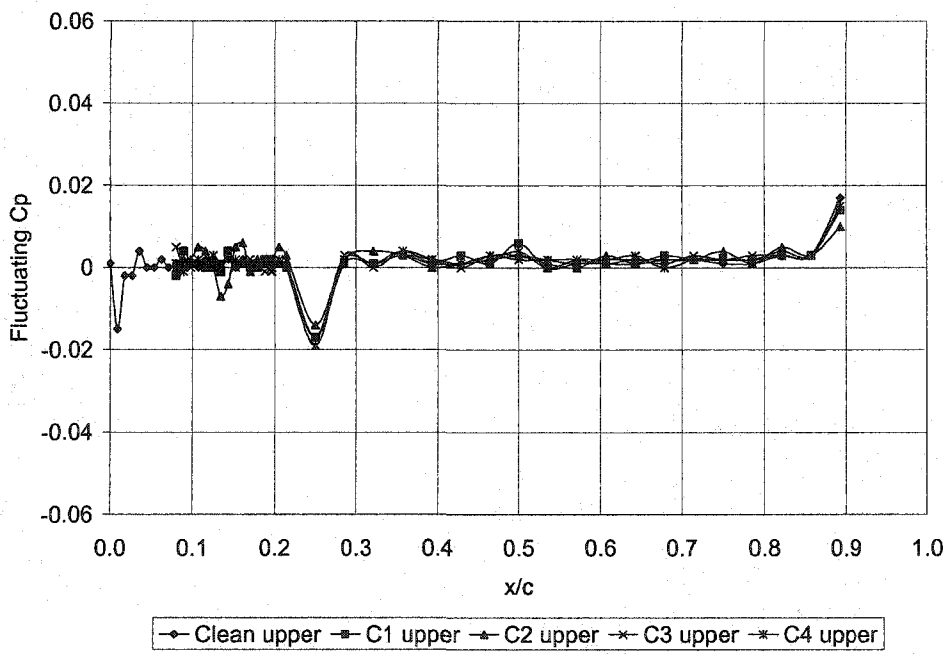

Figure 180 – Fluctuating Cp Dist., Re~1000000, α = 3 deg, Upper Surface

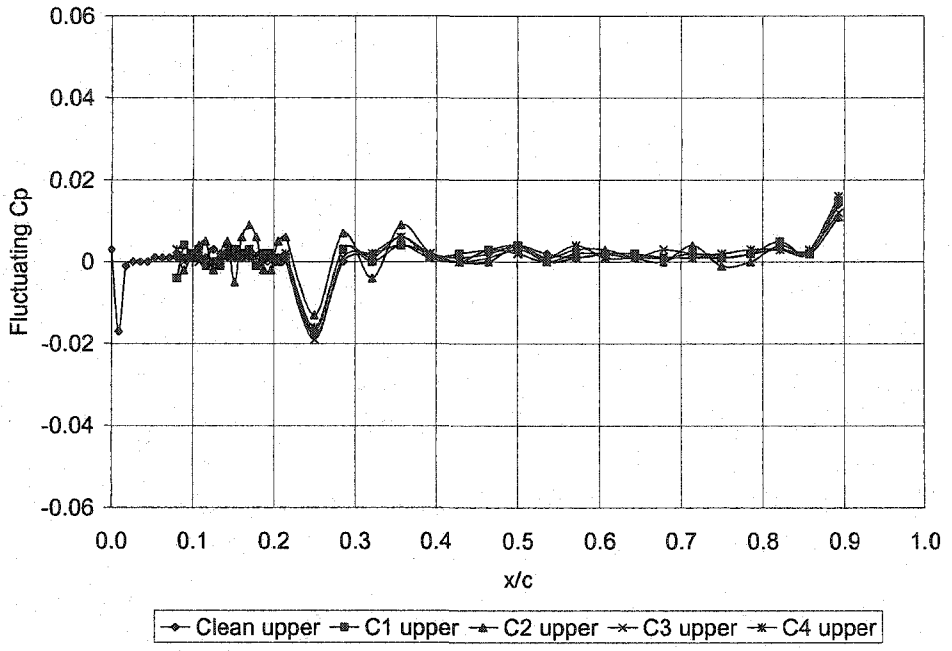

Figure 181 – Fluctuating Cp Dist., Re~1000000, α = 4 deg, Upper Surface

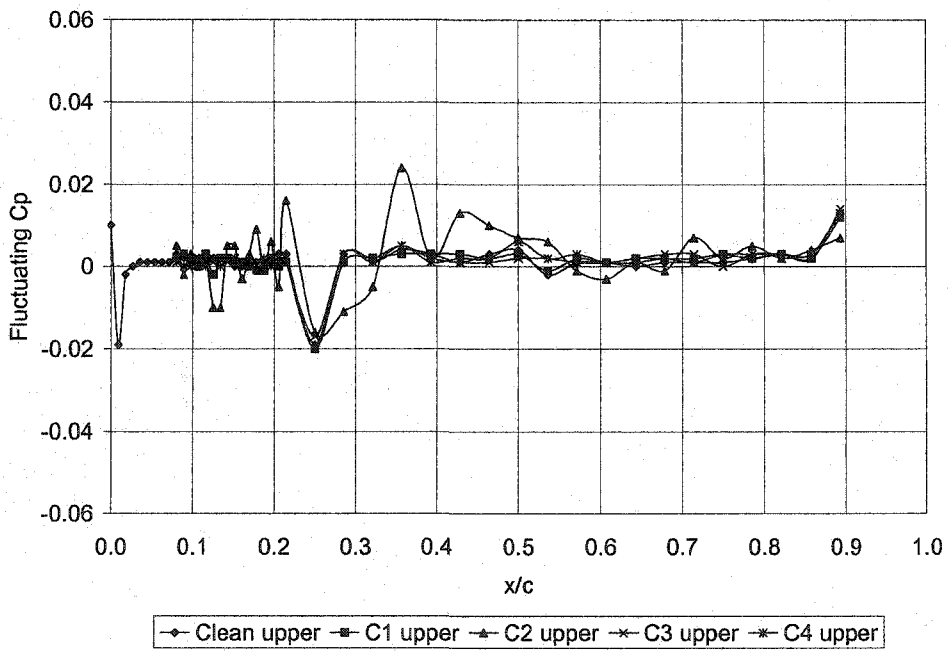

Figure 182 – Fluctuating Cp Dist., Re~1000000, α = 5 deg, Upper Surface

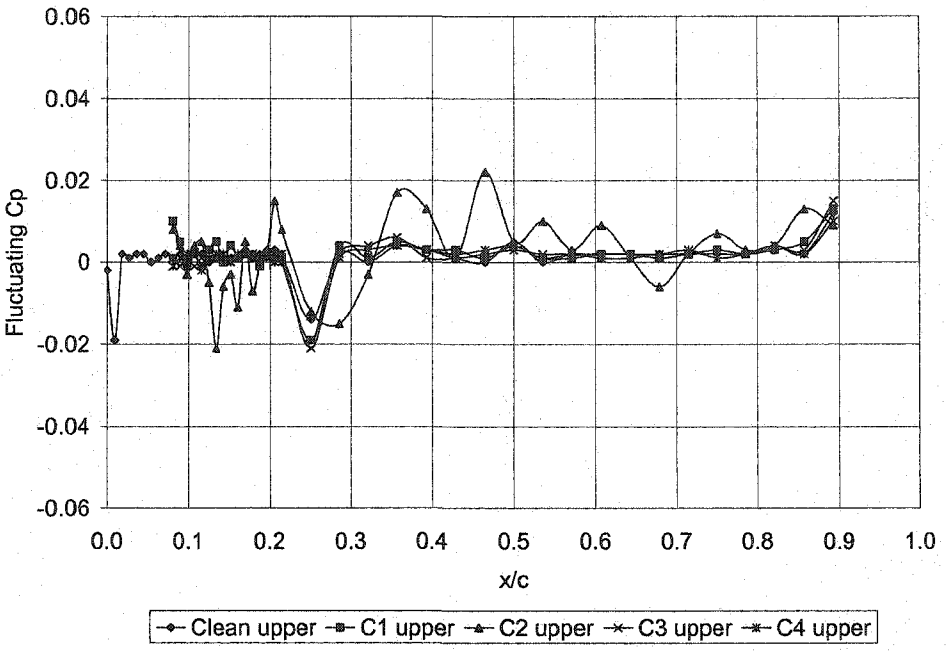

Figure 183 – Fluctuating Cp Dist., Re~1000000, α = 6 deg, Upper Surface

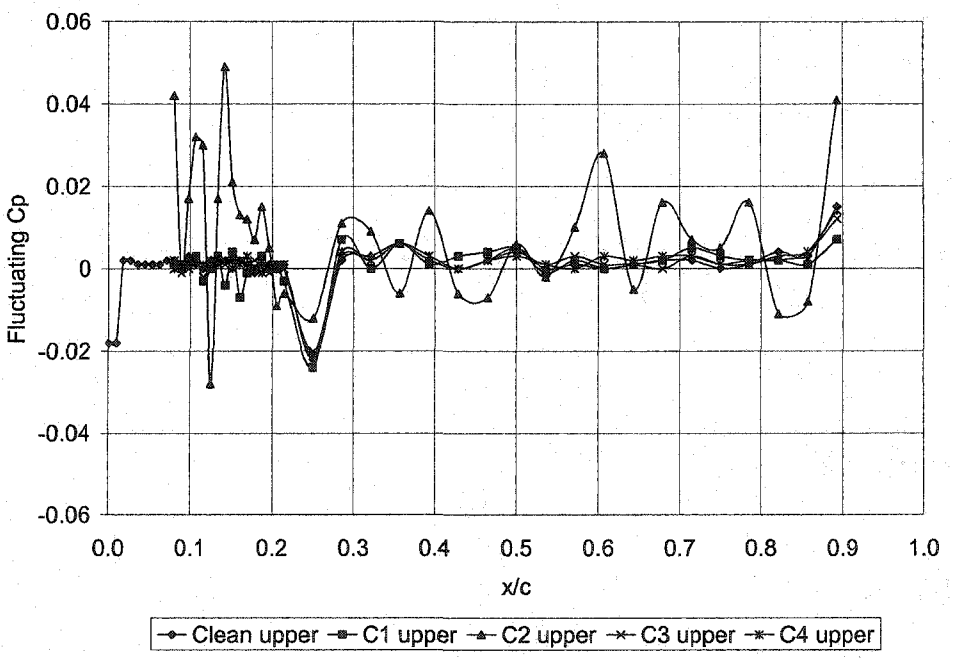

Figure 184 – Fluctuating Cp Dist., Re~1000000, α = 7 deg, Upper Surface

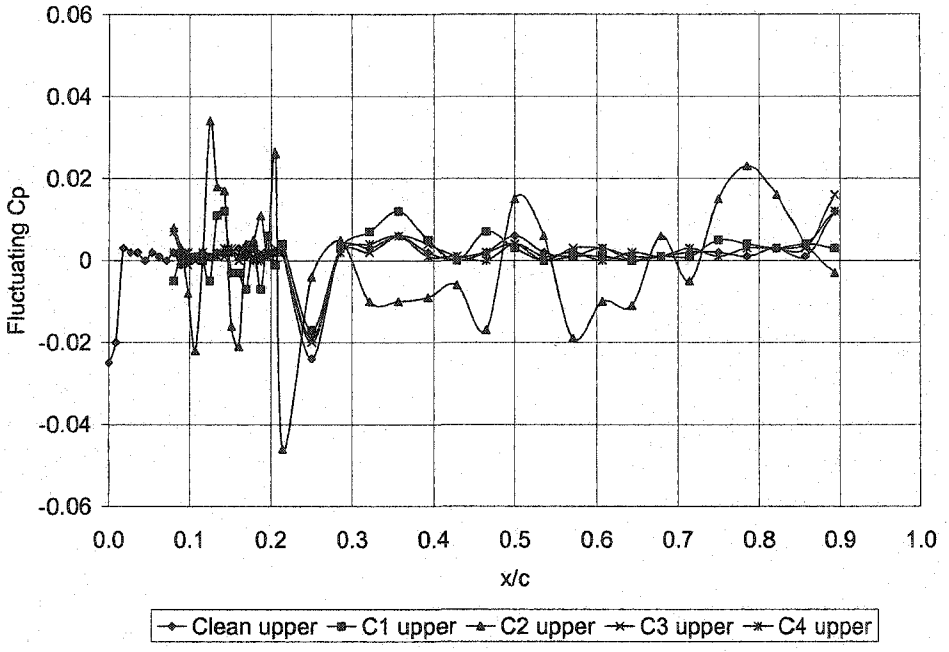

Figure 185 – Fluctuating Cp Dist., Re~1000000, α = 8 deg, Upper Surface

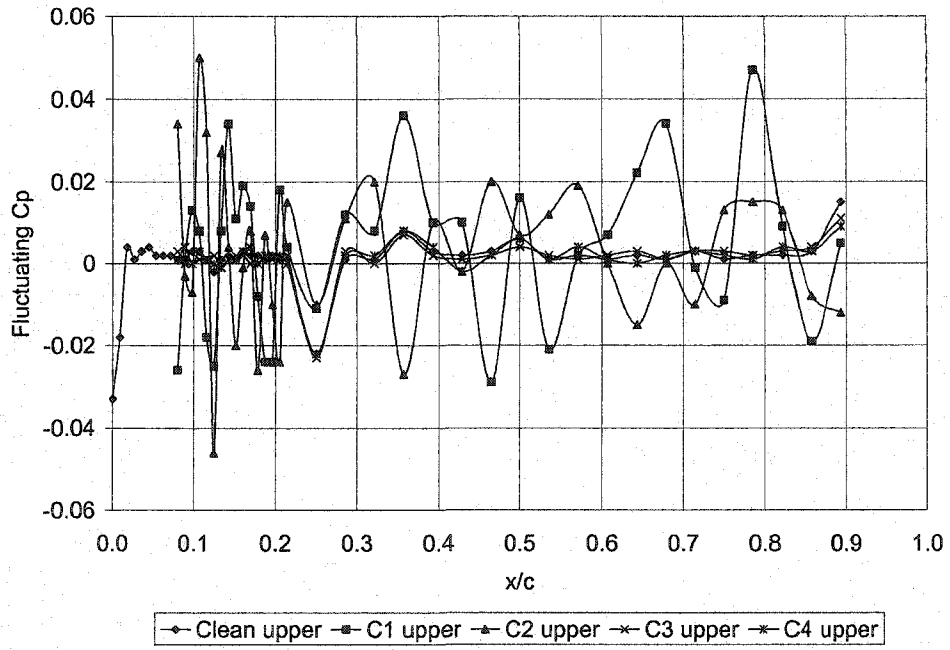

Figure 186 – Fluctuating Cp Dist., Re~1000000, α = 9 deg, Upper Surface

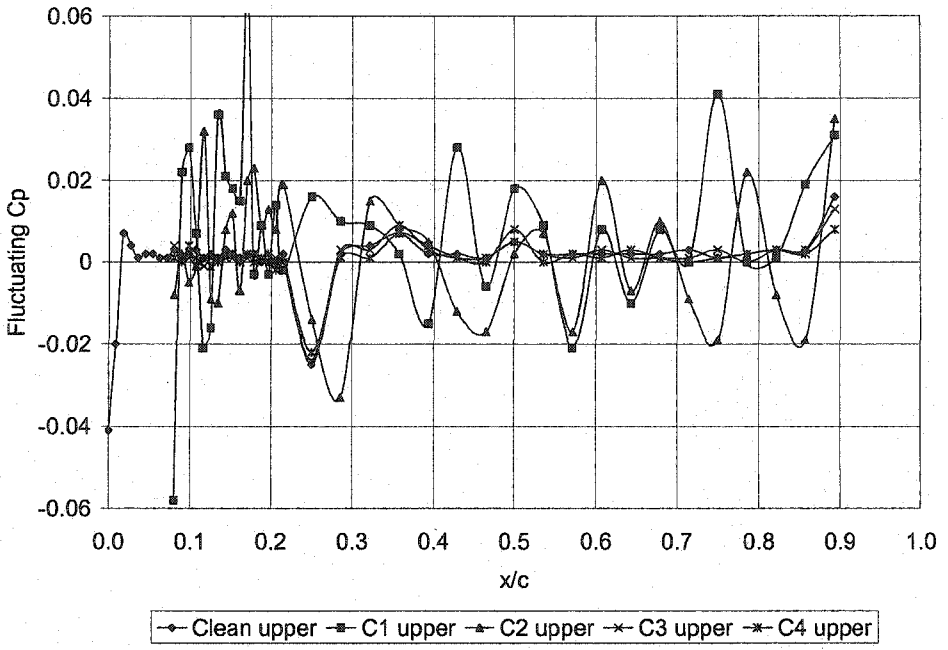

Figure 187 – Fluctuating Cp Dist., Re~1000000, α= 10 deg, Upper Surface

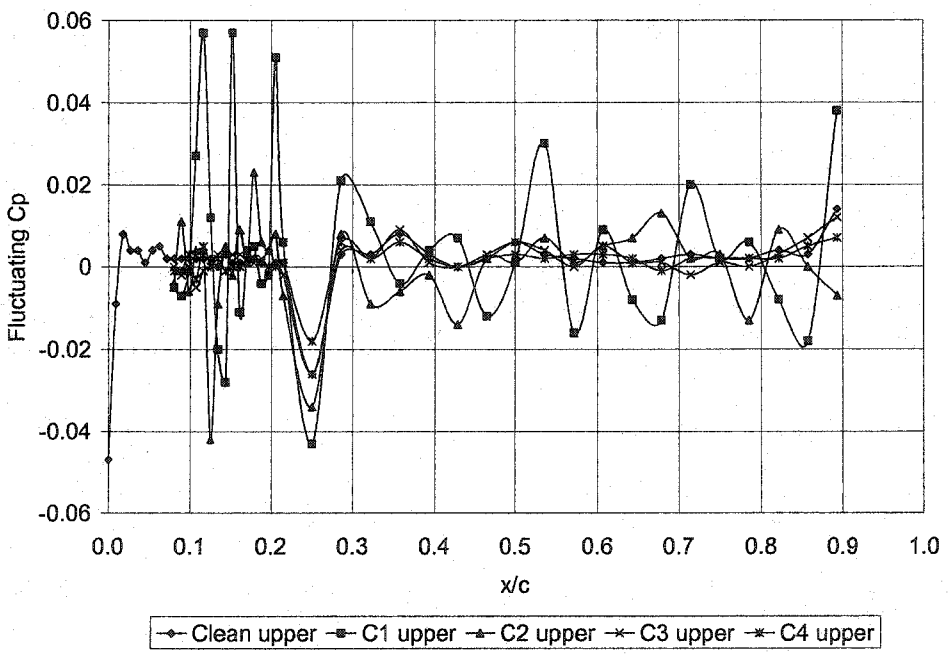

Figure 188 – Fluctuating Cp Dist., Re~1000000, α = 11 deg, Upper Surface

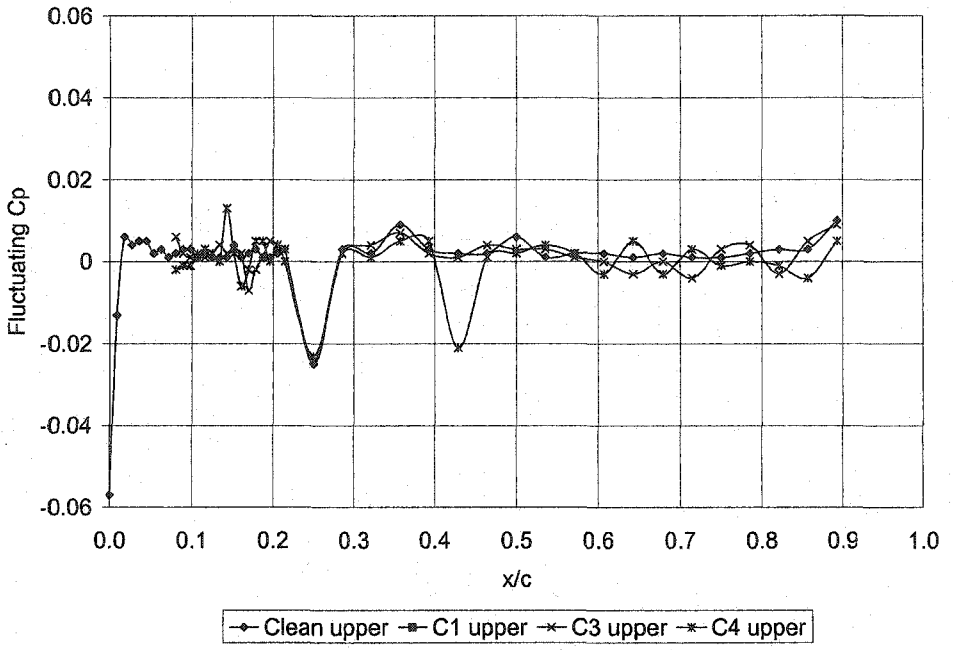

Figure 189 – Fluctuating Cp Dist., Re~1000000, α = 12 deg, Upper Surface

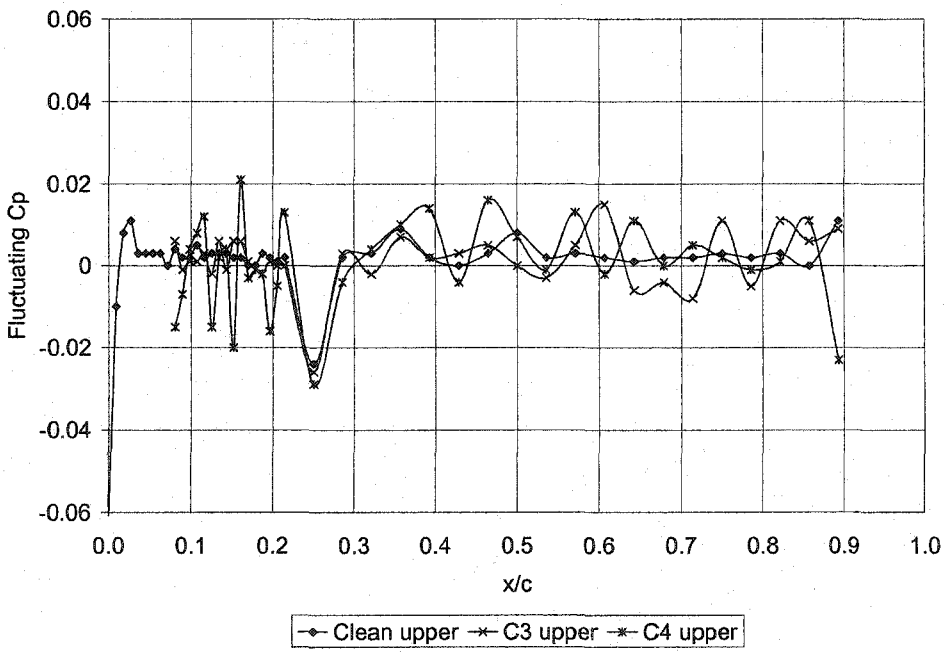

Figure 190 – Fluctuating Cp Dist., Re~1000000, α = 13 deg, Upper Surface

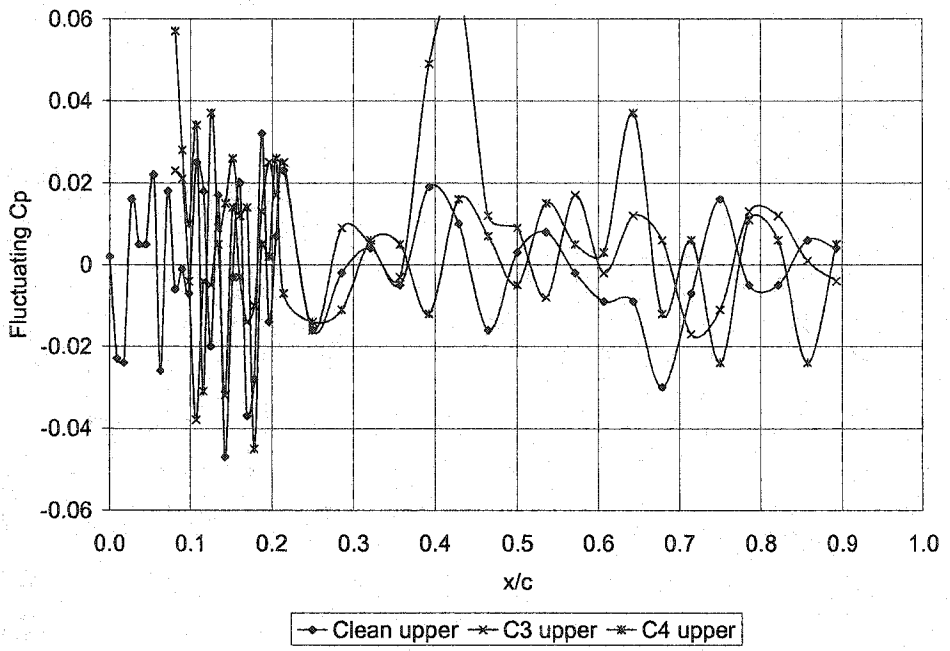

Figure 191 – Fluctuating Cp Dist., Re~1000000, α = 14 deg, Upper Surface

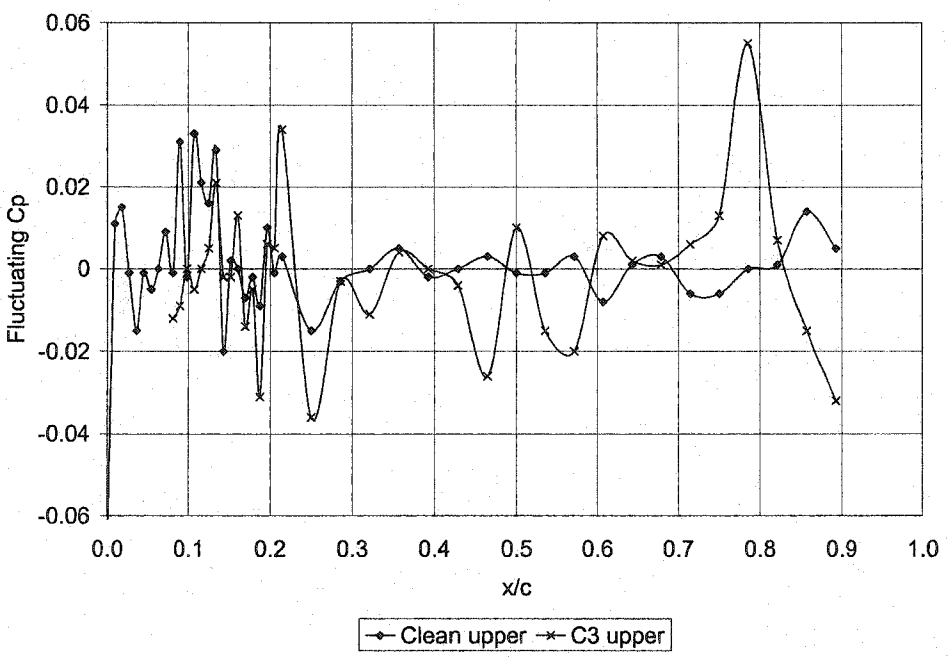

Figure 192 – Fluctuating Cp Dist., Re~1000000, α = 15 deg, Upper Surface

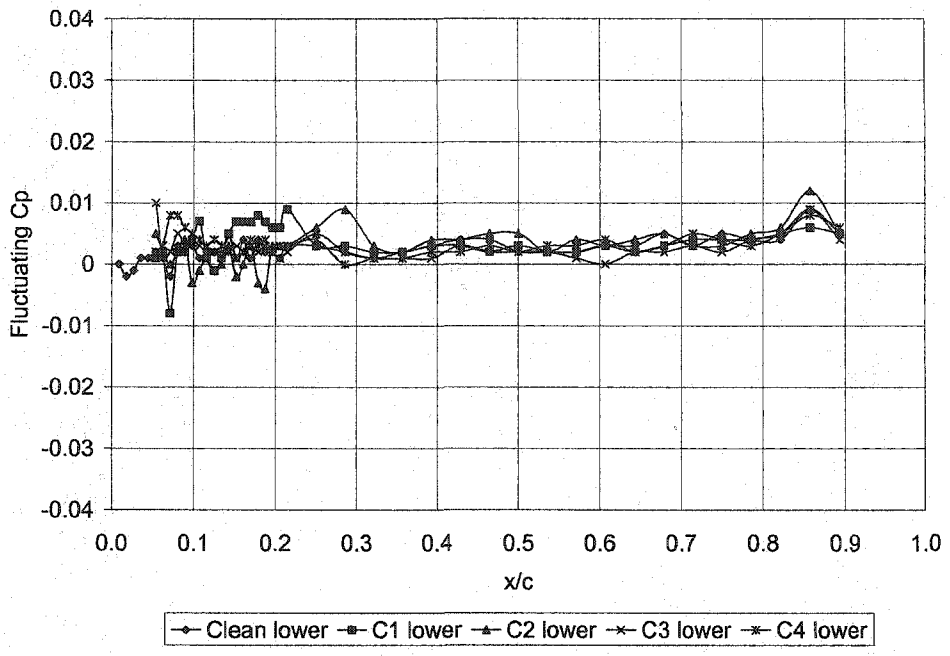

Figure 193 – Fluctuating Cp Dist., Re~1000000, α = 0 deg, Lower Surface

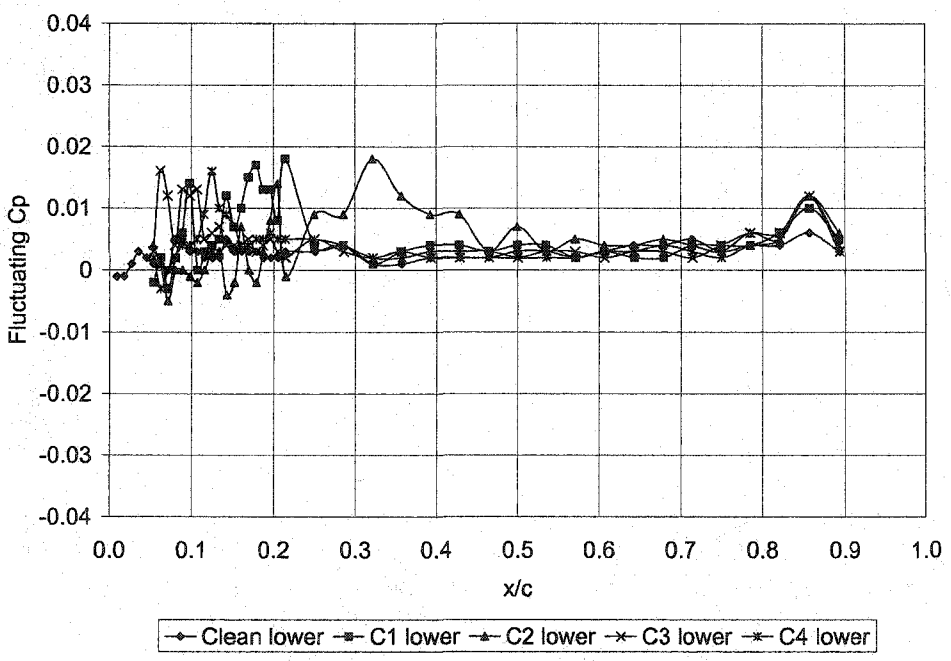

Figure 194 – Fluctuating Cp Dist., Re~1000000, α = 1 deg, Lower Surface

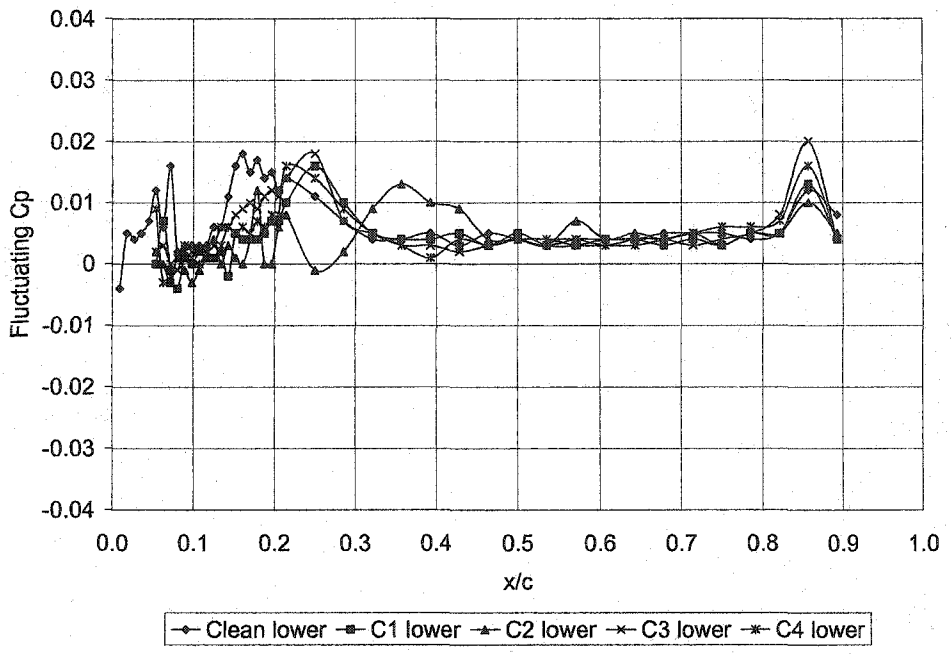

Figure 195 – Fluctuating Cp Dist., Re~1000000, α = 2 deg, Lower Surface

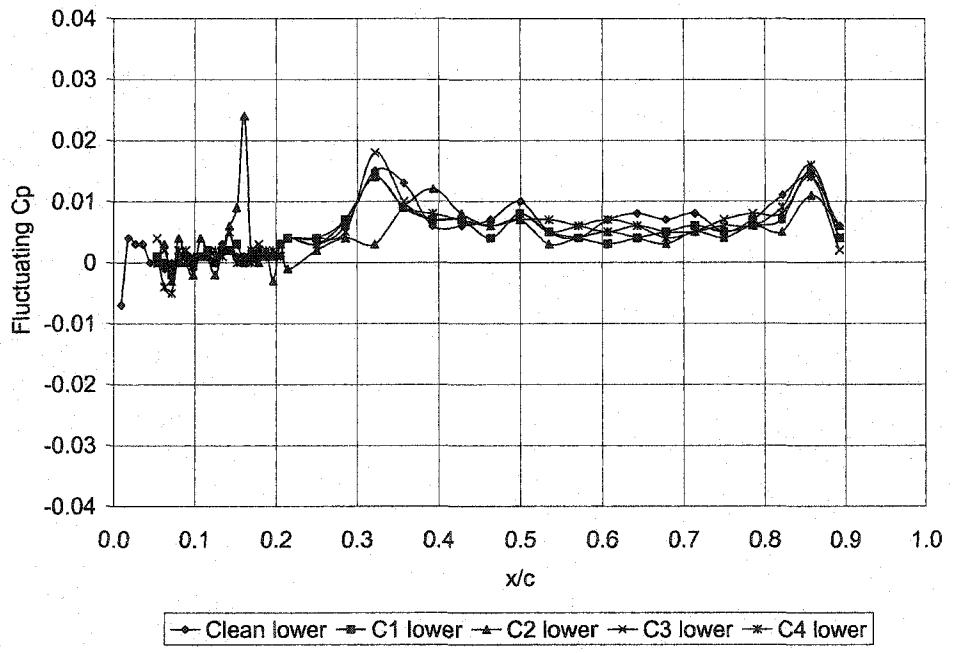

Figure 196 – Fluctuating Cp Dist., Re~1000000, α = 3 deg, Lower Surface

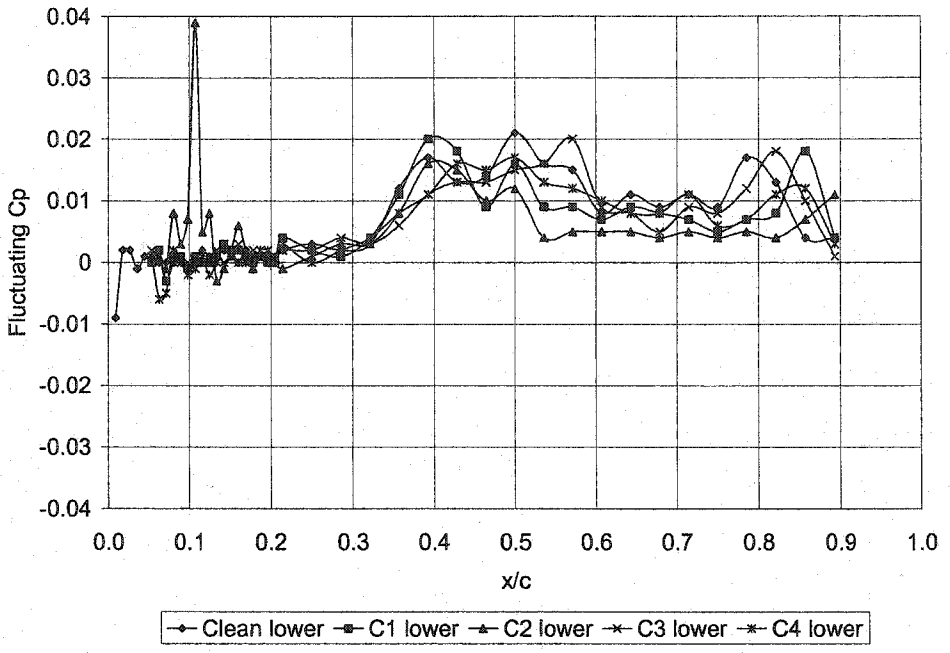

Figure 197 – Fluctuating Cp Dist., Re~1000000, α = 4 deg, Lower Surface

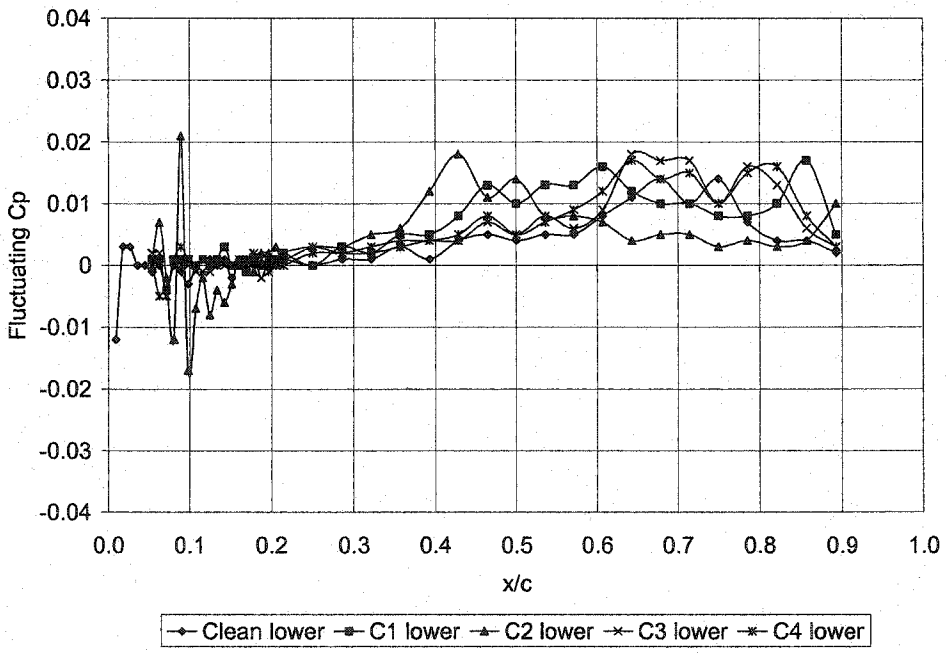

Figure 198 – Fluctuating Cp Dist., Re~1000000, α = 5 deg, Lower Surface

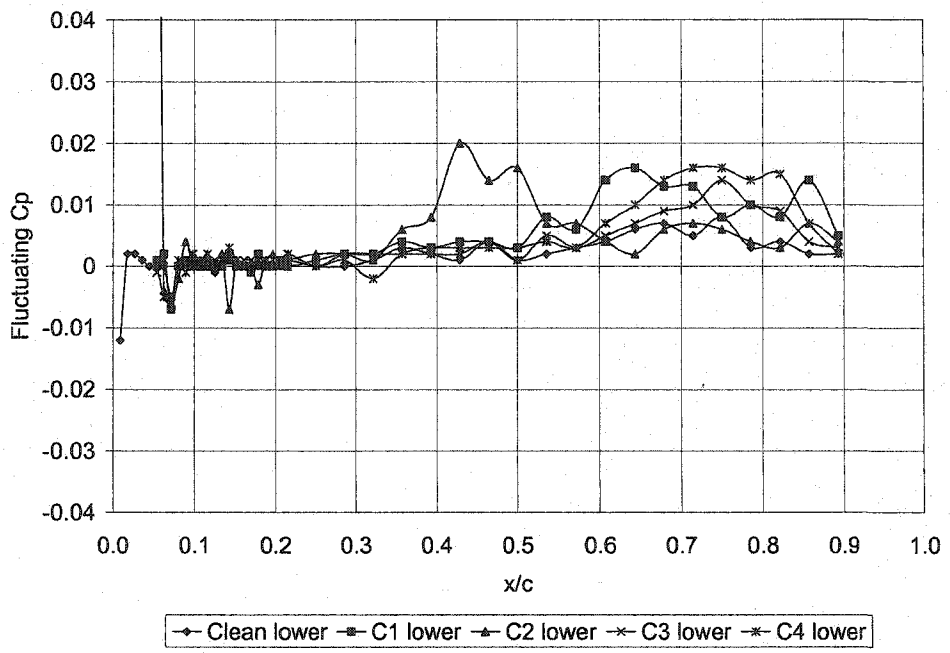

Figure 199 – Fluctuating Cp Dist., Re~1000000, α = 6 deg, Lower Surface

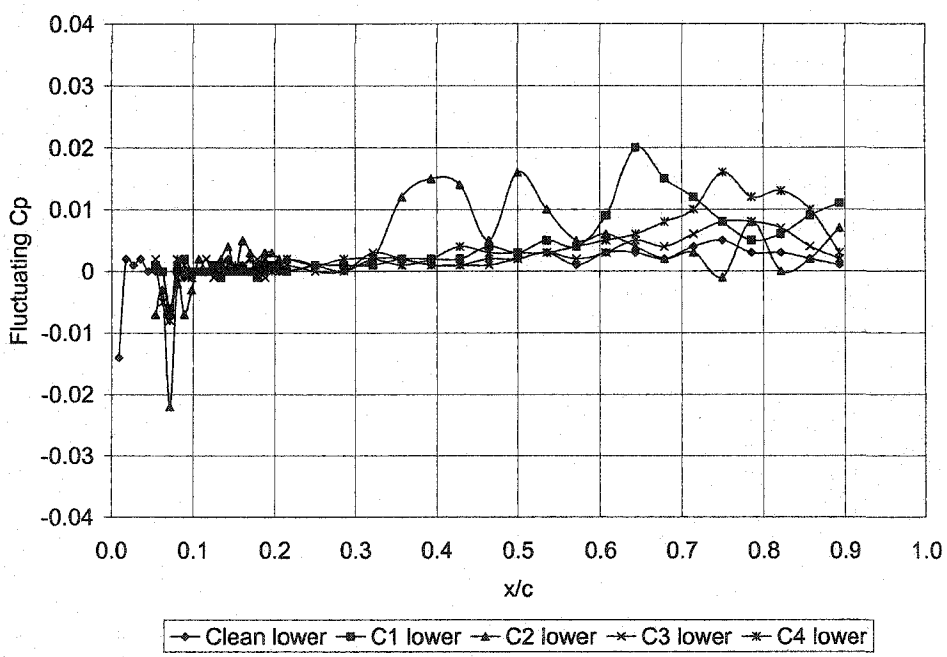

Figure 200 – Fluctuating Cp Dist., Re~1000000, α = 7 deg, Lower Surface

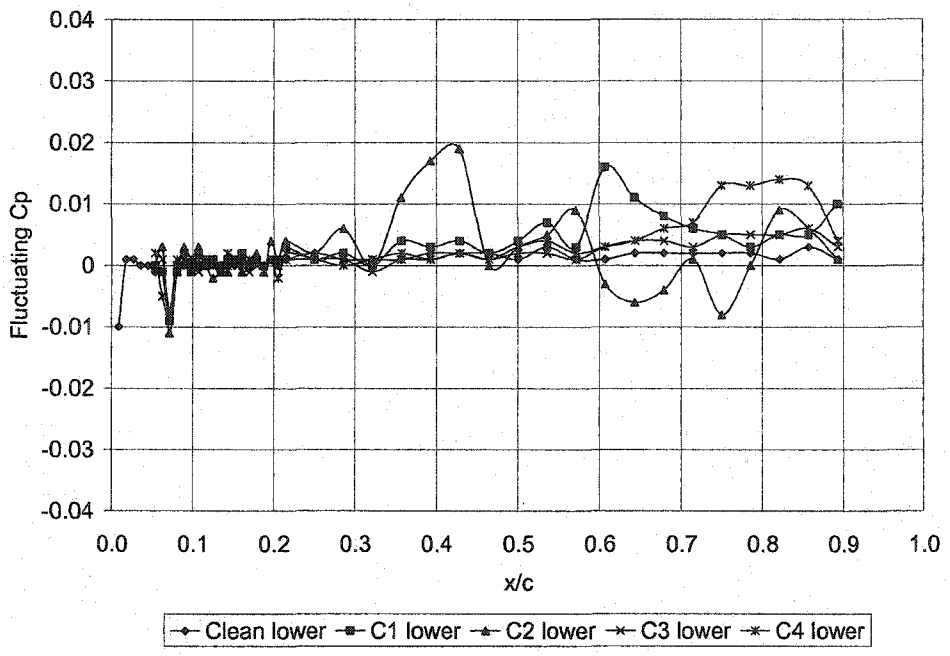

Figure 201 – Fluctuating Cp Dist., Re~1000000, α = 8 deg, Lower Surface

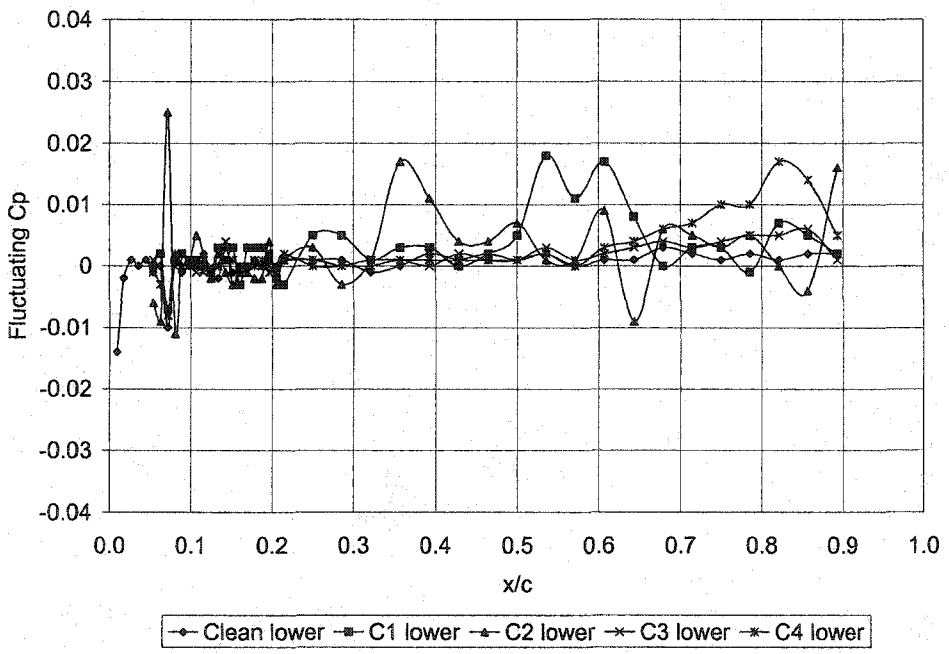

Figure 202 – Fluctuating Cp Dist., Re~1000000, α = 9 deg, Lower Surface

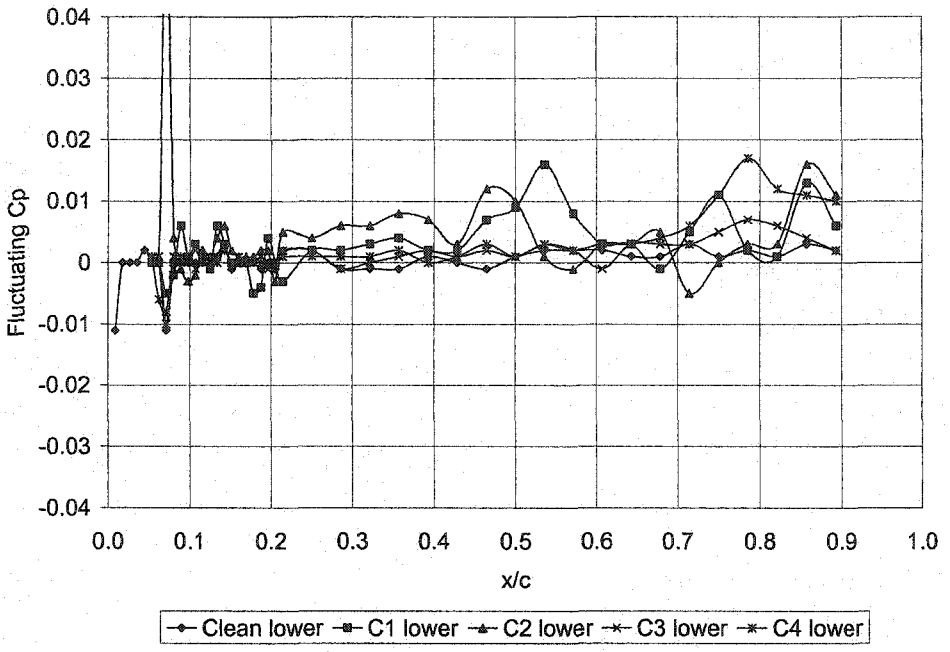

Figure 203 – Fluctuating Cp Dist., Re~1000000, α = 10 deg, Lower Surface

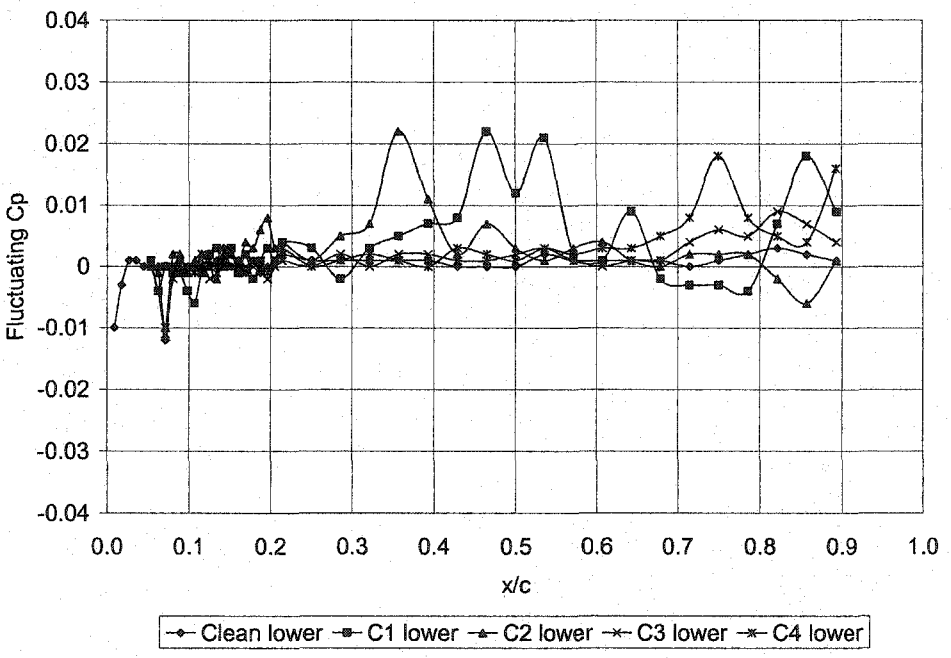

Figure 204 – Fluctuating Cp Dist., Re~1000000, α = 11 deg, Lower Surface

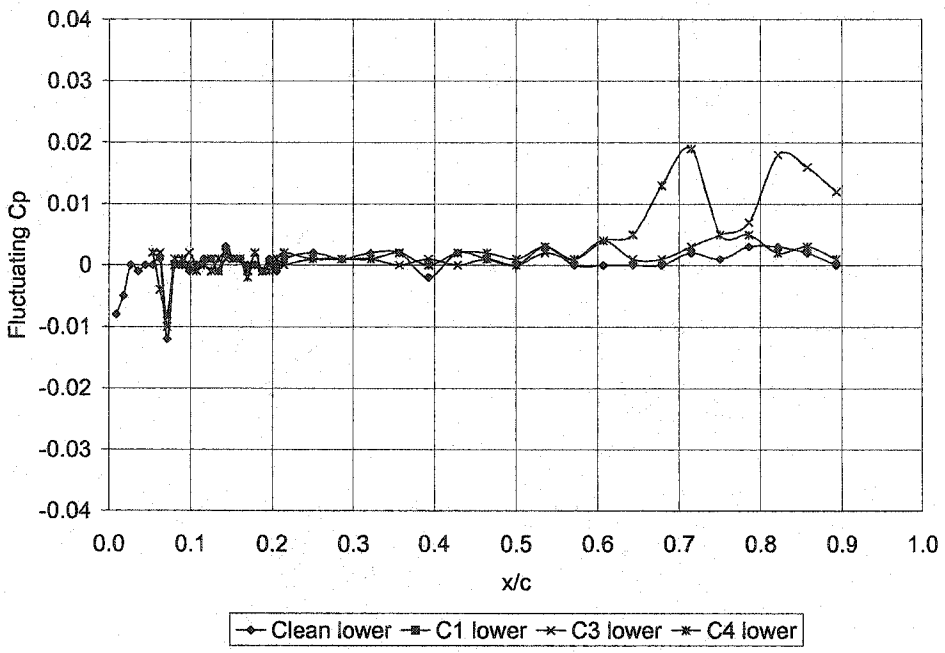

Figure 205 – Fluctuating Cp Dist., Re~1000000, α = 12 deg, Lower Surface

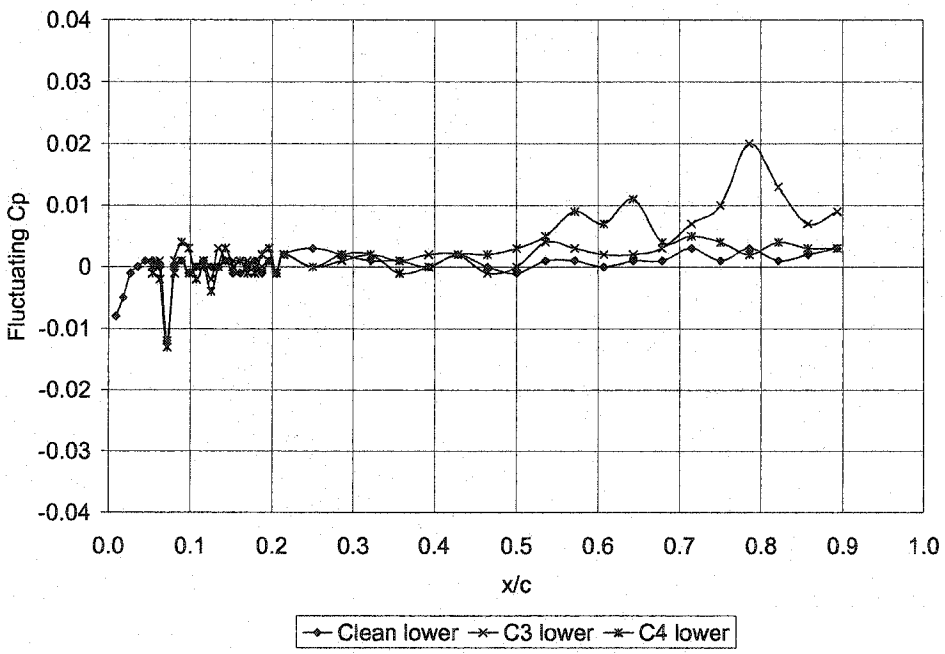

Figure 206 – Fluctuating Cp Dist., Re~1000000, α = 13 deg, Lower Surface

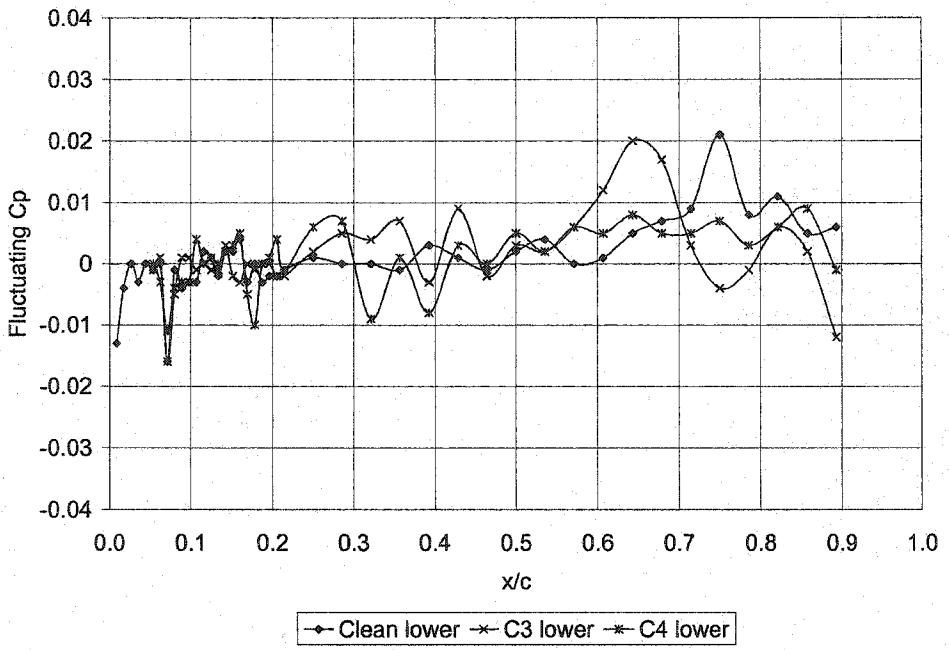

Figure 207 – Fluctuating Cp Dist., Re~1000000, α = 14 deg, Lower Surface

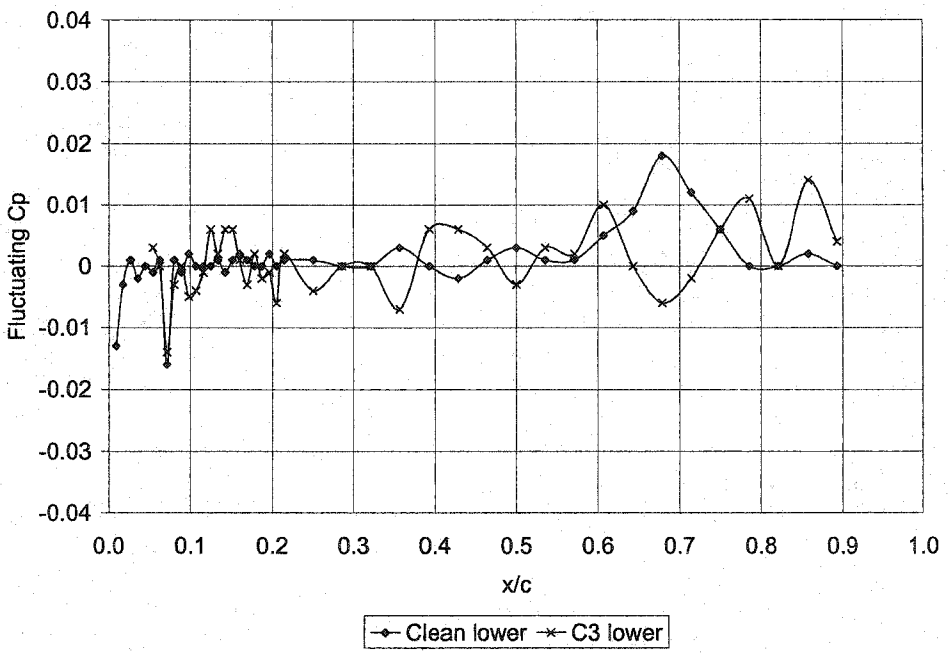

Figure 208 – Fluctuating Cp Dist., Re~1000000, α = 15 deg, Lower Surface

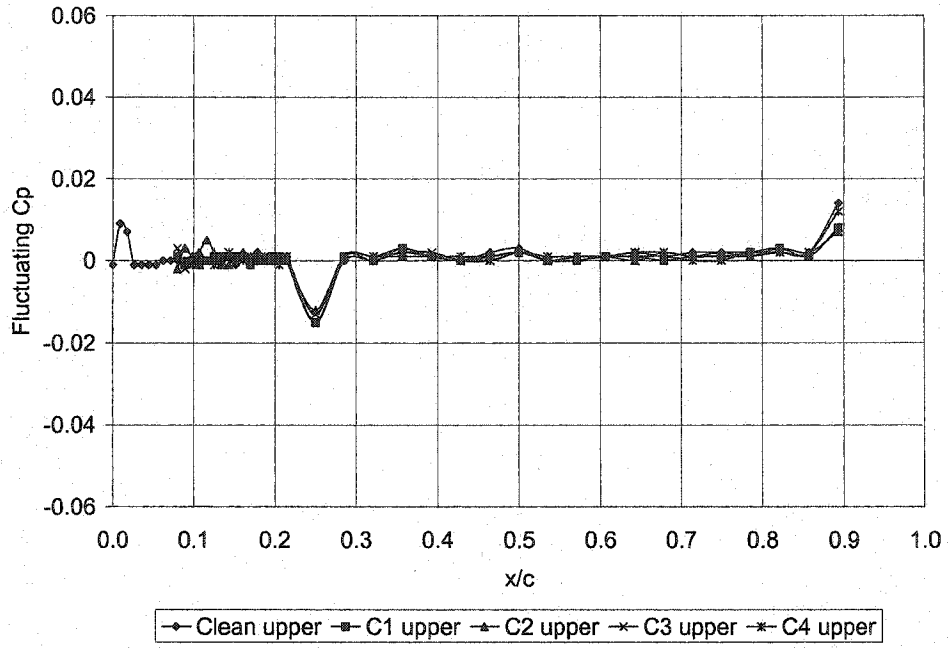

Figure 209 – Fluctuating Cp Dist., Re~1300000, α = 0 deg, Upper Surface

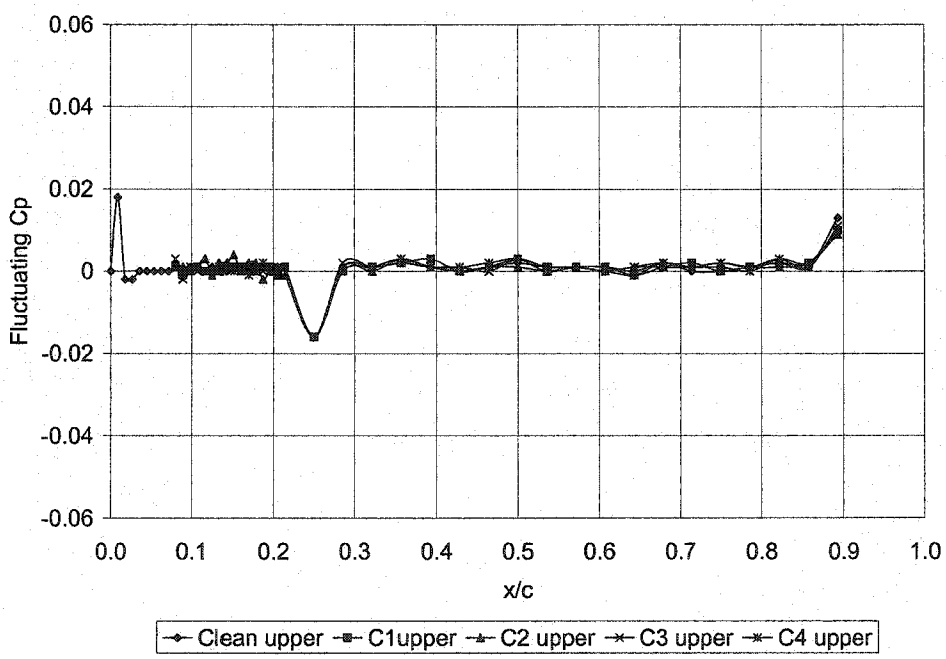

Figure 210 – Fluctuating Cp Dist., Re~1300000, α = 1 deg, Upper Surface

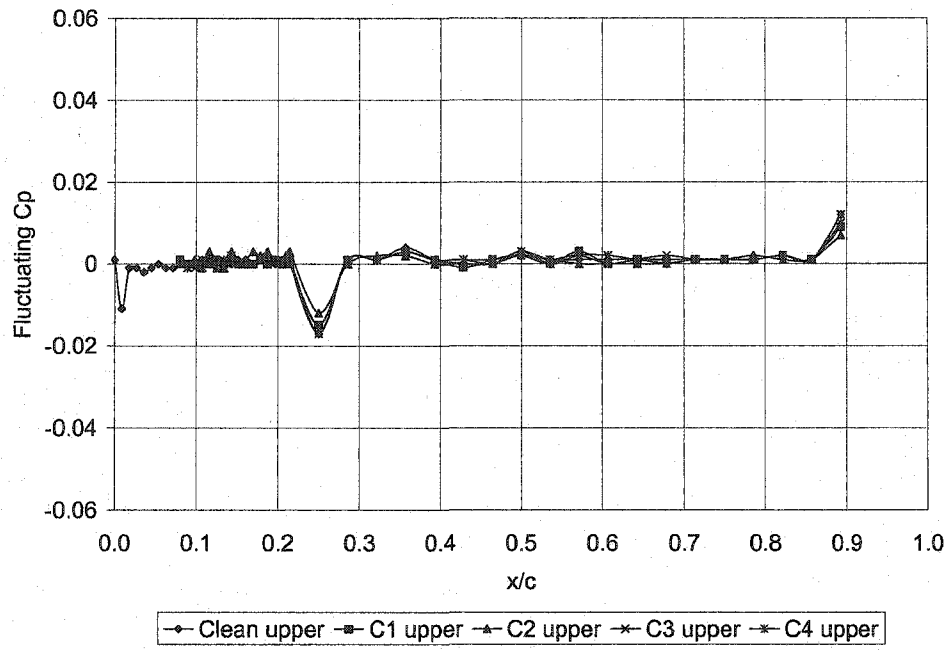

Figure 211 – Fluctuating Cp Dist., Re~1300000, α = 2 deg, Upper Surface

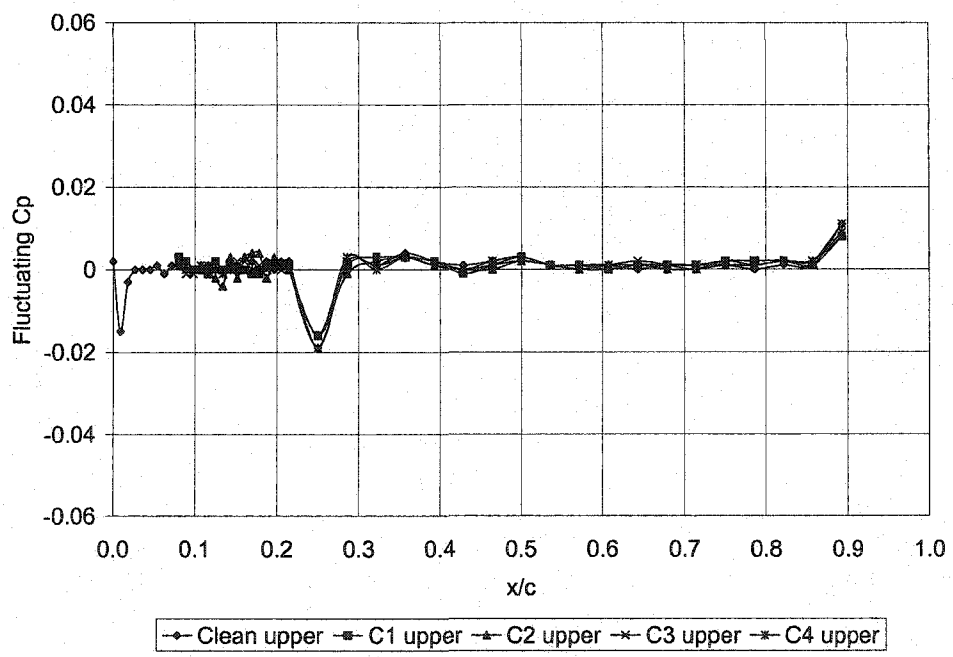

Figure 212 – Fluctuating Cp Dist., Re~1300000, α = 3 deg, Upper Surface

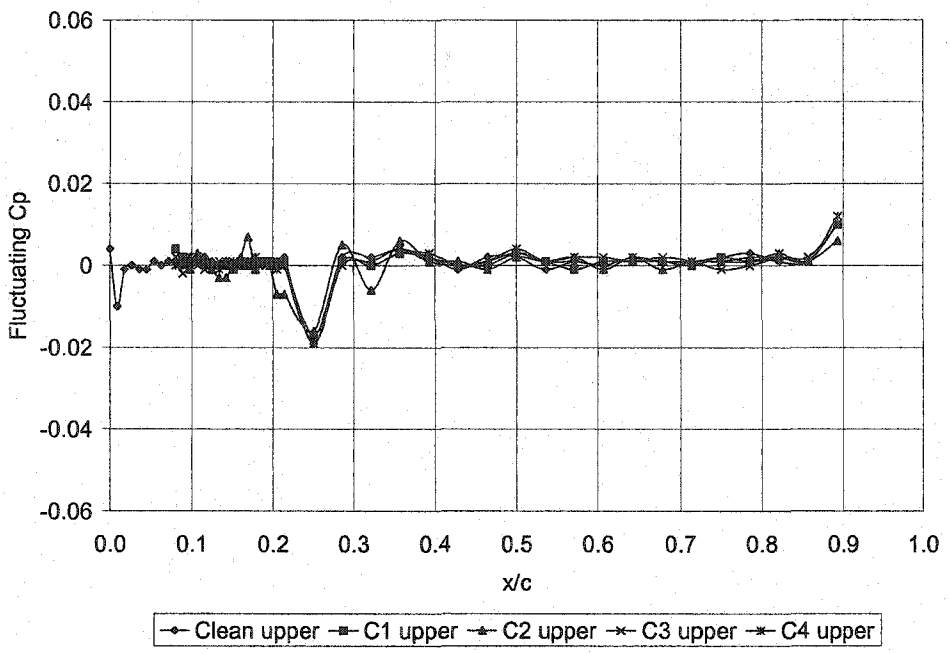

Figure 213 – Fluctuating Cp Dist., Re~1300000, α = 4 deg, Upper Surface

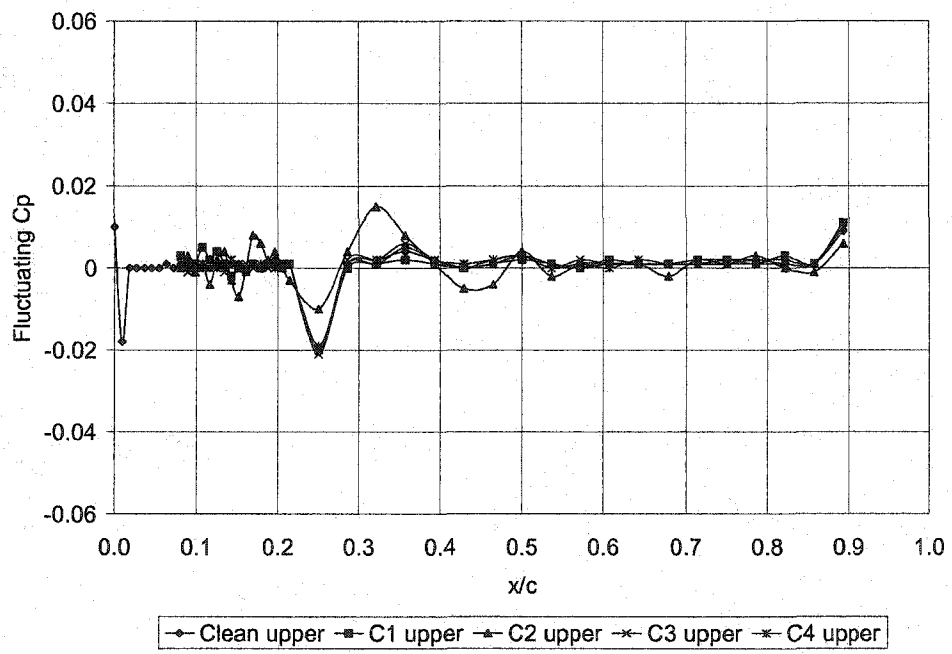

Figure 214 – Fluctuating Cp Dist., Re~1300000, α = 5 deg, Upper Surface

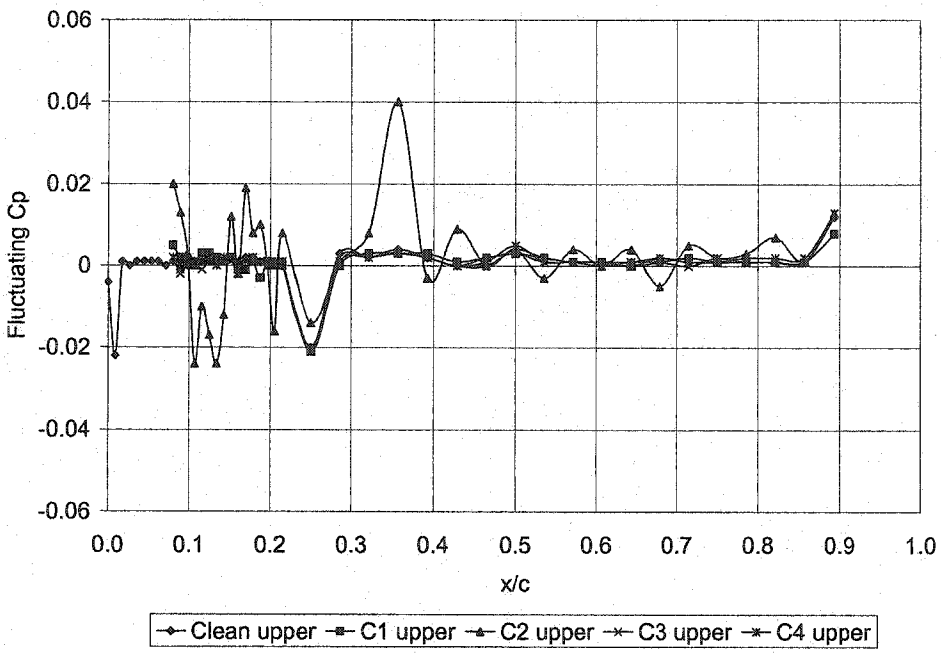

Figure 215 – Fluctuating Cp Dist., Re~1300000, α = 6 deg, Upper Surface

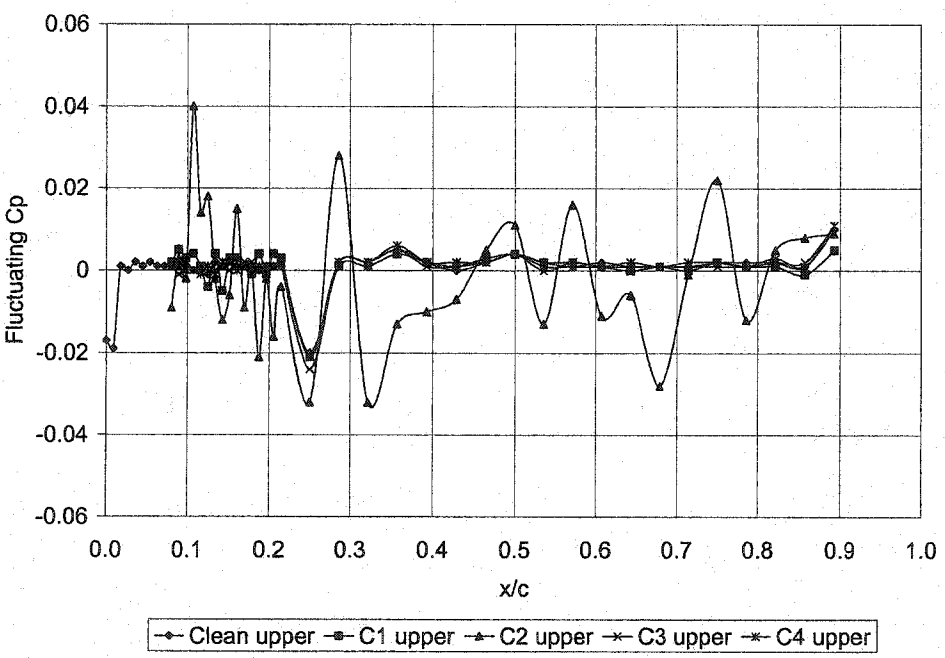

Figure 216 – Fluctuating Cp Dist., Re~1300000, α = 7 deg, Upper Surface

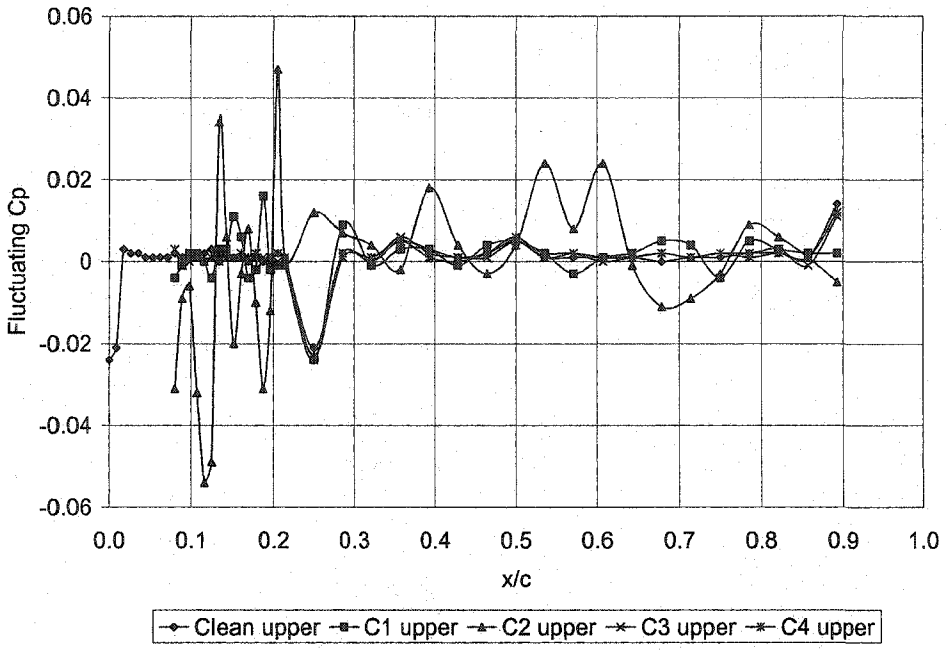

Figure 217 – Fluctuating Cp Dist., Re~1300000, α = 8 deg, Upper Surface

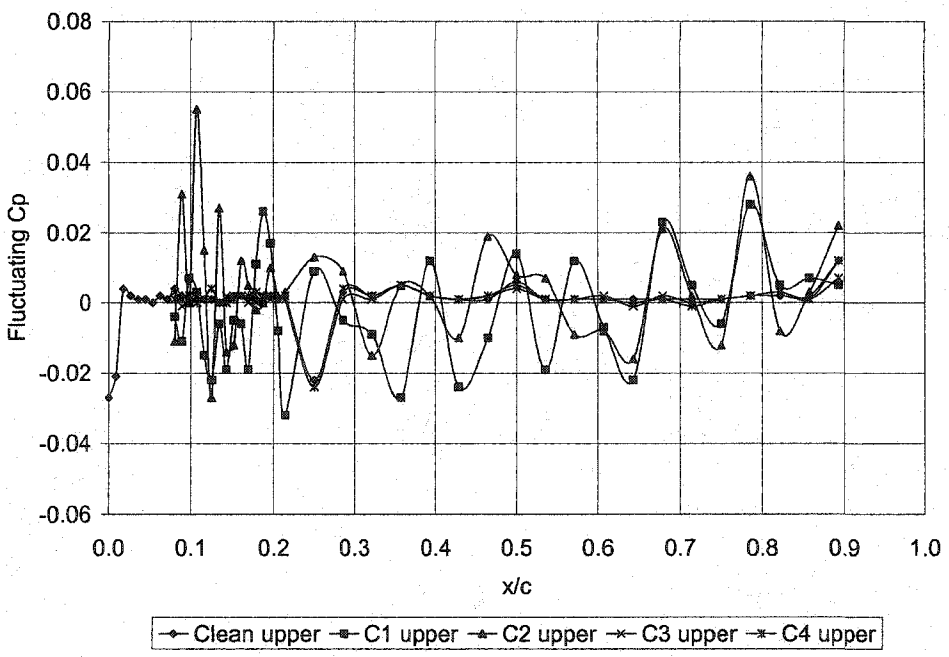

Figure 218 – Fluctuating Cp Dist., Re~1300000, α = 9 deg, Upper Surface

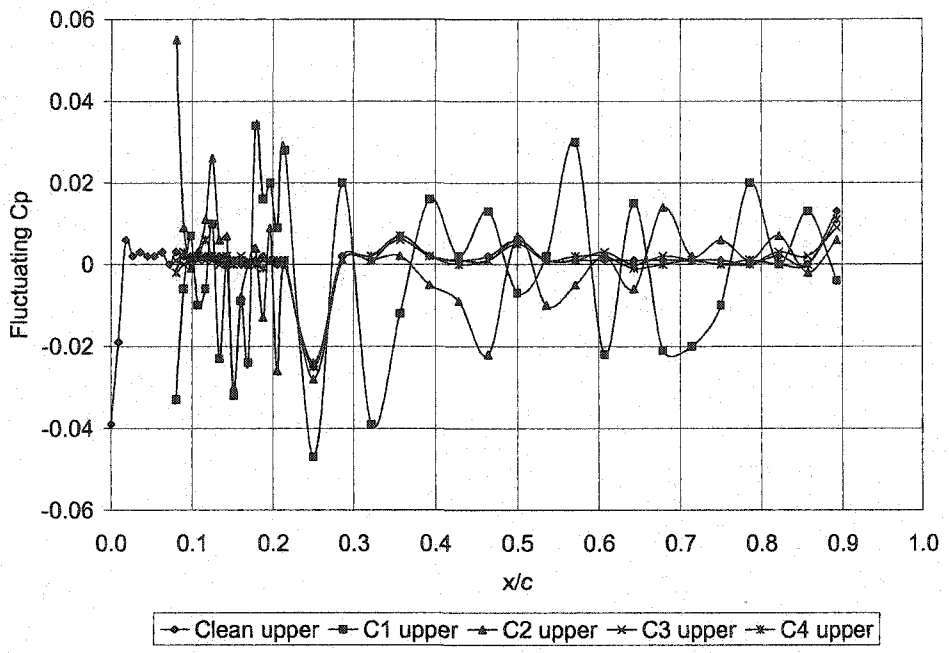

Figure 219 – Fluctuating Cp Dist., Re~1300000, α = 10 deg, Upper Surface

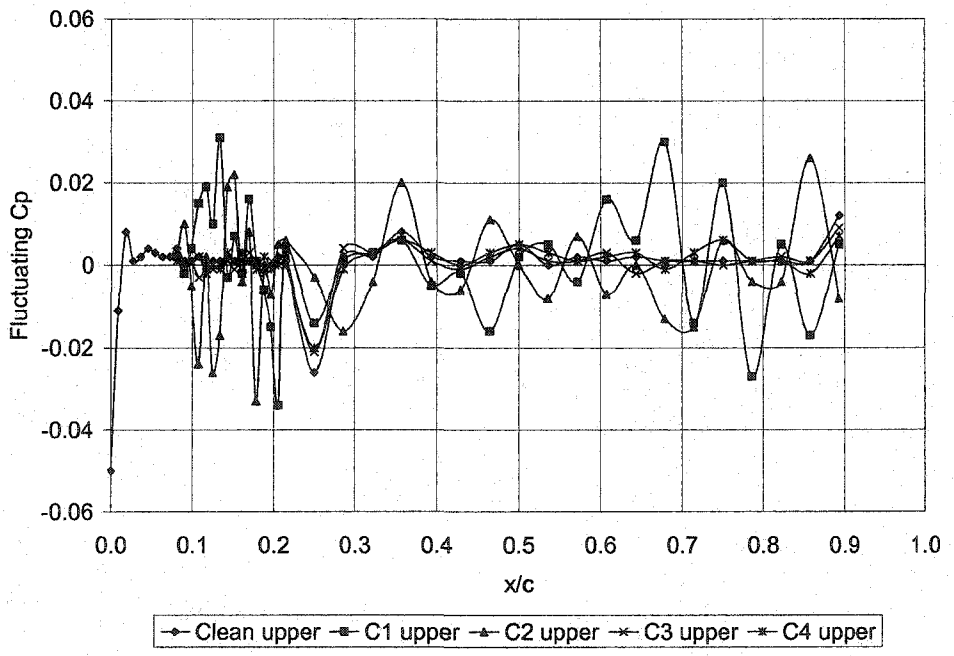

Figure 220 – Fluctuating Cp Dist., Re~1300000, α = 11 deg, Upper Surface

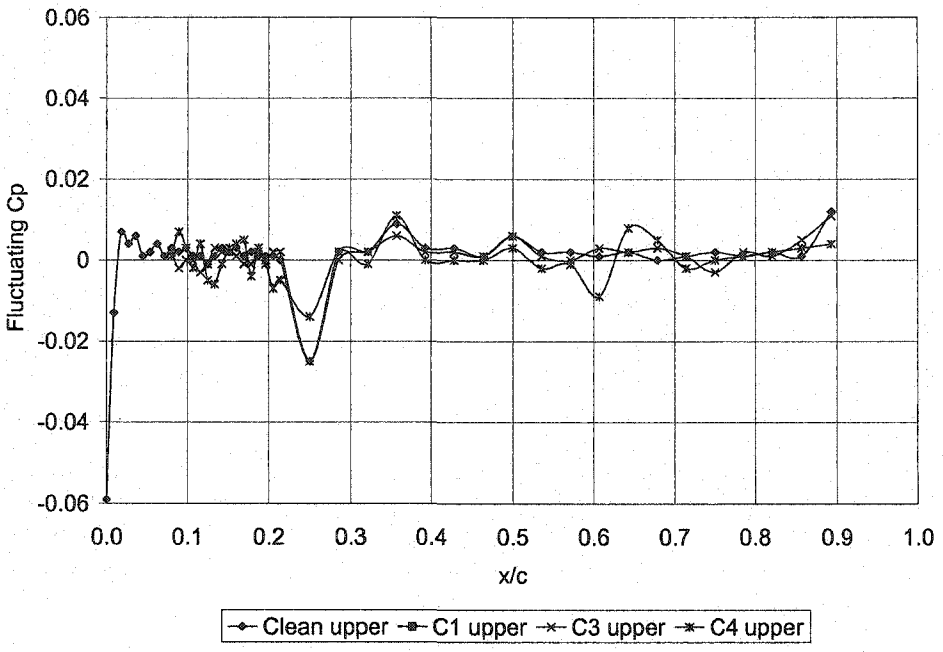

Figure 221 – Fluctuating Cp Dist., Re~1300000, α = 12 deg, Upper Surface

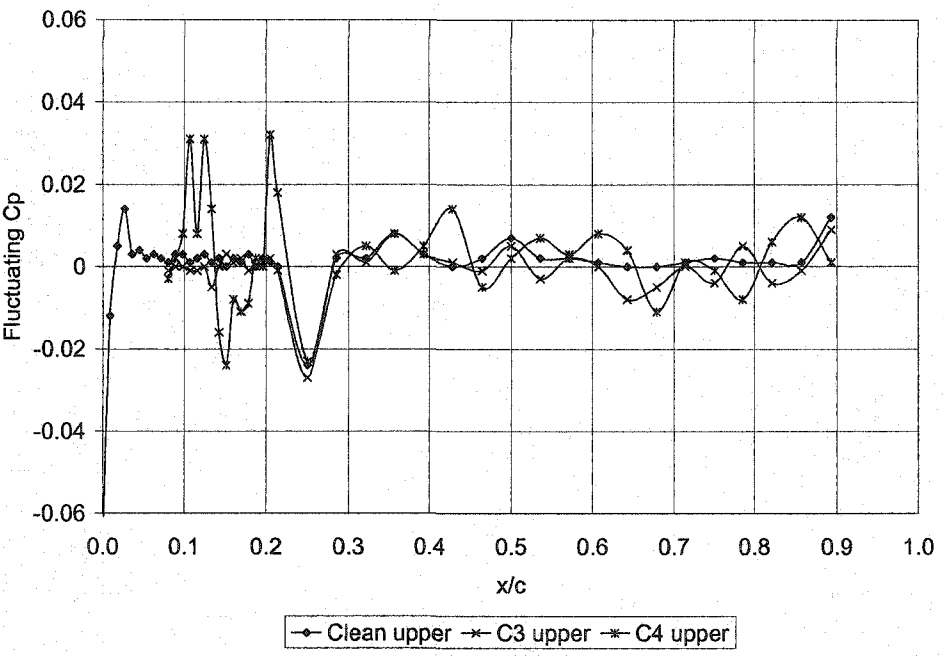

Figure 222 – Fluctuating Cp Dist., Re~1300000, α = 13 deg, Upper Surface

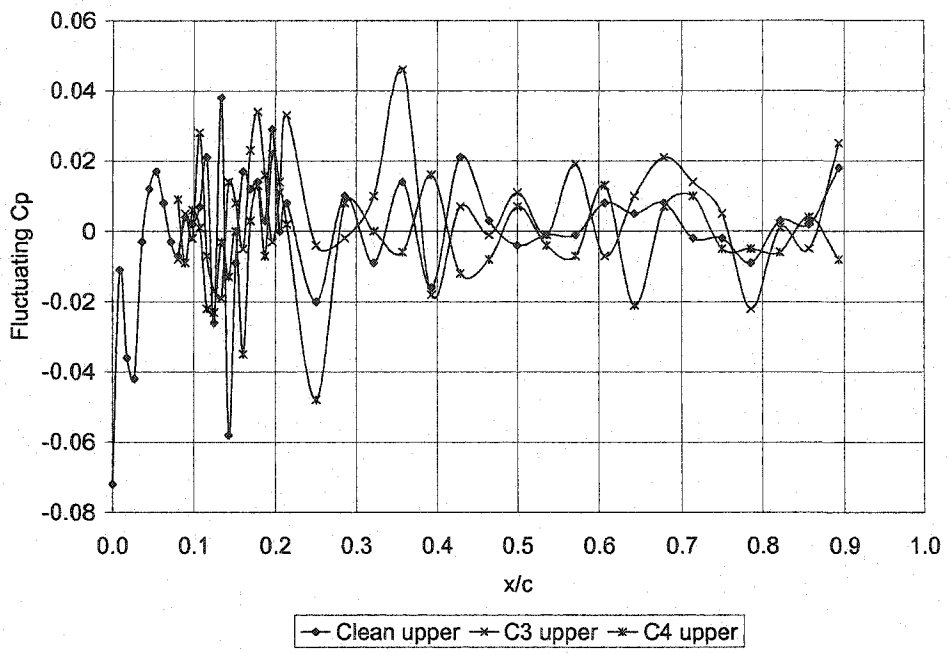

Figure 223 – Fluctuating Cp Dist., Re~1300000, α = 14 deg, Upper Surface

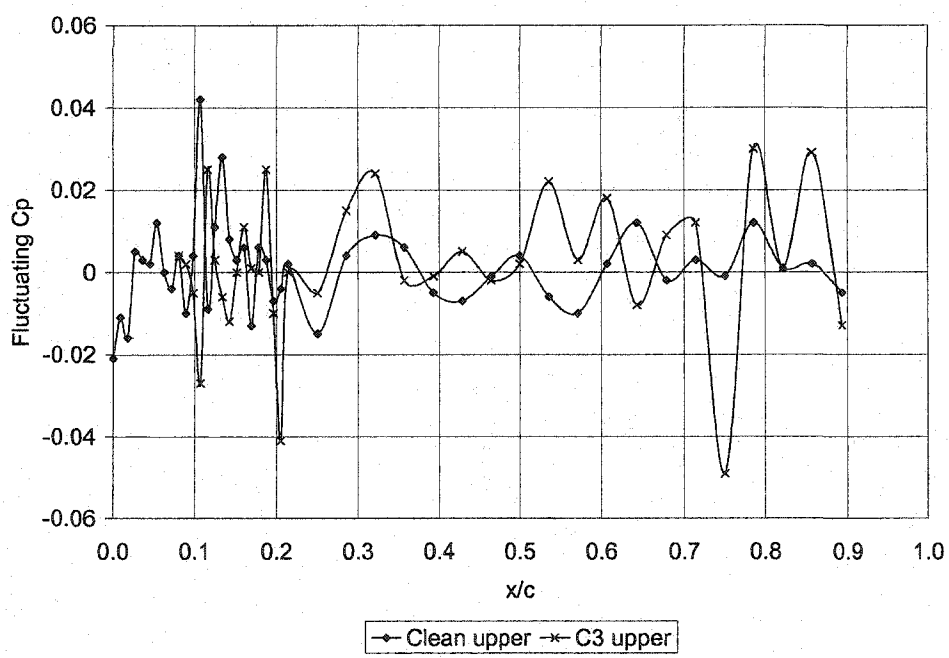

Figure 224 – Fluctuating Cp Dist., Re~1300000, α = 15 deg, Upper Surface

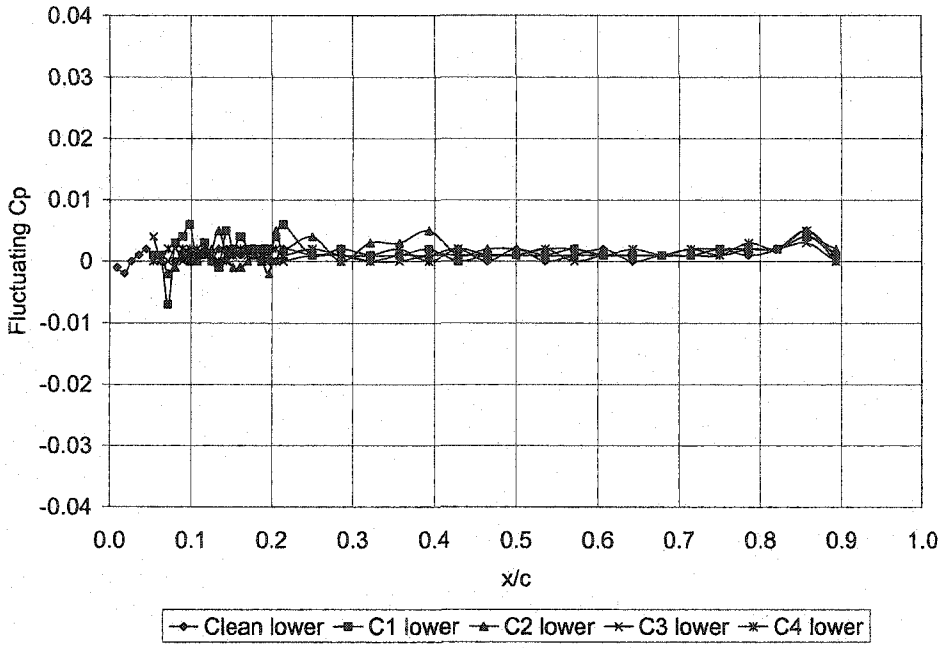

Figure 225 – Fluctuating Cp Dist., Re~1300000, α = 0 deg, Lower Surface

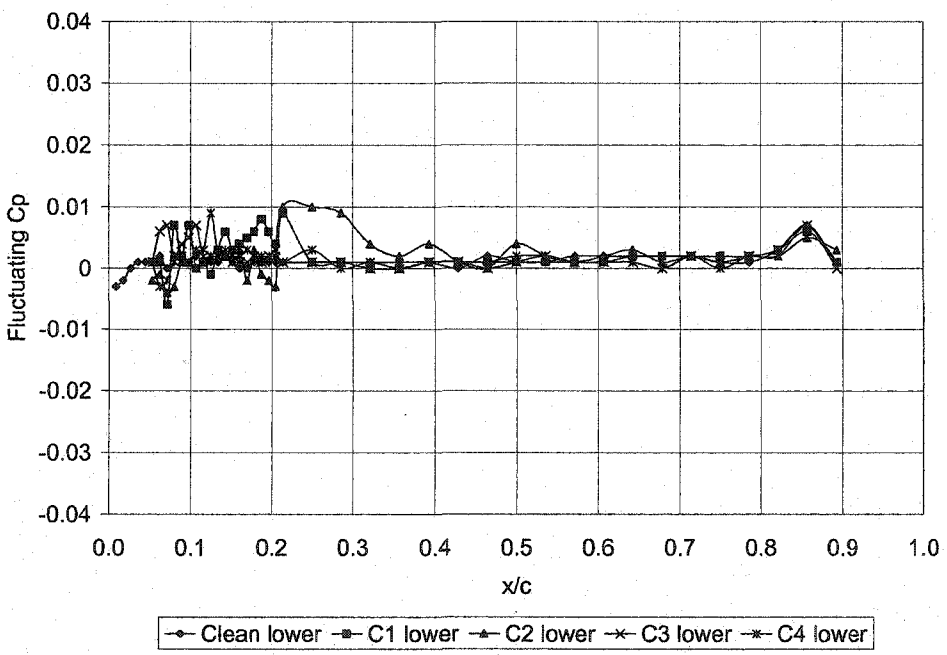

Figure 226 – Fluctuating Cp Dist., Re~1300000, α = 1 deg, Lower Surface

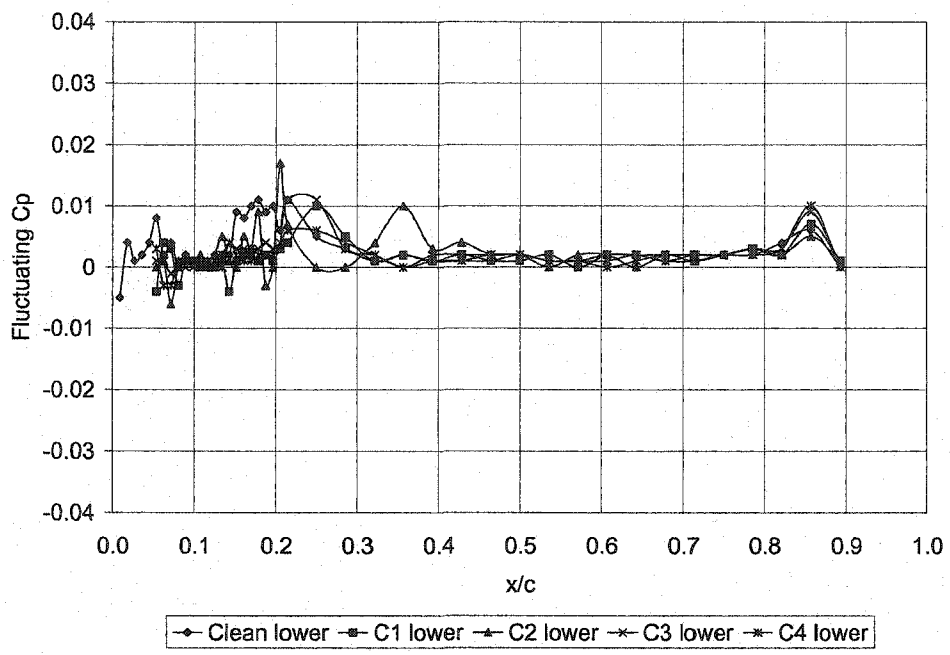

Figure 227 – Fluctuating Cp Dist., Re~1300000, α = 2 deg, Lower Surface

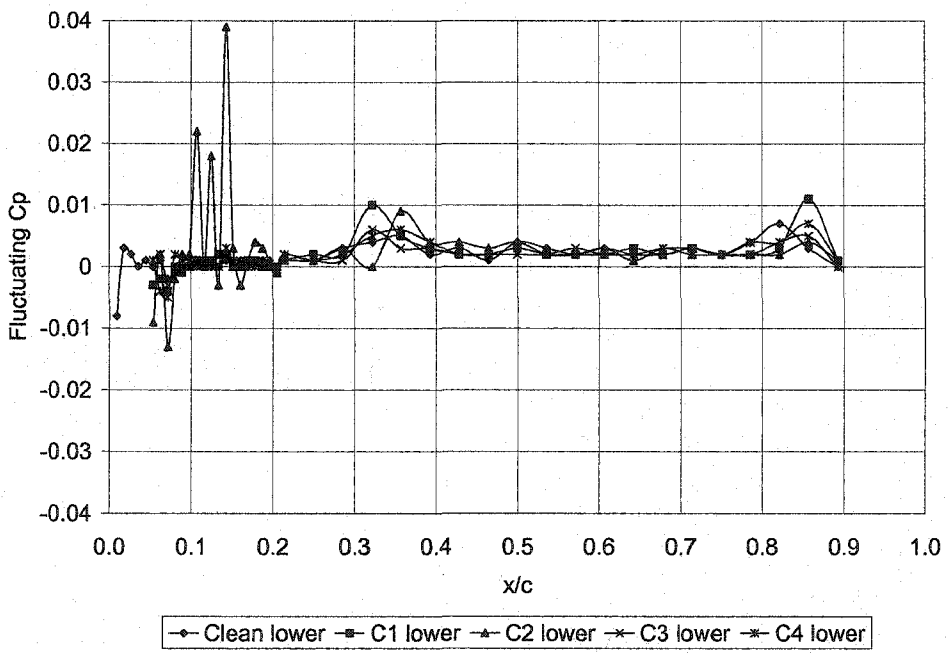

Figure 228 – Fluctuating Cp Dist., Re~1300000, α = 3 deg, Lower Surface

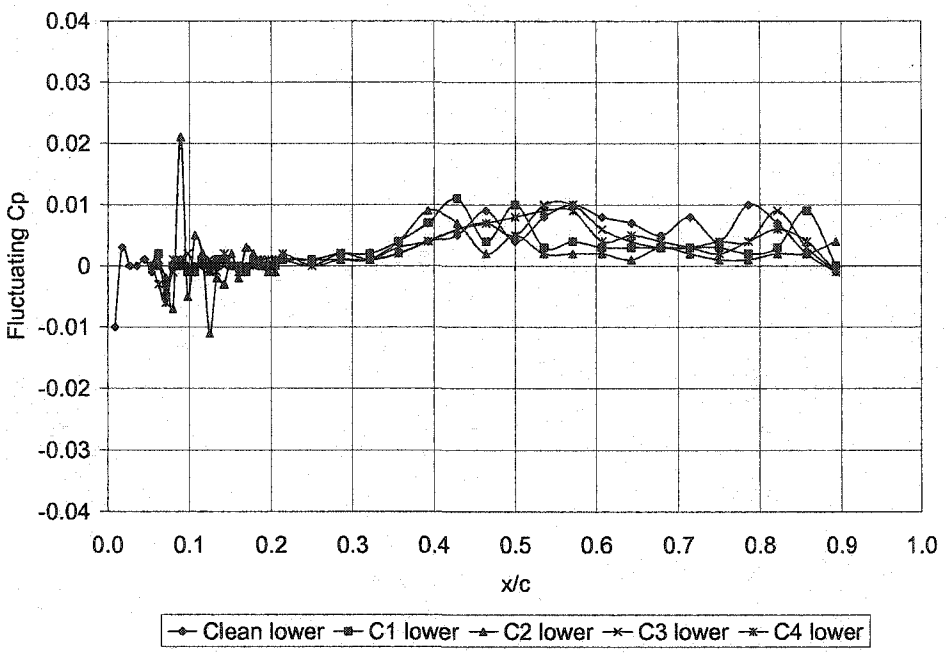

Figure 229 – Fluctuating Cp Dist., Re~1300000, α = 4 deg, Lower Surface

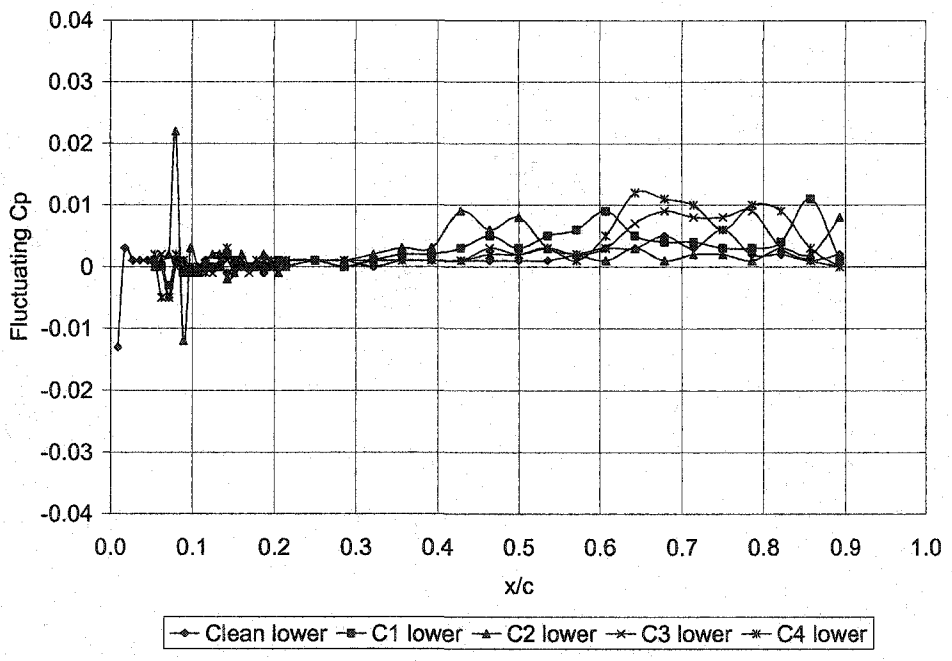

Figure 230 – Fluctuating Cp Dist., Re~1300000, α = 5 deg, Lower Surface

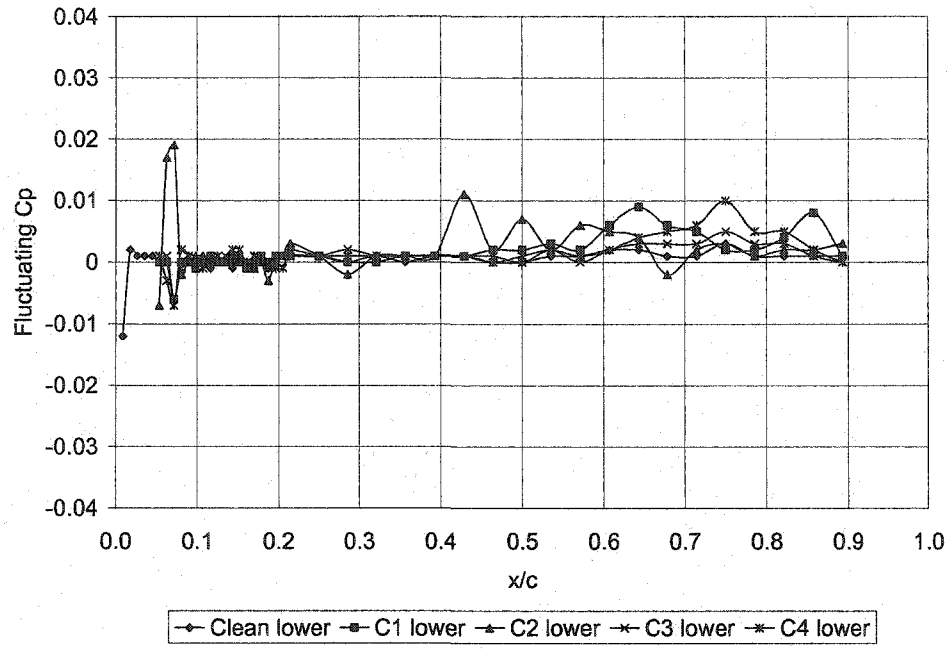

Figure 231 – Fluctuating Cp Dist., Re~1300000, α = 6 deg, Lower Surface

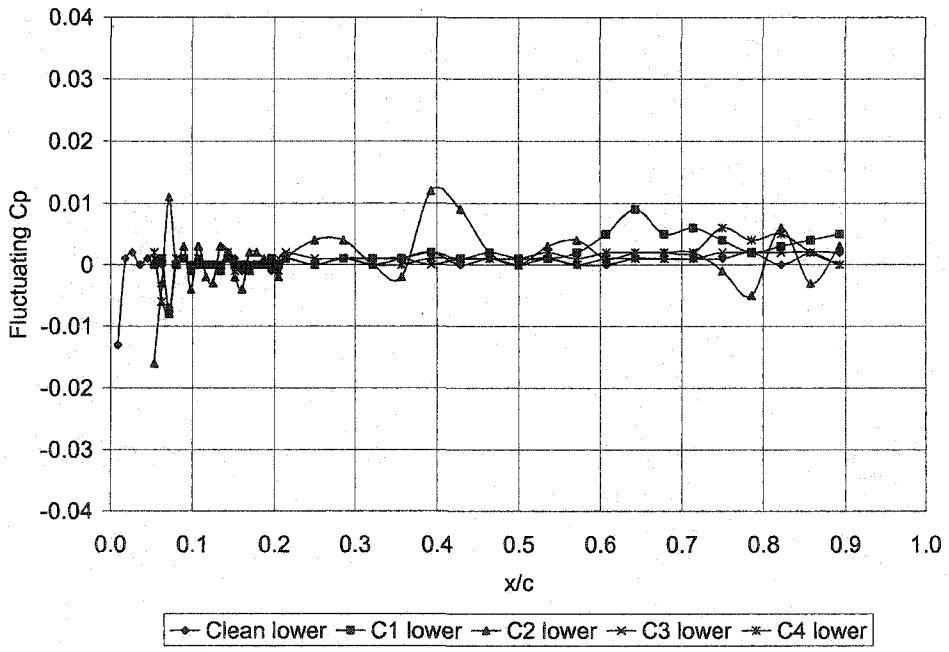

Figure 232 – Fluctuating Cp Dist., Re~1300000, α = 7 deg, Lower Surface

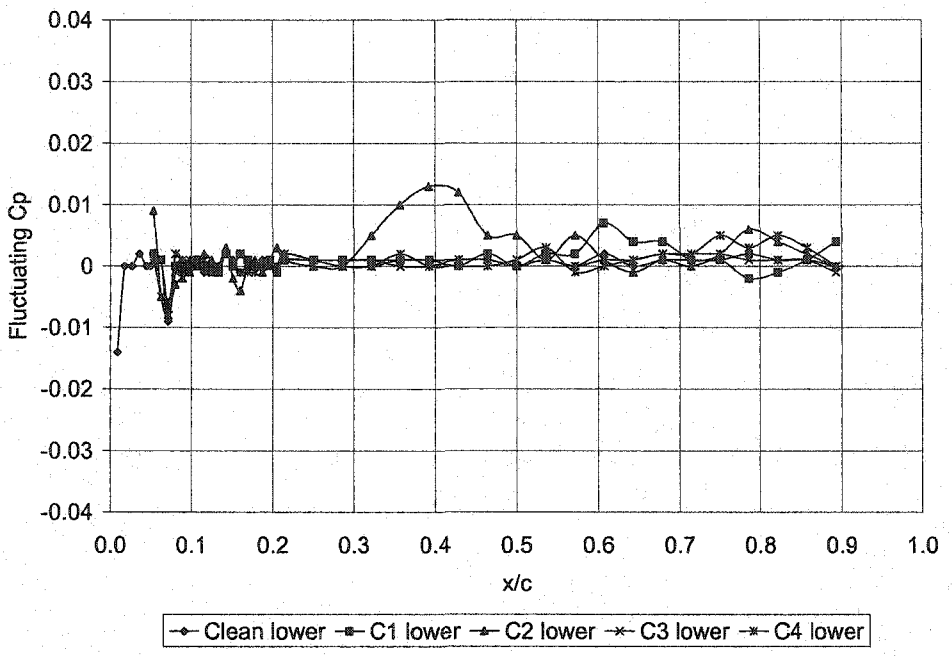

Figure 233 – Fluctuating Cp Dist., Re~1300000, α = 8 deg, Lower Surface

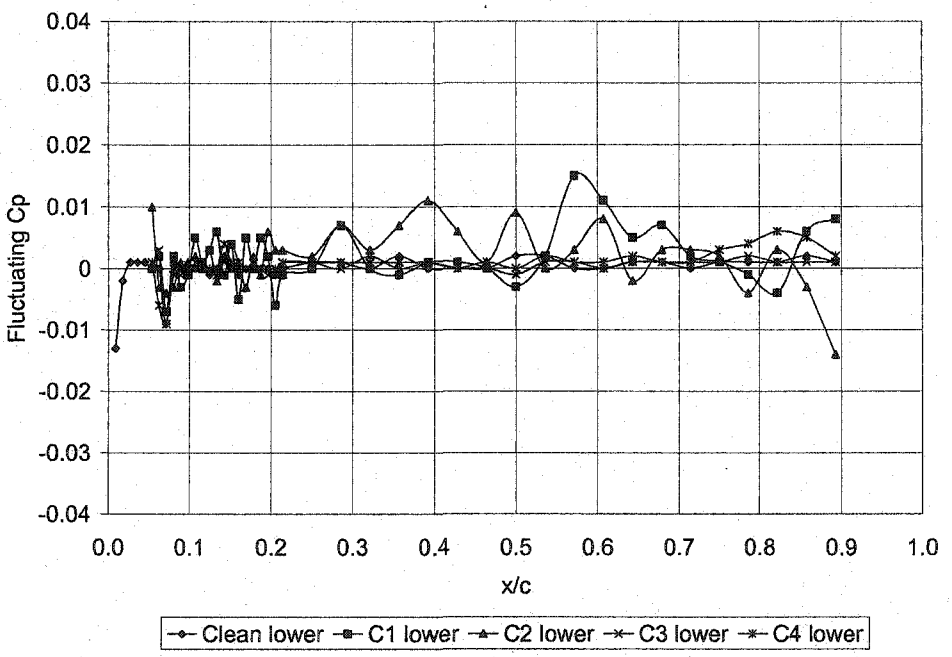

Figure 234 – Fluctuating Cp Dist., Re~1300000, α = 9 deg, Lower Surface

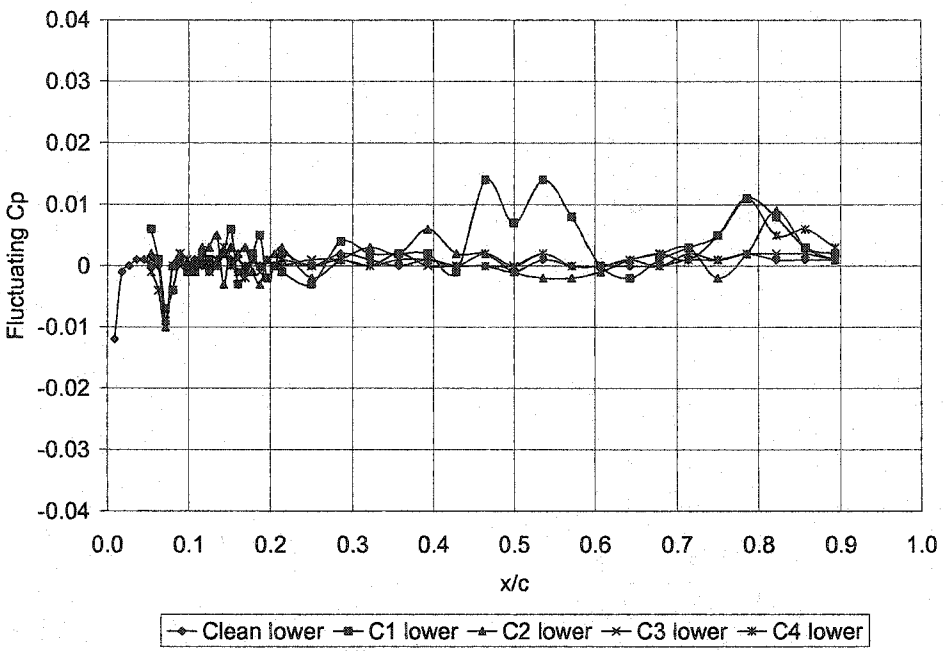

Figure 235 – Fluctuating Cp Dist., Re~1300000, α = 10 deg, Lower Surface

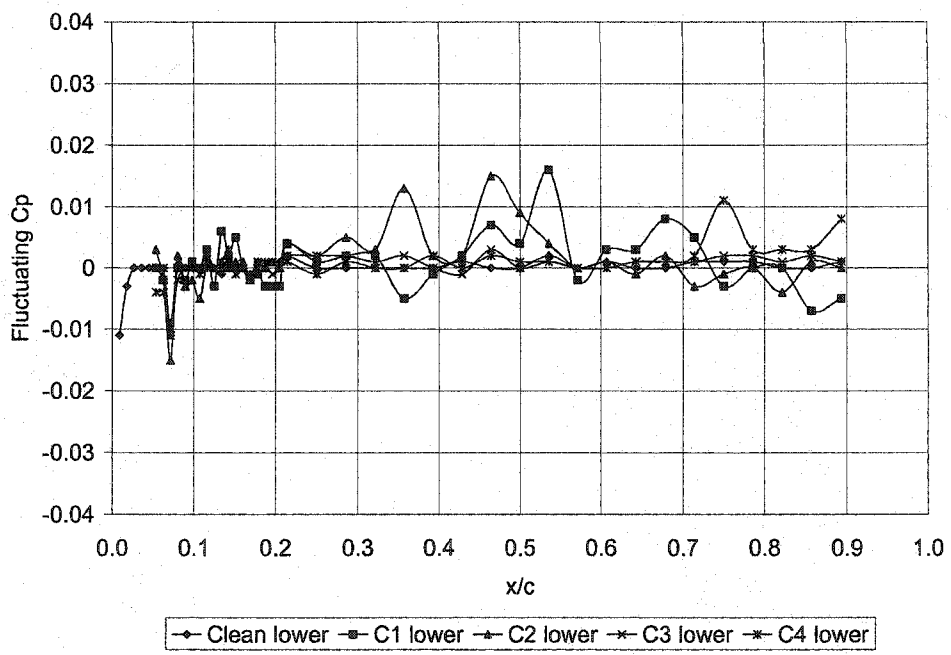

Figure 236 – Fluctuating Cp Dist., Re~1300000, α = 11 deg, Lower Surface

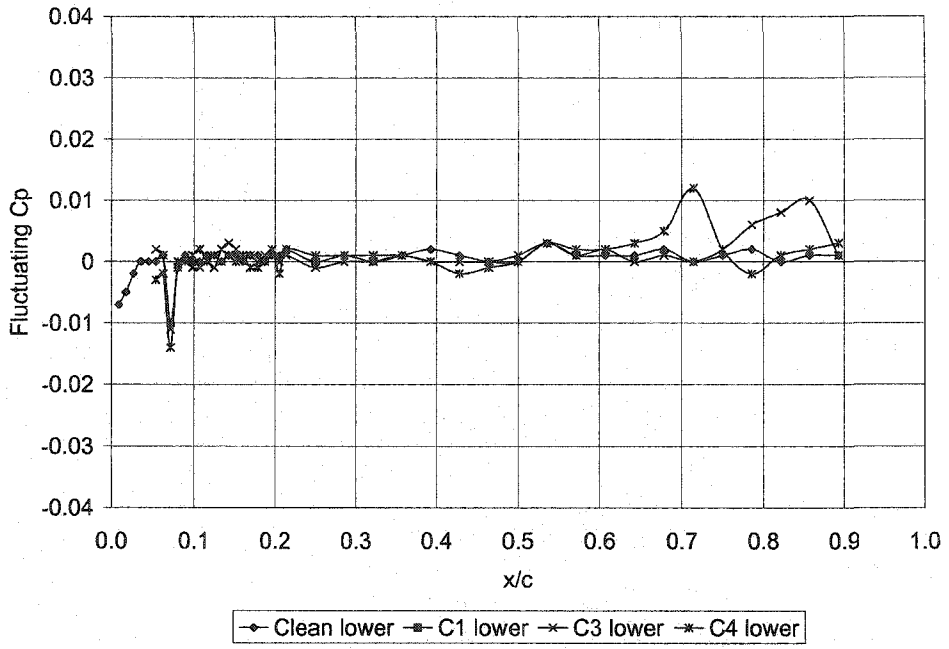

Figure 237 – Fluctuating Cp Dist., Re~1300000, α = 12 deg, Lower Surface

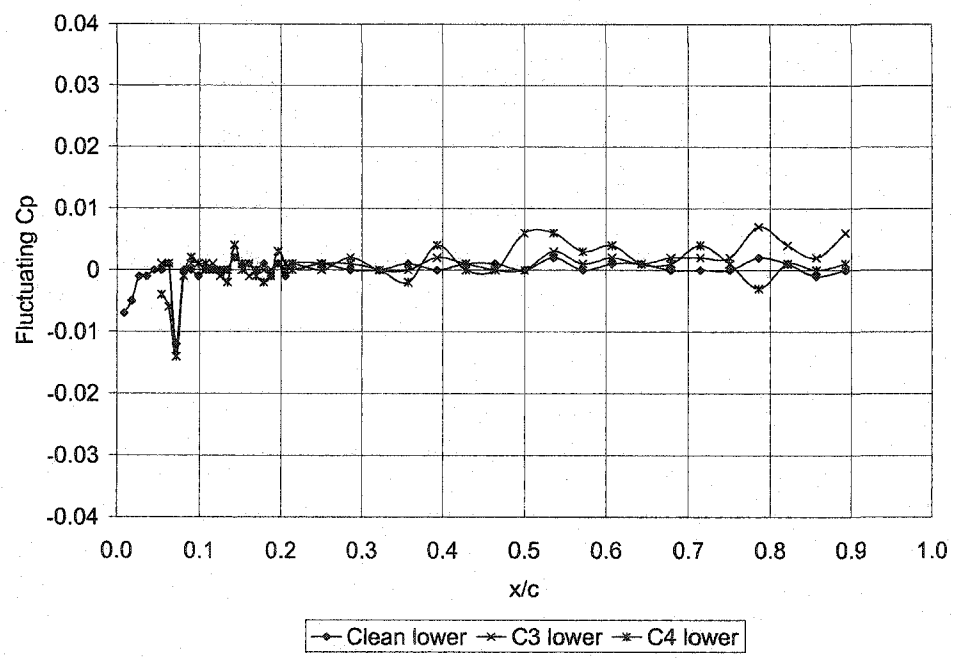

Figure 238 – Fluctuating Cp Dist., Re~1300000, α = 13 deg, Lower Surface

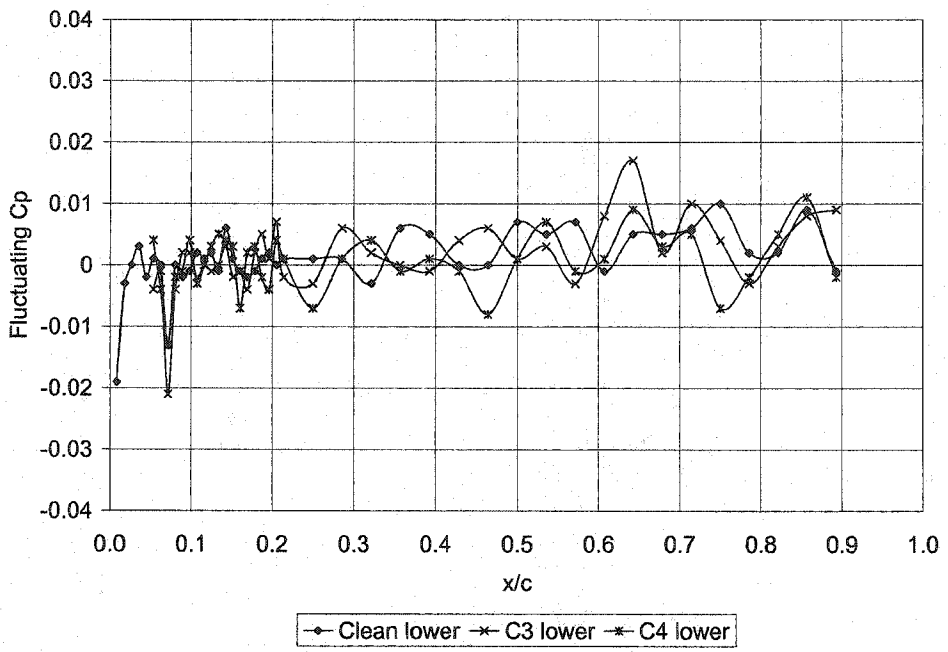

Figure 239 – Fluctuating Cp Dist., Re~1300000, α = 14 deg, Lower Surface

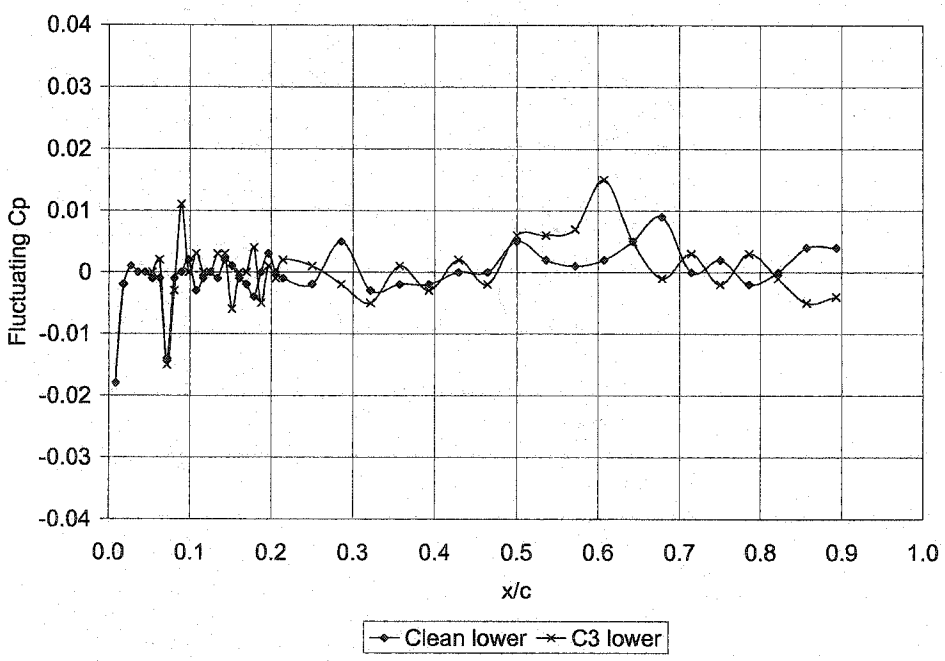

Figure 240 – Fluctuating Cp Dist., Re~1300000, α = 15 deg, Lower Surface

APPENDIX C – PRESSURE DISTRIBUTION RE# COMPARISON

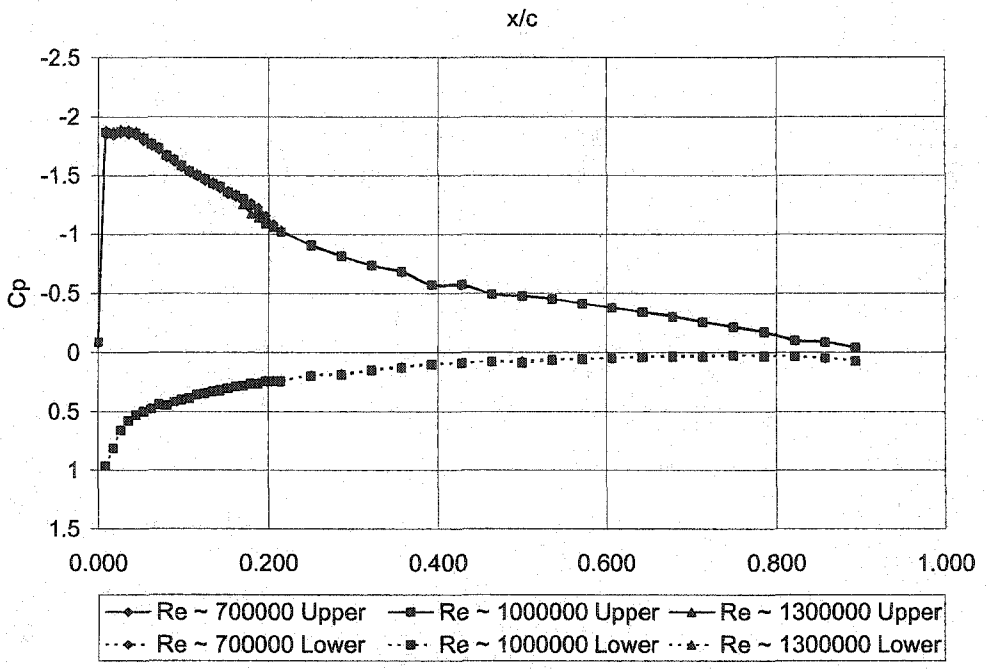

Figure 241 – Cp vs. x/c Reynolds Comparison for Clean AOA 6 Degrees

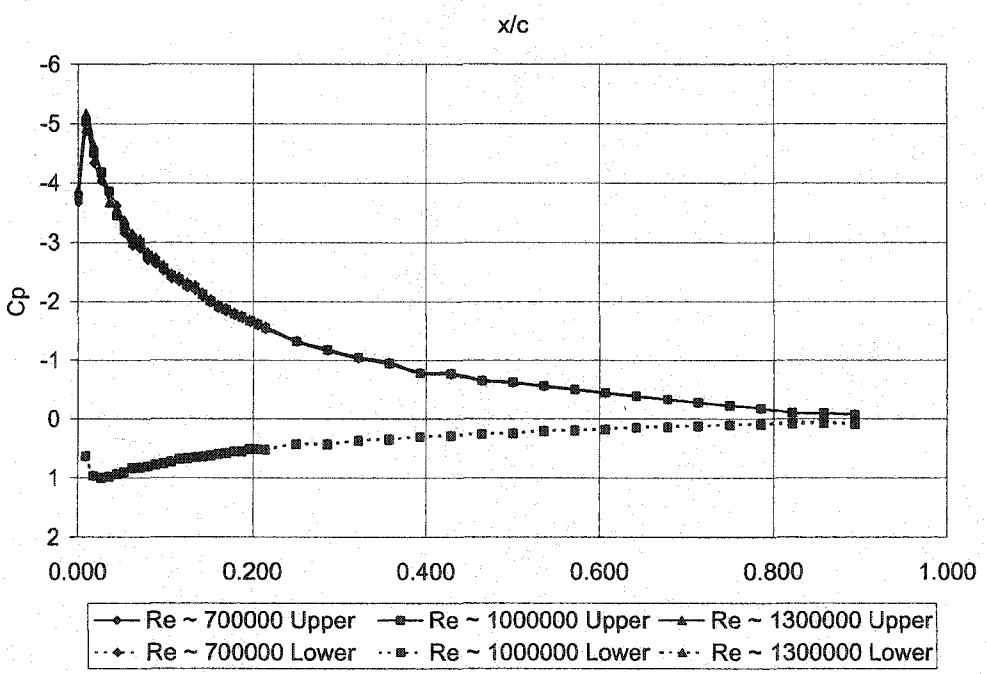

Figure 242 – Cp vs. x/c Reynolds Comparison for Clean AOA 12 Degrees

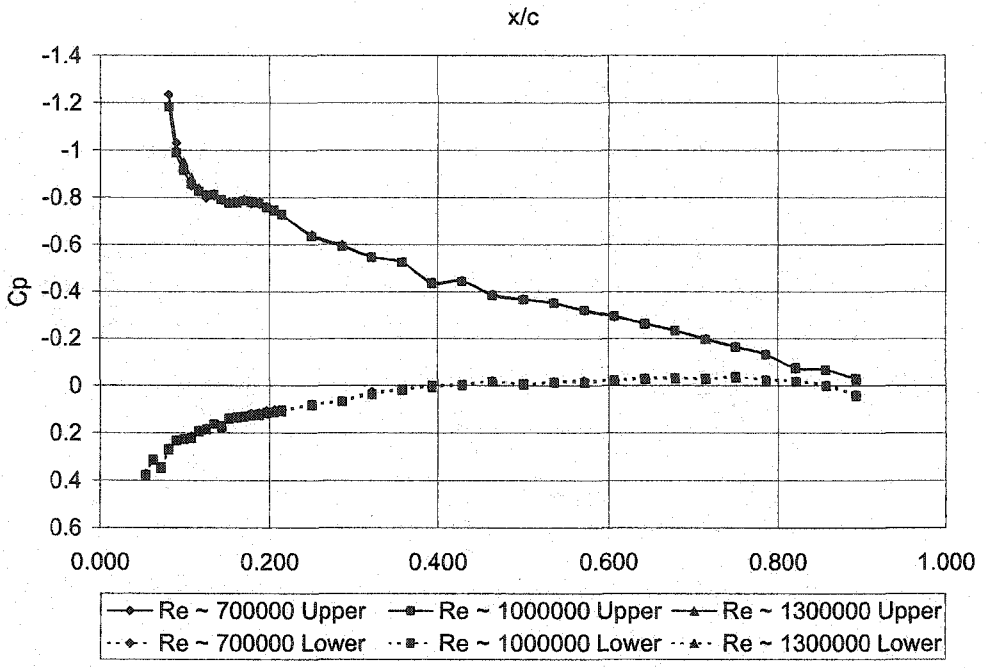

Figure 243 – Cp vs. x/c Reynolds Comparison for C1 AOA 4 Degrees

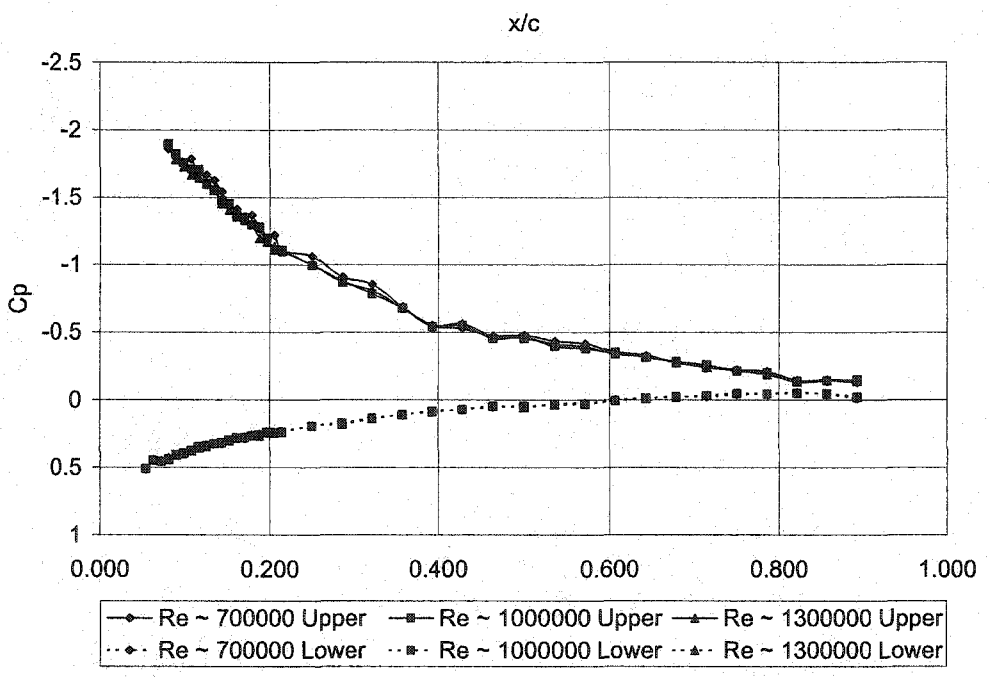

Figure 244 – Cp vs. x/c Reynolds Comparison for C1 AOA 8 Degrees

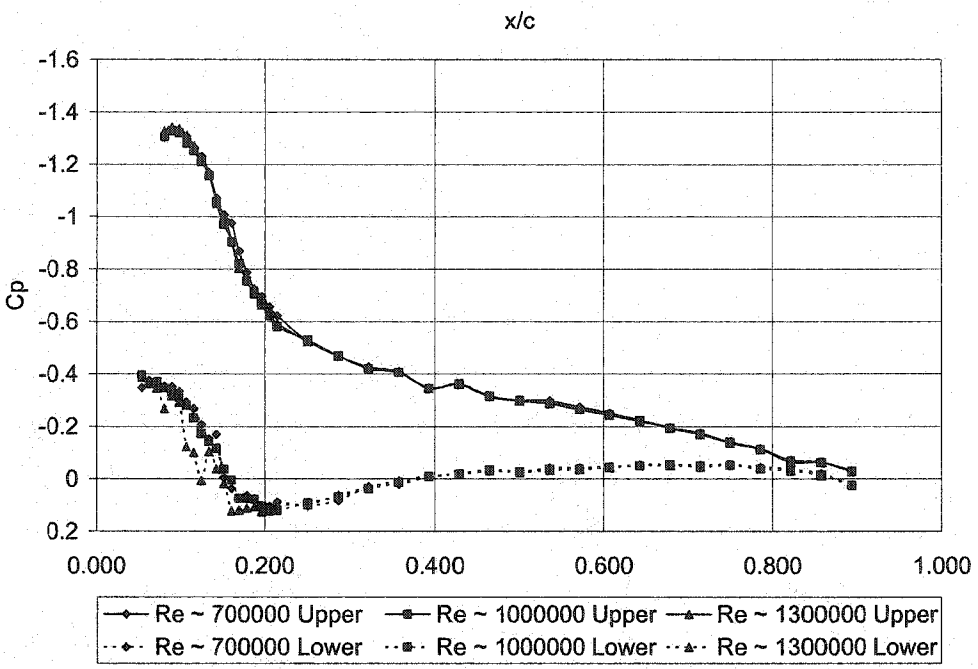

Figure 245 – Cp vs. x/c Reynolds Comparison for C2 AOA 3 Degrees

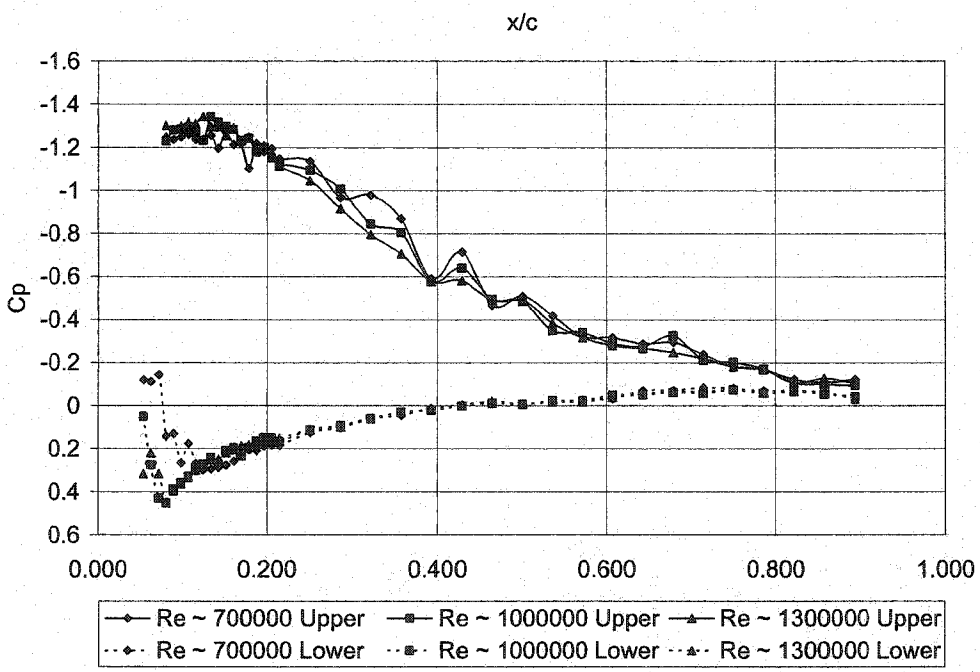

Figure 246 – Cp vs. x/c Reynolds Comparison for C2 AOA 6 Degrees

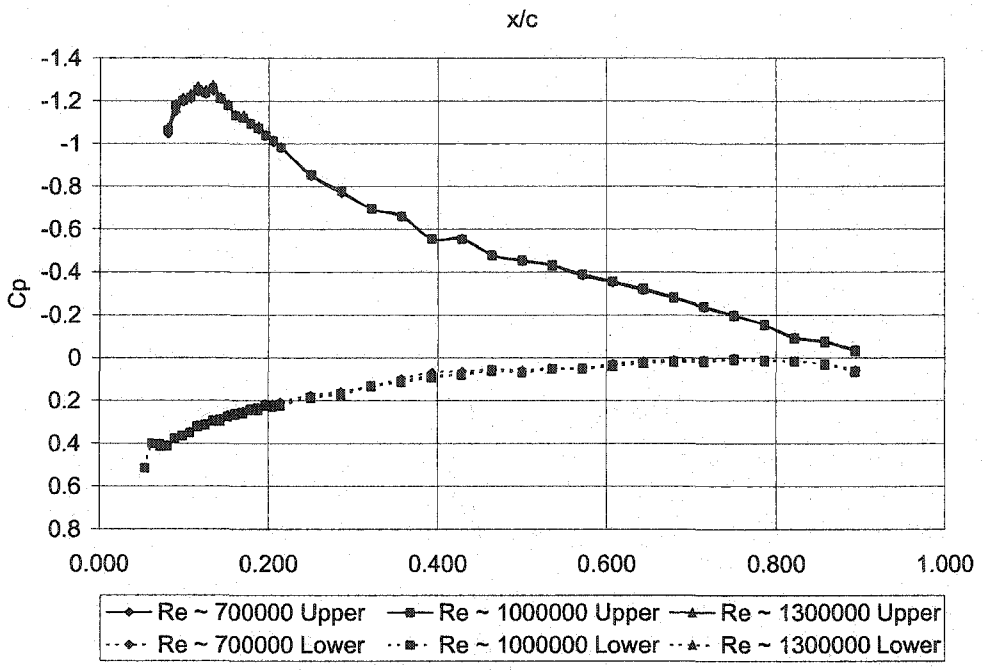

Figure 247 – Cp vs. x/c Reynolds Comparison for C3 AOA 6 Degrees

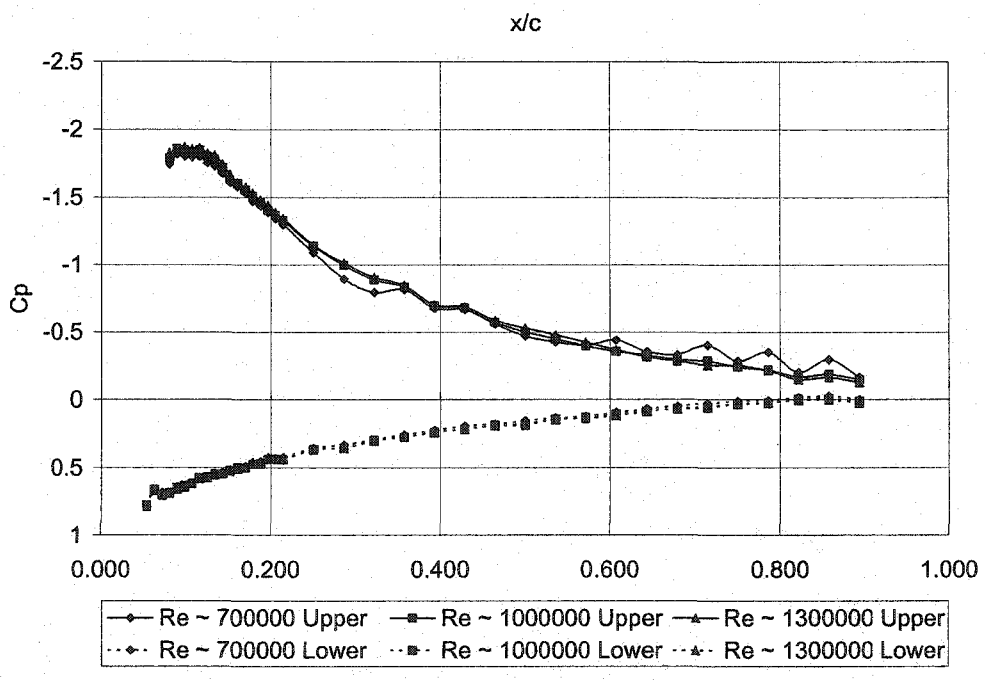

Figure 248 – Cp vs. x/c Reynolds Comparison for C3 AOA 12 Degrees

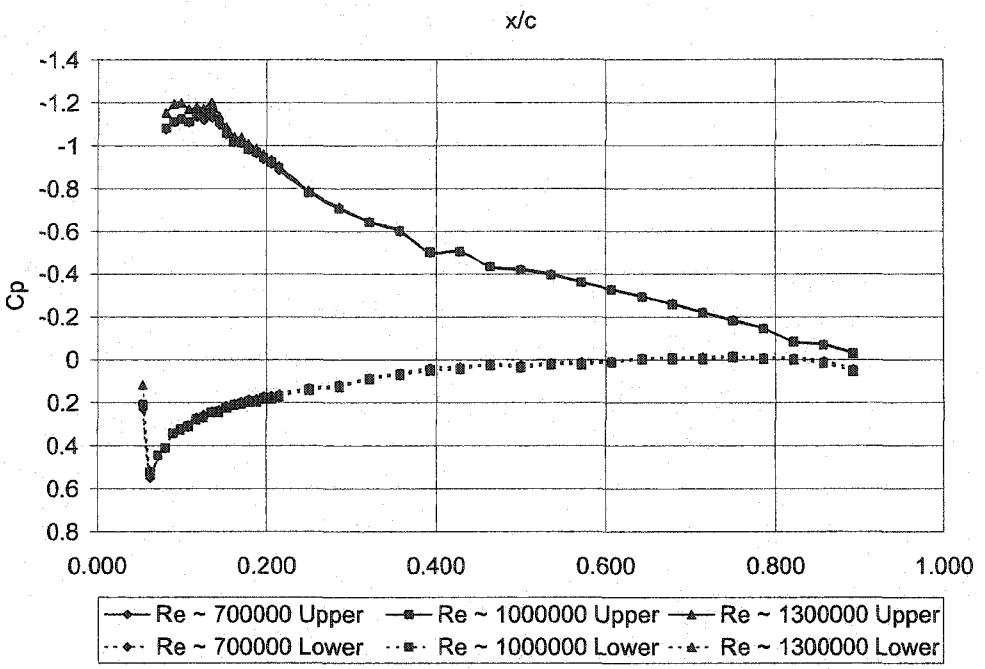

Figure 249 – Cp vs. x/c Reynolds Comparison for C4 AOA 5 Degrees

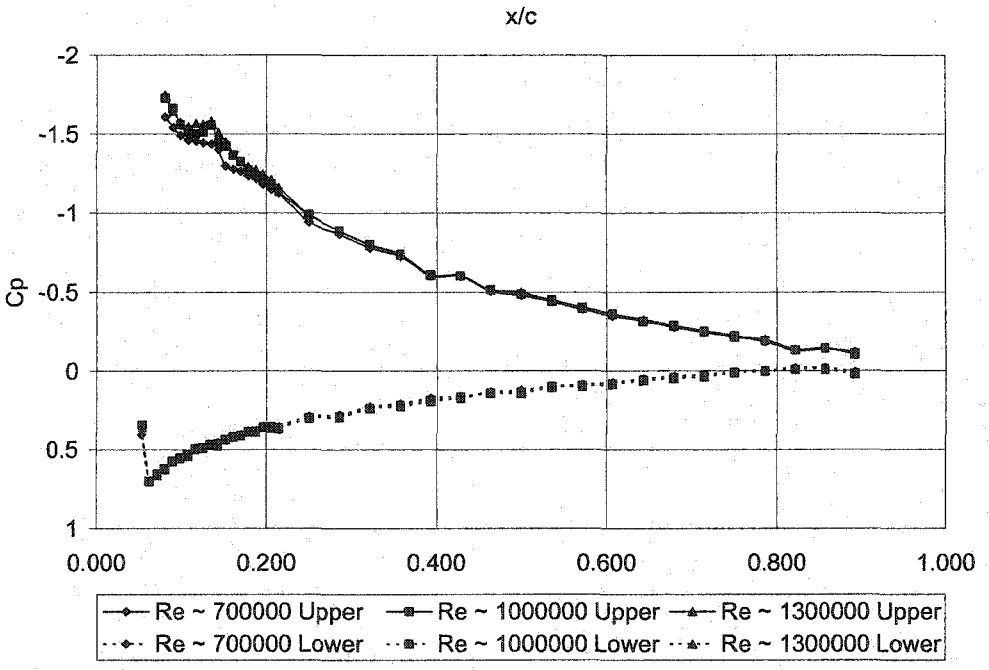

Figure 250 – Cp vs. x/c Reynolds Comparison for C4 AOA 10 Degrees

APPENDIX D – STALL MARGIN PORTS, RE# COMPARISON

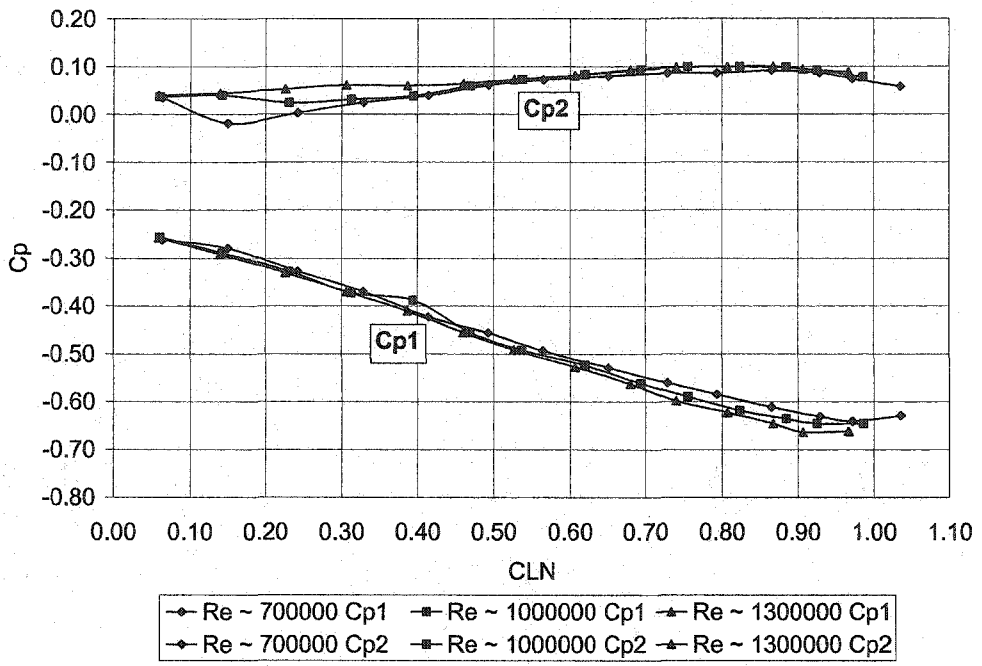

Figure 251 – Cp vs. C_{LN} Reynolds Comparison for Clean ports Cp1 and Cp2

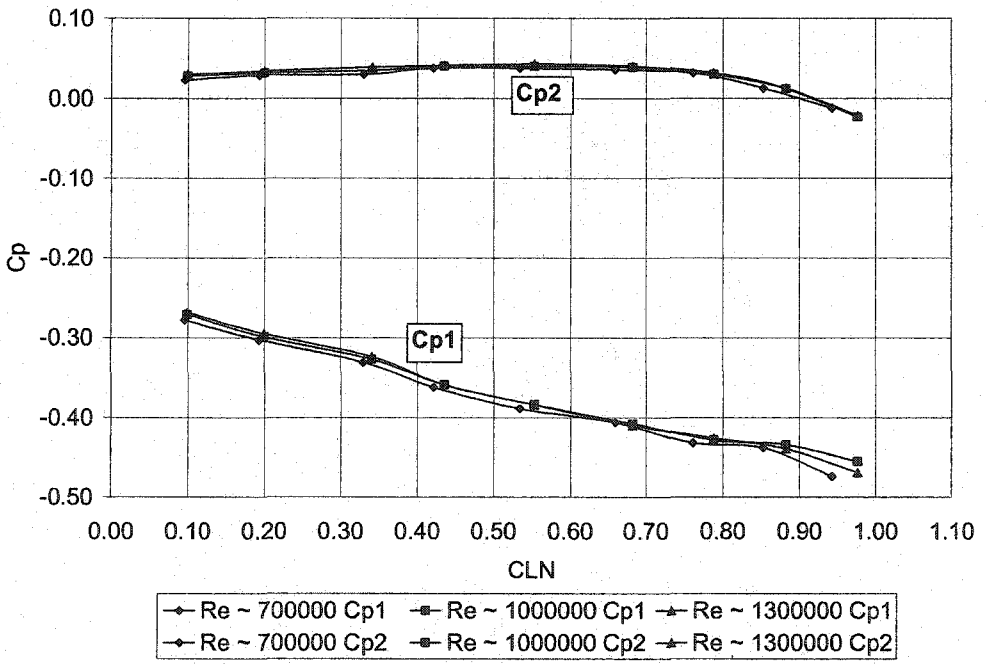

Figure 252 – Cp vs. C_{LN} Reynolds Comparison for Ice C1 ports Cp1 and Cp2

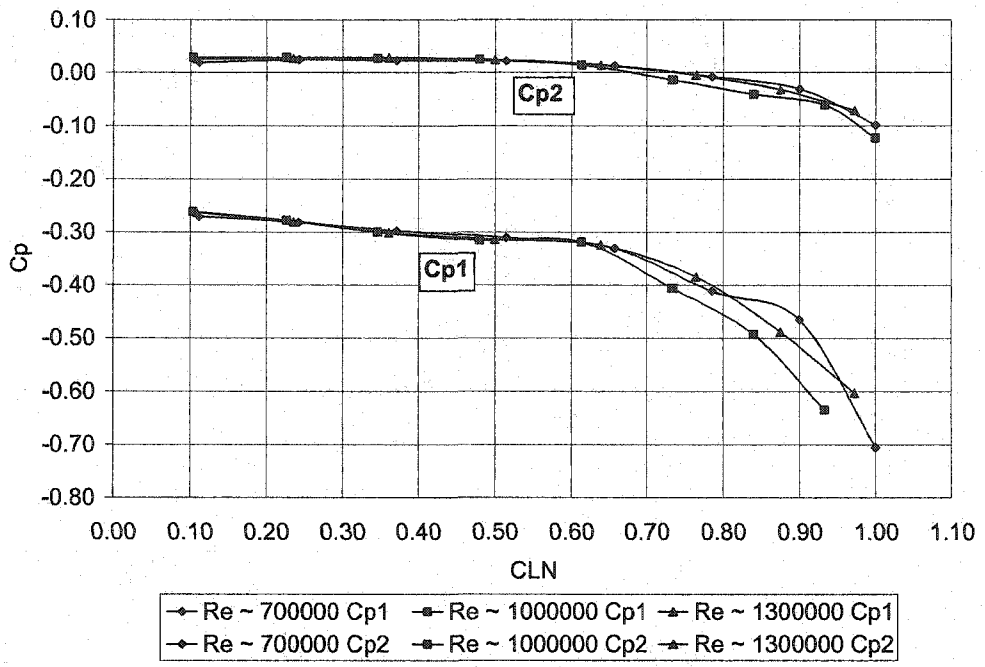

Figure 253 – Cp vs. C_{LN} Reynolds Comparison for Ice C2 ports Cp1 and Cp2

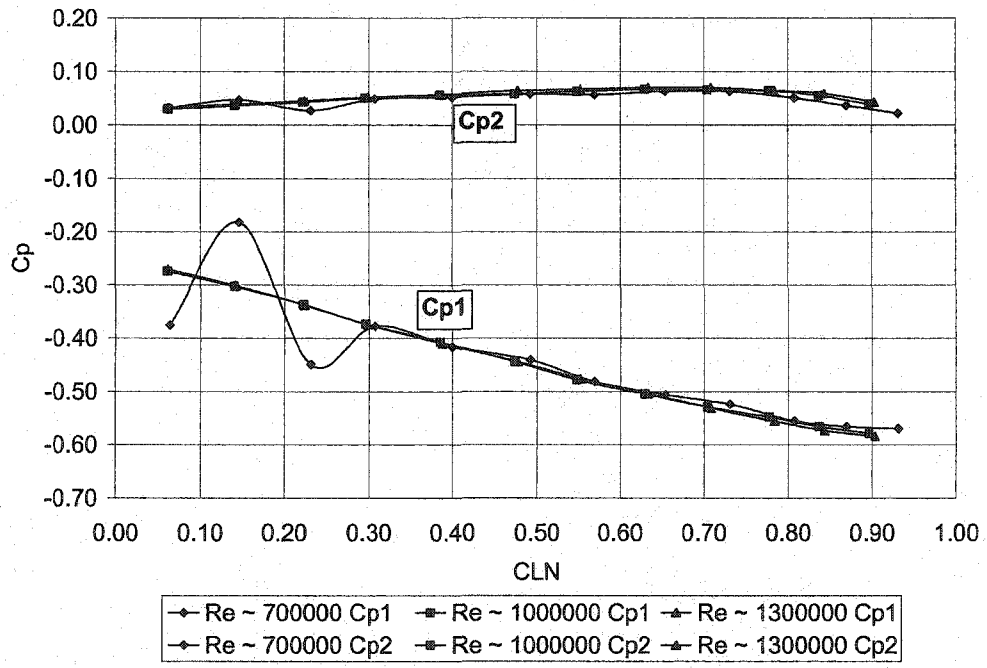

Figure 254 – Cp vs. C_{LN} Reynolds Comparison for Ice C3 ports Cp1 and Cp2

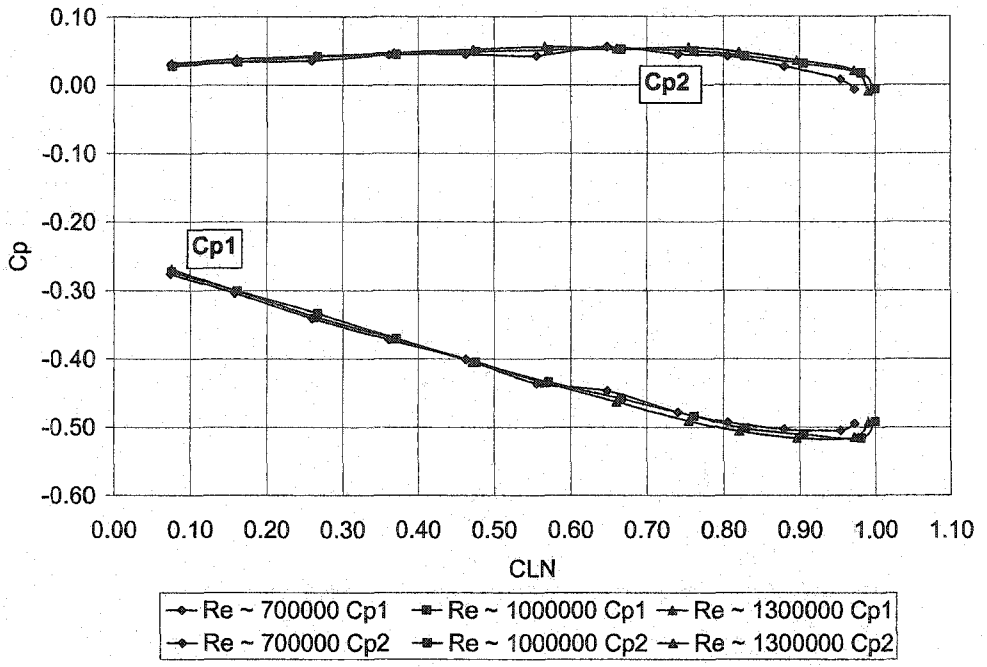

Figure 255 – Cp vs. C_{LN} Reynolds Comparison for Ice C4 ports Cp1 and Cp2

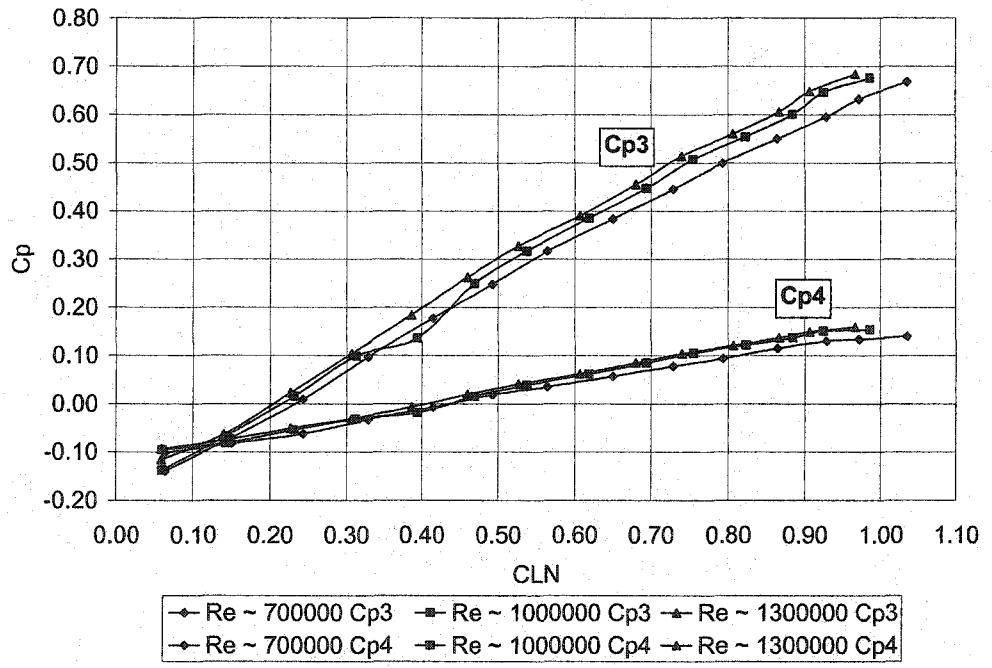

Figure 256 – Cp vs. C_{LN} Reynolds Comparison for Clean ports Cp3 and Cp4

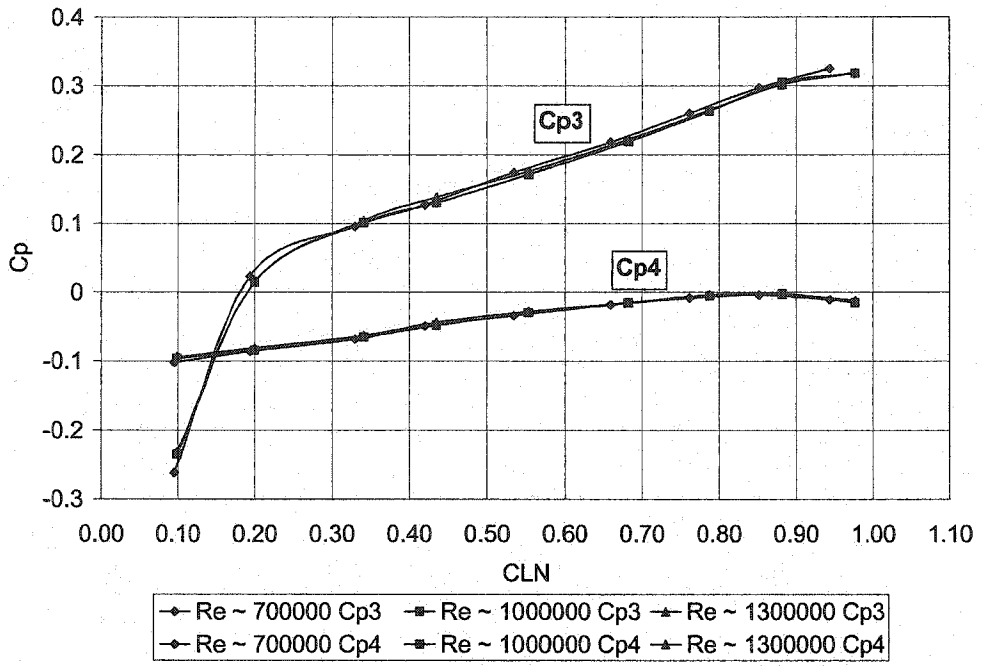

Figure 257 – Cp vs. C_{LN} Reynolds Comparison for Ice C1 ports Cp3 and Cp4

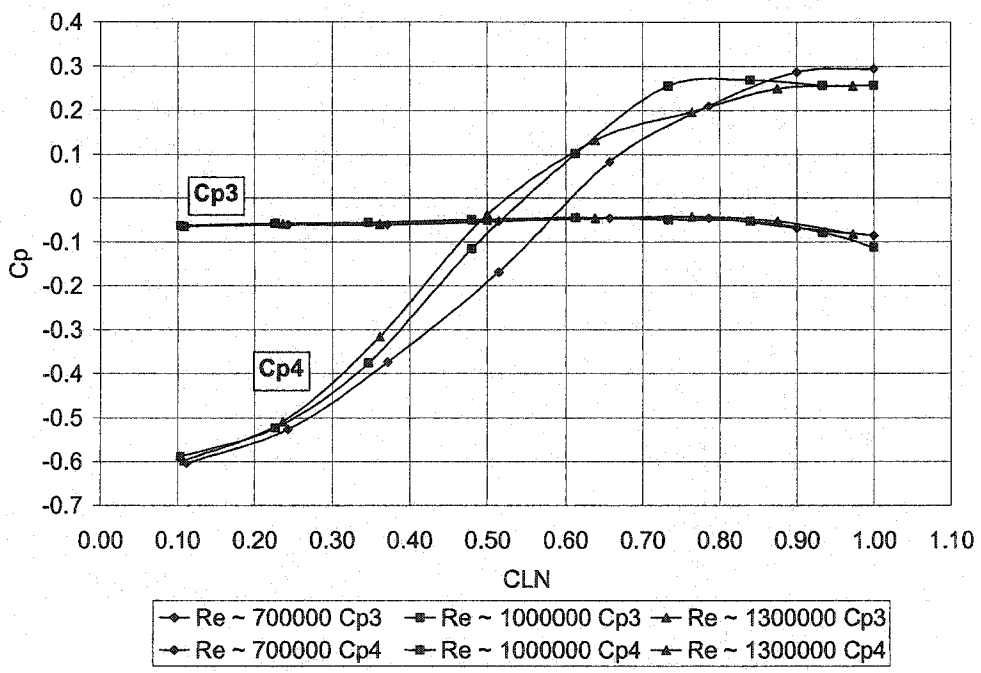

Figure 258 – Cp vs. C_{LN} Reynolds Comparison for Ice C2 ports Cp3 and Cp4

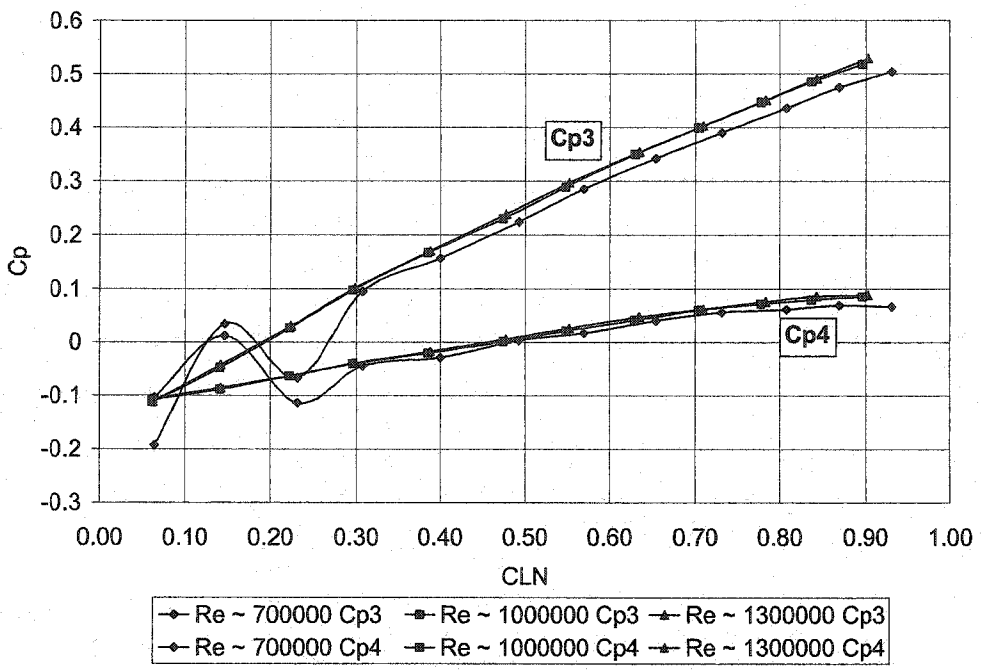

Figure 259 – Cp vs. C_{LN} Reynolds Comparison for Ice C3 ports Cp3 and Cp4

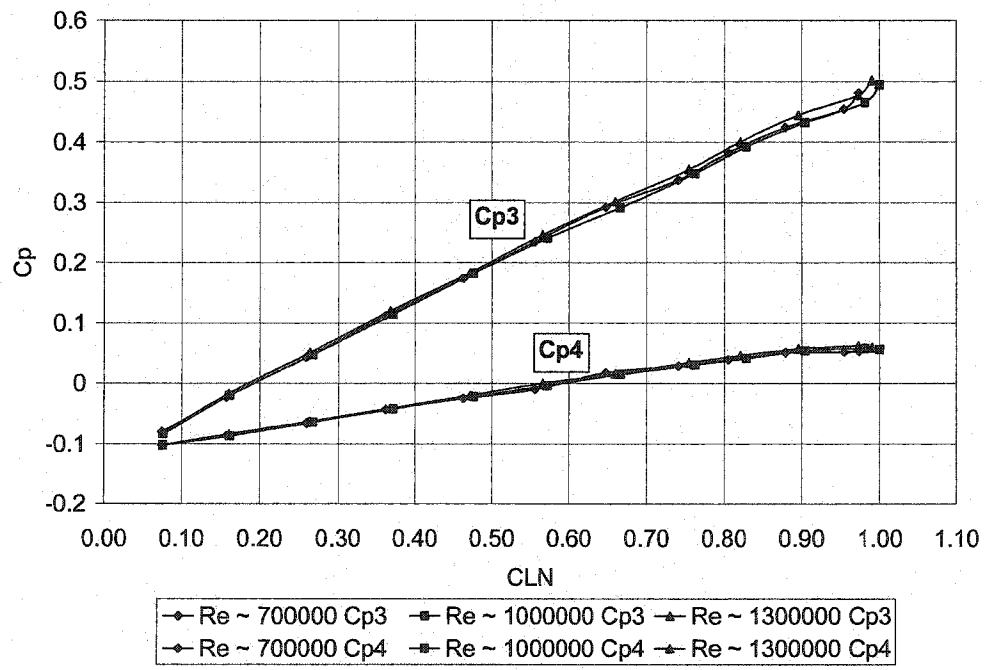

Figure 260 – Cp vs. C_{LN} Reynolds Comparison for Ice C4 ports Cp3 and Cp4

APPENDIX E – SMOKE WIRE FLOW VISUALIZATION

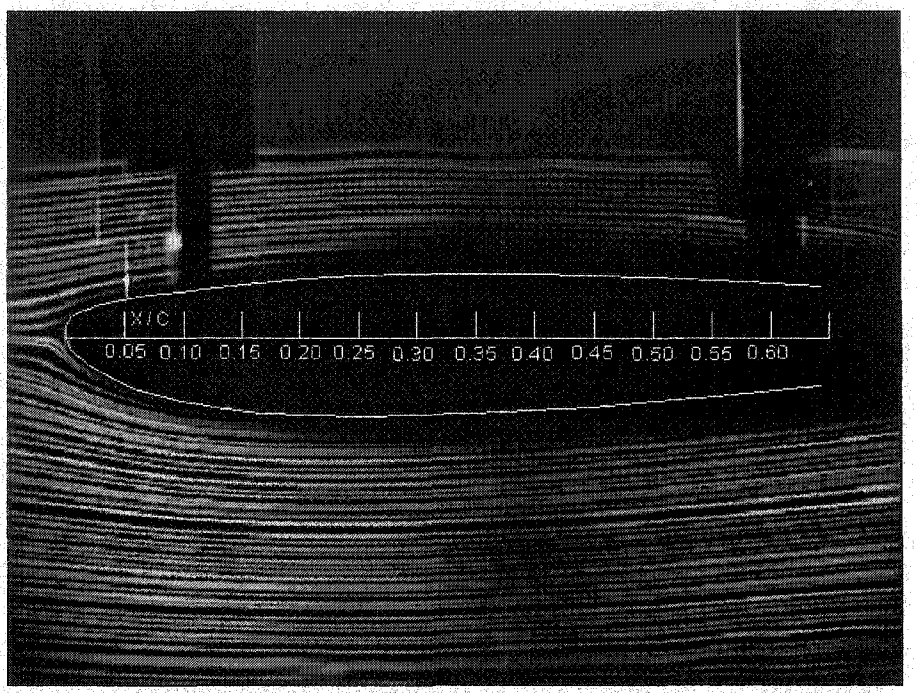

Figure 261 – Clean AOA 0 degrees

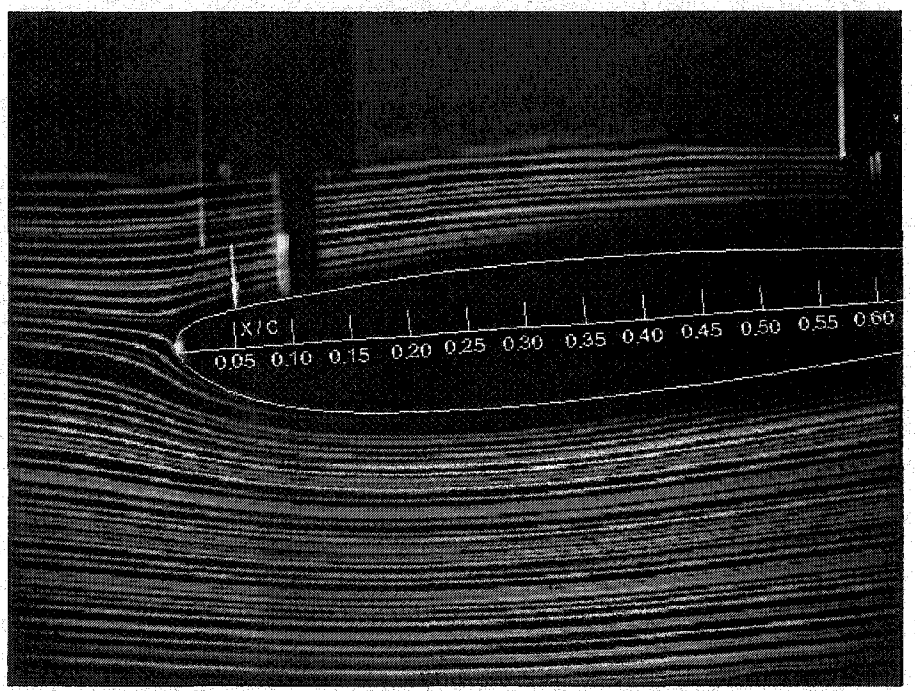

Figure 262 – Clean AOA 4 degrees

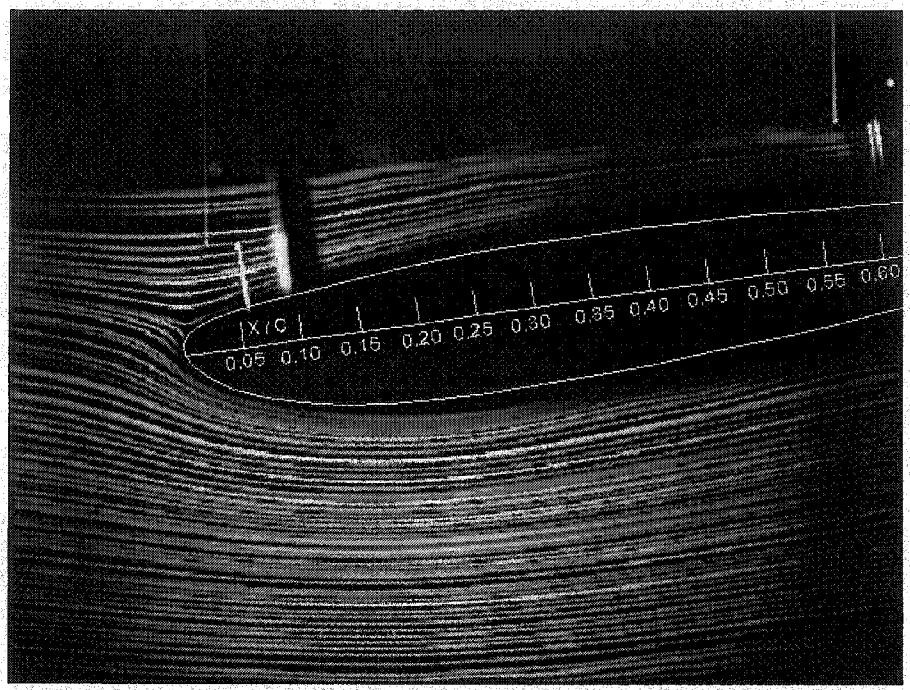

Figure 263 – Clean AOA 8 degrees

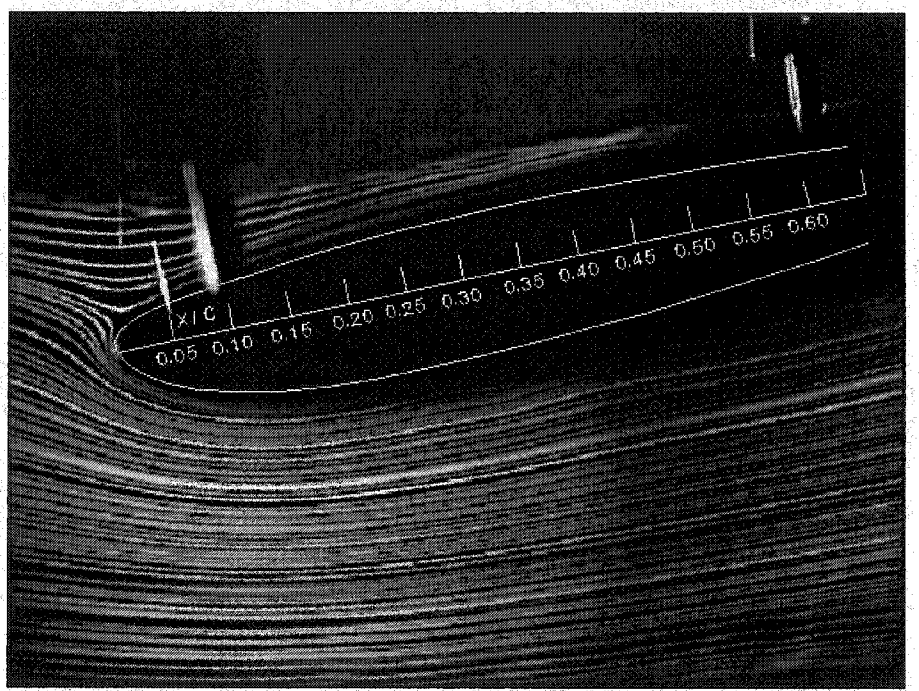

Figure 264 – Clean AOA 12 degrees

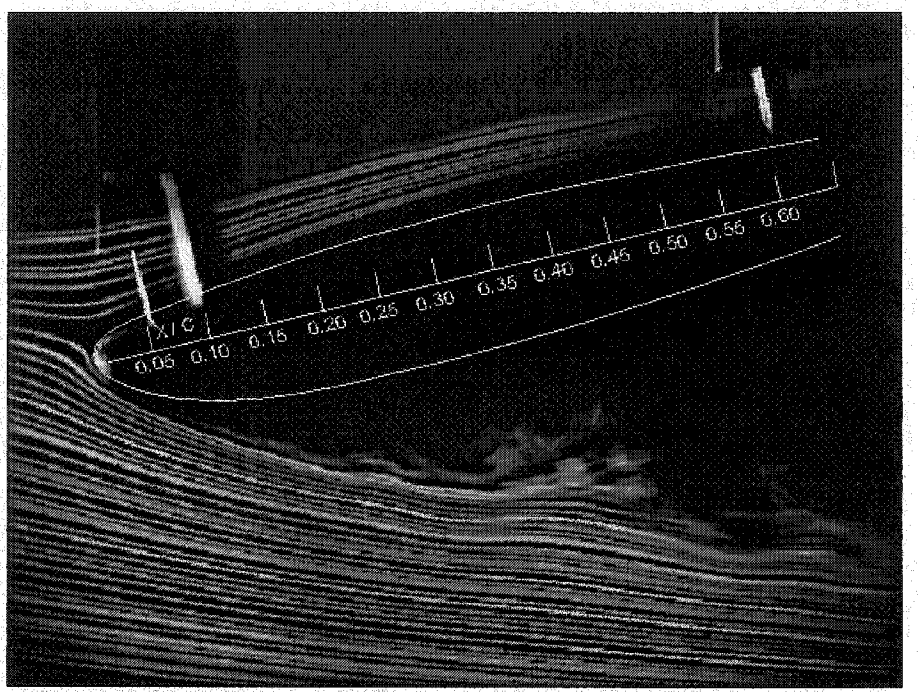

Figure 265 – Clean AOA 13.5 degrees

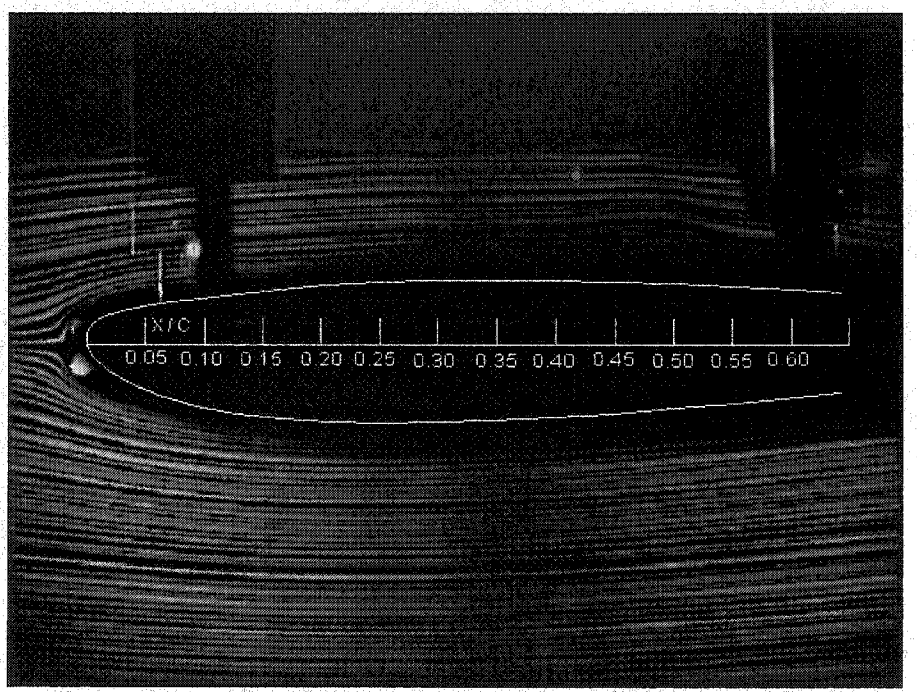

Figure 266 – C1 AOA 0 degrees

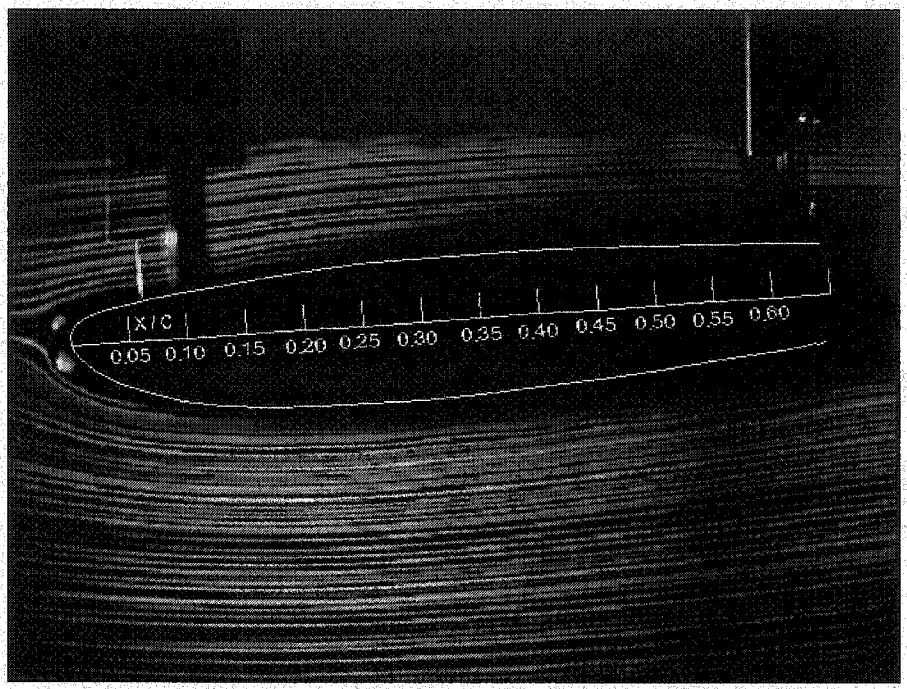

Figure 267 – C1 AOA 4 degrees

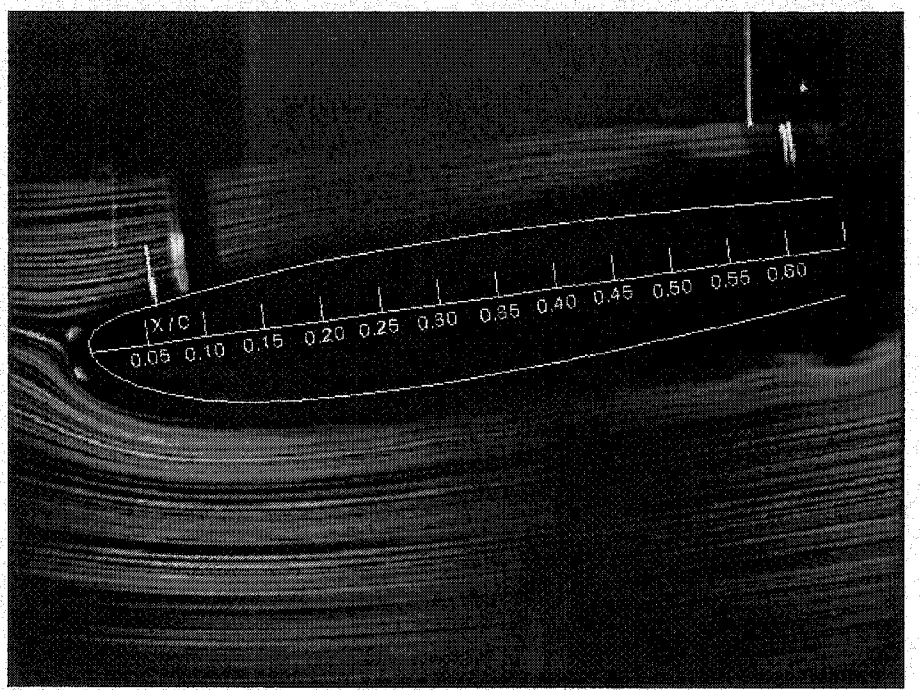

Figure 268 – C1 AOA 8 degrees

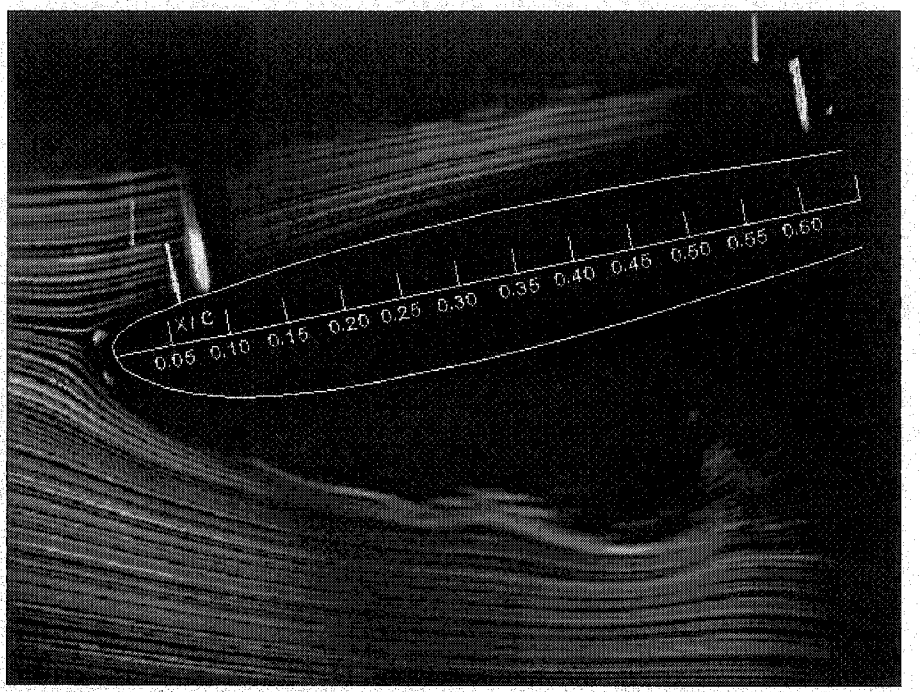

Figure 269 – C1 AOA 12 degrees

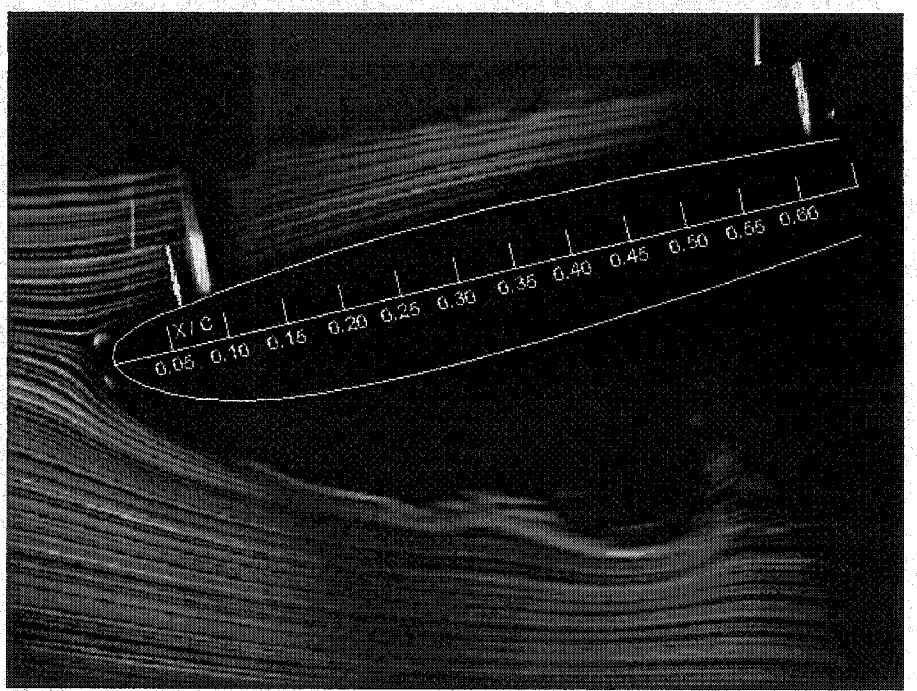

Figure 270 – C1 AOA 13.5 degrees

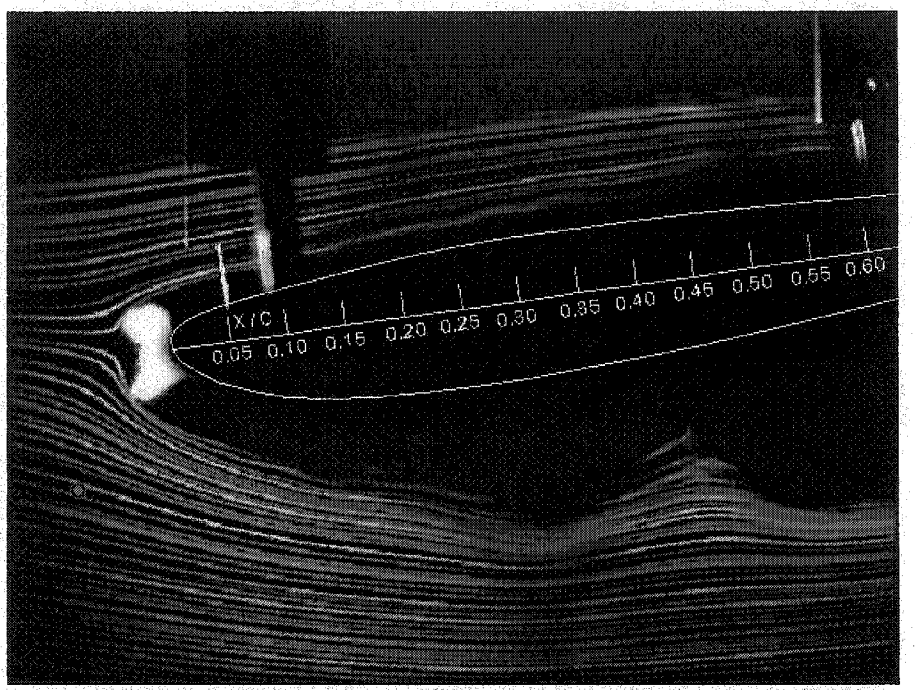

Figure 273 – C2 AOA 8 degrees

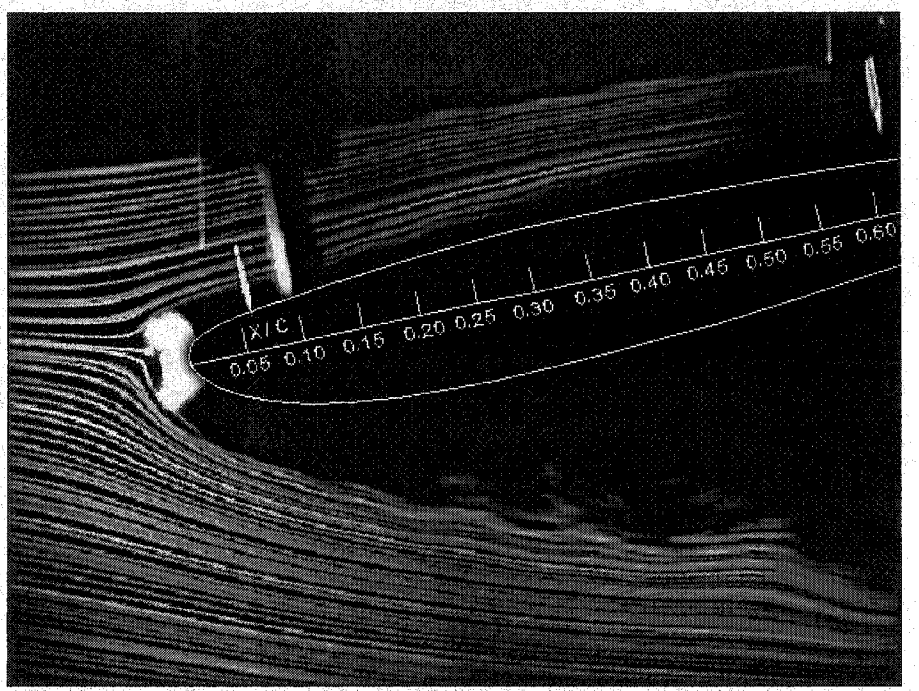

Figure 274 – C2 AOA 12 degrees

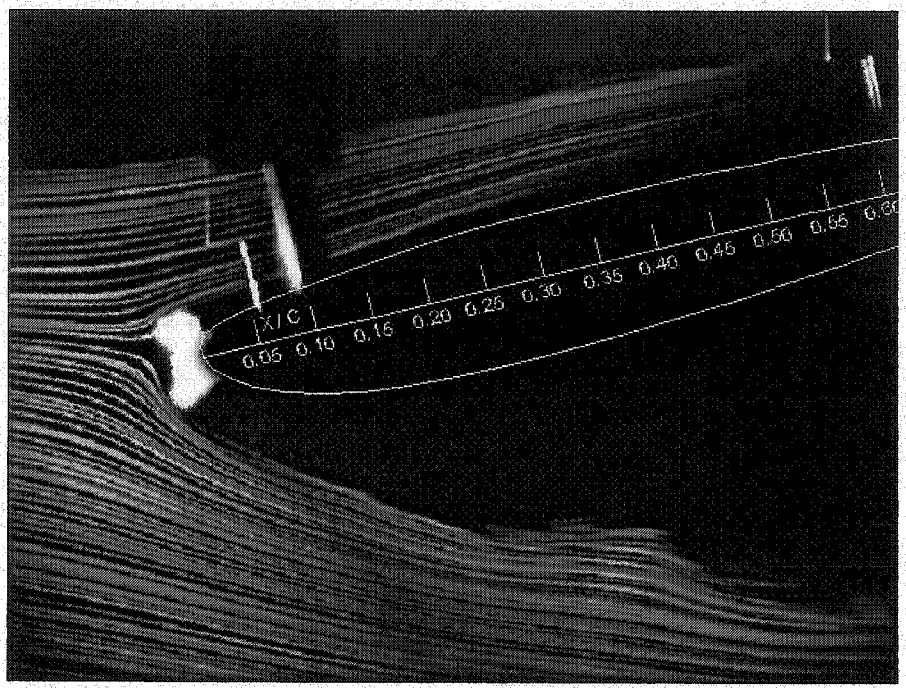

Figure 275 – C2 AOA 13.5 degrees

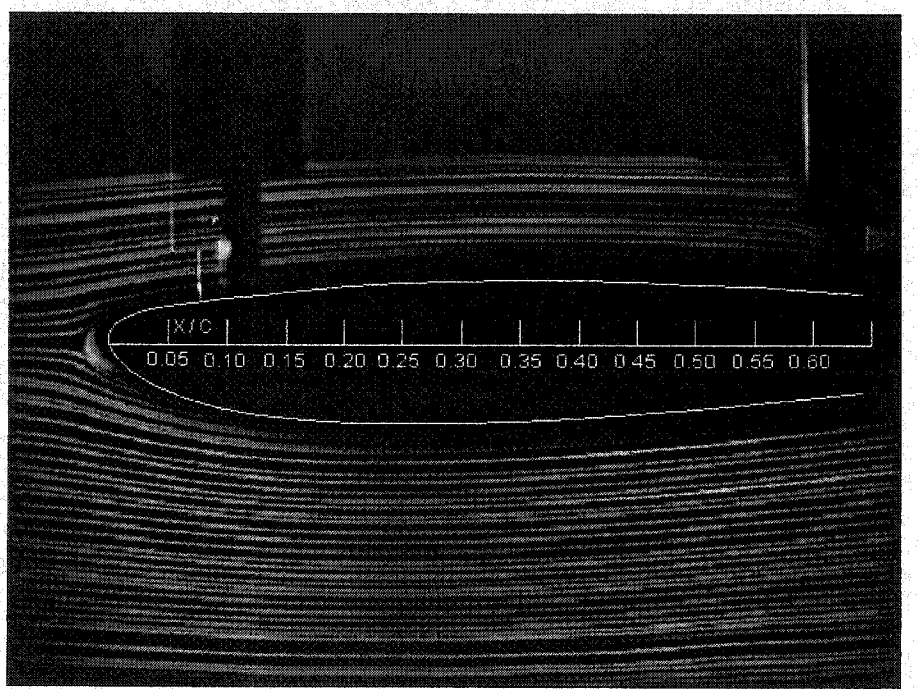

Figure 276 – C3 AOA 0 degrees

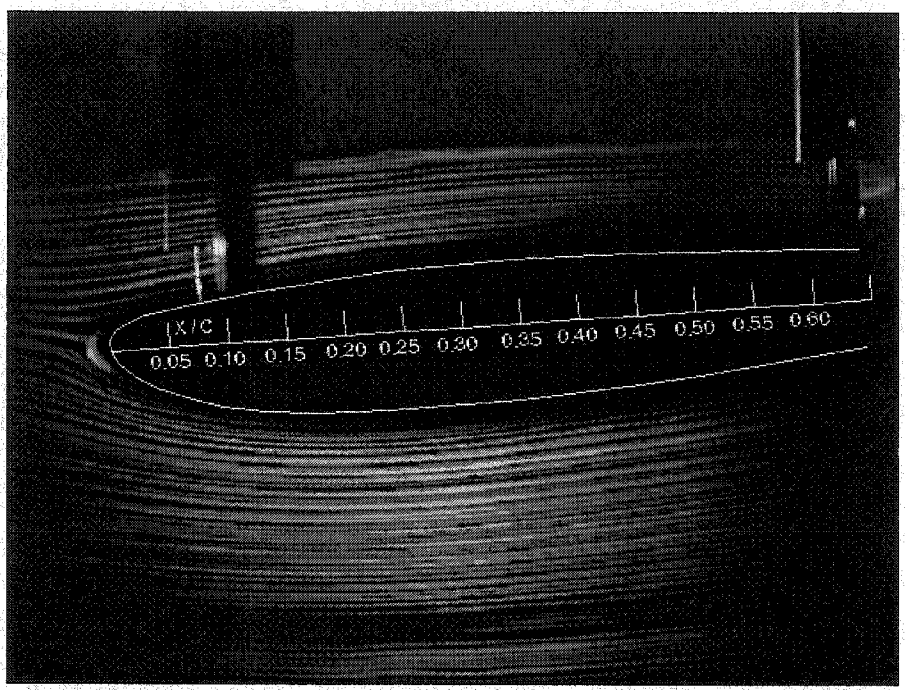

Figure 277 – C3 AOA 4 degrees

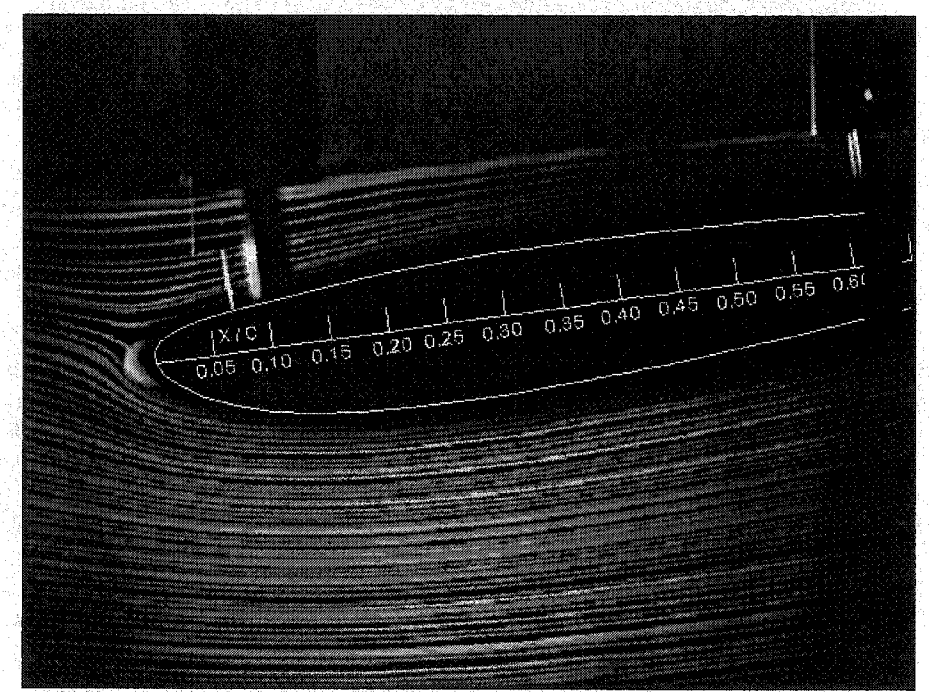

Figure 278 – C3 AOA 8 degrees

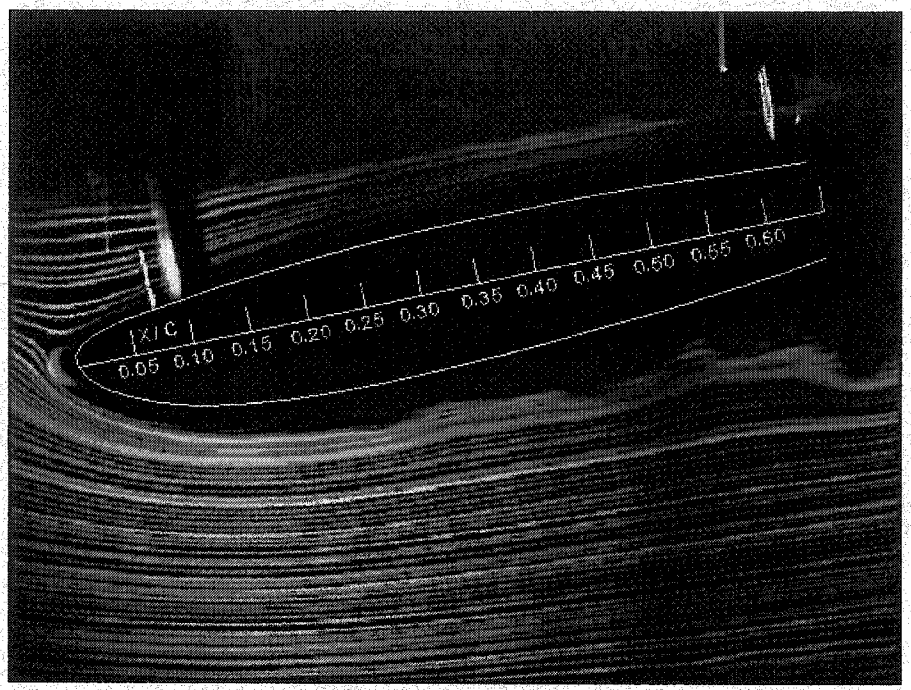

Figure 279 – C3 AOA 12 degrees

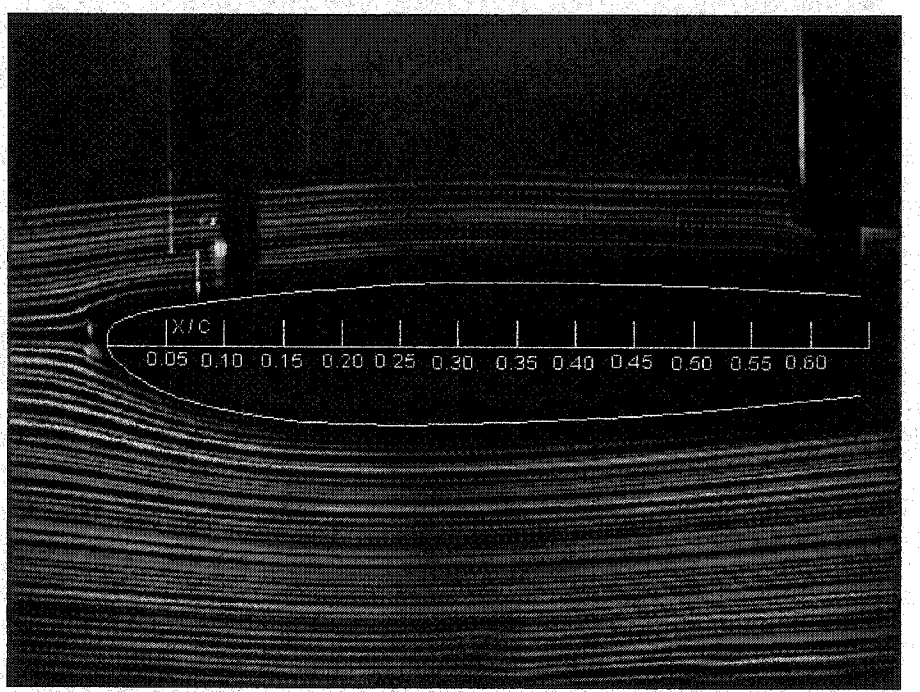

Figure 280 – C4 AOA 0 degrees

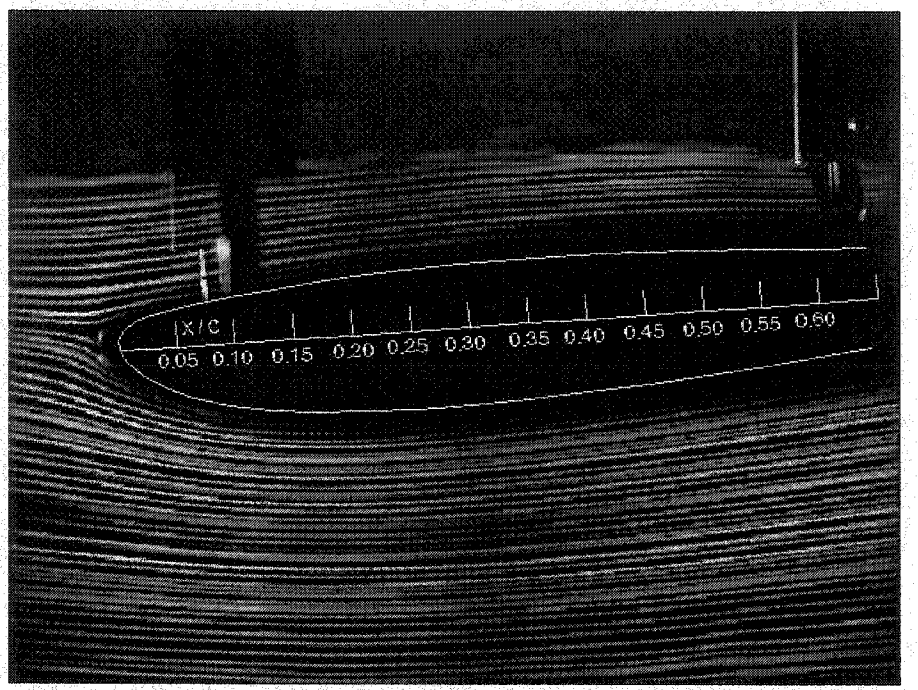

Figure 281 – C4 AOA 4 degrees

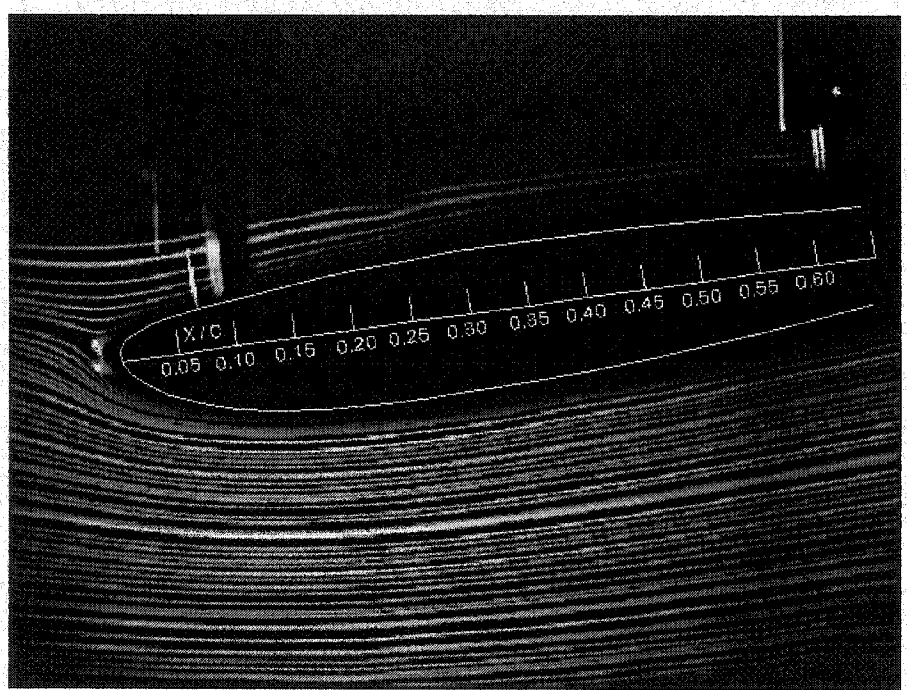

Figure 282 – C4 AOA 8 degrees

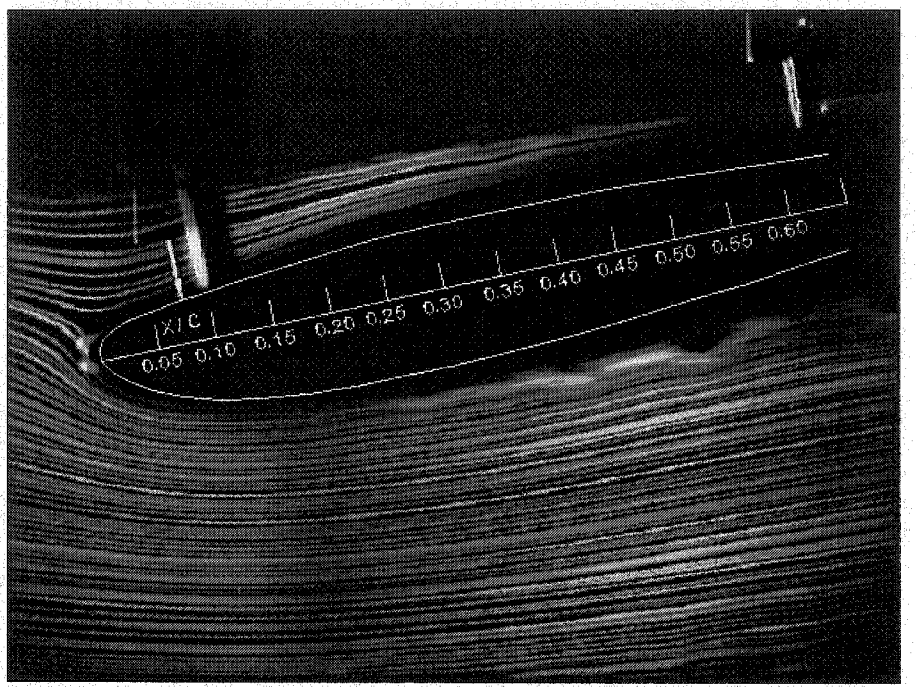

Figure 283 – C4 AOA 12 degrees

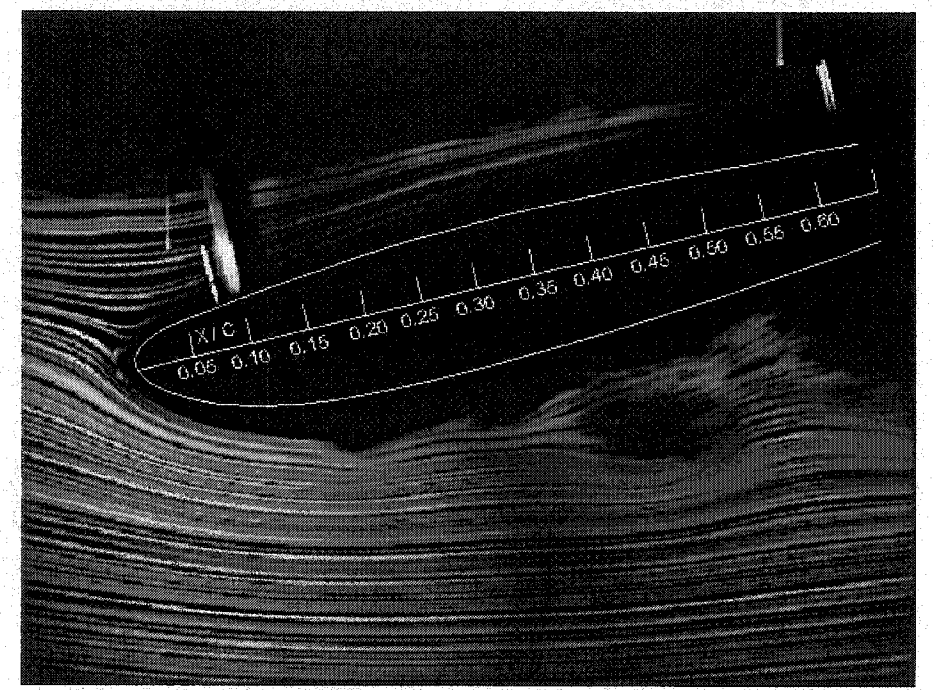

Figure 284 – C4 AOA 13.5 degrees